Stokes polarimetry and magnetometry using a thermal Rb vapour in the Voigt geometry with large magnetic field

PONCIANO-OJEDA, FRANCISCO,SEBASTIAN

Stokes polarimetry and magnetometry using a thermal Rb vapour in the Voigt geometry with large magnetic fields

Francisco Sebastian Ponciano-Ojeda

Abstract

We present investigations of magneto-optical phenomena using a ^{87}Rb thermal vapour in large magnetic fields. At this point, in the hyperfine Paschen-Back regime, optical transitions can be separated by more than their Doppler-broadened linewidth, providing a high level of control over the atomic system and a simpler theoretical model for studying atom-light-magnetic field interactions. In this context, we study the spectra of ^{87}Rb at magnetic fields of 0.4 T and 1.5 T in the Voigt geometry. In both cases we find excellent agreement between experimental and theoretical absorption spectra. With the 1.5 T field we also study polarisation changes induced in the light by the atoms subject to a large magnetic field. Using this approach, we consider the practical applications of our system as a vector magnetometer. We present a scheme that eliminates most sources of systematic errors in the measurement of the field strength by using pairs of transitions that cancel excited-state terms in the energy shifts. Finally, we extend the concepts and ideas investigated to an application in precision thermometry. We discuss how good understanding of the spectra and the magnetic field strength potentially allow detection of small differences in different spectral features, which could then be traced to the effect of the Boltzmann factor, $k_{\mathrm{B}}T$, on the atomic populations.

Stokes polarimetry and magnetometry using a thermal Rb vapour in the Voigt geometry with large magnetic fields

Francisco Sebastian Ponciano-Ojeda

A thesis submitted in partial fulfilment
of the requirements for the degree of
Doctor of Philosophy

Department of Physics
Durham University

20th July 2021

Contents

List of Figures

List of Tables

Declaration

I confirm that no part of the material offered has previously been submitted by myself for a degree in this or any other University. Where material has been generated through joint work, the work of others has been indicated.

Francisco Sebastian Ponciano-Ojeda
Durham, 20th July 2021

Acknowledgements

First and foremost, I would like to thank my supervisors, Prof. Ifan Hughes and Prof. Charles Adams, for the incredible opportunity to carry out my studies at Durham. Ifan has been a great source of encouragement and motivation in both my academic and professional development over the past three and a half years. His supply of anecdotes and light-hearted conversation have always created a very pleasant working environment, and from the start of my PhD his welcoming attitude made me feel at home in Durham. Without his support, I would likely have ended up elsewhere in the world and this thesis would not exist. The experience and creativity of Charles has helped give this research direction and insight from its conception to its current state. I would also like to take this opportunity to gratefully acknowledge the Durham Doctoral Scholarship provided to me by Durham University.

Over my PhD I was fortunate enough to see the evolution of AtMol (as it was known when I arrived) into the Quantum Light & Matter group in its current form. The years spent as a part of this group have been very enjoyable and have open my eyes to many new things, in great part thanks to the wonderful community of people I have been able to interact with. In particular, I would like to thank: Renju, James, Clare, Fraser, Danny and Liz for their willingness to listen and help with whatever problem was at hand, be it in or out of the lab; Nick, for making the early arrivals into the office a rich period of philosophical and engaging discussions; Josh, for his amazing kindness; and to all the members of fAtMol (long may it continue) for providing a space for forgetting about the woes of life in the lab with cakes.

Special thanks go to Fraser, who kindly provided a significant amount of time and energy to proof-reading this thesis – best of luck to him for the future. I am also greatly indebted to James, for without his help and expertise in many areas much of the work that was carried out would not have been anywhere near its current form. As an experimental physicist I must also express my gratitude to the hard work and skills of many of the staff at the Durham Physics Department that have made working in a lab possible. In particular, thanks to Stephen Lishman and the staff of the mechanical workshop, who helped with the construction of many of the mechanical components used in the various experiments.

And last, but not least, my everlasting thanks to my family, who have been the foundation and greatest support over more than a decade of studies. A mis padres, Francisco y Margarita, por todo su amor, su apoyo, y sus consejos para siempre seguir por el camino que he elegido hacia mis metas. A mi hermano Rodrigo, quien sin duda ha sido una de mis mayores motivaciones para mejorar como persona y enseñar con el ejemplo durante 27 años de convivencia y amistad. Y a Marieth, por toda su compañía, apoyo y amor durante los últimos años: me llena de alegría haber compartido esta experiencia contigo y espero con ansias nuestras siguientes aventuras juntos.

"Caminante, no hay camino, se hace camino al andar. Al andar se hace el camino y al volver la vista atrás se ve la senda que nunca se ha de volver a pisar." – Antonio Machado

A mis padres, por todo su apoyo a lo largo de este trayecto.
A mi hermano, por empujarme a siempre mostrar lo mejor de mi.
A Marieth, por acompañarme y compartir esta aventura conmigo.

– En memoria de mi papá, Francisco.

Chapter 1

Introduction

Atomic spectroscopy

The advent of the laser in 1960 [1] brought with it a renewed desire to carry out spectroscopic investigations of numerous media and materials. Since then, atomic spectroscopy has come to be one of the pillars of high precision measurements due to its relatively easy to use and accessible experimental setups. Applications of these spectroscopic atom-based sensors range from tests of fundamental physics [2, 3, 4] to precision time-keeping [5, 6, 7, 8], medical imaging [9, 10, 11] and measurement of electromagnetic fields [12, 13, 14, 15], among others. While operating these sensors at ultra-cold temperatures can provide advantages that may lead to an increase in precision, such as the macroscopic manifestation of quantum effects [16, 17, 18], these systems typically require complex experimental setups. Work can also be done with thermal atomic vapours, which have benefits and limitations of their own. In particular, thermal atomic vapours can provide simple, compact experimental platforms that allow the use of atom-based sensors in real-world applications and conditions.

Thermal vapours of alkali-metal atoms

Use of thermal atomic vapours in spectroscopy has historically been common due to the ease with which they can be handled. Of the different atomic species on the periodic table, the Group I elements –the alkali metals– have

been of particular interest because of their physical and chemical properties. These metals have relatively low melting points, with some existing in their liquid form at room temperature, and can be stored in glass cells under vacuum conditions or in protective atmospheres to prevent them from reacting with water vapour. Additionally, the atomic vapour pressure of these elements increases exponentially as a function of temperature, allowing an optically-dense medium to be used to easily carry out measurements using lasers [19, 20, 21, 22]. As such, these alkali-metal atoms have been extensively used in fundamental research [23, 24] and in practical applications such as microfabricated cells [25, 26], for use in atomic clocks [27, 28, 29] and magnetometry [30, 31, 32, 33], metrology [34, 35] and optical devices [36, 37, 38, 39].

While they are easy to use in experiments, thermal vapours may also present some challenges. To begin with, the thermal nature of the vapour introduces a velocity distribution for the atoms that in turn results in Doppler broadening of the lineshapes. For alkali-metal atoms this broadening is typically greater than the hyperfine splitting of the energy levels, complicating the theoretical description of the system and the ability to obtain well-resolved spectral features to measure. Not only this, but collisions between the atoms and cell walls can also lead to changes in the observed spectral lines [40, 41] and other characteristics of the vapour [42, 43, 44, 45]. Nevertheless, these challenges can be overcome with the use of Doppler-free [46, 47, 48] or velocity-selective [49, 50] spectroscopies and optical pumping [51]; collisions can also be controlled to a certain degree by the use of specially coated cell walls [52, 53, 54] and the presence of buffer gases in the cell [55, 56, 57]. Another way to deal with these effects is by introducing an external magnetic field to generate additional shifts in the atomic energy levels in order to better resolve the spectral lines [58, 59, 60].

Interactions of atomic vapours with external magnetic fields

The study of atomic vapours subject to an external magnetic field via spectroscopy is very well understood. Prior to the advent of the laser, experiments

in the late XIX century were carried out with light emitted by metallic salts introduced in flames provided evidence of the interaction between a magnetic field and light due to the presence of charged particles in the atom [61, 62, 63, 64, 65]. The subsequent discovery of the electron and its spin led to further understanding of the observed changes in the spectral emission when subject to large magnetic fields [66, 67, 68]. This work served as the foundation for many of the advances obtained with laser spectroscopy as it was now possible to interact with the internal energy levels of the atom more precisely, leading to the ability to trap and slow atoms [69, 70, 71].

Extensive studies have since been carried out in thermal vapours of alkali-metal atoms at both low- and high-densities [72, 73, 74, 75] looking at the magneto-optic effects that result from this interaction [76, 77, 78, 79]. However, this statement is true predominantly for fields that are stationary (*i.e.* DC) and typically below 1 T; under these conditions nuclear magnetic resonance (NMR) is commonly used due to its highly accurate measurements and the commercial availability of ready-to-use devices[1]. In addition to this, the convenience of using widely-available electronics to measure physically-relevant quantities, such as the Larmor precession frequency of the system [80], has been a deciding factor in promoting work at this lower end of the range of magnetic field strengths.

The limited amount of work done using atomic spectroscopy to study interactions with large (>1 T) external magnetic fields has been carried out in pulsed magnetic fields [81, 82] produced non-destructively, and with destructive techniques up to hundreds of T [83, 84]. Despite these precedents, there is little ongoing research directed at using atom-based sensors for measurement of large DC magnetic fields. This is because the interaction between an atom and an external magnetic field at these field strengths generates a decoupling of the nuclear and electronic spins, known as the hyperfine Paschen-Back (HPB) regime [85, 86]. The typical measurement of a Larmor precession frequency no longer proves to be a viable option as at these higher fields this

[1]Devices are readily available that claim <10 p.p.b. precision; see https://www.metrolab.com/products/pt2026/, accessed November 03, 2020

frequency becomes too large to measure by conventional electronics. Under these conditions, the interaction between the atoms and the magnetic field can be studied using alternative methods. Measurement of absorption spectra has been demonstrated to be a more straightforward way of obtaining information about the magnetic field strength in this case, as at high fields of the order of 1 T the Zeeman shift is large enough to create absorption spectra with characteristic features such as greater symmetry [87, 88]. Other detection methods, such as Stokes polarimetry [89], can also be used to detect the changes in the light used to probe the atoms due to magneto-optical rotation in the medium.

Atom-based magnetometers in the real world

Work with atom-based sensors for the measurement of magnetic fields has seen a rapid increase in interest thanks to the technological advances of recent years [90, 91, 92]. Building upon a solid understanding of the physical interactions involved in these atomic systems [76, 80, 93, 94, 95], this has allowed for these sensors to begin appearing in a number of different areas, ranging from bio-medical applications [96, 97, 98, 99, 100] to characterisation of materials and industrial techniques [101, 102, 103, 104]. Together with the wealth of experience in spectroscopy using thermal vapours, this has proven to be a novel way of realising precision measurements of magnetic fields. Various protocols for optical atomic magnetometry have been developed [105, 106, 107, 108, 109] to exploit several aspects of these systems with the intention of increasing their versatility and precision. Nevertheless, these techniques and protocols have been limited to the lower range of field strengths (< 10 mT) and have left open the possibility of translating the basic principles to work at higher (≥ 1 T) field strengths.

1.1 Motivation

The aim of the present investigation is to expand the study of thermal atomic vapours in the presence of large magnetic fields. Of particular interest here

will be the use of the Voigt geometry, *i.e.* when the laser beam propagates perpendicularly to the direction of the magnetic field, which will allow for specific sets of transitions to be selected as a function of the polarisation of the light used. The fields used in our experiments (0.4 and 1.5 T) will allow for a theoretical model of the system in the hyperfine Paschen-Back regime to be used and further validated. This line of research builds upon previous results from similar experiments, where alkali-metal atomic vapours were placed in large magnetic fields using the Faraday geometry. In such systems the advantages of carrying out measurements in the hyperfine Paschen-Back regime have been demonstrated [24, 60, 110, 111, 112]. However, these systems omit part of the available information by design, as they are not able to excite π transitions due to the geometrical constraints on the system.

In comparison, by setting the experimental system in the Voigt geometry all of the atomic transitions are excitable, thus allowing for increased benefits to the amount of information obtained and its precision. To highlight this we present results of a systematic investigation of these atomic systems, using tools such as the Stokes parameters, to obtain a complete set of information on the processes occurring in the atomic vapour. Quantitative comparison of said results to the predictions of a theoretical model will also be presented. We will also put forth ideas and results that show the increase in precision of certain measurements, such as that of the magnetic field strength, obtained by using an atomic system in the proposed configuration. In doing so it is our hope that the present work will contribute to the understanding of the interactions between atoms, light and magnetic fields, as well as providing points of interest for further spectroscopic research of thermal atomic vapours.

1.2 Thesis summary

Chapter 2 – A broad overview of the fundamental concepts behind the interaction of atoms and an external electromagnetic field is given. We then proceed to discuss the interaction of such an atom-light system in the presence of an additional external magnetic field, with a particular emphasis on the

effects of strong (≥ 1 T) fields and of the geometry of the physical system. The properties of alkali-metal atoms, in particular of rubidium, are mentioned in order to provide context for the experiments realised for this thesis.

Chapter 3 – The absorption spectroscopy of a thermal vapour of ^{87}Rb atoms subject to a 0.4 T external magnetic field is presented. The theory describing this particular experiment is briefly expanded upon, allowing use of a model to fit the results with excellent agreement. This enables for more precise determination of the magnetic field strength and of its orientation relative to the atom-light system; our method raises the possibility of atom-based, high-field vector magnetometry.

Chapter 4 – We expand on previous work to present a polarimetric investigation of a vapour of ^{87}Rb atoms at a field strength of 1.5 T. We find very good agreement between the experiment and fits using our theoretical model. From these fits we are able to precisely determine the field strength and relative orientation, with respect to our laser beam, of the field used. In addition to this, measurements of the Stokes parameters allow us to observe, and correct, birefringence due to the vapour cell windows in our experiment. The work presented provides the foundations for an all-optical scheme for precision atomic vector magnetometry in high fields.

Chapter 5 – We take advantage of the properties of an atomic vapour in the hyperfine Paschen-Back regime and the Voigt geometry to carry out precision magnetometry. Our method, relying on the measurement of frequency differences between particular transitions, allows us to determine field strengths with a precision of ~ 50 mT, limited by the precision of our frequency measurements in an absorption spectrum. A natural application of this experimental scheme, with rubidium or other alkali-metal atoms, is in all-optical precision magnetometry in high fields, an area little explored with atom-based sensors.

Chapter 6 – With the experience and knowledge from the experiments thus far presented, we investigate the possibility of realising precision thermometry with a thermal rubidium vapour. The necessary theory for doing so is briefly

discussed, and a proposal for an experimental realisation is given. The simulated precision of this method proves to be of metrological interest, possibly serving as an all-optical secondary standard for the determination of the Boltzmann constant.

Chapter 7 – The most significant results from the experiments carried out are summarised. A brief discussion of further applications and development of the work presented is also given.

1.3 Publications

The following papers have been published from the work described in this thesis:

J. Keaveney, F. S. Ponciano Ojeda, S. Rieche, M. J. Raine, D. P. Hampshire and I. G. Hughes, *Quantitative optical spectroscopy of* ^{87}*Rb vapour in the Voigt geometry in DC magnetic fields up to* 0.4 *T*, Journal of Physics B: Atomic, Molecular and Optical Physics **52**, 055003 (2019), 10.1088/1361-6455/ab0186 [113]

F. S. Ponciano-Ojeda, F. D. Logue and I. G. Hughes, *Absorption spectroscopy and Stokes polarimetry in a* ^{87}*Rb vapour in the Voigt geometry with a* 1.5 *T external magnetic field*, Journal of Physics B: Atomic, Molecular and Optical Physics **54**, 015401 (2021), 10.1088/1361-6455/abc7ff [114]

F. S. Ponciano-Ojeda, F. D. Logue and I. G. Hughes, *In preparation*, (2021)

1.4 Author contributions

F. S. Ponciano-Ojeda was responsible for carrying out the majority of experiments, most of the analysis of the results and contributed to the the writing of each of the above publications. J. Keaveney contributed to the design and realisation of the experiment, and the analysis of results, presented in the first of the articles. S. Rieche contributed to the experimental realisation of the first publication mentioned above. M. J. Raine contributed to the

design of the experimental setup used in, and the writing of, the first article. D. P. Hampshire contributed by kindly providing access to the electromagnet used in the experiment and in writing the first publication. F. D. Logue contributed to the experiment and analysis, as well as the writing of, the second of the above publications. I. G. Hughes contributed to the writing of each article and is the principal investigator for this project.

Chapter 2

Interactions between atoms, light and external magnetic fields

In this chapter we will give a broad overview of the main theoretical concepts behind the interaction of atoms with light and external magnetic fields. This will serve as a common starting point in order to understand the behaviour of the atomic systems studied. Additional theoretical details for specific cases of the experimental systems will be given in their respective chapters.

2.1 Atom-light interactions

We begin by addressing the theory behind experiments involving spectroscopic measurements – the interaction between an atom and an electromagnetic (EM) field. For the majority of experiments, including the work reported in this thesis, a semi-classical description of the interaction is sufficient. This means that while the atom is described by its quantum mechanical framework, namely the Schrödinger equation, the electromagnetic field is treated according to its classical description based on Maxwell's equations of electromagnetism. It is worth mentioning that this will give a description of the dynamics and interaction on the microscopic level, which will then be translated to macroscopic properties of an atomic medium in order to better

represent the conditions found in the laboratory.

2.1.1 Quantum-mechanical description of an atomic system

Consider an atom where the nuclear mass is much greater than that of the electrons, such that the system can be described in terms of its centre of mass. An equivalent assumption is that the nucleus does not move with respect to the electron. For the simplest non-relativistic case, neglecting effects due to the nucleus and quantum electrodynamics, an atom composed of a proton and a *single* orbiting electron (*i.e.* hydrogen) can be described in terms of the Hamiltonian

$$\hat{H} = \frac{\hat{\mathbf{p}}^2}{2\mu_{\text{atom}}} + \frac{-e^2}{4\pi\epsilon_0 \hat{r}}, \tag{2.1}$$

where $\hat{\mathbf{p}}$ is the momentum operator of the electron, μ_{atom} is the reduced mass of the atomic system, e is the fundamental charge of the electron, and $\hat{r}$ is the position operator describing the distance of the electron from the centre of mass [85, 86, 115]. Closer inspection will show that the two terms shown in equation 2.1 are the kinetic energy of the electron and the Coulomb force between the positively-charged proton and the electron. For the case of atoms with multiple nucleons and electrons, terms must be added to equation 2.1 to account for all of the Coulomb interactions between these [85, 86, 115, 116]. The resulting Hamiltonian is commonly referred to as the *bare-atom Hamiltonian*, $\hat{H}_0$.

Using the bare-atom Hamiltonian, we can proceed to solve the Schrödinger equation to obtain the quantum-mechanical description of the behaviour of the atom, expressed in terms of its wavefunction $\Psi(\hat{\mathbf{r}}, t)$. The quantised energies E_n of the electrons in the atom are obtained as solutions to the eigen-system created by use of the Schrödinger equation. As such, a set of solutions $(\Psi, E_{(n,L,m_L,S,m_S)})$ can be constructed, where the quantum numbers n, (L, m_L) and (S, m_S) serve to describe the discrete energy states of the atomic system. Having the wavefunctions and energies allows the atomic

system to be well-defined in terms of a complete set, which consequently provides a basis for incorporating further interactions both within the atom and with external fields.

The definition of an atom's behaviour as provided by the complete set of solutions $(\Psi, E_{(n,L,m_L,S,m_S)})$ allows us to begin describing said behaviour, yet it does not take into account many of the subtleties that arise from other phenomena within the atom. One of these phenomena is the interaction between the different angular momenta in the atom, which will play an important role in defining the interaction with electromagnetic fields seen in sections 2.1.2 and 2.2. We can begin to introduce the effects of angular momenta in the atomic system by considering the coupling between the intrinsic angular momentum of the electron, also known as its spin $\hat{\mathbf{S}}$, and the orbital angular momentum of the electron, given by the quantum number $\hat{\mathbf{L}}$:

$$\hat{H}_{\mathrm{FS}} = \gamma_{LS}(\hat{\mathbf{L}} \cdot \hat{\mathbf{S}}). \tag{2.2}$$

The constant γ_{LS} in equation 2.2 quantifies the magnitude of the *spin-orbit coupling* in the atom. Using the theory of addition of angular momenta [117], we can express the interaction between these two momenta as a quantity $\hat{\mathbf{J}} = \hat{\mathbf{L}} + \hat{\mathbf{S}}$ which will also be a good quantum number for the atom [85, 86, 115]. In the context of the atom, $\hat{\mathbf{J}}$ is referred to as the *total electronic angular momentum*, and the interaction that leads to it is known as the *fine interaction*. As a consequence of this coupling between angular momenta, the structure of the energy levels is modified and some of the initial degeneracy found in the energies $E_{(n,L,m_L,S,m_S)}$ is removed. At this point the atomic energy levels are said to be showing the *fine structure*.

Similar to the case of the fine interaction, a further coupling of angular momenta can be introduced to better explain the interactions within the atom. As a result of the intrinsic angular momenta of the protons and neutrons (*i.e.* their spin), the nucleus as a whole also has an intrinsic angular momentum, $\hat{\mathbf{I}}$. Once again, we use the theory of angular momenta [117]

to couple this nuclear angular momentum with the total electronic angular momentum $\hat{\mathbf{J}}$ in a new quantity, $\hat{\mathbf{F}} = \hat{\mathbf{I}} + \hat{\mathbf{J}}$, that also serves as a good quantum number for describing the atom. The quantity $\hat{\mathbf{F}}$ is thus associated to the *total atomic angular momentum*. This is known as the *hyperfine interaction* [85, 86, 115],

$$\hat{H}_{\mathrm{HFS}} = A_{\mathrm{HF}}(\hat{\mathbf{I}} \cdot \hat{\mathbf{J}}) + B_{\mathrm{HF}} \frac{3(\hat{\mathbf{I}} \cdot \hat{\mathbf{J}})^2 + \frac{3}{2}(\hat{\mathbf{I}} \cdot \hat{\mathbf{J}}) - I(I+1)J(J+1)}{2I(2I-1)J(2J-1)}, \tag{2.3}$$

with the first term of the right-hand sum corresponding to a magnetic dipole interaction and the second term corresponding to an electric quadrupole interaction. Here I and J are simply the eigenvalues associated with the operators $\hat{\mathbf{I}}$ and $\hat{\mathbf{J}}$, respectively. In equation 2.3 we have chosen not to write higher-order interactions as they are typically small [90, 118, 119]; in commonly used atomic systems they have been found to be at least three orders of magnitude smaller than the electric quadrupole interactions [120, 121, 122, 123, 124]. The effect of this coupling on the energy levels of the atom gives rise to the *hyperfine structure*, which further helps remove some of the degeneracies and provides greater details as to the internal structure of the atoms.

At this point we have given enough detail of the internal interactions of the atom so that we can begin to consider the effects of external interactions. We begin by noting that our bare-atom Hamiltonian now must also include the fine and hyperfine interactions [85, 86, 115], such that

$$\hat{H}_{\mathrm{atom}} = \hat{H}_0 + \hat{H}_{\mathrm{FS}} + \hat{H}_{\mathrm{HFS}}. \tag{2.4}$$

This Hamiltonian will encapsulate all of the information regarding the quantum-mechanical description of the behaviour of an atom. To deal with the additional complexity of the system, it will now become convenient to adopt a different notation for the atomic states, commonly known as *Dirac* notation, where rather than identifying the state by the wavefunction $\Psi(\hat{\mathbf{r}}, t)$ we use the quantum numbers that describe the system, $|nLm_L Sm_S Im_I\rangle$. A corollary of this change of notation is that we will now also be considering

the quantum mechanical observables (*e.g.* $\hat{\mathbf{p}}, \hat{\mathbf{r}}$) as hermitian operators in the equations covered thus far.

2.1.2 Interaction between an atom and an electromagnetic wave

To introduce the interaction of an atom with an external electromagnetic field we begin by recalling that in the presence of a classical EM field, the Hamiltonian describing the movement of a particle with charge q is [115, 125]

$$\hat{H}_{\mathrm{EM}} = \frac{1}{2m_q}\left(\mathbf{p} - q\mathbf{A}(\mathbf{r},t)\right)^2 + q\Phi(\mathbf{r},t). \tag{2.5}$$

Here we have taken $\mathbf{r}, \mathbf{p}$ as the position and momentum of the particle, m_q as its mass and $\Phi(\mathbf{r},t), \mathbf{A}(\mathbf{r},t)$ the scalar and vector potentials that describe the EM field. Introducing this classical interaction into the Hamiltonian for a hydrogen-like atom, we can make certain assumptions that allow for a more compact, yet accurate, expression for the atom-light interaction. Firstly, we will assume that in this interaction we work in the radiation gauge, which effectively allows us to consider $\Phi(\mathbf{r},t) = 0$ and $\left[\hat{\mathbf{p}}, \hat{\mathbf{A}}\right] = 0$ [126]. For the extent of this work we will also consider the EM field the atoms interact with as plane, monochromatic waves of the form $\exp[i(\mathbf{k}\cdot\mathbf{r} - \omega t)]$, with $\mathbf{k}$ the wave-vector of the light and $\omega = \frac{2\pi c}{\lambda}$ the frequency of the field.

As a result of the assumptions made, after some algebraic manipulation of equation 2.5 we can write the resulting Hamiltonian for an atom interacting with an EM field in the form

$$\begin{aligned}\hat{H} &= \hat{H}_{\mathrm{atom}} - \frac{Ze}{\mu_{\mathrm{atom}}}\hat{\mathbf{p}}\cdot\hat{\mathbf{A}}(\hat{\mathbf{r}},t) + \frac{Z^2e^2}{2\mu_{\mathrm{atom}}}\hat{\mathbf{A}}^2(\hat{\mathbf{r}},t), \\ &= \hat{H}_{\mathrm{atom}} + \hat{H}_{\mathrm{light}},\end{aligned} \tag{2.6}$$

where we have used the substitutions $q \to Ze$ and $m_q \to \mu_{\mathrm{atom}}$ for a general hydrogen-like atom. The atomic Hamiltonian $\hat{H}_{\mathrm{atom}}$, is that previously seen in equation 2.4 and already includes the $\hat{\mathbf{p}}^2$ term present in equation 2.5. The

remaining terms on the right hand side of equation 2.6 have been written as the interaction Hamiltonian between the atom and light, $\hat{H}_{\text{light}}$. For the majority of the work here presented, we will keep only the first-order term of the interaction Hamiltonian $\hat{H}_{\text{light}}$, $(\hat{\mathbf{p}} \cdot \hat{\mathbf{A}})$, as we assume the interaction between the EM field and the atom is weak in comparison to the internal interactions of the atom (*i.e.* we can omit the second-order $\hat{\mathbf{A}}^2$ term) [126, 127]. This Hamiltonian can then be substituted into the Schrödinger equation, where the interaction $\hat{H}_{\text{light}}$ can be treated as a perturbation using time-dependent perturbation theory [115].

With this framework we can now proceed to consider the special case of an atom interacting with light whose frequency is close to, or equal, to the energy difference between two atomic energy states. We denote the lower energy state the ground state, $|g\rangle = |nLm_L Sm_S Im_I\rangle$, and the higher energy state the excited state $|e\rangle = |n'L'm_{L'}S'm_{S'}Im_{I'}\rangle$. The probability density of the atom going from the ground state to the excited state when interacting with the light, given in terms of the matrix element $\langle g|\hat{H}|e\rangle$, can be expressed as

$$\begin{aligned} \langle g|\hat{H}|e\rangle &= \langle g|\hat{H}_{\text{atom}} + \hat{H}_{\text{light}}|e\rangle \\ &\approx \langle g|\frac{-Ze}{\mu_{\text{atom}}}\hat{\mathbf{p}} \cdot \hat{\mathbf{A}}(\hat{\mathbf{r}}, t)|e\rangle. \end{aligned} \tag{2.7}$$

In this expression we have taken the Hamiltonian $\hat{H}$ as defined in equation 2.6 and omitted the terms to second-order of the vector potential $\hat{\mathbf{A}}$. Note that the term $\langle g|\hat{H}_{\text{atom}}|e\rangle = 0$ by virtue of $|g\rangle, |e\rangle$ both being eigen-states of the atomic Hamiltonian.

The final expression in equation 2.7 can be rewritten in a more convenient manner by considering the relation between a particle's position and momentum operators, as well as the classical interaction between an electric dipole moment and an electric field. For the first of the aforementioned considerations, we use the commuter relation $\hat{\mathbf{p}} = im/\hbar \left[\hat{H}, \hat{\mathbf{r}}\right]$ [115] where the Hamiltonian in question corresponds in our case to the atomic hamiltonian as defined in equation 2.4. Substituting this into equation 2.7, we recall the fact

that the light in the interaction is a plane, monochromatic wave to write

$$\begin{aligned}
\langle g|\hat{H}|e\rangle &\approx \langle g|\frac{-\hat{\mathbf{p}}\,Ze}{\mu_{\text{atom}}}\cdot\hat{\mathbf{A}}(\hat{\mathbf{r}},t)|e\rangle \\
&= \langle g|\frac{-iZe\mu_{\text{atom}}}{\hbar\mu_{\text{atom}}}\left[\hat{H}_{\text{atom}},\hat{\mathbf{r}}\right]\cdot\hat{\mathbf{A}}_0\exp\left[i(\mathbf{k}\cdot\hat{\mathbf{r}}-\omega t)\right]|e\rangle \\
&= \langle g|\frac{-iZe}{\hbar}(\frac{-i}{\omega})\left[\hat{H}_{\text{atom}},\hat{\mathbf{r}}\right]\cdot\hat{\mathbf{E}}_0\exp\left[i(\mathbf{k}\cdot\hat{\mathbf{r}})\right]\exp\left[(-i\omega t)\right]|e\rangle \\
&= \langle g|\frac{-Ze}{\omega}\left(\frac{(E_g-E_e)}{\hbar}\right)\hat{\mathbf{r}}\cdot\hat{\mathbf{E}}_0\exp\left[i(\mathbf{k}\cdot\hat{\mathbf{r}})\right]\exp\left[(-i\omega t)\right]|e\rangle \\
&= \frac{\omega_{ge}}{\omega}\langle g|\hat{\mathbf{d}}\cdot\hat{\mathbf{E}}_0\exp\left[i(\mathbf{k}\cdot\hat{\mathbf{r}})\right]\exp\left[(-i\omega t)\right]|e\rangle. \qquad (2.8)
\end{aligned}$$

Here we have used the relation between the electric field $\mathbf{E}$ and the vector potential $\mathbf{A}$, $\mathbf{E}=-\frac{\partial}{\partial t}\mathbf{A}$. We recognise the quantity $\hat{\mathbf{d}}=-Ze\hat{\mathbf{r}}$ as the electric dipole moment to relate this expression with the classical interaction of the electric dipole moment with an electric field, $\hat{H}_{\text{dipole}}=\hat{\mathbf{d}}\cdot\hat{\mathbf{E}}$ [85, 116, 128].

The expression in equation 2.8 is responsible for defining the details of the interaction between an atom and light. In this context, the so-called *dipole transitions* are the excitations of the electrons in the atom between energy states resonant with the incident light; note that these are commonly studied in the literature [85, 86, 126, 127] after having carried out the *dipole* and *rotating-wave approximations*. In particular, the dipole approximation allows us to assume the charged particle interacts with the electromagnetic field at a single point in space (*i.e.* $|\mathbf{k}\cdot\hat{\mathbf{r}}|=kr\ll 1$) [86, 127, 128] while the rotating-wave approximation allows us to discard rapidly oscillating terms in the interaction (*e.g.* $\omega+\omega_{ge}$) and define a detuning close to resonance in the study of the interaction of the atom and light [86, 126, 128]. These transitions follow certain rules which are a result of the geometry of the atom-light system and some general considerations of the nature of the transitions. As we are considering electronic transitions, we note that the value of the projection of the nuclear angular momentum m_I does not change ($m_I=m_{I'}$). Furthermore, we recognise that the position operator $\hat{\mathbf{r}}$ has an odd parity (*i.e.* its components change sign under the transformation $\hat{\mathbf{r}}\to-\hat{\mathbf{r}}$), which means that the parity of $|g\rangle$ and $|e\rangle$ must be opposite in order for the matrix

element in equation 2.8 to be non-zero.

If we take the direction of propagation of the light along a Cartesian z-axis and label the components of $\hat{\mathbf{r}}$ as r_q in the helicity basis ($q = 0, \pm 1$), we can use the Wigner-Eckart theorem [85, 115, 129] to reduce the dipole matrix element $\langle g|\hat{H}_{\text{dipole}}|e\rangle$:

$$\begin{aligned}
\langle g|\hat{H}_{\text{dipole}}|e\rangle &= \langle nLm_L Sm_S Im_I|er_q|n'L'm_{L'}S'm_{S'}Im_I\rangle \\
&= \langle nLm_L|er_q|n'L'm_{L'}\rangle\langle S'm_{S'}|Sm_S\rangle \\
&= \langle nL||er||n'L'\rangle\langle L'm_{L'}1q|Lm_L\rangle\delta_{S,S'}\delta_{m_S,m_{S'}} \\
&= \langle nL||er||n'L'\rangle(-1)^{L'-1+m_L}\sqrt{2L+1} \\
&\quad \times \begin{pmatrix} L' & 1 & L \\ m_{L'} & q & -m_L \end{pmatrix} \delta_{S,S'}\delta_{m_S,m_{S'}}.
\end{aligned} \tag{2.9}$$

The quantity $\langle nL||er||n'L'\rangle$ is known as the *reduced dipole matrix element*, and is independent of the component of $\hat{\mathbf{r}}$ and of the projections $m_L, m_{L'}$ of the orbital angular momentum. In equation 2.9 we have begun by splitting the orbital (angular) and spin components of the dipole matrix element. This allows us to ensure that the matrix element is non-zero when we conserve the spin of the system, $S = S', m_S = m_{S'}$. For the orbital part, the Wigner-Eckart theorem can be applied to show that the conditions for the matrix element to be non-zero, by virtue of the properties of the 3-j symbol [85, 117, 129], are:

$$\begin{aligned}
m_{L'} + q = m_L \quad &\Rightarrow \quad \Delta m_L = |m_{L'} - m_L| = q = 0, \pm 1, \\
|L' - 1| \leq L \leq L' + 1 \quad &\Rightarrow \quad \Delta L = |L' - L| = 0, \pm 1, \text{ and} \\
L \quad + \quad L' \geq 1.&
\end{aligned} \tag{2.10}$$

These selection rules will prove of particular interest when looking at the interaction of an atoms and light in the presence of an external magnetic field (section 2.2), as will be seen later in the analysis of experimental spectra in chapters 3, 4 and 5.

2.1.3 Macroscopic effects of the atom-light interaction

Having considered the interaction between an atom and light, we are now concerned with finding a physical quantity that allows us to characterise this interaction in the laboratory. This is often done via atomic spectroscopy, with the transmission of light through an atomic *medium* being the quantity measured. Nevertheless, we recognise that there must be a link between the microscopic description of the interaction in section 2.1.2 and that for a macroscopic *medium*. For this we fall back on the optical concept of the *refractive index* of a medium, and the classical electromagnetic concept of the *susceptibility* of a medium.

We start by recalling that for an optical medium, its *refractive index* is in general a complex quantity, $n = n_{\Re} + in_{\Im}$ [125, 130, 131, 132]. The real part of said index affects the optical properties derived from the change in the speed of light through the medium, such as refraction, while the imaginary part is responsible for losses in the form of absorption. As our experimental interest lies in the transmission of light T_{light} through the medium, we can relate the absorption coefficient of the medium α and the imaginary part of the refractive index via a linear relation, $\alpha = 2kn_{\Im}$ [125]. Thus, using the Beer-Lambert law [125, 131, 132], we can write T as

$$T_{\text{light}} = \exp(-\alpha l) = \exp(-2kn_{\Im}l), \tag{2.11}$$

where l represents the length of the medium and k is the wavenumber of the light used.

The relation between the macroscopic and microscopic nature of the optical medium comes as a result of the link between the refractive index and the medium's *susceptibility*, χ, which is itself a complex-valued quantity ($\chi = \chi_{\Re} + i\chi_{\Im}$) [115, 125, 131]:

$$\begin{aligned} n &= n_{\Re} + in_{\Im} \\ &= \sqrt{1+\chi}. \end{aligned} \tag{2.12}$$

The macroscopic susceptibility of a medium χ can be described in terms of its microscopic components (*e.g.* atoms/molecules) by taking into account the effect an electric field has on the individual electric dipoles in the structure of the material. A case of interest is when the magnitude of the susceptibility (and thus the effect of the electric field) is small, $|\chi| \ll 1$, so that we can take a Taylor-series expansion of equation 2.12. This gives us, to first order [115, 125],

$$\begin{aligned} n &\approx 1 + \frac{\chi}{2} = 1 + \frac{\chi_{\Re}}{2} + i\frac{\chi_{\Im}}{2}, \\ \therefore\ & n_{\Re} \approx 1 + \frac{\chi_{\Re}}{2}, n_{\Im} \approx \frac{\chi_{\Im}}{2}. \end{aligned} \tag{2.13}$$

It is worth noting that here we have assumed the refractive index is linear; in strong electric fields (such as those obtained from intense laser beams) it is possible to observe non-linear effects involving changes in the refractive index as light propagates through the medium [130, 131, 133]. The above treatment will be useful for simplifying the calculations necessary to model and carry out the analysis of experimental spectra, as will be seen in chapters 3 and 4.

For the simplest case of a medium composed of atoms with two discrete energy levels interacting with light, the susceptibility can be written as [72]:

$$\begin{aligned} \chi(\Delta) &= \frac{C^2 d^2 \mathcal{N}}{\epsilon_0 \hbar} f(\Delta), \\ f(\Delta) &= \frac{i}{\Gamma/2 - i\Delta}, \end{aligned} \tag{2.14}$$

where C^2 is the strength of the transition given in terms of the square of the prefactors and the 3-j symbol in equation 2.9, d is the reduced dipole matrix element and $\mathcal{N}$ is the atomic number density of the medium. The function $f(\Delta)$ corresponds to the characteristic lineshape of the transition between the two levels, with a decay rate Γ, given as a function of the difference in angular frequency of the atomic transition and the light, $\Delta = \omega_{\text{light}} - \omega_{\text{atom}}$. Experimentally it will be more convenient to deal with *linear frequencies*, given in terms of $\Delta/2\pi$.

In reality, the atoms involved in the description of equation 2.14 are in motion. For the experiments presented in this work, the medium we use is a thermal atomic vapour. This means that the movement of the atoms is described by a Maxwell-Boltzmann distribution,

$$g(v) = \frac{\sqrt{m_a}}{\sqrt{2k_{\mathrm{B}}T\pi}} \exp\left[\frac{-v^2}{2k_{\mathrm{B}}T/m_a}\right], \tag{2.15}$$

with m_a the mass of an atom, k_{B} the Boltzmann constant, T the temperature of the vapour and v the velocity of the atoms along one dimension. We note the quantity $u = \sqrt{2k_{\mathrm{B}}T/m_a}$ is the root-mean-square (RMS) speed of the atoms, which defines the width of the distribution.

The effect of the movement of the atoms on the medium, particularly on its susceptibility, comes from the fact that the frequency of the light is Doppler-shifted proportional to their velocity. As such, the susceptibility is effectively averaged over the component along the direction of light propagation (*i.e.* parallel to the $\mathbf{k}$ vector of the plane wave; see section 2.1.2) of all of the atomic velocities in the Maxwell-Boltzmann distribution and results in what is commonly referred to as *Doppler broadening*. The expression for χ in equation 2.14 can thus be rewritten as

$$\begin{aligned} \chi(\Delta) &= \frac{C^2 d^2 \mathcal{N}}{\epsilon_0 \hbar} \mathcal{V}(\Delta), \\ \mathcal{V}(\Delta) &= \int_{-\infty}^{\infty} f(\Delta - kv) g(v) \mathrm{d}v, \end{aligned} \tag{2.16}$$

with the convolution between the lineshape of the transition and the Maxwell-Boltzmann distribution giving the well-known Voigt lineshape $\mathcal{V}$ [86, 116].

2.1.4 Stokes polarimetry

The choice of the Stokes parameters to characterise the transmitted electric field through an atomic medium is due to their convenience in this context. As will be seen in the section 2.2, the geometry of the interaction between atoms, light and magnetic fields results in propagation eigenmodes that can

readily be expressed in terms of the polarisation of light. As such, the Stokes parameters are a natural choice for studying these interactions. One needs only to measure the intensity ($I \propto |\vec{E}|^2$) of the beam in orthogonal polarisation bases to access information not only on the absorption of the medium, but also on the optical rotation it generates.

The Stokes parameters, $S_0, S_1, S_2 \,\&\, S_3$, are simply linear combinations of the measured orthogonal components of polarisation in different orthogonal bases [134]. For a beam that is incident on the medium with an intensity I_0, the Stokes parameter S_0 is defined as

$$S_0 \equiv \frac{I_x + I_y}{I_0} = \frac{I_{\nearrow} + I_{\searrow}}{I_0} = \frac{I_{\mathrm{RCP}} + I_{\mathrm{LCP}}}{I_0}, \tag{2.17}$$

and it represents the normalised *total* transmitted intensity through the medium. As can be seen, this makes the measurement of this particular parameter independent of the basis chosen. The remaining Stokes parameters,

$$S_1 \equiv \frac{I_x - I_y}{I_0}, \tag{2.18}$$

$$S_2 \equiv \frac{I_{\nearrow} - I_{\searrow}}{I_0}, \tag{2.19}$$

$$S_3 \equiv \frac{I_{\mathrm{RCP}} - I_{\mathrm{LCP}}}{I_0}, \tag{2.20}$$

provide information on the optical rotation of the light after passing through the atomic medium in terms of the difference between orthogonal polarisation components: S_1 is measured in the linear horizontal (I_x, I_y) basis; S_2 takes measurements in a diagonal $(I_{\nearrow}, I_{\searrow})$ basis and S_3 is measured in the helicity basis $(I_{\mathrm{RCP}}, I_{\mathrm{LCP}})$ composed of right- and left-hand circular polarisations. These last three parameters are also normalised with the incident intensity so as to form a complete basis to describe a normalised arbitrary polarisation state of light [89, 135, 136].

2.2 Effects of external fields on atom-light interactions

The interaction of an atom with an external magnetic field which we assume is time-independent, $\mathbf{B} = \mathbf{B}(\mathbf{r})$, can be described by the Hamiltonian

$$\hat{H}_{\text{Zeeman}} = -\hat{\boldsymbol{\mu}} \cdot \hat{\mathbf{B}}, \tag{2.21}$$

where $\hat{\boldsymbol{\mu}}$ is the magnetic dipole moment of the atom. This is commonly referred to as the *Zeeman effect*. The nature of $\hat{\boldsymbol{\mu}}$ lies in the well-known fact that a charged particle rotating about an axis will generate a small magnetic field as described by Maxwell's equations [125]. In writing equation 2.21 we have considered the paramagnetic response of the particle and omitted the diamagnetic contribution to the interaction, which can be linked to the $\hat{\mathbf{A}}^2$ term in equation 2.6 and can be shown to be on the order of $\sim$ 149 kHz/T^2 [90]. In addition to this, the intrinsic spin of the electron also contributes to the generation of an electronic magnetic dipole moment. Thus, in terms of the quantum description of the atom given in section 2.1.1, the magnetic dipole moment of the atom is related to the angular momenta of the protons and electrons via a direct proportional relation of the quantum numbers $\hat{\mathbf{I}}$, $\hat{\mathbf{L}}$ and $\hat{\mathbf{S}}$ to the nuclear magneton μ_N and the Bohr magneton μ_{B}, respectively [85, 86, 90, 116]:

$$\begin{aligned} \hat{\boldsymbol{\mu}} &= \hat{\boldsymbol{\mu}}_{\boldsymbol{e}} + \hat{\boldsymbol{\mu}}_{\boldsymbol{n}} \\ &= \frac{\mu_{\text{B}}}{\hbar}(g_L\hat{\mathbf{L}} + g_S\hat{\mathbf{S}}) + \frac{\mu_N}{\hbar} g_I \hat{\mathbf{I}}. \end{aligned} \tag{2.22}$$

In equation 2.22 we have written $\hat{\boldsymbol{\mu}}_{\boldsymbol{e}}$ as the electron magnetic dipole moment, $\hat{\boldsymbol{\mu}}_{\boldsymbol{n}}$ as the nuclear magnetic dipole moment, and g_L, g_S, g_I as constants of proportionality known as the *gyromagnetic ratios*. For the remainder of this work, we will assume these gyromagnetic ratios are independent of the field strength. These constants serve to quantify how strongly the atomic system will react in the presence of the external field $\mathbf{B}$; of the three here mentioned, g_S has been the subject of great interest as its value serves as one of the most

stringent tests of quantum mechanical theory to date [137, 138]. Furthermore, we also note that the nuclear magneton μ_N is three orders of magnitude smaller than the Bohr magneton μ_B, resulting in a smaller contribution to the interaction from the last term on the right-hand side of equation 2.22.

Given the relation between the magnetic dipole moment of the atom and the external magnetic field in equation 2.21, it is clear that the interaction has a significant dependence on the orientation of the system. While in the absence of an external magnetic field the atom-light interactions have a quantisation axis defined by the direction of propagation of the light, given by the wave-vector $\mathbf{k}$, in the presence of an external magnetic field we see that it is now the direction of the field $\mathbf{B}$ that defines the privileged axis in the interaction. Furthermore, the magnitude of the magnetic field is a parameter that effectively controls the strength of the interaction, allowing for different regimes to be accessed by simply tuning this value.

In the following subsections we explore one such regime of particular interest for the work in this thesis. We will also look at the two main geometric configurations for the interaction involving an external magnetic field, and set out the implications this has on the atom-light interactions previously described.

2.2.1 The hyperfine Paschen-Back regime

As mentioned previously, the strength of the interaction between an atom and an external magnetic field $\mathbf{B}$ can be determined by the magnitude of said field. At low magnetic field strengths, the atom-magnetic field interaction can be described using equation 2.21, where the magnetic dipole moment $\hat{\boldsymbol{\mu}}$ of the atom is now described in terms of the total angular momentum of the electron, $\hat{\mathbf{J}}$ and the nuclear angular momentum, $\hat{\mathbf{I}}$. Following the description of the hyperfine interaction given in section 2.1.1, we can use the total atomic angular momentum $\hat{\mathbf{F}}$ and its projection m_F as 'good' quantum numbers to describe the state of the atom. In this way, one can express the Zeeman effect,

under these conditions, as

$$\hat{H}_{\text{Zeeman}} = -\hat{\boldsymbol{\mu}} \cdot \hat{\mathbf{B}} \approx -\frac{\mu_{\text{B}} g_F}{\hbar} \hat{\mathbf{F}} \cdot \hat{\mathbf{B}}, \tag{2.23}$$

where the magnetic dipole moment $\hat{\boldsymbol{\mu}}$ has been written in terms of the total atomic angular momentum $\hat{\mathbf{F}}$, $\hat{\boldsymbol{\mu}} = \frac{\mu_{\text{B}}}{\hbar} g_F \hat{\mathbf{F}}$, with g_F the corresponding gyromagnetic ratio [85, 86, 116]. As a result of equation 2.23 the energy levels, described using the (F, m_F) quantum numbers, will see their energy shifted due to the Zeeman effect by an amount

$$\Delta E_{\text{Zeeman}} = \mu_{\text{B}} g_F m_F B, \tag{2.24}$$

with $m_F = -F, -F+1, ..., F-1, F$ the projection of the total atomic angular momentum $\hat{\mathbf{F}}$ along the quantisation axis and $B = |\mathbf{B}|$ the magnitude of the magnetic field [85, 86, 116].

The description of the Zeeman effect given by equations 2.23 and 2.24 is valid for low magnetic field strengths due to the fact that the hyperfine interaction in the atom, as described in section 2.1.1, is dominant. In this sense, the presence of the external magnetic field serves as a method of removing some of the degeneracy present in the hyperfine structure of the energy levels. However, this description is only valid as long as the energy shift created by the Zeeman effect is less than the shifts resulting from the hyperfine interaction in the atom. This is equivalent to asking at what point the shift in energy from the Zeeman effect is comparable to the shifts due to the hyperfine interaction, which can, in the first instance, be obtained by looking at the values of the hyperfine constants $A_{\text{HF}}, B_{\text{HF}}$. In particular, the ratio between these constants and the Bohr magneton μ_{B}, which serves as a base unit for the Zeeman-induced energy shifts, will give a value for the magnetic field strength necessary for the two interactions to be of comparable strength [85, 116, 139],

$$B_{\text{HPB}_{\text{min}}} = \frac{(A_{\text{HF}}/h)}{\mu_{\text{B}}}. \tag{2.25}$$

As the magnitude of the magnetic field increases the shift in energies caused by the Zeeman effect will increase proportionally, by virtue of equation 2.21, to the point where these become similar in value, and eventually equal or greater, to the hyperfine energy splitting in the atom. A similar expression to that given in equation 2.25 can be written for this limit in terms of the hyperfine splitting between the highest and lowest energy states, Δ_{HF},

$$B_{\mathrm{HPB}} = \frac{\Delta_{\mathrm{HF}}}{\mu_{\mathrm{B}}}. \tag{2.26}$$

When this occurs the atom can no longer be properly described by the (F, m_F) quantum numbers as the hyperfine interaction no longer dominates. In this case, the 'good' quantum numbers that describe the energy states of the system are (J, m_J) and (I, m_I), which correspond to the total angular momentum of the electron $\hat{\mathbf{J}}$ and the nuclear spin $\hat{\mathbf{I}}$, respectively. This transition between these two regimes for describing the energy states of the system is shown in figure 2.1. Once again, we can describe the interaction, using equation 2.21, by writing the magnetic dipole moment $\hat{\boldsymbol{\mu}}$ in terms of $\hat{\mathbf{J}}$ and $\hat{\mathbf{I}}$ [85],

$$\hat{H}_{\mathrm{Zeeman}} = -\hat{\boldsymbol{\mu}} \cdot \hat{\mathbf{B}} \approx \left(-\frac{\mu_{\mathrm{B}}}{\hbar} g_J \hat{\mathbf{J}} + -\frac{\mu_N}{\hbar} g_I \hat{\mathbf{I}} \right) \cdot \hat{\mathbf{B}}, \tag{2.27}$$

with g_J, g_I the gyromagnetic ratios for the total electronic angular momentum and the nuclear spin, respectively. The atom at this point is said to be in the *hyperfine Paschen-Back* (HPB) regime, and the shift in the energy levels can be described by the expression [85, 118, 116]

$$\Delta E_{\mathrm{Zeeman}} = \mu_{\mathrm{B}} \left(g_J m_J + \frac{m_e}{m_p} g_I m_I \right) B, \tag{2.28}$$

where $m_J = -J, -J+1, ..., J-1, J$ and $m_I = -I, -I+1, ..., I-1, I$ are the projections of $\hat{\mathbf{J}}$ and $\hat{\mathbf{I}}$ along the quantisation axis, respectively, and B is the magnitude of the magnetic field. We have also written the nuclear magneton μ_N in terms of the Bohr magneton μ_{B} via the relation $\mu_N = \frac{m_e}{m_p}\mu_{\mathrm{B}}$ which uses the mass of the electron m_e and the mass of the proton m_p. As this last ratio is small ($\approx 1/2000$) the last term in equation 2.28 will not contribute as

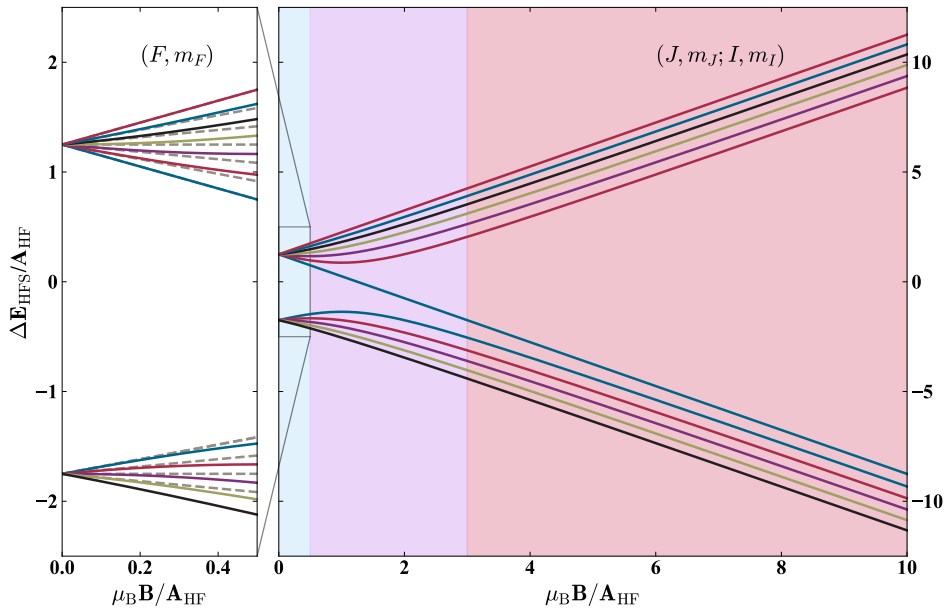

Figure 2.1: Breit-Rabi diagram for a $J = 1/2$ atomic system with $I = 5/2$, showing the transition between the linear Zeeman regime (left panel; blue shaded region), given by equation 2.24, and the hyperfine Paschen-Back regime (red shaded region), given by equation 2.28. The diagram is plotted in dimensionless units of $\Delta E_{\mathrm{Zeeman}}/A_{\mathrm{HF}}$, $\mu_{\mathrm{B}}B/A_{\mathrm{HF}}$, to demonstrate this behaviour without the necessity of specifying an atomic species. We note that in the intermediate points of the transition (*i.e.* purple shaded region), neither (F, m_F) or $(J, m_J; I, m_I)$ are good quantum numbers for the system, but linear combinations of either bases can be used to describe the energy levels. In the left panel, the linear dependence in B of the different energy levels in the (F, m_F) basis is plotted as a guide to the eye.

significantly to the shift in energies as the first term.

One way of visualising this change of regime is by looking at how the angular momenta precess about the direction of the external magnetic field $\mathbf{B}$, as seen in figure 2.2: while at low field strengths the total atomic angular momentum $\hat{\mathbf{F}}$ precesses about $\mathbf{B}$. Once the field strength is high enough, the angular momenta that make up $\hat{\mathbf{F}}$ (the total angular momentum of the electron $\hat{\mathbf{J}}$ and the nuclear angular momentum $\hat{\mathbf{I}}$) decouple and precess independently about $\mathbf{B}$.

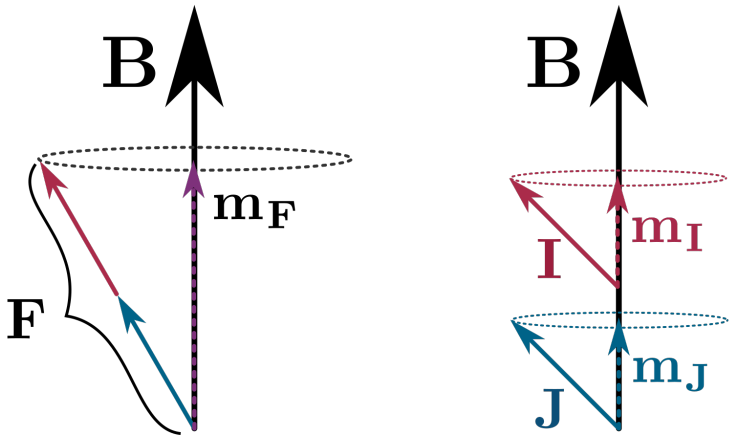

Figure 2.2: Diagram showing the precession of different angular momenta in the atom about an external magnetic field **B**. On the left, for a low magnetic field strength, the total angular momentum of the electron **J** and the nuclear spin **I** couple into the total angular momentum **F**; this then precesses about **B** given that (F, m_F) are the 'good' quantum numbers in this regime. On the right, at higher field strengths, the Zeeman shift of the energies is greater than or equal to the hyperfine structure of the atom, which causes (F, m_F) to no longer be a good quantum number to describe the energy states. Rather, the energy states can now be described by the quantum numbers (J, m_J) and (I, m_I) in what is known as the *hyperfine Paschen-Back* regime, and both **J** and **I** now precess independently about **B**.

2.2.2 Faraday geometry

As mentioned at the beginning of section 2.2, the interaction between an atom and an external magnetic field has a strong geometric dependence as described by equation 2.21. It is this, along with the geometric dependence of the atom-light interaction (see section 2.1.2), that determines geometries of particular interest in the study of interactions between atoms, light and magnetic fields. A basic scheme of these geometric considerations is given in figure 2.3. One such geometry is when we consider both of these interactions to have the same quantisation axis, *i.e.* when we assume the propagation of the light, given by the wave-vector $\mathbf{k}$, and the direction of the magnetic field $\mathbf{B}$ are parallel ($\mathbf{k} \parallel \mathbf{B}$, $\theta_B = 0$; see figure 2.3). This is commonly referred to as the *Faraday* geometry [59, 60, 140].

In this configuration we will assume that both $\mathbf{k}$ and $\mathbf{B}$ are oriented along the Cartesian z-axis. This means that for light, assumed to be a plane wave and as described by Maxwell's equations, we will have oscillating electric $\mathbf{E}_{\text{light}}$ and magnetic $\mathbf{B}_{\text{light}}$ fields in the $x - y$ plane. Defining the polarisation of the light as the direction of oscillation of the electric field $\mathbf{E}_{\text{light}}$, we see that the plane of polarisation is perpendicular to the quantisation axis defined by $\mathbf{k}, \mathbf{B}$. The result is that the matrix elements of the system, with a Hamiltonian composed of those given in equations 2.8 and 2.21, are non-zero for elements of the dipole operator with $q = \pm 1$. Said elements correspond to the light that interacts with the atom exciting only σ^+ ($q = 1$) or σ^- ($q = -1$) electronic transitions between the ground and excited energy levels [59, 74, 132, 141].

2.2.3 Voigt geometry

The second geometry of interest when looking at interactions between atoms, light and magnetic fields occurs when the aforementioned have different quantisation axes. The most significant of these configurations is the case of perpendicular quantisation axes as defined by the atom-light interaction and the interaction with an external magnetic field. In terms of the notation

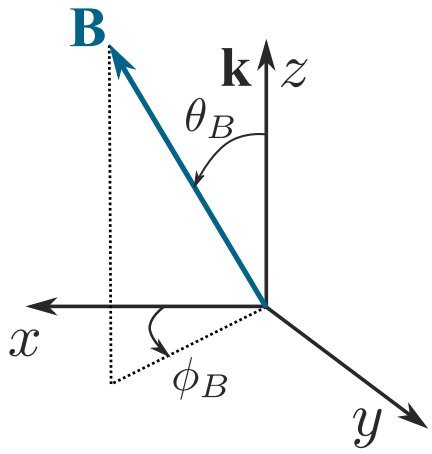

Figure 2.3: Basic scheme of the general geometry for experiments involving atom-light interactions in the presence of an external magnetic field. **k** is the wave-vector of the light, which indicates the direction of propagation of the light interacting with the atom and **B** is the direction of the external magnetic field. We introduce the angle θ_B to describe the relative orientation between **k** and **B**. The electromagnetic nature of light, as set forth by Maxwell's equations, implies that the oscillations of the electric and magnetic fields of the light occur in a perpendicular direction to the propagation for a plane wave; if we assume the direction of **k** lies along the Cartesian z-axis as shown, the electric and magnetic fields then lie in the $x-y$ plane. An arbitrary angle ϕ_B can be defined to describe the direction of the magnetic field relative to the Cartesian x-axis, which is conveniently taken as the direction of the electric field of the light.

provided in the previous section, this corresponds to the direction of propagation of the light and that of the magnetic field being at an angle of $\theta_B = \pi/2$ with respect to each other (*i.e.* $\mathbf{k} \perp \mathbf{B}$), as per the scheme given in figure 2.3. This is referred to as the *Voigt* geometry [134, 142, 143].

For the configuration described above we can assume the wave-vector $\mathbf{k}$ of the light as oriented along the Cartesian z-axis. This means that, per the conditions given for the Voigt geometry, the magnetic field $\mathbf{B}$ must be oriented in the $x - y$ plane. Without any loss of generality, we assume $\mathbf{B}$ to be along the x-axis. As a corollary of the above, we can see that in general we can define the electric field of the light $\mathbf{E}_{\text{light}}$ to be co-planar to the external magnetic field $\mathbf{B}$. We introduce an arbitrary angle, ϕ_B, to describe the orientation of $\mathbf{B}$ relative to that of $\mathbf{E}_{\text{light}}$, as seen in figure 2.3. This results in the ability to split $\mathbf{E}_{\text{light}}$, which also defines the polarisation state of the light, into two orthogonal components, one of which lies along the direction of $\mathbf{B}$ ($\phi_B = 0$), so that the system has a greater number of non-zero matrix elements. In particular, it can be seen that the component of $\mathbf{E}_{\text{light}}$ that is parallel to $\mathbf{B}$ gives matrix elements of the system are non-zero for the element of the dipole operator with $q = 0$. This means that, in contrast to the Faraday geometry, light interacting with the atom can excite π ($q = 0$) electronic transitions [113, 134]. Conversely, the component perpendicular to the direction of $\mathbf{B}$ can drive $\sigma^{\pm}$ ($q = \pm 1$) transitions in the atom (as in the Faraday geometry, but weighted by a factor $\sin^2(\phi_B)$) [114].

2.3 Atomic structure of an alkali metal

The theory presented in sections 2.1 and 2.2 is general and applies to many atomic species. However, the scope of this work is directed primarily at looking at alkali metals in part due to their similarity to the hydrogen atom and in part due to their prevalence among experimental work in recent history. These atomic species are characterised by having one uncoupled electron in the outermost energy level of the atom (*i.e.* a single valence electron) that interacts not only with other atomic species, but also with any external electromagnetic

fields. By virtue of this single valence electron, alkali-metal atoms have an electronic spin $\mathbf{S} = 1/2$, with projections $m_S = \pm 1/2$ along the quantisation axis. Another fact to note is that the total orbital angular momentum $\mathbf{L}$ of the system is simply the orbital angular momentum of the valence electron. As a result of this, alkali-metal atoms have a $n^2S_{1/2}$ ground state ($L = 0$) configuration, with $n \geq 2$ the principal quantum number of the atom; similarly, alkali-metal atoms have a fine-structure doublet in the first excited state ($L = 1$) corresponding to projections of the total electronic angular momentum $J = 1/2, 3/2$. Experimentally this is seen in the characteristic *D-lines* in the absorption spectra of these alkali metals [85, 86, 116, 139].

For the remainder of this thesis, all of the work presented will be carried out with the alkali-metal atom with $n = 5$: rubidium. Nevertheless, all of the work presented can be easily adapted to other common alkali-metal atoms such as caesium ($n = 6$), potassium ($n = 4$), sodium ($n = 3$) and lithium ($n = 2$).

2.3.1 Atomic structure of rubidium

In this section the structure of the atomic electron energy levels of rubidium is presented in order to give a foundation for the understanding of the remainder of this work. As mentioned previously in section 2.3, rubidium (Rb) is an alkali-metal atom with a principal quantum number of $n = 5$. Its atomic number is $Z = 37$, and the ground state electronic configuration is [Kr]5s. Atomic rubidium has two naturally occurring isotopes: rubidium 85 (^{85}Rb) with an abundance of 72.17% and nuclear spin $I = 5/2$ and rubidium 87 (^{87}Rb) with an abundance of 27.83% and nuclear spin $I = 3/2$. The former is stable, while the latter is radioactive with a half-life of 48.8×10^9 years and undergoes β^- decay [118].

In the absence of external electric and magnetic fields, the quantum-mechanical description of an atom formulated in section 2.1.1 is valid and the energy levels for the electron in a rubidium atom are given in the coupled (F, m_F) basis due to the hyperfine interaction. A simple energy level diagram showing

this structure for ^{87}Rb is shown in figure 2.4; the diagram for ^{85}Rb is similar with the exception of the values of F and the differences between the hyperfine energy levels. In the scope of this work we will focus on the isotope ^{87}Rb as the separation between the energy states is larger; the ground-state hyperfine energy levels are separated in frequency by ~ 6.83 GHz [119, 144]. This will prove to be an advantage as it will allow for the different absorption lines to be more clearly resolved, despite Doppler broadening, as will be seen in chapters 3, 4 and 5.

From the $5^2S_{1/2}$ ground state, the valence electron in rubidium can be excited with near-IR radiation to the 5^2P_J excited state. The electronic transition $5^2S_{1/2} \rightarrow 5^2P_{3/2}$ is known in the literature as the *D2 line*, while the transition $5^2S_{1/2} \rightarrow 5^2P_{1/2}$ is known as the *D1 line* [116, 118, 119]. Of these two, the D2 line is favoured experimentally as it has a closed hyperfine transition, greater transition strength [119, 144] and allows for greater signal-to-noise ratios in most measurements.

In the presence of an external magnetic field $\mathbf{B}$, the energy levels of a rubidium atom will change as per the theory discussed in section 2.2. As previously mentioned, the interaction with the external magnetic field can be characterised into two regimes of interest for this work. In the first, the magnitude of $\mathbf{B}$ is small enough to generate energy shifts smaller that the differences in energy of the hyperfine levels. This means that the system can be described in the coupled (F, m_F) basis, with the Zeeman energy shifts given by equation 2.24.

In the second, the strength of $\mathbf{B}$ is such that the atom transitions into the hyperfine Paschen-Back regime. The description of this regime is given in section 2.2.1, with the energy shifts due to the interaction expressed in equation 2.28. However, from figure 2.4 it is clear that the difference in splittings between hyperfine levels is smaller in the excited state than in the ground state, and this will cause the interaction with $\mathbf{B}$ to become dominant at different values of the field strength. This is easily quantified by comparing the hyperfine level splittings to the Bohr magneton μ_B and is shown in table 2.1 for the ground state and in table 2.2 for the excited state. These

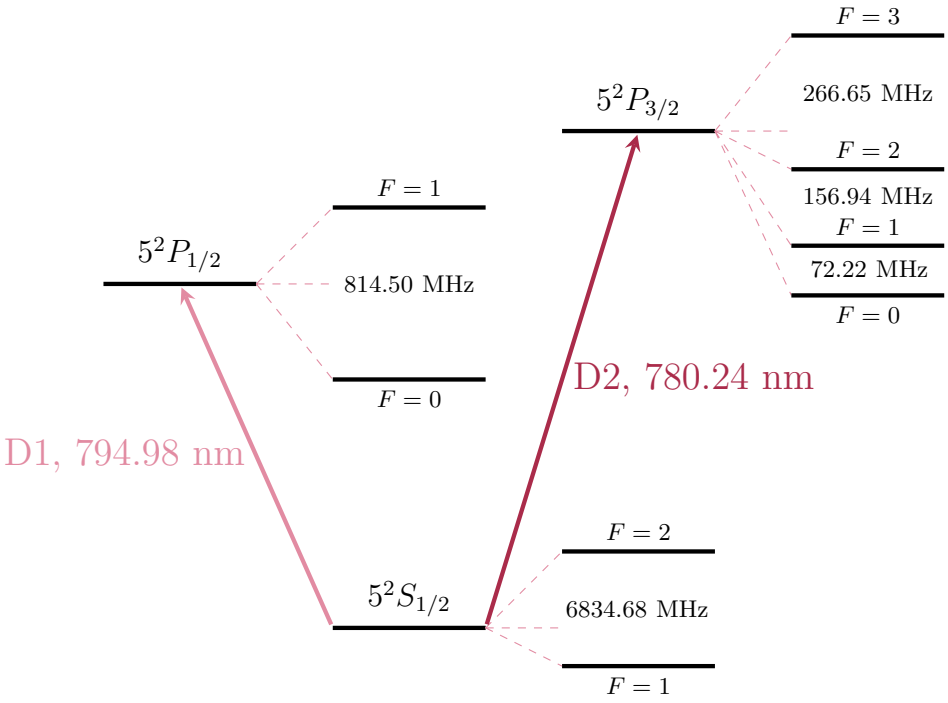

Figure 2.4: Energy level diagram for ^{87}Rb, showing the ground state, the fine structure doublet in the first excited state ($5^2P_{1/2}$ and $5^2P_{3/2}$) and hyperfine (F) energy levels in the absence of external electric and magnetic fields. The $5^2S_{1/2} \rightarrow 5^2P_{1/2}$ electronic transition is commonly referred to as the *D1 line* and has an excitation wavelength of 794.98 nm. Similarly, the $5^2S_{1/2} \rightarrow 5^2P_{3/2}$ electronic transition is referred to as the *D2 line* and has an excitation wavelength of 780.24 nm [144, 145].

Isotope	$\mathbf{A_{HF}/h}$ **(MHz)**	$B_{\mathrm{HPB}_{\mathrm{min}}}$	**HF splitting (MHz)**	B_{HPB}
^{85}Rb	1011.91	~ 0.07 T	3035.73	~ 0.22 T
^{87}Rb	3417.34	~ 0.24 T	6834.68	~ 0.49 T

Table 2.1: Minimum magnetic field values for atoms to enter the hyperfine Paschen-Back regime, $B_{\mathrm{HPB}_{\mathrm{min}}}$ (equation 2.25), and for the Zeeman shift in energy to be equal to the hyperfine splitting, B_{HPB} (equation 2.26), in the ground state ($5^2S_{1/2}$) of the rubidium atom. The values for the hyperfine constants A_{HF} are obtained from [141]. To obtain the values of the magnetic field, the hyperfine constant/ground-state splitting is compared to the Bohr magneton μ_{B}, expressed in units of frequency shift per unit magnetic field ($\mu_{\mathrm{B}} = 1.399624 \times 10^4$ MHz/T).

State	**Isotope**	$\mathbf{A_{HF}/h}$ **(MHz)**	$\mathbf{B_{HF}/h}$ **(MHz)**	$B_{\mathrm{HPB}_{\mathrm{min}}}$ **(T)**	**Manifold splitting (MHz)**	B_{HPB} **(T)**
$5^2P_{1/2}$	^{85}Rb	120.64	-	~ 0.009	361.58	~ 0.03
	^{87}Rb	406.15	-	~ 0.03	814.50	~ 0.06
$5^2P_{3/2}$	^{85}Rb	25.04	26.01	~ 0.002	213.41	~ 0.02
	^{87}Rb	84.72	12.50	~ 0.006	495.81	~ 0.04

Table 2.2: Minimum magnetic field values for atoms to enter the hyperfine Paschen-Back regime, $B_{\mathrm{HPB}_{\mathrm{min}}}$ (equation 2.25), and for the Zeeman shift in energy to be equal to the hyperfine splitting, B_{HPB} (equation 2.26), in the $5^2P_{1/2}, 5^2P_{3/2}$ excited states of both Rb isotopes.The values for the hyperfine constants $A_{\mathrm{HF}}, B_{\mathrm{HF}}$ are obtained from [141]. To obtain the values of the magnetic field, the hyperfine constant/ground-state splitting is compared to the Bohr magneton μ_{B}, expressed in units of frequency shift per unit magnetic field ($\mu_{\mathrm{B}} = 1.399624 \times 10^4$ MHz/T).

limits can be seen in figures 2.5 and 2.6 for ^{87}Rb, which show the energy shifts due to the Zeeman effect in the ground and excited states, respectively, as a function of field strength B.

2.4 Numerical calculations of theoretical spectra using *ElecSus*

We can now take the general theoretical concepts covered thus far in this chapter and incorporate additional details to enrich them in order to verify

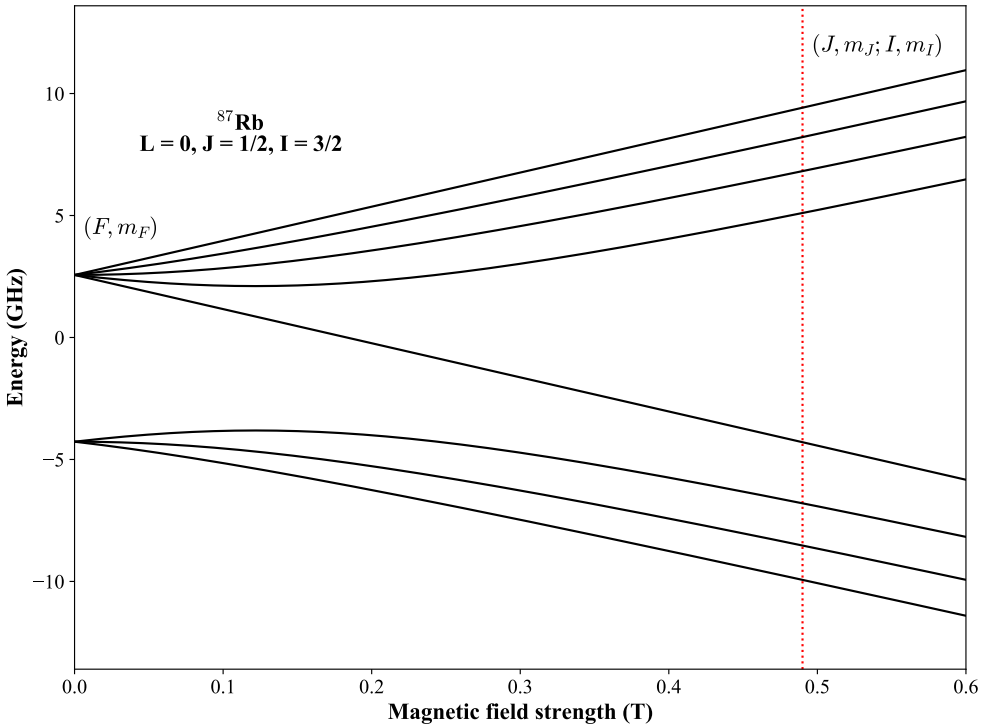

Figure 2.5: Diagram of the energy level shifts as a function of field strength B for the $5^2S_{1/2}$ ground state of ^{87}Rb. On the left of the diagram, the energy levels are described by their (F, m_F) quantum numbers. As the field strength increases, these are no longer "good" quantum numbers for the system. The transition to the hyperfine Paschen-Back regime (B_{HPB}; see section 2.2.1), indicated by the vertical line and given by the value in table 2.1, means that the energy levels can now be described by the quantum numbers (J, m_J) and (I, m_I). This diagram is commonly known in literature as the Breit-Rabi diagram.

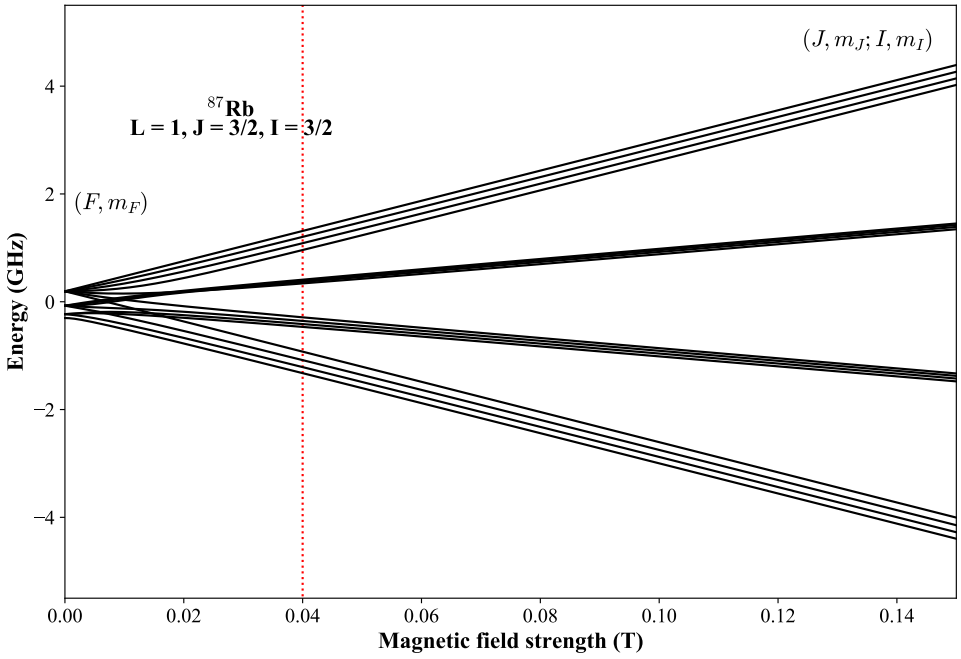

Figure 2.6: Diagram of the energy level shifts as a function of field strength B for the $5^2P_{3/2}$ excited state of ^{87}Rb. On the left of the diagram, the energy levels are described by their (F, m_F) quantum numbers. As the field strength increases, these are no longer "good" quantum numbers for the system. The transition to the hyperfine Paschen-Back regime (B_{HPB}; see section 2.2.1), indicated by the vertical line and given by the value in table 2.2, means that the energy levels can now be described by the quantum numbers (J, m_J) and (I, m_I). We note how, in comparison to the $5^2S_{1/2}$ ground state, the transition to the hyperfine Paschen-Back regime occurs at a much lower field in this case. This is a result of the smaller hyperfine level splittings, given by the constants A_{HF} and B_{HF} in table 2.2.

and validate our experimental results, which will be presented further on in chapters 3, 4 and 5. All of these concepts and details are incorporated in a single, easy-to-use model in the form of the publicly-available software package *ElecSus*[1]. This has been extensively validated previously [134, 141], and we find that it remains valid over the parameter space we present in our experimental fits and simulated datasets. As such, we only give a brief overview of how *ElecSus* carries out the numerical calculations, and refer readers to references [134, 141] for greater detail on how the software operates.

Of particular interest in this work will be the simulating the case of the interaction of an alkali-metal atomic thermal vapour with a near-resonant laser field whilst in the presence of an external magnetic field. In the experiments, the atom-light system is placed in an external magnetic field oriented as per the Voigt geometry. Furthermore, we will also consider the strength of the magnetic field used to be such that the alkali-metal vapour (in this case a ^{87}Rb vapour) is in the hyperfine Paschen-Back regime. We will thus, without loss of generality, consider the atomic states in the uncoupled $|m_L, m_S, m_I\rangle$ basis, taking into account the internal energy levels of the atom and the energy shifts due to the Zeeman effect. More detail of what these considerations imply is given in sections 2.2.1 and 2.2.3. As we will be looking at realising measurements arising from these interactions, we consider the macroscopic effects as visible in a laboratory environment (see section 2.1.3).

The numerical calculations begin by taking the key parameters of the system (*i.e.* the constants and values associated to the atomic species of choice) and using them to construct the atomic Hamiltonian, given by equation 2.4, in the uncoupled $|m_L, m_S, m_I\rangle$ basis; a separate Hamiltonian is constructed for the n^2S ground state and for the n^2P excited state. At this point it is also possible to add the Zeeman Hamiltonian, using equations 2.21 and 2.22, to consider the interaction of the atom with an external magnetic field of strength B. It is worth noting that the Hamiltonians at this point are constructed assuming the rotating-wave approximation has been taken (allowing a detuning Δ to be defined and to consider the system in the

[1] https://github.com/jameskeaveney/ElecSus

rotating frame), and that the direction of light propagation is along the z-axis, setting this as the quantisation axis for the system. From here, matrix operations are implemented to numerically diagonalise the Hamiltonian, effectively finding the set of eigenstates and eigenvalues which give the atomic states and their respective energies. The atomic transitions of interest in the system are obtained by selecting rows in the ground-state and excited-state Hamiltonians, following the selection rules given in equation 2.10 and considering the geometry of the system (see section 2.2.1).

With this we can now consider the complex electric susceptibility $\chi(\Delta)$ of a two-level atom, in this case between an energy level in the ground state and one in the excited state, given in general by equation 2.14. The corresponding transition strength C and resonant frequency are determined by operating with the rows of the Hamiltonians and the energies corresponding to the selected states. The movement of the atoms in the thermal vapour gives rise to a Doppler shift, modifying the susceptibility to arrive at the expression given in equation 2.16. This expression can be extended to a multi-level atom composed of j transitions (*e.g.* the complete diagonalised Hamiltonian previously discussed), such that each transition can be associated to a susceptibility $\chi_j(\Delta_j)$ that has a well-defined detuning Δ_j, strength C_j and reduced dipole matrix element d_j. By virtue of the principle of superposition, and assuming there are no coherent effects in the system, we can write the total susceptibility of the atomic medium χ_{T} as,

$$\chi_{\mathrm{T}}(\Delta) = \sum_j \chi_j(\Delta - \Delta_j), \tag{2.29}$$

where we have taken Δ as a global detuning common to all transitions. It is important to note that Δ is defined as an angular frequency, while experimentally a linear frequency (*i.e.* $\Delta/2\pi$) is measured.

With the total electric susceptibility of the medium χ_{T} now defined, we can now consider the phenomena of atomic absorption. Using equations 2.11 and 2.12, we can use the Beer-Lambert law to write the atomic absorption coefficient and an expression for the total amount (intensity, I) of light

transmitted through the medium,

$$\begin{aligned} \alpha_{\text{atom}}(\Delta) &= k\Im[\chi_{\text{T}}(\Delta)], \\ T_{\text{light}} \equiv I(l) &= I_0 \exp(-\alpha_{\text{atom}}(\Delta)l) = I_0 \exp(-k\Im[\chi_{\text{T}}(\Delta)]l). \end{aligned} \quad (2.30)$$

Here we have assumed the absorption is a function of the length l of the atomic medium and k is the magnitude of the propagation vector of the laser field; I_0 is the intensity of the light incident on the medium. In order for equation 2.30 to be valid, we maintain the approximation used in equation 2.13, namely that $|\chi| \ll 1$; this is equivalent to assuming that work is being carried out in the weak-probe regime [51]. Previous work [146] in a dense rubidium vapour has also shown that the maximum value of the susceptibility is $\chi = 0.3$, allowing us to use the aforementioned approximation for easier calculation of the properties of the atomic system.

With the complex susceptibility defined, we can now use the relation between susceptibility and refractive index given in equations 2.12 and 2.13 to define the complex refractive index of the atomic medium. From here the wave equation can be solved in order to find the two propagation eigenmodes, each associated with a complex refractive index n_i that couples to the atomic transitions in a distinct manner. As was mentioned in section 2.1.3, a complex refractive index has effects on both the dispersive and absorptive properties of the medium: the differences in these complex refractive indices associated with their respective eigenmodes mean that the atomic medium is both *dichroic* and *birefringent*.

We can calculate the combined result of all of these effects on the light transmitted by transforming the electric field into the eigenbasis coordinate system, propagating each refractive index over the length l of the atomic medium by multiplying using a factor $e^{in_i kl}$, and finally transforming back to the laboratory coordinates that are most relevant. The components of the latter are analysed via Stokes polarimetry [89, 135]. As defined in section 2.1.4, these are a set of parameters easily accessible in the laboratory obtained by measuring the intensity of light in different sets of orthogonal polarisation

bases. Of particular interest is the Stokes parameter S_0,

$$S_0 \equiv I(l)/I_0 = \exp(-\alpha_{\text{atom}}(\Delta)l) \tag{2.31}$$

which represents the normalised total transmitted intensity of the light, thus giving a measurement independent of the basis used to measure the components.

Assuming the propagation of linearly-polarised plane wave along the Cartesian z-axis, the polarisation of this light will lie in the $x-y$ plane. Taking the direction of polarisation (the electric field $\mathbf{E}$) to lie along the x-axis, we define the polarisation angle ϕ_B as the angle between $\mathbf{E}$ and the external magnetic field $\mathbf{B}$. We recall once again that we are working in the Voigt geometry (see section 2.2.3), such that $\mathbf{k} \perp \mathbf{B}$. In our case, the refractive indices are associated with the propagation of linearly polarised light as a result of the geometry. Light polarised so that $\phi_B = 0$ will drive π transitions while light polarised such that $\phi_B = \pi/2$ will drive $\sigma^{\pm}$ transitions. From this geometry it must be noted that the relative phase between polarisation components of $\mathbf{E}$ is unimportant, *i.e.* for circularly polarised light of either left- or right-handedness, the light couples to the atoms as linearly polarised light with equal x and y components ($\phi_B = (2n-1)\pi/4; n \in \mathbb{Z}$) would.

All of the above processes for numerically calculating atomic spectra with *ElecSus* can be summarised in the block diagram shown in figure 2.7. We note that *ElecSus* provides a graphical user interface (GUI) as well as access via an API for external Python scripts in order to carry out these calculations.

For the purpose of this work, some modifications were made to the *ElecSus* code in order to proceed more efficiently with the analysis of our results. The first of such changes was to incorporate analytical expressions [148] for solving the wave equation associated with propagation eigenmodes obtained in an *arbitrary geometry*, *i.e.* when the system is neither in the Faraday or Voigt geometries. These expressions allow for faster calculation of the theoretical spectra in this general case. The second notable change was the inclusion of

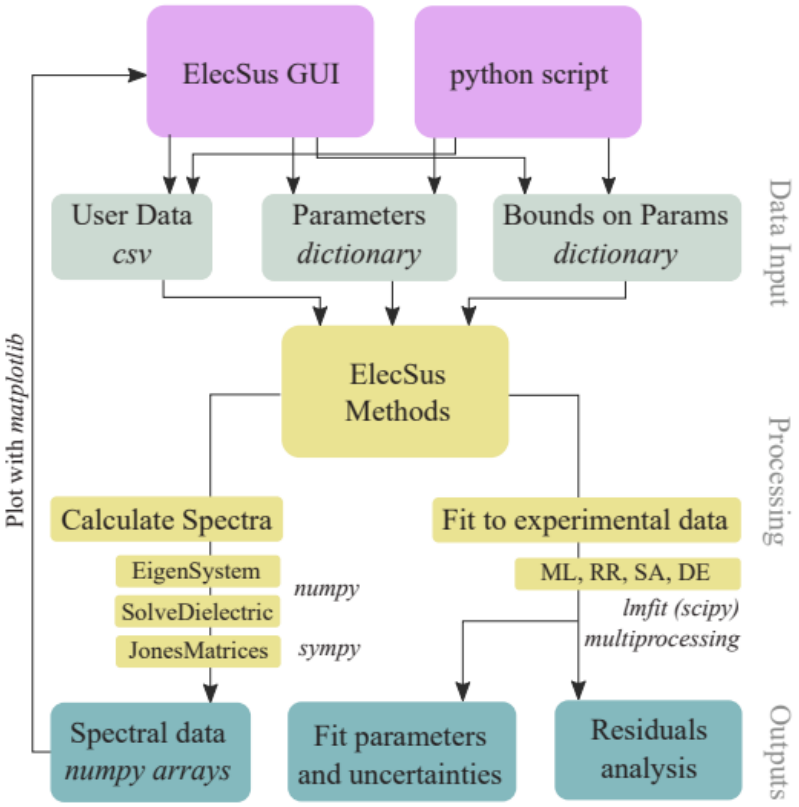

Figure 2.7: Block diagram showing the general flow of information in the *ElecSus* software. In order to numerically calculate a theoretical spectra, the user must first introduce the system parameters into the software. These are then processed according to the process described in this section in order to obtain the atomic spectra of interest. The software also allows for fitting experimental data to the theoretical model, which is discussed in more detail in section 2.4.1 and in later chapters. This figure is taken from [147].

a module in order to allow for calculation of spectra with variations in the ground-state populations (see chapter 6 for further details). These changes, while extending and improving the functionality of the software, do not substantially modify the procedure for calculating atomic spectra described in this section.

2.4.1 Fitting of experimental data

In addition to numerical calculations, *ElecSus* also allows for experimental spectra to be fit directly with the theoretical model. In order to do this, the frequency-calibrated experimental data is introduced into the code in `.csv` format. The experimental parameters are also introduced as the starting parameters for the calculations, and a fitting routine is chosen. Fitting is done with the `lmfit` Python package [149, 150] to allow for boundaries on the fit parameters to be set, as well to allow for determination of the uncertainties in these. A block diagram of the fitting process is shown in figure 2.7.

The fits carried out with *ElecSus*, through use of the `lmfit` package, allow for multi-parameter fits where individual parameters can be fixed or bound to vary within a range of values [134]. Furthermore, a choice of several fit algorithms is available to allow for local minima and the global minimum of the parameter space to be found. Specific details on these algorithms, their operation and advantages is beyond the scope of this work; detailed information can be found on the documentation pages for `lmfit` [149, 150]. The output from carrying out a fit with this package consists of a set of optimised parameters and their uncertainties, as well as the fit residuals and best-fit curve. For the purposes of this work it is important to note that the uncertainties obtained from these fits, taken to represent the *estimated statistical standard error* (1σ uncertainty)[2], will be reported in the experimentally-determined values. These errors are obtained from calculating the covariance matrix for the fit parameters, which also allows for correlations amongst the different parameters

[2]See documentation at https://lmfit.github.io/lmfit-py/fitting.html#uncertainties-in-variable-parameters-and-their-correlations for a more detailed discussion.

to be determined. As such, this information can be used for additional corrections to the calculated uncertainty to be calculated if necessary. It is also worth noting that the fits are carried out assuming a uniform weight for the data, and the fitted function has been adequately scaled before minimisation (in the case of *ElecSus* this is true, as the absorption is scaled between 0 and 1).

2.5 Summary

In this chapter we have presented a theoretical framework for describing the interaction between atoms, light and external magnetic fields. We have seen the semi-classical formalism that describes the quantum mechanical nature of the atom and the classical electromagnetic interaction between the electrons in the atom and light in the form of an electromagnetic field. From this we have studied the macroscopic manifestations of this interaction, as measured by atomic spectroscopy experiments. We then gave details on the interaction between the atom-light system and an external magnetic field, looking in particular at the hyperfine Paschen-Back regime and the importance of geometry in the interaction. We concluded by looking at the significance and structure of alkali-metal atoms in this framework, with emphasis on the case of rubidium. For the analysis of experimental results presented in the following chapters of this work, the above theory forms the basis of the model implemented in the *ElecSus* [134, 141] software package used. With this we will look at experiments carried out in the Voigt geometry at different magnetic field strengths, and some applications of these experiments to fields such as metrology.

Chapter 3

Spectroscopy of a Rb vapour in the Voigt geometry at 0.4 T

This chapter is based on the following publication:

J. Keaveney, F. S. Ponciano Ojeda, S. Rieche, M. J. Raine, D. P. Hampshire and I. G. Hughes, *Quantitative optical spectroscopy of* ^{87}*Rb vapour in the Voigt geometry in DC magnetic fields up to* 0.4 *T*, Journal of Physics B: Atomic, Molecular and Optical Physics **52**, 055003 (2019), 10.1088/1361-6455/ab0186

3.1 Introduction

In the hyperfine Paschen-Back (HPB) regime, discussed in section 2.2.1, the decoupling of the nuclear and electronic spins introduces an additional geometric constraint on the system derived from the fact that the magnetic field now acts as a quantisation axis. The simplest case of this constraint, and the most commonly used thus far, is the Faraday configuration, as previously defined in section 2.2.2. In this configuration spectroscopic measurements taken serve only to quantify the magnitude of the magnetic field [93]. However, another case of this geometric constraint is possible, when the external magnetic field and the wave-vector of the light are now perpendicular. This configuration,

where $\mathbf{k} \perp \mathbf{B}$, is known as the Voigt configuration (see section 2.2.3). Here, spectroscopic measurements allow both the magnitude *and* the relative direction of the magnetic field to be determined. While both configurations allow determining the magnitude of the field used, the added ability to determine the relative direction of the magnetic field on a plane perpendicular to $\mathbf{k}$, a fact not possible in the Faraday configuration, presents the option of carrying out 2D vector magnetometry when using the Voigt configuration.

Together with the decoupling generated at high fields, the Voigt configuration allows for new possibilities of expanding previous work of atomic spectroscopy in the presence of external magnetic fields. The shift in energies and decoupling generated in the hyperfine Paschen-Back regime provide atomic systems that can be more easily described by the appropriate theoretical treatment [24, 60, 110, 112, 151], while the geometry of the Voigt configuration allows 2D vector magnetometers to be developed. In this chapter we present both the theory and experimental methods necessary to study a thermal vapour of ^{87}Rb in the Voigt geometry with a variable-strength magnetic field up to 0.4 T. This allows us to demonstrate how for a given initial light polarisation we can obtain a value for the magnetic field strength and its relative direction to the propagation of the light, with well understood sensitivity of the atomic spectra to changes in both of these parameters.

3.2 Theoretical model

The work presented in this chapter can be described by the general theoretical concepts covered in chapter 2. In particular, our interest is to analyse experimental results by comparing them, through numerical fits, to theoretical spectra. These will be carried out using the model implemented in the publicly-available software *ElecSus*; a brief overview of how this software carries out these numerical calculations is given in section 2.4. In this case we wish to examine the interaction of a ^{87}Rb thermal vapour with a near-resonant laser field tuned on the D2 line, while also in the presence of an external magnetic field of 0.4 T in the Voigt geometry (see section 2.2.3). Under these

conditions, the system can be better described by the characteristics of the hyperfine Paschen-Back regime, discussed in section 2.2.1.

3.3 Experiment

3.3.1 Experimental setup

For the experiments carried out, the experimental setup consists of two main sets of equipment. A diagram of the general experimental setup can be seen in figure 3.1 showing these two sets. Both use a single source of light, provided in this case by a tunable distributed feedback (DFB) laser[1] whose central emission wavelength is 780 nm, with a linewidth specified by the manufacturer to be < 2 MHz and typical output power of ~ 80 mW. The tuneability of the laser, via changes in the operating temperature of the laser diode, allows for mode-hop-free frequency scans over many hundreds of GHz. An optical isolator (OI) is placed at the output of the DFB laser to prevent unwanted back-reflections from generating instability in the emission mode of the laser medium.

Light emitted from the laser, after passing through the OI, is split into two separate beams using a polarising beam-splitter (PBS) and a half-wave retarder plate ($\lambda/2$); this allows for control of polarisation purity and beam power in the resulting beams. From here, one of the beams is sent to the set of equipment that will act as the reference optics for the experiment. The signals obtained from the photodiodes (PD) placed in these reference optics are then used to linearise and calibrate the laser scan as described in section 3.3.2 and Appendix B.

The second beam generated from the first PBS is transmitted towards the second set of equipment used in the experiment, which in this case provides the measurements of interest for this chapter. Prior to entering the vapour cell where the atomic medium is contained, the beam first passes through an acousto-optic modulator (AOM), controlled by a custom-made PID servo

[1]Eagleyard Photonics; part number EYP-DFB-0780-00080-1500-TOC03-0002.

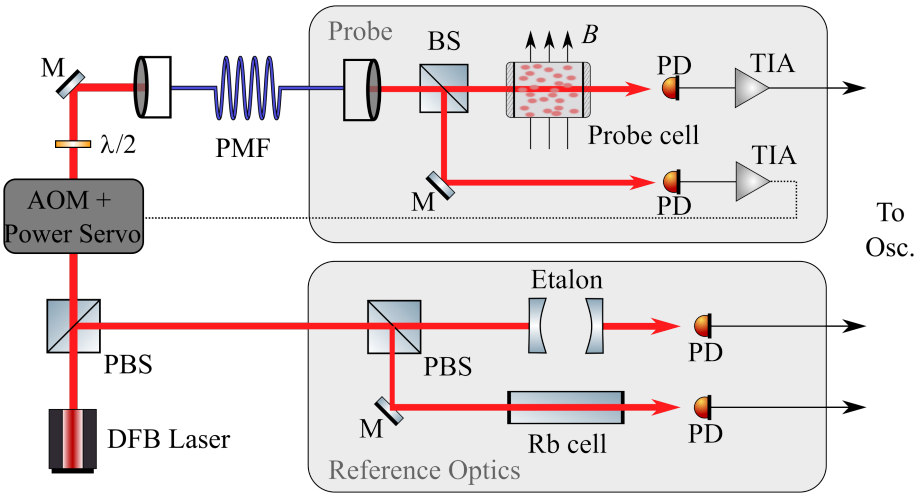

Figure 3.1: Simple scheme of the two experimental optical layouts used: one for reference optics and the other for the experimental (probe) optics. Both layouts have a common light source in the form of a distributed feedback (DFB) laser whose output is split using a polarising beam-splitter (PBS) cube. For the reference optical layout, the light is once again split into two beams, one of which is transmitted through a Fabry-Pérot etalon and a second beam that is transmitted through a reference, natural abundance 75 mm Rb cell; the signals from the photodiodes (PD) in this setup are used to calibrate the laser scan as described in B.1. In the probe layout, light from the laser arrives after passing through an acousto-optical modulator (AOM) and a polarisation maintaining fibre (PMF). Once inside the probe, the light is once again split using a beam-splitter cube (BS) in order to provide a feedback signal for a power-stabilisation servo circuit using the AOM [152]. The laser light is also used to measure the transmission through an isotopically enriched (99% ^{87}Rb) 1 mm vapour cell placed in a variable magnetic field, in the Voigt geometry (see section 2.2.3). **M**: mirror; **Osc.**: oscilloscope; **TIA**: trans-impedance amplifier.

controller, for the purposes of beam-power stabilisation [152]. The resulting beam, the first diffracted order from the AOM, then goes through a further step of polarisation filtering using a combination of a PBS & $\lambda/2$ wave-plate before being coupled into a single-mode polarisation maintaining optical fibre (PMF). The output of the optical fibre is located inside a specially designed probe that allows for the vapour cell to be placed inside an electromagnet, with field magnitudes adjustable up to 0.4 T via an external power supply.

In order to operate the experiment in the desired Voigt configuration, a specially designed probe was designed to allow the vapour cell to be placed in a way such that the field generated by the electromagnet used was perpendicular to the propagation of the light through the cell. For this purpose, a cylindrical probe shape was chosen to allow for the necessary optical and electronic components to be arranged in the interior while allowing for adequate positioning within the electromagnet, as shown in figure 3.2. A central bed of copper, housing a heater and commercially calibrated resistance thermometer[2] [153] that is insensitive to magnetic fields, provides a stable base as well as thermal mass for the experimental system. Upon this base a fibre collimator couples light from the PMF into an optical system consisting of a 5 mm beam-splitter (BS) cube, a vapour cell with a 1 mm cavity length containing isotopically enriched rubidium (99% purity ^{87}Rb) [74] and two photodiodes. The photodiodes are mounted on a custom printed circuit board (PCB) with low-noise trans-impedance amplifiers (TIA) that provide a feedback reference signal for the AOM and PID servo used for stabilising the beam power and a signal with the absorption of light through the atomic medium.

The power of the beam is stabilised to around 1 μW, which for a beam with a $1/e^2$ waist of around 0.5 mm allows for optical pumping effects to be avoided. This is to ensure the atoms interact with the laser beam in the weak-probe regime [51]. As a corollary to this, given the beam waist of ~ 0.5 mm we can also set the effective spatial resolution of the probe to be approximately equal to the volume of atoms that are interrogated, in this case a cylinder of length 1 mm and radius ~ 0.5 mm.

[2]Cernox 1070 temperature sensor, CX-1070-SD-HT-4M; Lakeshore Cryotonics, Inc.

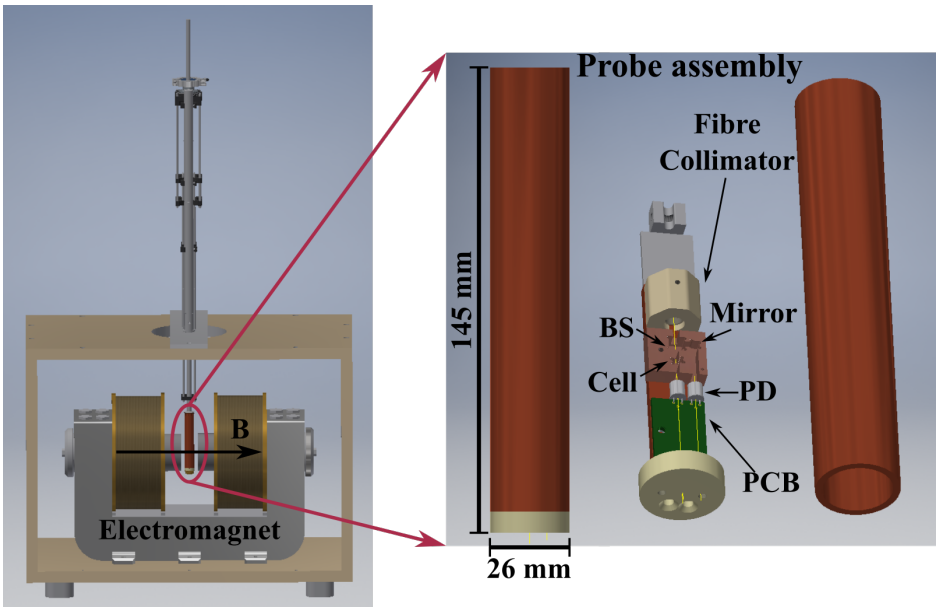

Figure 3.2: Rendered diagram of the custom-built probe for placing the atomic vapour cell in the Voigt geometry inside the variable-strength field generated by an electromagnet. Shown on the left is the position of the probe relative to the electromagnet and the direction of the magnetic field **B** generated between the two pole pieces, separated by 44 cm. The insert on the right shows the interior details of the cylindrical probe. Inside the copper cylinder of the probe assembly is a smaller bed of copper upon which are placed a fibre collimator for delivering light for the experiments, a beam-splitter (BS) cube for dividing the light into two separate beams, the vapour cell and a custom printed circuit board (PCB) with the necessary electronics for detection of the transmission signals generated.

Thermal stability for the system is provided by both passive and active components in the probe design. The central bed of copper is in weak thermal contact with a copper shield that surrounds it; this shield is itself isolated from the environment using a layer of Aerogel insulation. The copper shield also has two flexible silicon heaters attached onto it. These flexible heaters allow a background temperature close to the desired point to be established by delivering a constant power to them. The temperature stability of the vapour cell is then maintained at the desired point by using the internal heater and Cernox thermometer as source for a feedback signal to a PID temperature controller[3]. All of these elements allow for a thermal stability, over the course of an experimental run ($\sim$ 30 min), of better than 100 mK as recorded by the Cernox thermometer and PID controller.

3.3.2 Frequency calibration of experimental spectra

In order for the experimental data obtained to be analysed it must first be processed so that the signals observed can be described in terms of the linear frequency of the laser scan. For this, a set of reference optics consisting of a Fabry-Pérot etalon and a natural abundance rubidium reference cell, each with its respective photodiode, are used. These signals are used to convert the x-axis coordinates of the data, all of which are initially equally spaced in time due to their being acquired with an oscilloscope, into points along a frequency axis; these are then calibrated to an appropriate zero value that represents the interactions in the atomic system [72, 73, 154]. A brief discussion of the most important aspects of this process will be given in this section, with complementary material also given in Appendix B.

Each of the experimental spectra in these experiments is acquired simultaneously with the signals from the reference optics mentioned above. These 'raw' signals can be seen in figure 3.3. As mentioned in section 3.3.1, the signals are obtained by changing the operating temperature of the laser diode, thus changing its frequency of emission, as a function of time. In this way,

[3]Lakeshore Cryotronics Model 336; see manufacturer's page for more information and specifications.

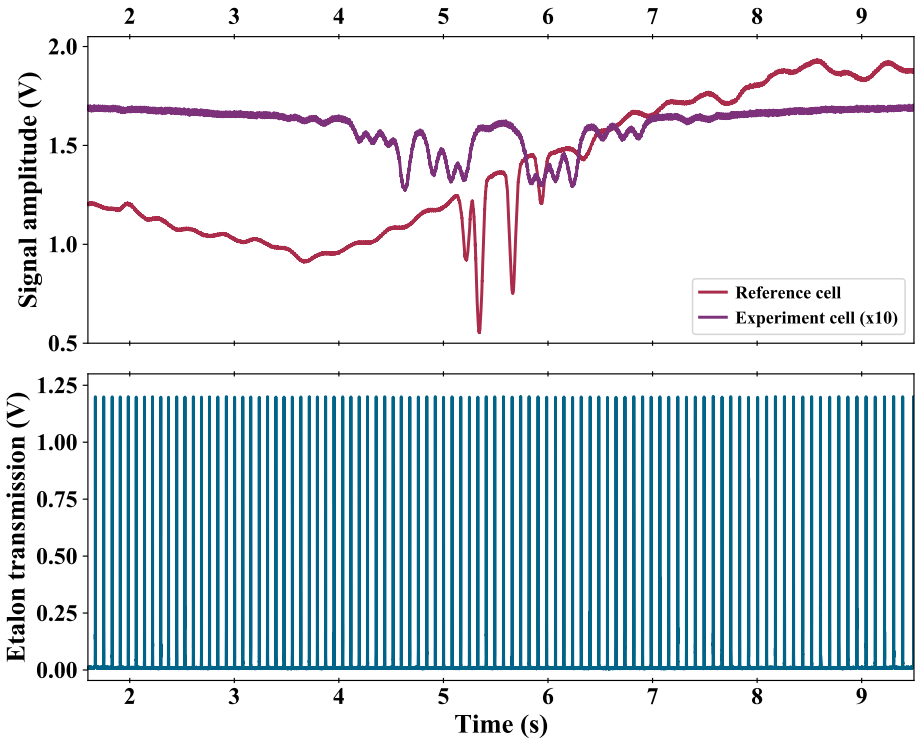

Figure 3.3: Sample raw signals taken with our experimental setup. Shown are the signals from the reference optics (blue curve for the etalon and red curve for the natural abundance Rb reference cell) and the experiment cell (purple curve); the signal from the experiment cell has been multiplied by a factor of 10 for visibility. The signals shown here were acquired using a Tektronix™ digital oscilloscope, with a sample rate of 200,000 points per channel and 50 μs (20K samples/s) resolution.

a wide mode-hop-free scanning range can be obtained, but at the cost of a relatively slow ($\sim$ 10 s) non-linear scan as the thermoelectric element in the laser attempts to stabilise the diode at the set operating temperature. We note that due to the nature of the signal used to scan the temperature of the laser (*i.e.* a triangular waveform), the raw signals are cropped in order to show just one full scan.

To begin the calibration process, we first look at the raw signal obtained for the etalon in the reference optics. Over the range of the laser scan in figure 3.3 it is clear that there are a large number of transmission peaks from the etalon;

this transmission can be characterised by the free spectral range (FSR) of the etalon and a well-known lineshape [130, 132]. As such, we can use the position (in time) of the centre of these peaks to obtain a conversion factor that will allow us to linearise the time axis in preparation for the change to frequency further ahead. Ideally, the distance between adjacent transmission peaks (*i.e.* the FSR) will remain constant over the range of the laser scan, allowing a linear fit to be made between the peak number and its position in time. However, this is not the case in our experiments and in figure 3.3 there is a deviation from the expected position (*i.e.* a deviation from the linear fit) of the transmission peaks. This is shown in figure 3.4; the effect of this deviation can be taken into account by fitting a high-order polynomial function (≥ 5) to the measured positions of the peaks. The resulting curve is then used to convert the non-linear time axis to a linear time axis by evaluating the polynomial at the time corresponding to each data point and subtracting the resulting correction from the data's original time value.

Once the x-axis of our data has been processed to be a linear time axis, it is necessary to locate a zero frequency for said axis that relates the signal to the frequencies observed in the atom-light interactions. For this, we make use of the hyperfine ground-state splitting of ^{87}Rb , which has been carefully measured and reported in literature [119, 144]. To obtain said frequency reference, we make use of the signal from the natural abundance reference cell, shown in figure 3.3. To this signal we fit a theoretical transmission spectra, calculated by *ElecSus* (see section 2.4), with an added linear background. The values of the slope and intercept from the previous fit then allow for the time axis to be scaled and shifted, respectively, to correspond to the value of zero detuning of the atomic system. The result, shown in figure 3.5, is then a frequency calibrated horizontal axis for the signals obtained.

The process described in this section is then carried out for each experimental spectrum acquired. Furthermore, the process can also be applied to scans over a much larger range of frequencies, as will be shown in chapters 4 and 5.

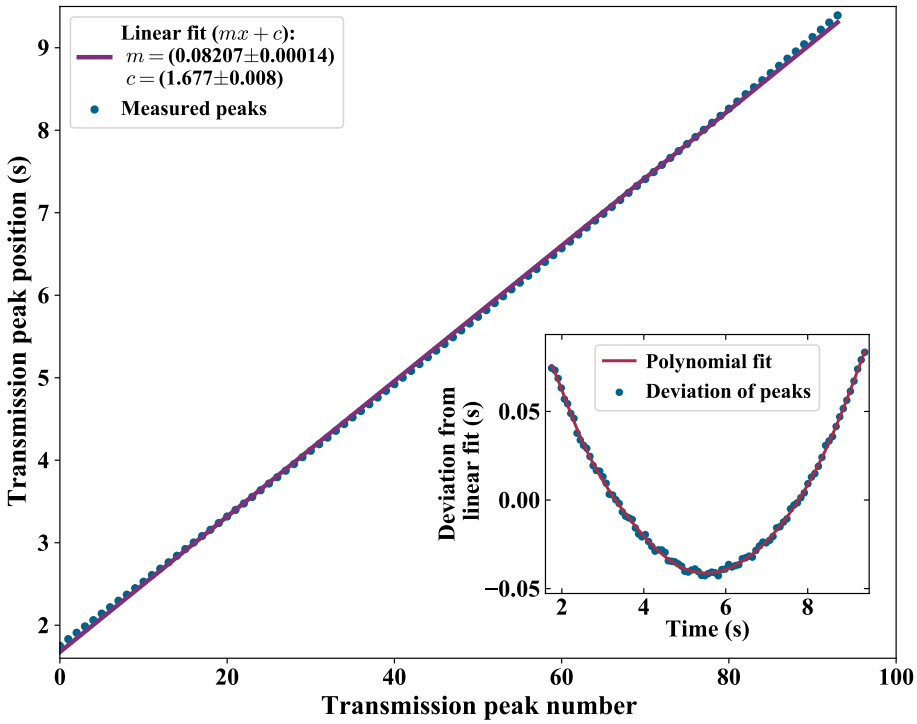

Figure 3.4: Deviation from linear fit of peak position as a function of peak number, for the transmission peaks in the sample etalon signal shown in figure 3.3. The etalon can be characterised by its free spectral range (FSR), which we assume to be constant over the range of the laser scan. As such, a linear relation (purple curve) can be calculated as a function of the number of peaks and their positions in time. By comparing the measured positions of these transmission peaks to their expected positions, given by the aforementioned linear relation, we obtain the deviation for each peak, as shown in the inset of the figure. These points are then fit using a high-order (≥ 5) polynomial (red curve) in order to obtain a correction factor to linearise the horizontal axis and later allow the conversion from time to frequency.

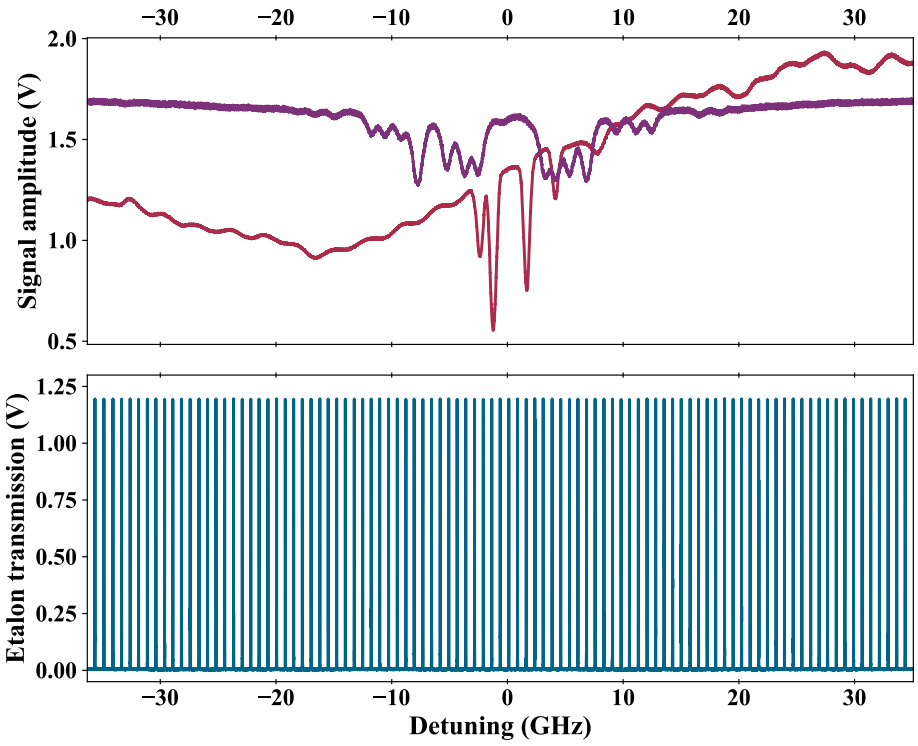

Figure 3.5: Sample calibrated signals taken with the experimental setup described in section 3.3.1. Shown are the signals from the reference optics (blue curve for the etalon and red curve for the natural abundance Rb reference cell) and the experiment cell (purple curve); the signal from the experiment cell has been multiplied by a factor of 10 for visibility. All of the signals have been frequency calibrated with the process described in the present section.

Uncertainties in the frequency calibration process

We now proceed with a brief discussion regarding the uncertainties present in the frequency calibration process described in section 3.3.2. Although our discussion will be carried out with data and examples from the experimental setup in this chapter, the general points are applicable to similar experiments such as those presented in chapters 4 and 5.

To discuss the uncertainties in our frequency calibration of experimental spectra we must begin by considering the uncertainty in the horizontal axis of the raw data. In the first instance this will be determined by the equipment used in the acquisition of the raw signals. For the sample data shown in the previous section, with a resolution of 50 μs, the manufacturer specifications state a ± 2.5 p.p.m accuracy in the oscilloscope time base and an overall time resolution of 250 fs[4]. As such, we consider this to give an uncertainty of 2.5 μs in the position of points along the time axis of the raw signals, considering the oscilloscope time base range of 1 s/division.

We now continue to consider the uncertainties in the determination of the positions of the etalon peaks. As previously mentioned, this allows for the time axis to be converted to a frequency axis, and will consequently carry on the uncertainty in time to one in frequency. In order to determine the positions in time of the transmission peaks, numerical packages in Python are used; further details can be found in Appendix B. As the resolution of our data is limited to 50 μs, the determination of our peaks is limited to a similar precision. We thus consider each peak to have an associated uncertainty of ± 25 μs due to this constraint.

In addition to this, the uncertainty in the determination of the linear relation between the positions of these peaks must be taken into account. Using the example shown in figure 3.4, we see that the fit parameters in this case are $m = (8.207 \pm 0.014) \times 10^{-2}$ s/peak and $c = (1.677 \pm 0.008)$ s. Together this gives an uncertainty in the position of $(8.207 \times 10^{-2}) \times 25 \approx \pm 2$ μs per peak.

[4]Tektronix DPO7254; more information available at https://uk.tek.com/datasheet/dpo7000-series.

To this we must then add the effects of the non-linear correction applied to correct the deviations from the expected positions of the etalon peaks. Using the polynomial function derived for said deviations, with the above uncertainty in the peak position (± 2 μs) we obtain an uncertainty of $\sim \pm 8$ ns. From this, we can assume that the dominant uncertainty in the position of the points along the linearised time axis is that corresponding to the positions of the etalon peaks, ± 25 μs.

The final contribution to the uncertainty in the calibration process comes from the translation of the frequency axis to the zero detuning of the atomic system. As mentioned in section 3.3.2, this is done by using the hyperfine ground-state splitting of ^{87}Rb. For the sample data shown, the resulting parameters of the slope and y-axis intercept are (9.07 ± 0.04) GHz/s and (-49.7 ± 0.2) GHz, respectively. The uncertainty in these parameters can then be used to calculate the error in the frequency calibration, as shown in figure 3.6. Further details on this calculation are given in Appendix B. From said figure we can see that the error in the frequency calibration has a minimum at zero detuning, due to the process followed to calibrate our axis and whose value is directly related to the uncertainty in the y-axis intercept, and increases following a quadratic trend towards the ends of the scan. Over the region of interest in our experiments, we determine from figure 3.6 an error of 1.5% (15 MHz/GHz) over a scan of 40 GHz centred around zero detuning, measured by taking the difference between minimum of the curve (at 0 GHz) and the value of the error at ± 20 GHz.

3.3.3 Results

Using the theoretical model described in chapter 2 and in section 2.4 (in the form of the *ElecSus* software [134, 141]) we generate an initial prediction of the evolution of the atomic states up to, and the resulting spectrum at, an external field strength of 0.4 T. These are shown in figure 3.7. In the upper panels the calculated spectra for an isotopically enriched (99% purity) ^{87}Rb vapour cell at $T = 80°$C and $B = 0.4$ T are shown: in the top panel the spectrum for π transitions can be seen while in the bottom panel the spectrum

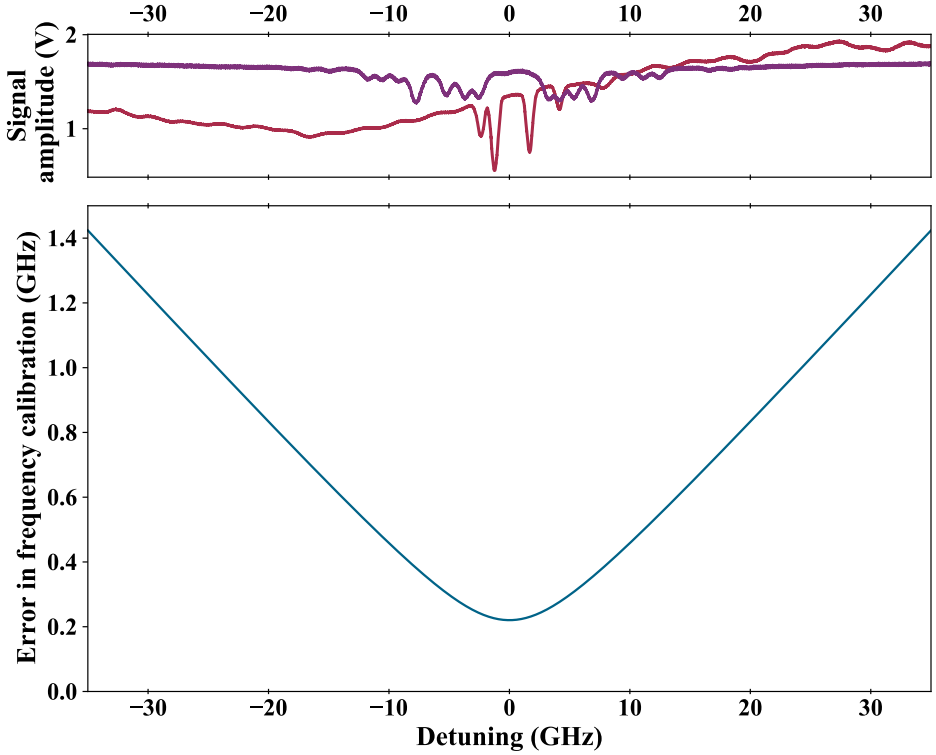

Figure 3.6: Error in the frequency calibration process used in our analysis of experimental data. Using the uncertainties in the parameters obtained for the conversion from linearised time to frequency, the error in the calibration is determined via propagation of errors and shown as the blue curve in the bottom panel. In the top panel, the reference absorption spectrum (red curve) of natural abundance Rb and the experimental spectrum (purple curve) are shown. We note that the error follows a quadratic trend as a function of detuning, with a minimum determined by the value of the uncertainty in the y-axis intercept (~ 0.2 GHz). As our region of interest in the laser scan is defined by the extension of absorption features in our experimental spectrum, we observe that the error in the calibration is approximately 600 MHz over 40 GHz, as given by the values taken at ± 20 GHz. This can then be used to calculate, via a linear relation, an error of 15 MHz/GHz, or equivalently 1.5%, over the extension of the region of interest.

shows $\sigma^{\pm}$ transitions. We note that the isotopic impurity in our cell, 1% ^{85}Rb, is taken into account in these calculations, yet it is sufficiently small so that it has no significant contribution in the spectra. In the bottom of the figure an energy level diagram shows the ground- and excited-state manifolds ($5^2S_{1/2}$ & $5^2P_{3/2}$, respectively) for ^{87}Rb as a function of the magnetic field strength B. At $B = 0.4$ T the manifold decompositions in the $|m_J, m_I\rangle$ basis are shown, along with the initial and final states involved in each of the transitions, as indicated by the coloured vertical arrows: olive for π ($m_{J'} = m_{J'}$), blue for σ^+ ($m_{J'} = m_J + 1$) and purple for σ^- ($m_{J'} = m_J - 1$) transitions. The coloured vertical lines, using the same colour code as the vertical arrows, serve as indicators of the frequency at which the laser scan is in resonance with these transitions, with the zero corresponding to the weighted D2 line centre of naturally abundant Rb in the absence of a magnetic field [72].

At a field strength $B = 0.4$ T, the energy levels in the $5^2P_{3/2}$ manifold strongly decouple into the $|m_J, m_I\rangle$ basis (the HPB regime), as can be confirmed by the values presented in section 2.3.1. This results in four groups of lines (multiplets) that are organised by their $m_J = \pm 3/2, \pm 1/2$ projection, with an internal structure defined by the $m_I = \pm 3/2, \pm 1/2$ projection values. The same cannot be said of the levels in the $5^2S_{1/2}$ ground state manifold due to a stronger hyperfine interaction that prevents the atomic system from being completely within the HPB regime. As a result of this, there is a small admixture of states with the opposite m_J projection in the decomposition into the $|m_J, m_I\rangle$ basis, as seen on the bottom right of figure 3.7; more details regarding the nature of this decomposition are given in reference [151]. Experimentally, this admixture results in groups of three 'weak' transitions seen far towards the ends of the absorption spectra in addition to the 'strong' multiplets of transitions closer to zero detuning.

Another feature of note in these spectra is the presence of areas where the absorption lines overlap. This comes as a result of the Zeeman splitting not being large enough (compared to the ground-state hyperfine structure) in order to completely resolve all the individual transitions at $B = 0.4$ T. In particular, lines corresponding to the 'strong' $|m_J = 1/2, -3/2\rangle \rightarrow |m_{J'}, -3/2\rangle$ and

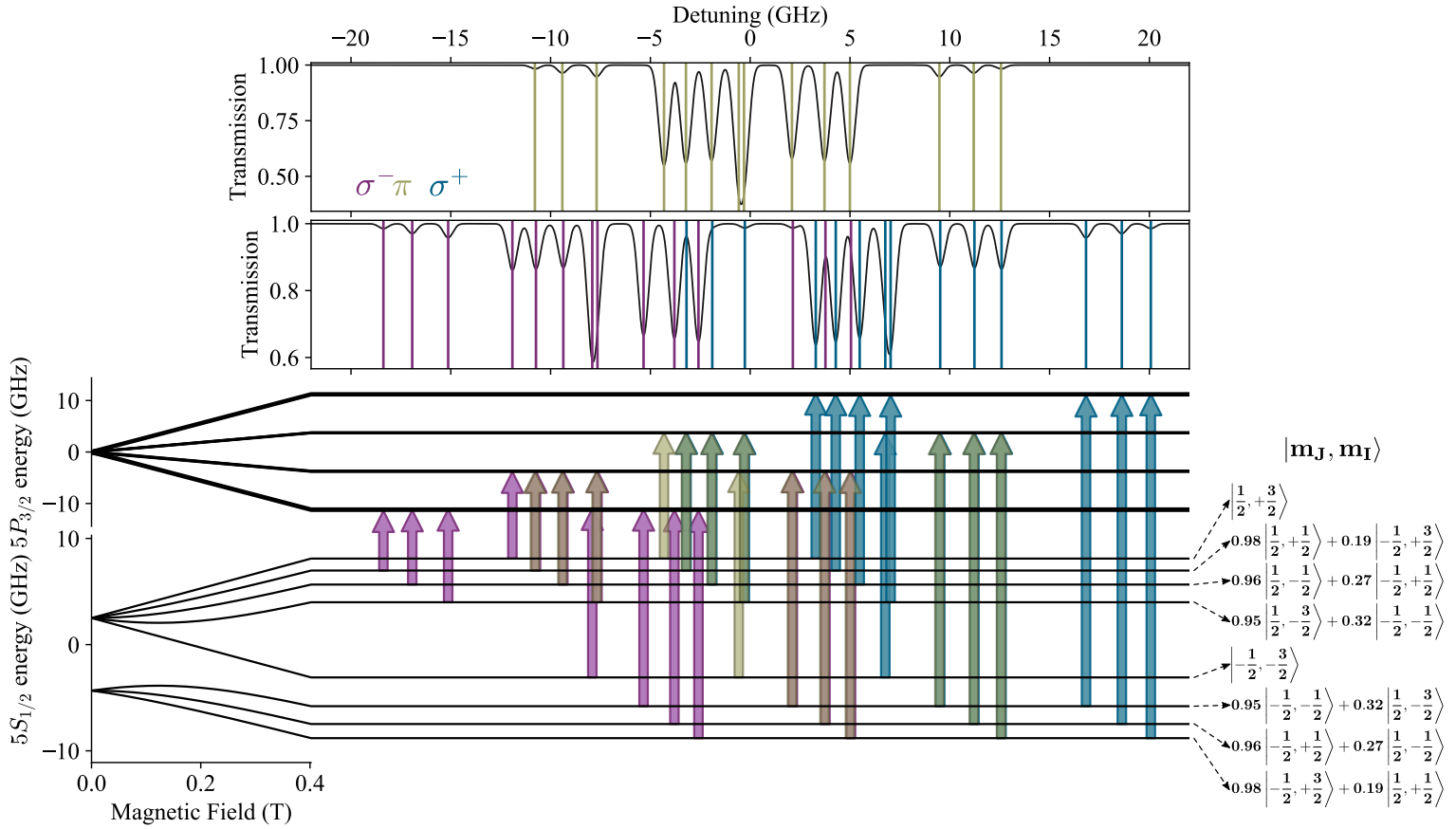

Figure 3.7: Calculated spectra and energy levels of the ^{87}Rb D2 line for a magnetic field strength of 0.4 T in the Voigt geometry. The spectra are shown as a function of linear detuning to coincide with the experimentally measured quantities. In the bottom left of the diagram, the evolution of the $5^2S_{1/2}$ and $5^2P_{3/2}$ energy levels as a function of the magnetic field strength B is shown up to $B = 0.4$ T. To the right, the decomposition of each level in the $|m_J, m_I\rangle$ basis is shown as well as the initial and final states in each transition, indicated with coloured arrows: olive for π transitions, blue for σ^+ transitions and purple for σ^- transitions. The top panels show the calculated absorption spectra for these transitions (π: top; $\sigma^\pm$: bottom) at $B = 0.4$ T.

$|m_J = -1/2, -3/2\rangle \rightarrow |m_{J'}, -3/2\rangle$ transitions are separated by less than the Doppler width ($\Gamma_{\text{Doppler}} \approx 2\pi \times 555$ MHz at $T = 80°$C), so that in the spectra they overlap almost completely. For π transitions this is evident at ~ 1 GHz, while for the $\sigma^{\pm}$ transitions this occurs at ± 7 GHz, respectively. This, while not ideal for the purpose of identifying the individual transitions in a spectrum, may prove to be an advantage for magnetometry, as the overlap of the absorption features causes the spectrum to change rapidly with relatively small changes in the magnetic field strength and direction. This will be discussed with more detail further ahead in this chapter.

Analysis of absorption spectra

Figure 3.8 shows an experimentally acquired absorption spectrum (S_0) that has been fit with *ElecSus* together with the residuals of the fit R, multiplied by a factor of 100 for clarity. We note that the uncertainties in the experimental data points ($\sim 3 \times 10^{-3}$) are too small to be seen in the plot and are of the same order of magnitude as the residuals. For the spectrum shown, the RMS error between theory and experiment is 0.3%; along with the lack of discernible structures in the residuals, this indicates an excellent fit [155]. The fit was run as a function of four parameters: the magnetic field strength B, the temperature of the atomic vapour T, the angle of the magnetic field relative to the polarisation of the light ϕ_B and the amount of inhomogeneous broadening Γ_{Buf} due to the presence of buffer gases in our vapour cell. These parameters were chosen to carry out the fit as they were the most significant physical parameters varied, or in the case of the inhomogeneous broadening, unknown, in our setup. The rest of the parameters were fixed by our experimental geometry and setup, and were thus included in the model generated by *ElecSus* to carry out said fit (see section 2.4.1).

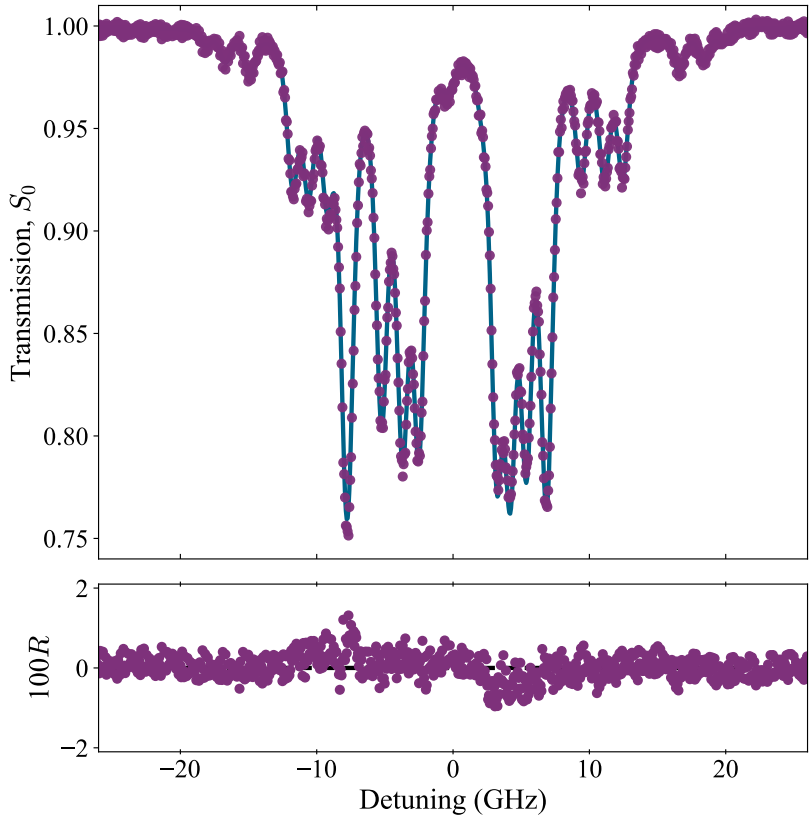

Figure 3.8: Experimental data (purple dots) and model fit (blue solid line) using *ElecSus* for the absorption spectrum of the ^{87}Rb D2 line in the Voigt geometry (average polarisation angle $\phi_B = (\pi/2 \pm 0.02)$), for a measured magnetic field strength $B_{\text{Hall}} = (390 \pm 1)$ mT. The difference between the data and fit, shown as the residuals R (multiplied by a factor of 100 for better visibility), is very small and shows a lack of structure. In combination with the small RMS error of 0.3%, this indicates an excellent agreement between theory and experiment [155]. From the fit we extract a magnetic field strength $B = (394 \pm 4)$ mT, temperature $T = (81.23 \pm 0.02)°$C, angle $\phi_B = (1.412 \pm 0.004)$ rad and an inhomogeneous broadening $\Gamma_{\text{Buf}}/2\pi = (631 \pm 3)$ MHz.

From the fit we can extract the following values for our parameters: $B = (394 \pm 4)$ mT, $T = (81.23 \pm 0.02)°$C, $\phi_B = (1.412 \pm 0.004)$ rad and $\Gamma_{\text{Buf}}/2\pi = (631 \pm 3)$ MHz. Uncertainties in the values are obtained from our fit of a spectrum, using the Levenberg-Marquardt algorithm for least-square minimisation, as described in section 2.4.1. We can compare the values for the magnetic field strength B and the temperature of the atomic vapour T with direct measurements from other equipment in our experimental setup. Using a

commercial Hall probe we measured a value for the field strength of $B_{\text{Hall}} = (390 \pm 1)$ mT. For the temperature of the atomic vapour, we used the Cernox thermometer placed inside the probe to obtain a value of $T_{\text{Cernox}} = (82.32 \pm 0.04)$°C. We see that the value obtained for the magnetic field from our experiment agrees, within the error bars, with that reported by the Hall probe. In the case of the temperature, we see that the experimental value is not in agreement with that of the Cernox thermometer. This could be a result of the larger thermal conductivity of the copper block compared to that of the vapour cell, as well as of the location of the Cernox thermometer on the block.

The inhomogeneous broadening in our vapour cell is suspected to come from previous experiments in which the vapour cell was exposed to a helium-rich gas environment while being heated to a high temperature (~ 100°C). This would cause diffusion of helium atoms through the cell windows, resulting in an elevated concentration of a buffer gas in the cell. We note that the presence of this buffer gas does not generate any significant shift in the position of the atomic transitions. The effects of buffer gases in atomic spectroscopy are well-known [57] and we explore this in further detail in appendix A. We also note that subsequent experiments using this cell, reported in chapter 4, the amount of inhomogeneous broadening in the cell decreased. We attribute this to the diffusion of the helium out of the cell through the glass windows [156, 157].

Using our experimental setup, our theoretical model was tested over a range of field strengths up to 0.4 T. Figure 3.9 shows a summary of the measurements carried out over this range. Each of the points corresponds to a result obtained from the weighted average of 5 fits to the experimental spectra, all taken during a single run. The temperature T, polarisation angle ϕ_B and inhomogeneous broadening $\Gamma_{\text{Buf}}/2\pi$ were also allowed to float during these fits, giving global average values of $T = (102.26 \pm 0.01)$, $\phi_B = (1.34 \pm 0.07)$ and $\Gamma_{\text{Buff}}/2\pi = (675 \pm 2)$ MHz. Example spectra are shown for values of the external magnetic field $B \approx 0.15, 0.35$ T; the field strength was simultaneously measured using a commercial Hall probe in order to have a comparison to

commercially available equipment. Consequently, this allows us to determine the accuracy of our setup compared to that of the commercial equipment by fitting a straight-line ($B_{\text{Hall}} = mB+c$) to the data. Keeping the intercept fixed to zero (which assumes no systematic errors in the commercial equipment), we extract a value of the gradient $m = (0.995 \pm 0.009)$. If, on the other hand, we fit the line with the intercept as a free parameter (taking into account the systematic errors in the commercial equipment), we extract a value of $m = (1.015 \pm 0.002)$ for the gradient and $c = (-5 \pm 1)$ mT for the intercept.

The results from the comparison of the values measured for the field strength from the spectra and the Hall probe indicate a systematic 1.5% difference between the two methods. We attribute this difference predominantly to inaccuracies in the calibration of the Hall probe used, quoted by the manufacturer to be $\pm 1\%$ at a 1 mT resolution. Other systematic errors that contribute in this analysis are the scaling and linearisation of the frequency axis (a 15 MHz/GHz error in the calibration of our scan is an error of ~ 1 mT/GHz; see section 3.3.2 and Appendix B.1 for details), misalignment in the axis of the Hall probe with respect to the direction of the magnetic field during measurement and the numerical uncertainties in our theoretical calculations. Furthermore, the field homogeneity was measured to be < 1 mT within a 14 mm central diameter sphere volume between the pole pieces of the electromagnet at all field strengths tested.

From this comparison we can assume our atomic technique for measuring field strengths as an accurate and precise method for characterising the strength of an external field. Our technique is independently sensitive to field strength and relative orientation (*i.e.* angle of the field with respect to light polarisation) without any mechanical adjustments to the sensor head. This comes as a result of the atom-light interactions and the interaction with the external magnetic field, as described in greater detail in chapter 2. The Zeeman shift, which depends on the strength of the external field, sets the position of the atomic resonances, whilst the strength of the coupling of the atom's electronic transitions is dependent on the relative direction between the electric field of

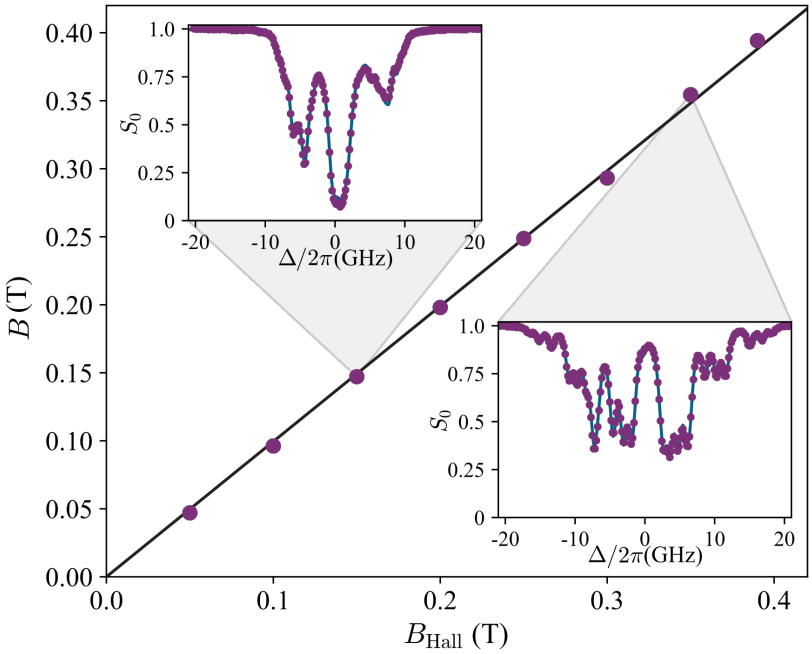

Figure 3.9: Comparison of measurements of magnetic field strength obtained through fits of experimental spectra, B, and by using a commercial Hall probe, B_{Hall}. Each of the points on the plot corresponds to the weighted average of 5 measurements; the error bars of each point, obtained from the average of the uncertainties of the 5 measurements, are approximately 1 mT in size and are too small to be seen on the current scaling of the figure. The comparison is carried out by fitting a linear function to the data in two ways. Fitting with the y-axis intercept fixed to 0 ($c = 0$), we extract a gradient of $m = (0.995 \pm 0.009)$ (black solid line). Fitting with both the gradient and intercept as free parameters, we obtain a value of $m = (1.015 \pm 0.002)$ for the gradient and $c = (-5 \pm 1)$ mT for the intercept. Shown as insets are two sample experimental absorption spectra (S_0) taken at $B \approx 0.15$, 0.35 mT, with their respective fits, as a function of the linear detuning $\Delta/2\pi$.

the light, *i.e.* its polarisation, and the direction of the magnetic field. This is an advantage over conventional Hall probe measurements, where the angle between the Hall probe and the direction of the external field affects the accuracy of the field strength measured. Combined with the relatively high and scalable spatial resolution of our technique, these considerations serve as proof-of-concept for atomic-based spectroscopy to be used as a replacement for commercial Hall probes in applications such as simultaneous mapping of both magnitude and direction of magnetic fields (*e.g.* vector magnetometry). An extension of these considerations are presented in the remainder of this section.

At this point it is worthwhile to note that for all of the previous results no magnetic shielding was used. This is due to the fact that the effect of the Earth's magnetic field, or of any other sources of parasitic magnetic fields, are negligible in our system as they are typically orders of magnitude smaller ($\sim 10^{-4}$) when compared to the strength of the fields in this work. Also, we note that no significant changes in temperature or polarisation occurred during an experimental run; the polarisation drift across individual measurements was $< 10\%$ and the temperature drift was $< 1°$C. The latter is consistent with the small changes, < 100 mK, registered by the Cernox thermometer.

Sensitivity of spectra to changes in geometry and field strength

As mentioned earlier, the partial overlap between absorption features due to the atomic system not being completely in the HPB regime can cause rapid changes in the spectra as a function of changes in the magnetic field strength and direction. It can be argued that this is a desirable feature to consider in a system for magnetic field sensing. To begin, we consider the change in the absorption spectrum with respect to changes in the magnetic field strength, $\mathrm{d}S_0/\mathrm{d}B$. We have used *ElecSus* to calculate these changes over the width of the ^{87}Rb D2 line spectrum, for values up to 0.5 T, and present them in figure 3.10. The regions of interest, corresponding to higher sensitivities to changes in the magnetic field strength, are visible at a detuning of ~ 1 GHz at 0.1 and 0.23 T, and at fields of strength $\lesssim 0.05$ T. In the former cases, the

sensitivity arises from the overlap of the absorption features due to the $5^2S_{1/2}$ ground state not being fully in the HPB regime whilst in the latter case it is the overlap of absorption features due to the $5^2P_{3/2}$ excited state not being fully in the HPB regime that generates high sensitivity.

For these calculations, the system is taken to be in the Voigt geometry (see section 2.2.3), with the light linearly polarised along the Cartesian x-axis. We conveniently define said axis so that the angle between the polarisation direction and the direction of the magnetic field is $\phi_B = \pi/2$. This is chosen as it is the angle that drives $\sigma^{\pm}$ transitions the strongest, thus creating a larger energy splitting between the two sets of transitions (see figure 3.7) relative to zero detuning. As such, at lower field strengths the overlap between the σ^+ and σ^- transitions also contributes to the increase in sensitivity. At the higher field strengths, closer to the lower limit of the HPB regime (see chapter 2), the energy shifts in the ground and excited states provide up to a factor of $3\mu_{\mathrm{B}}B$ in the field-strength sensitivity of the system: the ground state level shifts down in energy by $\mu_{\mathrm{B}}B$ while the excited state level shifts up by $2\mu_{\mathrm{B}}B$.

In addition to the previous statements, the angle between the direction of polarisation and the direction of the magnetic field (ϕ_B) can also be varied to study the sensitivity of the absorption spectra with respect to changes in said angle. For this case we consider the quantity $\mathrm{d}S_0/\mathrm{d}\phi_B$, making use once again of *ElecSus* to calculate the changes over the width of the ^{87}Rb D2 line absorption spectrum. From the theory given in chapter 2 and section 2.4, we know that ϕ_B changes the relative coupling of the π and $\sigma^{\pm}$ electron transitions in the atom, with a $\cos^2(\phi_B)$ and $\sin^2(\phi_B)$ dependence, respectively. As such, we can expect for the sensitivity of the spectra to be greatest at an angle of $\phi_B = \pi/4$, where the gradient of both of these functions is greatest and the relative coupling is equal.

Figure 3.11 demonstrates this by showing both experimental data and the calculated values of $\mathrm{d}S_0/\mathrm{d}\phi_B$, as a function of detuning, at three values of interest for ϕ_B: 0, $\pi/4$ and $\pi/2$. The absorption (S_0) spectra at these values are shown in the upper top panels, with the plot of $\mathrm{d}S_0/\mathrm{d}\phi_B$ in the lower top

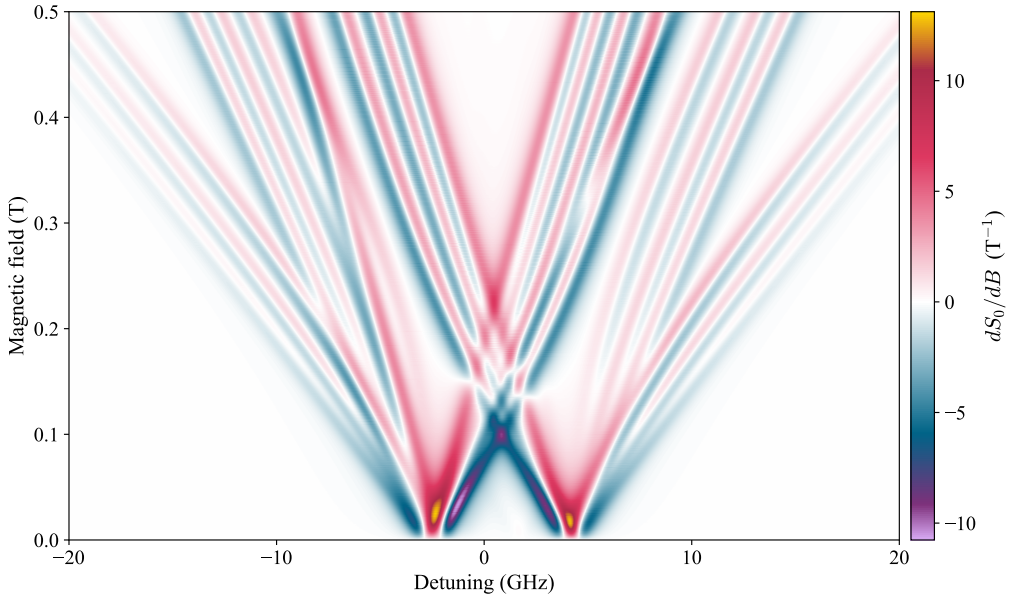

Figure 3.10: Change in spectral absorption as a function of change in magnetic field strength, $\mathrm{d}S_0/\mathrm{d}B$, plotted as a function of detuning and magnetic field. The regions of interest, here indicated by bright purple/yellow and dark red/blue areas on the colour map, are the result of the overlap between absorption lines in the ^{87}Rb D2 line spectrum and point to areas of the spectrum with high sensitivity to changes in the field strength. All calculations for construction of the colour map were carried out using *ElecSus* [134, 141] with the following values of the spectrum parameters: cell length $L = 1$ mm, vapour temperature $T = 80°$C, polarisation angle $\phi_B = \pi/2$ rad, buffer gas broadening $\Gamma_{\mathrm{Buf}}/2\pi = 650$ MHz and field strengths up to $B = 0.5$ T. These values were chosen to match the experimental parameters as closely as possible.

panels. The vertical lines indicate points of interest in the spectra where the overlap between absorption features is clearly visible. In the lower panel, the evolution of $\mathrm{d}S_0/\mathrm{d}\phi_B$ at these values of detuning is shown as a function of the polarisation angle ϕ_B; the sinusoidal dependence is clearly visible, with the global maximum/minimum located, as expected, at a value of $\phi_B = \pi/4$.

Note that while this technique is sensitive to changes in the polarisation angle ϕ_B, the spectra produced are not unique: there are two equivalent values of ϕ_B, obtained by reflection of this angle around the x- and y-axes, that yield the same spectrum. In order to be able to uniquely determine ϕ_B a full

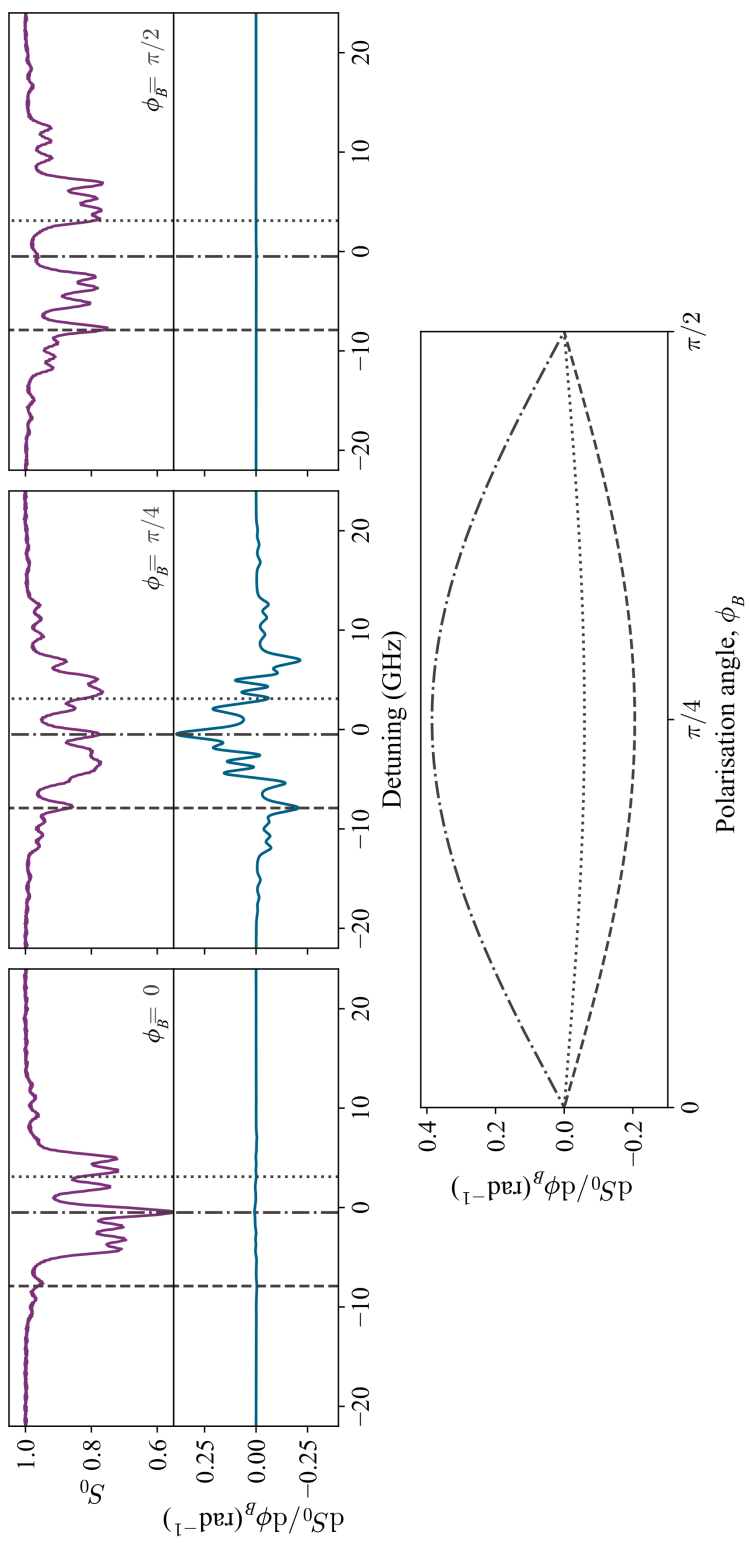

Figure 3.11: Sensitivity of absorption spectra S_0 to changes in polarisation angle ϕ_B. In the top panels, experimental absorption spectra (purple curves) at a given value of ϕ_B are shown, for common values of the magnetic field strength of $B = 0.39$ T, cell temperature $T = 80°$C and buffer gas broadening $\Gamma_{\mathrm{Buf}}/2\pi = 650$ MHz. Directly below these spectra are the calculated values of the gradient $\mathrm{d}S_0/\mathrm{d}\phi_B$ (blue curves); all of the plots of have been equally scaled to highlight the much lower sensitivity of the spectra at $\phi_B = 0, \pi/2$ when compared to that at $\phi_B = \pi/4$. The vertical broken lines in the top panels correspond to the values of detuning selected for evaluating the change in $\mathrm{d}S_0/\mathrm{d}\phi_B$ as a function of ϕ_B, shown in the bottom panel of the figure.

polarimetric analysis of the light transmitted through the medium would be necessary. Also, it should be noted that the relative sensitivities to magnetic field strength and polarisation angle also have an implicit dependence on the linewidth of the absorption features in the spectra. This comes from the fact that the sensitivity depends, as initially stated, on the overlap of the spectral lines, which is in turn affected not only by the relative position but also by the width of the lines. As the features become narrower, the changes in the spectrum become sharper, allowing for the possibility of more sensitive measurements to be made.

3.4 Summary

In summary, we have presented the results of the experimental investigation of a thermal ^{87}Rb atomic vapour in the Voigt geometry. The strength of the magnetic field used varied up to 0.4 T, allowing us to see the change in absorption spectra up to the lower limit of the hyperfine Paschen-Back regime. These results have been shown to have excellent agreement with our theoretical model, allowing for a precise determination of the magnetic field strength and relative angle between the polarisation of the light and the direction of the magnetic field. As a result, we have been able to use this method to introduce the idea of using atomic vapours and optical signals as a viable method for high-field vector magnetometry. In the next chapter we extend this work to experiments carried out at higher fields, well within the hyperfine Paschen-Back regime of the atomic vapour defined in section 2.3.1, and looking at systematics (such as birefringence of the cell windows) that become important under said conditions.

Chapter 4

Stokes polarimetry of a Rb vapour in the Voigt geometry at 1.5 T

This chapter is based on the following publication:

F. S. Ponciano-Ojeda, F. D. Logue and I. G. Hughes, *Absorption spectroscopy and Stokes polarimetry in a ^{87}Rb vapour in the Voigt geometry with a 1.5 T external magnetic field*, Journal of Physics B: Atomic, Molecular and Optical Physics **54**, 015401 (2021), 10.1088/1361-6455/abc7ff

4.1 Introduction

As has been seen up to this point in the present work, the use of atomic systems for the measurement of magnetic fields is a promising area of research. While the majority of the literature covers work with low field strengths (~ 10 mT) and frequency measurements in these experiments, spectroscopic techniques provide a more straightforward way of obtaining information about the magnetic field. These have been studied in a wide range of conditions for the atomic systems [72, 74, 73, 75], allowing very good understanding of the physics involved. Of particular interest is the interaction between atoms and

external magnetic fields –the Zeeman effect–, whose nature allows for these systems to operate in different regimes (such as the hyperfine Paschen-Back regime [158, 159, 160, 161] or the Paschen-Back regime [67, 68, 162]) and different geometries (*e.g.* the Faraday or the Voigt geometry). In chapter 2 we presented the fundamental theory behind these techniques. This theory was then applied to the experiments presented in chapter 3, where we studied the interaction between an alkali-metal vapour in a large magnetic field (0.4 T) in the Voigt geometry (*i.e.* $\mathbf{k} \perp \mathbf{B}$).

From the results presented in the previous chapter it was possible to observe some of the advantages of working in the Voigt geometry. Rather than providing information only on the magnitude of the magnetic field (B) used, spectroscopic measurements in the Voigt geometry also provide some information on the direction of the field relative to that of the laser beam used to excite the atoms. This comes as a result of the change in atomic selection rules when compared to those in the Faraday geometry (*i.e.* $\mathbf{k} \parallel \mathbf{B}$) [163] which allows access to a wider range of transitions, including some not typically allowed [164] in said case. The result is a richer description not only of the magnetic field, but also of the interactions of said field with, and the changes it generates in, the atomic system. We highlight the importance of being able to access π transitions in the Voigt geometry, and the ability to excite $\sigma^{\pm}$ transitions as in the Faraday geometry, by selecting the polarisation of the light to have components parallel and perpendicular to the direction of B. Our theoretical model, described in chapter 2 and implemented with the *ElecSus* software, allowed us to obtain this information from fits to experimental absorption spectra.

In the present chapter we will expand upon the work done at 0.4 T by carrying out experiments with a thermal vapour of ^{87}Rb in the Voigt geometry at a larger magnetic field strength of 1.5 T. These conditions allow for the system to be well within the hyperfine Paschen-Back regime, allowing for spectra with clearly resolved absorption features to be obtained. Similarly to the results in chapter 3, we use the absorption of light passing through the atomic vapour to obtain a precision measurement of the magnetic field strength

and its orientation within the overall experimental system, relative to the direction of propagation of light; the validity of our theoretical model is also demonstrated in this regime as we continue to analyse the experimental data with numerical calculations from *ElecSus*. Furthermore, we use polarimetric techniques (*e.g.* the Stokes parameters) to study optical rotation phenomena within the vapour, as well as other systematic effects in the experiment, such as cell window birefringence.

4.2 Theoretical model

The theoretical model for describing the experiments in this chapter builds largely upon the concepts covered in chapter 2; these are implemented in the underlying model for the *ElecSus* software that is used to fit our results to theory. More details on said implementation can be found in section 2.4 and in references [134, 141]. For the particular experiments in this chapter we will consider the case of a ^{87}Rb thermal vapour in the presence of an external magnetic field, arranged in the Voigt geometry, strong enough to drive the system into the hyperfine Paschen-Back regime (see section 2.2.1). The vapour will be probed with a near-resonant laser beam tuned to the D2 line to observe the changes in the atomic medium due to the magnetic field via the atom-light interactions. This allows for polarimetric techniques that take advantage of the changes in the dichroic and birefringent response of the atomic refractive indices to be used to study the system. In particular, we will look at using Stokes polarimetry [89, 135] to analyse our results and take these effects into account. Details of the Stokes parameters used in this analysis have been given in section 2.1.4.

4.3 Experiment

4.3.1 Experimental setup

The experiments in this chapter were carried out with a setup similar to that in chapter 3. In these experiments however, the difference is that the

external magnetic field was provided by a permanent magnet, thus allowing a higher strength field to be accessed. Figure 4.1 shows the experimental setup used. As in the previous experiments presented, the setup consists of two sets of equipment using a common source of light in the form of a tunable DFB laser with an output power of ~ 80 mW[1]. This laser, with a central emission wavelength of 780 nm and specified linewidth of < 2 MHz, is tuned by changing the operating temperature of the laser diode with a commercial PID controller[2] to generate frequency scans over many hundreds of GHz without mode-hops. This sets an upper limit on the duration of the scan, of the order of the controller's bandwidth, as the diode temperature must stabilise after feedback is provided. As such, a typical scan over the hundreds of GHz takes ~ 2 seconds.

An optical isolator (OI) is placed at the output of the DFB laser in order to prevent back-reflections to the diode that could cause mode-hops during the scan. Approximately half of the light emitted from the laser is sent to the set of reference optics shown in figure 4.1 by a combination of a half-wave retarder plate ($\lambda/2$) and a polarising beam-splitter (PBS), as also seen in the setup in section 3.3.1. This set of optics, made up of a free-standing Fabry-Pérot etalon and a natural abundance Rb cell, allows for the raw data to be linearised and calibrated according to an absolute frequency reference, as specified in 3.3.2 and B.1, to obtain a spectra as a function of linear detuning. The remainder of the emitted light is passed through several additional steps that serve to filter the polarisation and, if necessary, control the beam power arriving at the experiment cell. Half- and quarter-wave ($\lambda/2$ & $\lambda/4$, respectively) retarder plates placed before the light enters the cell allow for a linear or circularly polarised beam to be used. While the function of the setup is similar to that used in chapter 3, here the light going to the experiment cell is not fibre coupled as in the former case; the photodiodes, etalon and reference cell used, while fulfilling the same functions, are also different to those previously used.

[1]Eagleyard Photonics; part number EYP-DFB-0780-00080-1500-TOC03-0002.
[2]ThorLabs TED200C Laser Diode Temperature Controller

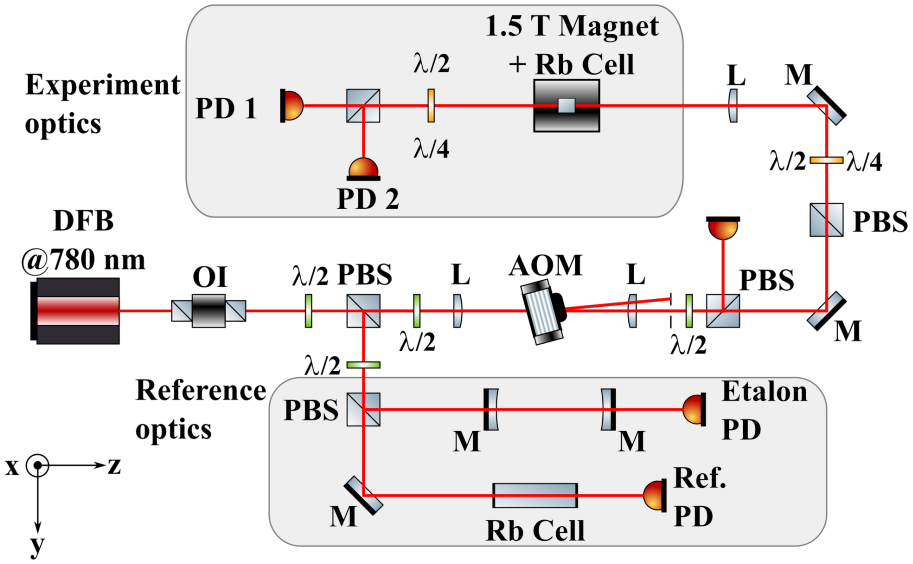

Figure 4.1: Schematic of the optical setup used for spectroscopy experiments with a permanent magnet. Two main setups, one of reference optics and the other of the experiment optics, are shown. A common light source, a distributed feedback (DFB) laser emitting at 780 nm, passes through an optical isolator (OI) before being split into two beams using polarisation optics. One of the beams is used in the reference optics setup, composed of a commercial natural abundance Rb vapour cell and a Fabry-Pérot etalon made with two mirrors (M), to linearise and calibrate the frequency of the laser scan in a zero magnetic field environment (see B.1 for more details). The second beam is sent to the experiment optical setup via an acousto-optic modulator (AOM), which allows for stabilisation of the beam power [152], and combinations of polarising beam-splitter (PBS) and half-/quarter-wave retarder plates ($\lambda/2$ & $\lambda/4$, respectively) to filter and generate the desired polarisation state of light for use in spectroscopic measurements. The experiment optics are composed of a 1 mm ^{87}Rb isotopically enriched ($\sim$ 99% purity) vapour cell placed in a cylindrical magnet designed to give a mostly axial field of 1.62 T at its centre [165]; detection of the transmitted light is achieved with a polarisation-sensitive setup consisting of a PBS, retarder wave plate and two balanced photodiodes (PD). This allows a voltage signal with information on the absorption and optical rotation of the atomic medium to be easily measured. Several plano-convex lenses (L) are used in order to resize the beam along the optical path in order to ensure the size is such that there is no significant clipping.

The experimental measurements are made using a cuboidal microfabricated vapour cell with a cavity length of 1 mm and filled with isotopically enriched (99% ^{87}Rb) rubidium. This cell was the same as used in the experiments at 0.4 T reported in section 3.3.3. In order to obtain the atomic density (and consequently, optical depth) to observe the phenomena of interest the cell must be heated. Previous studies [74, 166, 167, 168] have found that at these optimal operating temperatures microfabricated cells such as the one used in this work exhibit birefringent properties. Further details on the fabrication methods of our cell can be found in reference [169].

The cell, as well as basic optics to steer the beam (*i.e.* uncoated right-angle prisms), are mounted on a custom copper mount. This bed of copper also provides space for a resistive heater[3] to be housed, as is shown in figure 4.2. Applying a constant voltage to the heater allows the temperature of the copper block to be raised during operation of the experiment; passive temperature stability of the cell is maintained by allowing the cell to thermalise with its surroundings. A cylindrical PTFE shield surrounds this entire assembly, making weak thermal contact with the copper block so as to avoid sudden, sharp fluctuations in the temperature of the system. The spatial footprint of the system is reduced due to the central bore size of the magnet, and this meant it was not possible to include a temperature sensor in the mount for active stabilisation of the operating temperature.

In order to obtain higher field strengths for these experiments a cylindrical permanent magnet was used. The magnet has a central bore of 22 mm along its axis and was designed using the "magic sphere" configuration described in [165]; this design, as well as the fabrication, was carried out at the *Institut de Recherche sur les Systemes Atomiques et Moleculaires Complexes*[4] in Toulouse, France and later donated to our research group in Durham. In general, the "magic sphere" configuration consists of using a distribution of magnetisation in a region of space extending between two concentric spheres

[3]ThorLabs HT15W Resistive Cartridge Heater
[4]Laboratoire Collisions, Agrégats, Réactivité, UMR 5589, CNRS—Université de Toulouse, Université Paul Sabatier

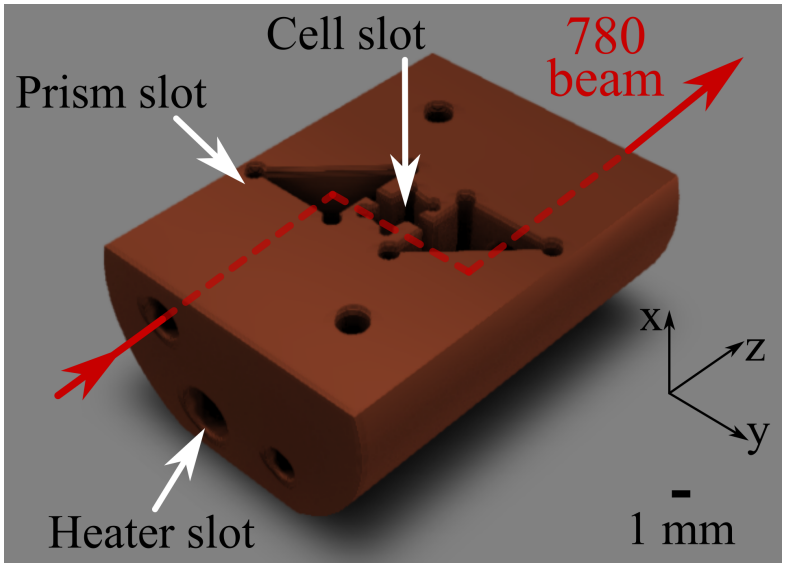

Figure 4.2: Copper heater block used to carry out measurements in the Voigt geometry in a permanent magnet. Seen here is the base of the copper block with an angled slot ($\sim 2°$) for the microfabricated 1 mm vapour cell to avoid back-reflections from the cell windows and two spaces for 5 mm uncoated right-angle prisms to steer the beam. The laser light follows the path of the red arrows, entering and exiting the block through two optical access holes (entry hole seen in the upper left of the end face); the right-angle prisms allow for the light to pass through the cell in a direction perpendicular to its original direction of propagation upon entry and also exit in this original direction. Indicated also in the bottom-centre of the end face of the block is the hole that houses the resistive heater which allows for the temperature of the block, and consequently of the vapour in the interior of the cell, to be raised to the operating point. The block is covered by a copper lid (not shown) and housed inside a hollow, custom-made PTFE cylinder that allows optical access and cable feed-through in order to carry out experiments while placed inside the permanent magnet.

of different radii to generate a field at the origin that is homogeneous inside the internal sphere and vanishes once outside the outermost sphere [165, 170]. This allows for the maximum value of the magnet's field to be 1.62 T at its centre, with it quickly falling radially outwards to the ends as seen in figure 4.3. On the outside of the magnet, the field strength is kept to below hundreds of mT by design.

The custom-made PTFE and copper heater block assembly that houses the experiment cell sits inside the magnet's bore. Together with the design of the magnet, this gives a well-characterised field along the axis that ensures field homogeneity across the length of the experiment cell (1 mm). Details on the design, construction and characterisation of the magnet can be found in reference [165]. We note that the length of the heater block assembly described above (28 mm) is significantly smaller than the length of the magnet (152 mm), which generates difficulties in the alignment of the axis of the heater block once inside the magnet relative to the laboratory frame of reference. As a result, we recognise there is a slight roll of the heater block about the axis of the magnet (*i.e.* the z-axis) that results in a relative orientation of the x, y-axes of the atom and those of the laboratory; this can be described easily with our theoretical model by taking the polarisation angle ϕ_B and adding an effective offset.

As in experiments at lower field strengths (see chapter 3), the power of the laser beam that probes the atomic medium is kept in the weak-probe regime [51, 94] to avoid optical pumping effects. In this case, physical constraints of the system limit the maximum beam waist ($1/e^2$) to approximately 0.7 mm, such that the optical power must be ~ 1 μW. This gives an effective spatial resolution of our system determined by the volume of atoms interrogated by the laser beam, which is roughly equal to a cylinder of length 1 mm and radius 0.7 mm.

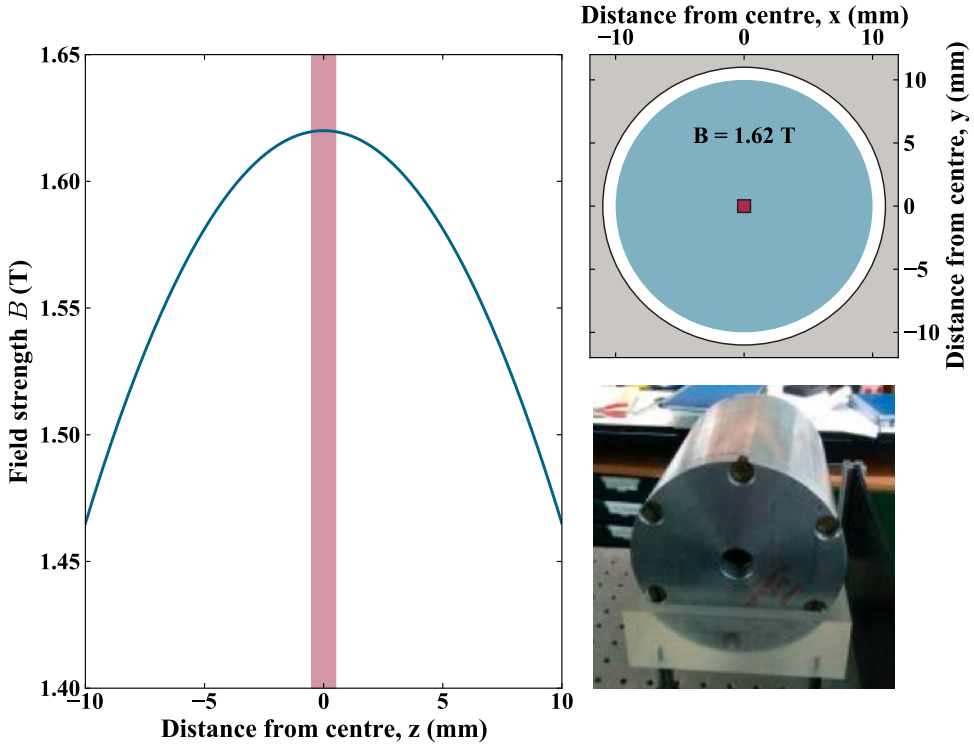

Figure 4.3: Axial (z) field profile (blue curve) for the cylindrical permanent magnet used to generate the field for our experiments. The red shaded area corresponds to the length of the experiment cell (1 mm). In the top right, the radial ($x-y$ plane) profile of magnetic field is shown. The blue shaded area corresponds to the region at $z = 0$ where the maximum field value of 1.62 is constant, with the experimental cell indicated by the red shaded region, the magnet bore indicated by the solid black line and the grey shaded area corresponding to the magnet walls. The field profile along the z-axis was calculated using the quadratic expression of the field profile based on the "magic sphere" design given in reference [165], $B(z) = B_{z,0} + B_{z,2}(z - z_c)^2/2 + \mathcal{O}^4$; information is also provided in reference [165] for the radial characteristics of the field. In this case, the values for the coefficients, taken from said reference, are: $B_{z,0} = 1.62$ T, $B_{z,2} = -0.0031$ T/m^2, $z_c = 0$. Higher order terms were excluded as they are almost negligible [165]. An image showing the mounted magnet in the lab is provided in the bottom right.

4.3.2 Results

In order to better understand the physics of the experiments realised we have used the theory described in chapter 2 and section 4.2 to generate the expected spectra at, and the evolution of the atomic energy levels up to, a field strength of 1.5 T. These calculations are shown in figure 4.4 for an atomic vapour of isotopically enriched ^{87}Rb (99% purity) at a temperature $T = 100°$C in the Voigt geometry. The upper half of the figure corresponds to the calculated absorption (S_0) spectra for π (upper panel) and $\sigma^{\pm}$ (lower panel) transitions. The coloured vertical lines shown in the upper panels indicate the frequency, given in terms of a linear detuning, at which the atomic resonance lines are found, with the colour of the line itself serving to indicate the type of transition that is excited at said resonance: olive green for π transitions, blue for σ^+ transitions and purple for σ^- transitions. Underneath the absorption spectra one can see the energy level diagrams for the $5^2S_{1/2}$ ground- and $5^2P_{3/2}$ excited-state manifolds evolving as a function of field strength B up to $B = 1.5$ T. For each transition, the initial and final states involved are shown as the end-points of the coloured arrows, with the colour code being the same as that of the vertical lines. Transparency of the coloured arrows highlights the fact that there are still overlapping transitions in the system due to the small remnant admixture in the state decomposition as a result of the hyperfine interaction [151, 163]. Said decompositions can be seen in the lower-right corner and are given in the $|m_J, m_I\rangle$ uncoupled basis.

At the field strength used (1.5 T), the atomic system is well into the hyperfine Paschen-Back (HPB) regime, as defined in chapter 2. In comparison to previous work [24, 110, 113] (see also section 3.3.3), this means that the two initial hyperfine ground states, as well as the $5^2P_{3/2}$ excited state manifold, are strongly decoupled into the $|m_J, m_I\rangle$ basis. The $5^2P_{3/2}$ excited states decouple into four groups of absorption features, organised by their m_J projection ($m_J = 3/2, 1/2, -1/2, -3/2$), with an internal structure dictated by the $m_I = \pm 3/2, \pm 1/2$ projections. Similarly, the ground state is split into two distinct groups of features, one each correspond-

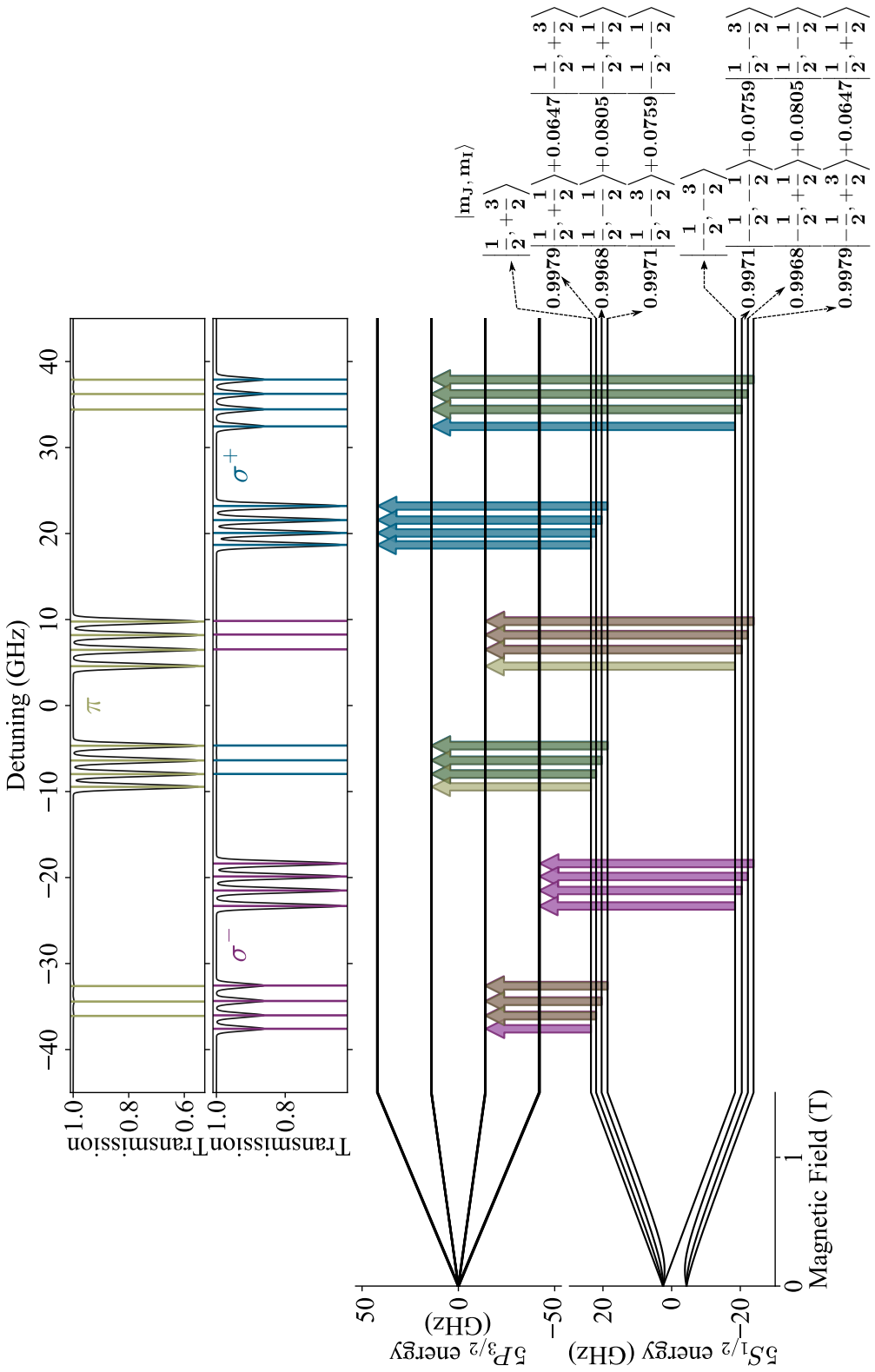

Figure 4.4: Theoretical calculations for absorption spectroscopy of the ^{87}Rb D2 line in the Voigt geometry, for a field strength of 1.5 T. In the bottom half of the figure the evolution of the $^2 5S_{1/2}$ and $^2 5P_{3/2}$ atomic energy levels in ^{87}Rb are shown as a function of the field strength B, up to 1.5 T, and the state decomposition in the $|m_J, m_I\rangle$ uncoupled basis: the small admixtures are a result of remnant effects of the hyperfine interaction in the hyperfine Paschen-Back (HPB) regime. The semi-transparent coloured arrows indicate the initial and final states involved in each transitions (olive for π transitions, blue for σ^+ transitions and purple for σ^- transitions), as well as transitions of different types that overlap due to the small admixture opposite m_J states. The upper half of the figure shows two panels with the calculated absorption spectra (S_0) for π (top) and $\sigma^\pm$ (bottom) transitions as a function of linear detuning. The vertical lines indicate the position of the atomic resonances for each type of transition, with the colour code the same as that used for the vertical arrows.

ing to the $m_J = \pm 1/2$ projections, where the internal structure is given by clearly defined $m_I = 3/2, 1/2, -1/2, -3/2$ states despite the Doppler-broadening ($\Gamma_{\text{Doppler}}/2\pi \approx 550$ MHz) in the vapour. Overall, this gives four well-defined multiplets of 'strong' transitions ($|m_J, m_I\rangle \rightarrow |m_{J'}, m_I\rangle$, with $m_{J'} = m_J\,(\pi), m_J + 1\,(\sigma^+), m_J - 1\,(\sigma^-)$). Less visible multiplets of 'weak' transitions are also present, a result of the ground states not being pure eigenstates in the $|m_J, m_I\rangle$ basis, and originate from a small ($< 1\%$) admixture of the opposite m_J state in the decomposition. This can be seen on the bottom right of figure 4.4, with more details on the nature of this admixture given in reference [151].

Atomic absorption spectra at high fields

Experimental data of the absorption spectra (S_0) obtained with our setup are shown in figures 4.5 and 4.6. Each of the spectra shown is an average over five spectra, all acquired in similar conditions and processed to remove any remaining background noise as described in appendix B.2, and have been fit using *ElecSus*, which is the practical implementation of our theoretical model. More details regarding the basic process behind the fitting of our spectra is presented in section 2.4.1. The error bars for the data points shown are on the order of 1×10^{-3}, and are thus not visible in our experimental spectra. Also shown in each figure are the residuals R of the fit, in this case multiplied for clarity by a factor of 100. We note that the residuals are of the same order of magnitude as the error bars, and we thus proceed with using the absolute residuals for analysis. From this we calculate an RMS difference between the theory and experimental data of 1.2%; together with the lack of discernible structure in the residuals, this indicates a very good fit [155].

For each spectrum the fit is carried out by using three of the physically-relevant quantities as free parameters: T, the temperature of the atomic vapour in our experiment cell; B, the magnitude of the magnetic field as experienced by the atoms and ϕ_B, the polarisation angle which indicates the angle between the magnetic field and the direction of polarisation of the laser beam–here we take the beam polarisation to be linear, along the x-axis in

figure 4.5 and along the y-axis in figure 4.6. The angle θ_B, the angle of the magnetic field relative to the direction of propagation of the light, is fixed by the geometry of the experimental setup–for the Voigt geometry, $\mathbf{k} \perp \mathbf{B}$ and so $\theta_B = \pi/2$ with an uncertainty of $< 1\%$. The other significant experimental parameters, *e.g.* those relating to the effects that result from the presence of buffer gas in the vapour cell ($\Gamma_{\text{Buf}}, \delta_{\text{shift}}$), are kept fixed during the fitting process. Their values are obtained by fitting the individual spectra from the same experimental run as those averaged and shown; these are then averaged and used in the fit of the averaged spectra. Of these two parameters, δ_{shift} has no significant correlation (*i.e.* a correlation coefficient of $< |0.1|$) to the other parameters while Γ_{Buf} has weak correlations to T ($c_{\text{corr},\Gamma_{\text{Buf}}\leftrightarrow\text{T}} \approx -0.4$), B ($c_{\text{corr},\Gamma_{\text{Buf}}\leftrightarrow\text{B}} \approx -0.2$) and ϕ_B ($c_{\text{corr},\Gamma_{\text{Buf}}\leftrightarrow\phi_\text{B}} \approx -0.2$). We note that while the time needed for a spectrum to be acquired (*i.e.* the time for a complete scan of the laser frequency) is on the order of a second, the time needed to analyse and fit spectra such as those shown here is on the order of minutes due to the complexity of the physical parameter space.

We attribute the significant buffer gas broadening in our spectra ($\Gamma_{\text{Buf}}/2\pi = (350 \pm 2)$ MHz) to the presence of He atoms trapped in the interior of the cell. As mentioned in section 3.3.3, this is due to the cell being previously exposed to a He-rich environment. Furthermore, we note that there is an associated small shift ($\delta_{\text{shift}} = (50 \pm 1)$ MHz) in the position of the resonance lines. We can use the literature values for the broadening coefficient of He [57] (see also appendix A) to translate this broadening to a He pressure of ~ 18 torr (~ 24 mbar) in our experiment cell. It is worth noting here that the amount of He in the cell is significantly lower than that previously seen in the results of chapter 3 taken several months prior to this experiment.

For the spectrum in figure 4.5 we obtain a value of $\phi_B = (0.4491 \pm 0.0007)$ radians ($\phi_B = (25.74 \pm 0.04)^\circ$) from the fit realised. The value obtained from the fit for figure 4.6 is $\phi_B = (2.0082 \pm 0.0007)$ radians ($\phi_B = (115.05 \pm 0.04)^\circ$). Both values differ from their corresponding expected values ($\phi_B = 0, \pi/2$, respectively) by approximately $\Delta\phi_B = 0.45$ radians ($\approx 25^\circ$), which we attribute to a systematic error due to the orientation of the cell heater block

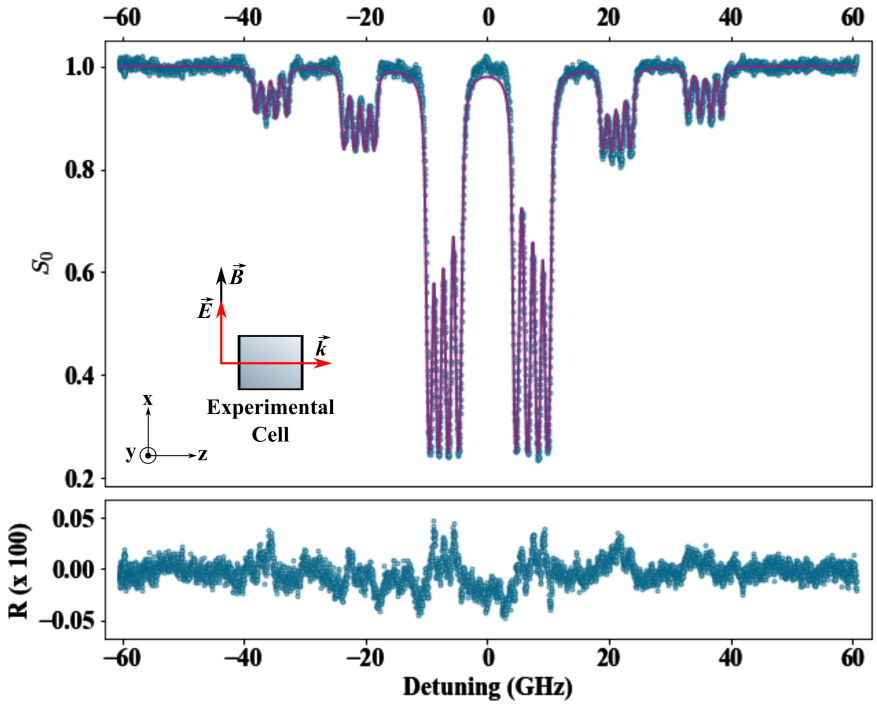

Figure 4.5: Experimental absorption spectrum (S_0; blue circles) as a function of linear detuning, averaged over five spectra, using horizontally polarised light as input. The corresponding fit (purple line) generated using *ElecSus*, as well as the residuals R of the fit (bottom panel), are also shown. Very good agreement between the data and theory is found, with an RMS error of 1.2% [155]. The free parameters used to fit this spectrum are: T, the temperature of the atoms; B, the magnetic field strength and ϕ_B, the angle of the magnetic field with respect to the x-axis (*i.e.* the direction of the polarisation of the light). From the fit, averaged values obtained for these parameters are $T = (108.94 \pm 0.04)$°C, $B = (1.52 \pm 0.08)$ T and $\phi_B = (0.4491 \pm 0.0007)$ rad. The remaining parameters for describing the system are fixed as follows: $\theta_B = \pi/2$, $\Gamma_{\text{Buf}}/2\pi = (350 \pm 2)$ MHz and $\delta_{\text{shift}} = (50 \pm 1)$ MHz.

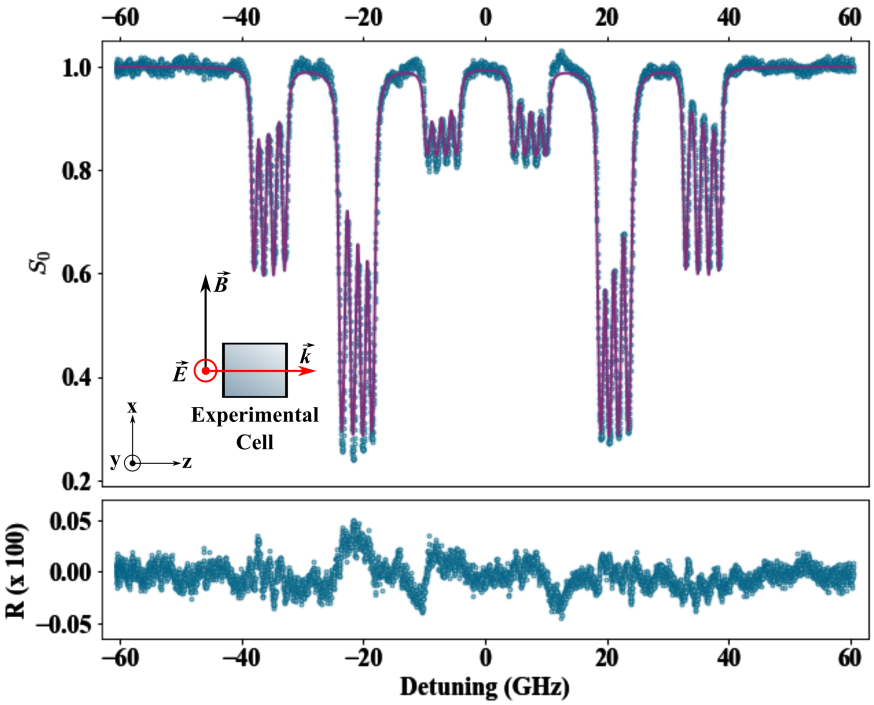

Figure 4.6: Experimental absorption spectrum (S_0; blue circles) as a function of linear detuning, averaged over five spectra, using vertically polarised light as input. The corresponding fit (purple line) generated using *ElecSus*, as well as the residuals R of the fit (bottom panel), are also shown. Very good agreement between the data and theory is found, with an RMS error of 1.2% [155]. The free parameters used to fit this spectrum are: T, the temperature of the atoms; B, the magnetic field strength and ϕ_B, the angle of the magnetic field with respect to the y-axis (*i.e.* the direction of the polarisation of the light). From the fit, averaged values obtained for these parameters are $T = (110.23 \pm 0.03)$°C, $B = (1.52 \pm 0.07)$ T and $\phi_B = (2.0082 \pm 0.0007)$ rad. The remaining parameters for describing the system are fixed as follows: $\theta_B = \pi/2$, $\Gamma_{\text{Buf}}/2\pi = (350 \pm 2)$ MHz and $\delta_{\text{shift}} = (50 \pm 1)$ MHz.

once inside the bore of the cylindrical magnet described in section 4.3.1. As a result, both spectra show excitation of both π and $\sigma^{\pm}$ transitions as there are both parallel and perpendicular components of $\mathbf{B}$ projected onto the direction of polarisation of the light. Our theoretical model takes this into account by giving each type of transition a different relative strength, as mentioned in 2.2.3. In our case, the difference in strength is given by the factor $\cos^2(\Delta\phi_B)$ for the parallel component and $\sin^2(\Delta\phi_B)$ for the perpendicular component, resulting in an approximate $4:1$ ratio; this is clearly visible in both figures 4.5 and 4.6.

Similarly, the value obtained for the magnetic field strength from both fits is $B = 1.52$ T, with an uncertainty of 80 mT for figure 4.5 and of 70 mT for figure 4.6. The latter are mainly attributed to the linearity in the laser scan realised for acquiring the spectra in this experiment. While the DFB laser we use allows for large mode-hop-free scans (~ 150 GHz in this case), this scanning range comes at a cost of a non-linearity as the temperature, and thus emission frequency, of the laser is changed; a shift in the position of the atomic resonances will affect the value of B obtained, particularly as the fit calculates the value of B that best fits *all* 24 transitions. As such, we assume the non-linearity generates a shift by a different amount for each transition and is thus responsible for the above uncertainties. Along with other systematic errors in the calibration and scaling of the frequency axis of our spectra (see section 3.3.2 and appendix B for more details), this is the primary source of uncertainty in our measurements. Future work aims to redesign the experiment in a way that the non-linearity of the scan is reduced so as to be able to increase the precision of the measurements of B.

We can at this point take the results presented thus far, expanding on those presented in section 3.3.3, to propose this atomic spectroscopy as a technique for measurement of large magnetic fields and their relative orientation. Once the atomic system is completely in the hyperfine Paschen-Back regime, the Zeeman shift in all the atomic resonance lines allows for a more accurate determination of the magnetic field strength. The ability to more clearly observe the relative strength between different sets of transitions (namely,

π and $\sigma^{\pm}$) as a result of geometrically-induced differences in the coupling strengths between the atoms and light in this regime provides a more precise method to determine the relative direction between the magnetic field and the direction of the electric field vector (*i.e.* the polarisation) of the light. Thus, the experimental setup and technique presented in this work leads to a natural application of atomic-based spectroscopy in the area of vector magnetometry.

Sensitivity of optical rotation signals to cell window birefringence

In addition to being able to work in the hyperfine Paschen-Back regime, the use of large magnetic field strengths in this work also provides additional information about the atomic medium in the form of optical rotation phenomena [59, 93, 171]. For the present work, we note that the optical rotation can be measured by the Stokes parameters, defined in section 2.1.4, giving greater insight into the interactions between the atoms and the external magnetic field. We present the results of experimental measurements of the dichroism and birefringence of the ^{87}Rb atomic medium in the orthogonal polarisation bases that correspond to the S_1, S_2 and S_3 parameters, shown in figures 4.7, 4.8 and 4.9, respectively. To acquire these spectra, the set of polarisation optics (PBS+$\lambda/2$, $\lambda/4$) and balanced photodiodes shown in the experiment optics (figure 4.1) were used to record orthogonal polarisation components simultaneously; these were subsequently processed into the corresponding Stokes parameters for the chosen polarisation basis.

Figure 4.7 shows the spectrum for the S_1 parameter, corresponding to the difference between orthogonal linear (*i.e.* horizontal and vertical) polarisations (equation 2.18). Figure 4.8 shows the spectrum for the S_2 parameter, which corresponds to the difference between orthogonal linear polarisations rotated anti-clockwise by $\pi/4$, resulting in diagonal components in a Cartesian basis (equation 2.19). Figure 4.9 shows the spectrum for the S_3 parameter, which is defined as the difference between orthogonal circular polarisations in the helicity basis (*i.e.* left-hand and right-hand circular) (equation 2.20). Together, these Stokes parameters provide information regarding the linear and circular

birefringence of the atomic medium for a given well-defined input polarisation of light.

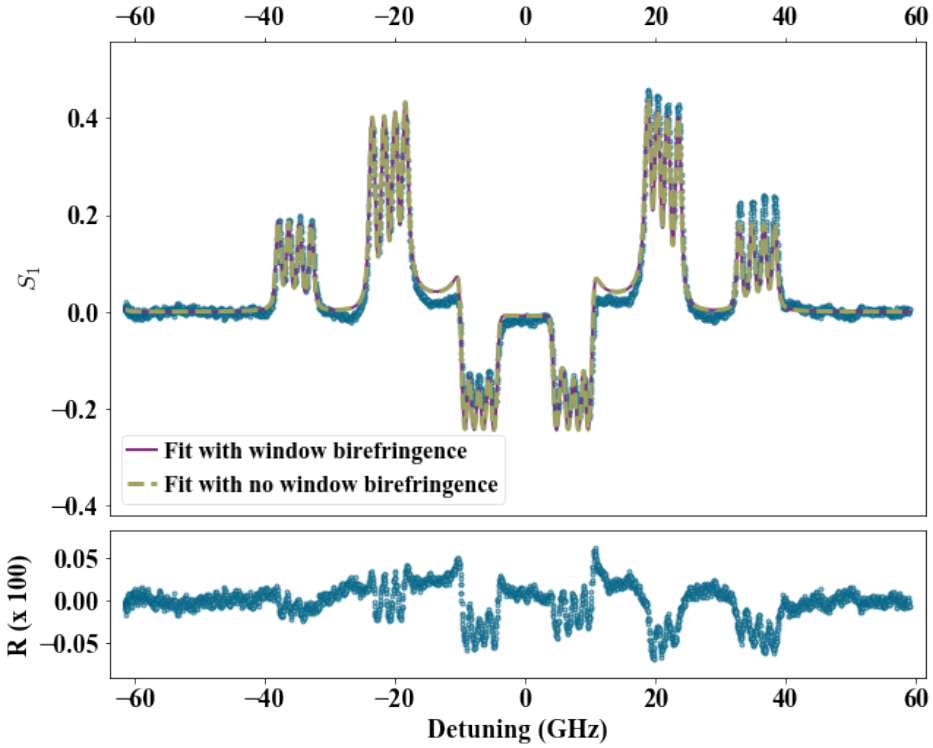

Figure 4.7: Experimental spectrum (blue circles) of the S_1 Stokes parameter, taken as a function of linear detuning with a linearly polarised input beam. A fit taking cell window birefringence into account (purple line), and the residuals R, are shown; very good agreement (RMS error of $\sim 2\%$) [155] is found between experiment and theory. In this case, the fit parameters allowed to vary are the temperature T, magnetic field strength B, polarisation angle ϕ_B and the birefringence of the cell windows, as characterised by the angles θ_{BR} and ϕ_{BR}. The remaining parameters in the fit are kept fixed: $\Gamma_{\mathrm{Buf}}/2\pi = (350 \pm 2)$ MHz, $\delta_{\mathrm{shift}} = (50 \pm 1)$ MHz and $\theta_B = \pi/2$. A fit without the effects of the cell window birefringence (broken green line) is included for comparison.

We used our theoretical model, implemented by *ElecSus*, to fit the experimental data to the each of the Stokes parameters mentioned above. This gives very good agreement between the data (blue circles) and theory (broken green curve) [155] seen in figures 4.7, 4.8 and 4.9. However, there are still small visible discrepancies between the data and theoretical model. We try

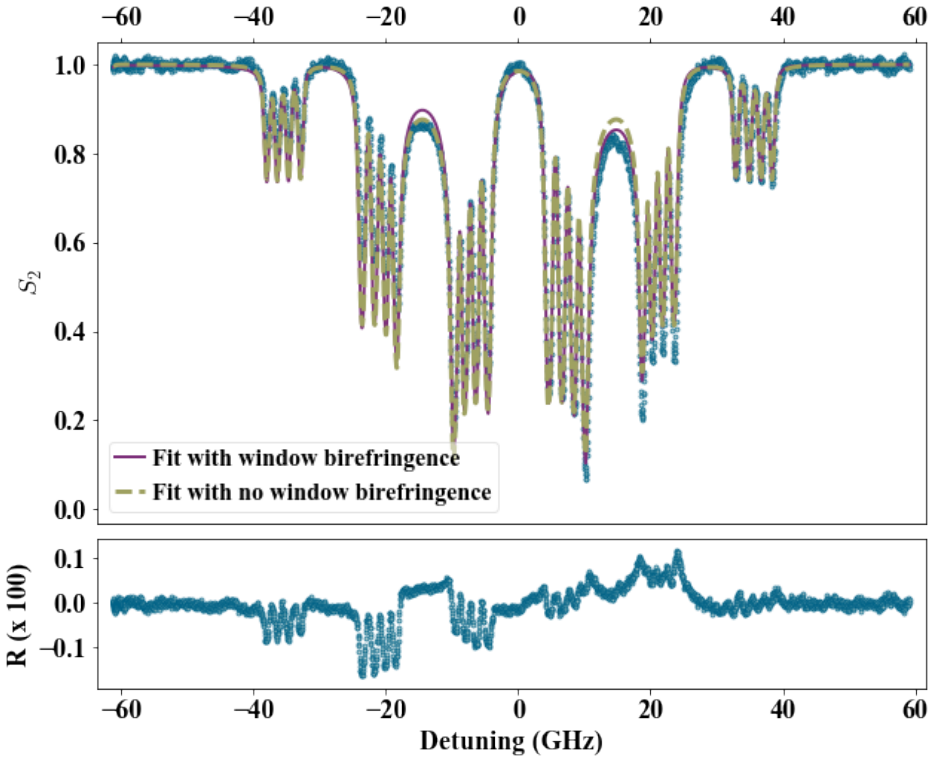

Figure 4.8: Experimental spectrum (blue circles) of the S_2 Stokes parameter, taken as a function of linear detuning with a linearly polarised input beam. A fit taking cell window birefringence into account (purple line), and the residuals R, are shown; very good agreement (RMS error of $\sim 3\%$) [155] is found between experiment and theory. In this case, the fit parameters allowed to vary are the temperature T, magnetic field strength B, polarisation angle ϕ_B and the birefringence of the cell windows, as characterised by the angles θ_{BR} and ϕ_{BR}. The remaining parameters in the fit are kept fixed: $\Gamma_{\mathrm{Buf}}/2\pi = (350 \pm 2)$ MHz, $\delta_{\mathrm{shift}} = (50 \pm 1)$ MHz and $\theta_B = \pi/2$. A fit without the effects of the cell window birefringence (broken green line) is included for comparison.

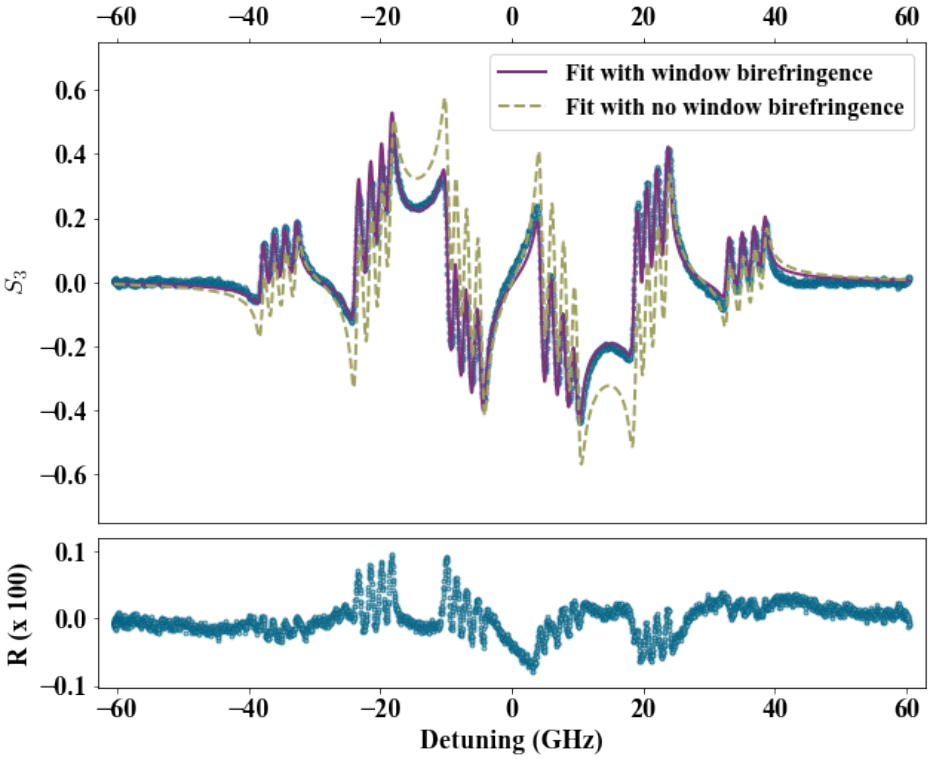

Figure 4.9: Experimental spectrum (blue circles) of the S_3 Stokes parameter, taken as a function of linear detuning with a linearly polarised input beam. A fit taking cell window birefringence into account (purple line), and the residuals R, are shown; very good agreement (RMS error of $\sim 2\%$) [155] is found between experiment and theory. In this case, the fit parameters allowed to vary are the temperature T, magnetic field strength B, polarisation angle ϕ_B and the birefringence of the cell windows, as characterised by the angles θ_{BR} and ϕ_{BR}. The remaining parameters in the fit are kept fixed: $\Gamma_{\mathrm{Buf}}/2\pi = (350 \pm 2)$ MHz, $\delta_{\mathrm{shift}} = (50 \pm 1)$ MHz and $\theta_B = \pi/2$. A fit without the effects of the cell window birefringence (broken green line) is included for comparison.

and remove some of these errors by taking into account the birefringence of the cell windows in our experiment. In the theoretical framework established in chapter 2 for the interaction of atoms with an electromagnetic field, we include in our model the effect of two thin, birefringent windows that interact with the electric field of our laser beam on two occasions: once just before the beam enters the atomic medium in the cell cavity and once when the light has passed the atomic medium and exits the cell. To carry out the calculations, we use the Jones matrix formalism [134, 172] so that the transmitted electric field $\mathbf{E}_{\text{out}}$ through the vapour cell in our experiment can be written as

$$\mathbf{E}_{\text{out}} = \mathcal{E}(\theta_{\text{BR}}, \phi_{\text{BR}}) \times \mathcal{J}_{\text{atoms}} \times \mathcal{E}(\theta_{\text{BR}}, \phi_{\text{BR}}) \times \mathbf{E}_{\text{in}}, \tag{4.1}$$

where $\mathbf{E}_{\text{in}}$ is the electric field incident on the cell, $\mathcal{E}(\theta_{\text{BR}}, \phi_{\text{BR}})$ is the Jones matrix representation of a birefringent window and $\mathcal{J}_{\text{atoms}}$ is the Jones matrix that represents the dichroic and birefringent atomic medium. The angles θ_{BR} and ϕ_{BR} correspond to the axis of birefringence and the angle of optical rotation generated in light passing through a birefringent medium, respectively. The presence of $\mathcal{E}(\theta_{\text{BR}}, \phi_{\text{BR}})$ twice in the above expression takes into account the behaviour described above for the entry and exit windows of the experiment cell. The resulting transmitted electric field $\mathbf{E}_{\text{out}}$ through the cell can then be multiplied by the appropriate Jones' matrices to give the desired orthogonal polarisation components (in the laboratory frame of reference), which in turn are processed into the different Stokes parameters.

Using the modifications to our model, given in equation 4.1, we can generate another fit to the experimental data for the Stokes parameters. A summary of the values obtained for the fit parameters is given in table 4.1. These allow us to determine that the birefringence introduced by the cell windows is considerably small. Our experiment cell has windows of 300 μm thickness each [169]; at the wavelength of the light used to excite the Rb D2 line ($\sim$ 780 nm), this can be used together with the reported value for the Verdet coefficient of glass [173] to calculate an induced rotation of $\approx 0.05^{\circ}$ from each window. In equation 4.1 we have initially assumed that both of the cell windows have identical birefringent properties. The fits, seen as the broken

green curve in figures 4.7, 4.8 and 4.9, show very good agreement with the experimental data, as evidenced by the residuals R and an RMS error of $\sim 2\%$ [155].

From these fits to the different Stokes parameters we obtain average values of $\theta_{\mathrm{BR}} = (0.96 \pm 0.16)$ radians $((55 \pm 9)^\circ)$ and $\phi_{\mathrm{BR}} = (0.06 \pm 0.03)$ radians $((3 \pm 2)^\circ)$, as seen in table 4.1. We note that these values correspond to the combined effect of *both* of the cell windows on the electric field transmitted through the experiment cell. The discrepancy between the calculated induced rotation ($\approx 0.1^\circ$) and the measured value for ϕ_{BR} can be assumed to be a result of the cell windows being heated and of mechanical stresses applied during the fabrication process and the placement of the cell in the optical setup. Upon closer inspection of the fits with and without the birefringent effects of the cell windows, we see that these effects are particularly evident in the spectrum of the S_3 parameter shown in figure 4.9. From the definition of said parameter (equation 2.20), we proceed to state that the cell windows have a predominantly circular birefringence. Here we have exploited the sensitivity of the atomic system to optical rotation phenomena, in this case in the basis of orthogonal circular polarisation states, to experimentally enhance these effects so that they are more clearly visible. In particular, we have taken advantage of the dichroism and circular birefringence of the atomic medium to obtain a highly sensitive signal in the form of the S_3 Stokes parameter. As such, this experimental system provides a tool to characterise the birefringent effects due to vapour cell windows, allowing for them to be quantified and in this way reduce systematic errors in future measurements.

	Fit parameters				
	T (°C)	**B (T)**	ϕ_B **(rad)**	θ_{BR} **(rad)**	ϕ_{BR} **(rad)**
S_1	(107.16 ± 0.07)	(1.52 ± 0.24)	(-0.3289 ± 0.0018)	(1.17 ± 0.18)	(0.01 ± 0.02)
S_2	(109.14 ± 0.17)	(1.52 ± 0.29)	(-0.049 ± 0.003)	(0.93 ± 0.22)	(0.03 ± 0.03)
S_3	(104.30 ± 0.08)	(1.52 ± 0.14)	(-0.1735 ± 0.0013)	(0.78 ± 0.08)	(0.14 ± 0.03)
Average	(106.87 ± 0.11)	(1.52 ± 0.22)	(-0.184 ± 0.002)	(0.96 ± 0.16)	(0.06 ± 0.03)

Table 4.1: Values of the floating parameters used in the fits of the S_1, S_2 and S_3 Stokes parameters shown in figures 4.7, 4.8 and 4.9, respectively. We include in the table the values of the angles θ_{BR} and ϕ_{BR} used to take the birefringence from the cell windows into account. We note that for all of the fits realised the values of the magnetic field B are in agreement, while the values of temperature T are sufficiently similar to not generate a noticeable difference in the spectra. In addition to these parameters, the fit used fixed values for the buffer gas broadening ($\Gamma_{\mathrm{Buf}} = (350 \pm 2)$), buffer gas shift ($\delta_{\mathrm{shift}} = (50 \pm 1)$) and $\theta_B = \pi/2$. The fits were carried out using the `lmfit` Python package, as described in section 2.4.1, which gives the quoted uncertainties as the standard error after a least-square minimisation.

4.4 Summary

In the course of this chapter we have presented experimental results of a spectroscopic investigation using a vapour of ^{87}Rb in the Voigt geometry which allows us to measure the absolute magnetic field strength and relative orientation of the field. We have taken advantage of a high field strength of 1.5 T to drive the atomic system well into the hyperfine Paschen-Back regime, where the atomic resonance lines can be clearly resolved and measurements of all the Stokes parameters can be made. The very good agreement between our data and theoretical model allows us not only to determine the field strength and polarisation angle, but also the changes in optical rotation phenomena within the atomic medium and systematic effects such as the cell window birefringence due to the strong magnetic field. While the results presented use an isotopically enriched sample of ^{87}Rb, the experimental method and setup is applicable to other alkali-metal atoms. As such, we demonstrate an all-optical scheme for precision atomic vector magnetometry in field strengths up to the order of Teslas. The following chapter builds further upon this technique, making use of the description of the atomic system in the hyperfine Paschen-Back regime to provide a scheme for potentially increasing the precision of the field strength measurements to levels that could in the future allow for new areas of research, such as measurement of fundamental constants via precision thermometry, to be pursued.

Chapter 5

Magnetometry using Rb vapour in the Voigt geometry

5.1 Introduction

As mentioned previously in chapters 3 and 4, atom-based magnetometry has seen a surge in interest in recent years. New technologies [91, 92] and measurement protocols [105, 106, 107, 108] have been developed thanks to a solid understanding of the physical interactions between atoms and external magnetic fields. Together with in-depth knowledge of atom-light interactions in the presence of magnetic fields [59, 74, 76, 80], the applications for optical atomic magnetometry continue to grow into a number of diverse areas [11, 98, 99, 100, 103, 104]. Nevertheless, this work has been focused on measurements at the lower end of the range of field strengths (~ 10 mT), leaving open the possibility of translating the basic principles to work at higher (≥ 1 T) field strengths.

Work at high magnetic field strengths has historically required the use of systems that provide an easily measured quantity in the laboratory. As such, techniques such as nuclear-magnetic resonance (NMR) [174, 175], electron-spin resonance (ESR) [176] and superconducting quantum interference (SQUID) [177, 178] devices have come to be start-of-the-art for this

purpose. However, these techniques impose constraints such as the use of cryogenic environments or large equipment footprint. Thus, a natural interest in use of atom-based sensors for measurement of high magnetic field strengths comes from their relatively simple operating environments and the comparably small footprint of the equipment necessary. In particular, the use of atom-based spectroscopic techniques for this purpose has been previously explored; the nature of the interaction between the atoms and an external magnetic field (*i.e.* the Zeeman effect) introduces a geometric dependence that can provide access to a more detailed description of the system, as discussed in sections 2.2.2 and 2.2.3, and seen in the work presented in chapters 3 and 4.

The work presented in this chapter aims to provide support for the use of atom-based magnetometers at high fields by providing the theoretical and experimental demonstration of an all-optical scheme for precision measurements of the operating field strength. The scheme takes advantage of the effect of the high field strengths on a thermal vapour of atoms–namely, the hyperfine Paschen-Back regime–and the operating geometry, as recorded by absorption spectra. From these spectra, pairs of transitions are specifically chosen to provide a method of calculating the field strength that is limited in precision by the precision of the frequency measurement of the difference in position of the two transitions. In this case, we have used a vapour of ^{87}Rb to determine our operating field strength with a relative uncertainty of 3.5×10^{-2}

5.2 Theory

For the experiments in this chapter we will make use of the theoretical concepts touched upon previously in chapter 2, albeit at a greater level of detail. Whereas our previous interest was looking at the interactions between atoms, light and a magnetic field via their compound macroscopic effects, here we will change the focus to be more practical. We will consider the case of an alkali-metal atomic vapour in the presence of an external magnetic field, probed by a near-resonant laser beam: the difference from work in previous

chapters will be in the approach taken to determine the field strength.

As we are again dealing with an atom-light system inside an externally-applied magnetic field, and in particular, oriented in the Voigt geometry, the theoretical basis is that described in chapter 2. Our focus here will be looking at the interaction with the magnetic field, so that we will concentrate on the Zeeman effect as described in 2.2. We recall that both the geometry and the field strength determine the strength of the interaction (equation 2.21), so that we can focus on looking at the Zeeman-induced energy shifts of the atomic states to grasp at these parameters.

Without loss of generality, we assume that we will be working with field strengths such that the atomic system is in the hyperfine Paschen-Back regime (see section 2.2.1). This means the description of the atomic states can best be done using the uncoupled $|m_J, m_I\rangle$ basis and the energy shift from the Zeeman effect can be described by equation 2.28. Thus, taking the total Hamiltonian of the physical system ($\hat{H} = \hat{H}_{\text{atom}} + \hat{H}_{\text{light}} + \hat{H}_{\text{Zeeman}}$; see sections 2.1.1, 2.1.2 and 2.2.1 for details on each term), we write the shift in the energy of the levels of the atom as

$$E(J, m_J; I, m_I) = A_{\text{HF}} m_J m_I + B_{\text{HF}} \frac{6(m_J m_I)^2 + 3m_J m_I - 2I(I+1)J(J+1)}{4I(2I-1)J(2J-1)} + \mu_{\text{B}}(g_J m_J + g_I m_I)B, \tag{5.1}$$

which is obtained by diagonalising the Hamiltonian in the $|m_J, m_I\rangle$ basis and projecting the system along the quantisation axis (*e.g.* the z-axis). It is important to note here that the energy is expressed in frequency units. The magnetic-dipole and electric-quadrupole constants $A_{\text{HF}}, B_{\text{HF}}$, respectively, remain from the hyperfine interaction in the atom, and are here used as scaling factors for the energy shift. J, I are, respectively, the eigenvalues of the total electronic angular and nuclear angular momenta; m_J, m_I represent their projections along the chosen quantisation axis.

For alkali-metal atoms, the general electronic structure of the atom (section 2.3) allows us to rewrite equation 5.1 in two relevant forms. The ground

state of these atoms has a well-defined total electronic angular momentum $J = 1/2$ and no electric-quadrupole hyperfine interaction ($B_{\mathrm{HF}} = 0$), such that

$$E(J = {}^1\!/_2, m_J; I, m_I) = A_{\mathrm{HF}} m_J m_I + \mu_{\mathrm{B}}(g_J m_J + g_I m_I)B. \tag{5.2}$$

Similarly, we know that the first excited state in alkali-metal atoms has two possible values for the total electronic angular momentum: $J = 1/2$ for the $n^2P_{1/2}$ state (the so-called D1 line) and $J = 3/2$ for the $n^2P_{3/2}$ state (the D2 line). For the former there is also no electric-quadrupole hyperfine interaction. Thus, the $n^2P_{1/2}$ excited state has an shift in energies of the same form as that of the ground state (equation 5.2). The latter excited state ($n^2P_{3/2}$) has both magnetic-dipole and electric-quadrupole interactions; we can thus write the energy shift as [85, 90]

$$\begin{aligned} E(J = {}^3\!/_2, m_J; I, m_I) = {} & A_{\mathrm{HF}} m_J m_I + B_{\mathrm{HF}} \\ & \times \frac{6(m_J m_I)^2 + 3m_J m_I - 2I(I+1)({}^3\!/_2)({}^3\!/_2+1)}{4I(2I-1)({}^3\!/_2)(2({}^3\!/_2)-1)} \\ & + \mu_{\mathrm{B}}(g_J m_J + g_I m_I)B \\ = {} & A_{\mathrm{HF}} m_J m_I \\ & + B_{\mathrm{HF}} \frac{6(m_J m_I)^2 + 3m_J m_I - 2I(I+1)({}^{15}\!/_4)}{4I(2I-1)(3)} \\ & + \mu_{\mathrm{B}}(g_J m_J + g_I m_I)B. \end{aligned} \tag{5.3}$$

Looking at equations 5.2 and 5.3 it is clear that, given the appropriate choice of levels (*i.e.* values of m_J, m_I) it is possible to cancel out terms in certain transitions. The cancellation of terms provides a way of increasing the precision in the measurements taken, as there are less sources of error [155] that contribute to the overall uncertainty. This fact has been exploited in previous experiments [81, 179, 180, 181] that look to obtain information on the excited state g-factors or hyperfine interactions in other atoms; an added result of this is the measurement of field strengths down to parts per million. For a system such as ours in the hyperfine Paschen-Back regime, the selection

rules for electric-dipole transitions constrain the possible values for the ground and excited states used in each transition.

We now consider the case of atomic Rb, in particular that of ^{87}Rb ($I = 3/2$), in the hyperfine Paschen-Back regime. To begin, we can look at the transition that occurs between the extreme (*i.e.* stretched) energy levels both in the ground and excited states. We note that this corresponds to the system studied in reference [81], and will only give a summary of the main points. For the ground state, this means we will be using the level with $m_J = 1/2, m_I = 3/2$, while for the excited state we will use the level corresponding to $m_J = 3/2, m_I = 3/2$. Substituting these values into the corresponding equations for the ground and excited state energy shifts (equations 5.2 and 5.3, respectively), we take the difference $E(J = {}^3\!/_2 = m_J; I = {}^3\!/_2 = m_I) - E(J = {}^1\!/_2 = m_J; I = {}^3\!/_2 = m_I) \equiv \Delta E$,

$$\Delta E = \mu_{\mathrm{B}} \frac{3g_{J'} - g_J}{2} B + \frac{3(3A'_{\mathrm{HF}} - A_{\mathrm{HF}})}{4} + \frac{B'_{\mathrm{HF}}}{4}, \tag{5.4}$$

where we can take $\Delta E = h\nu_{\mathrm{Laser}}$ corresponding to the laser detuning, with respect to the hyperfine manifold centre of gravity, of the transition in question. The primed variables in equation 5.4 correspond to values for the excited state. We see also that there is no longer a dependence on the value of the nuclear angular momentum projection m_I by virtue of the dipole selection rules (see section 2.1.2).

We can observe that the expression above depends linearly on B, so that by knowing the laser detuning we can determine the magnetic field strength,

$$B = \frac{2}{\mu_{\mathrm{B}}(3g_{J'} - g_J)} \left[h\nu_{\mathrm{Laser}} - \frac{1}{4}\left(B'_{\mathrm{HF}} + 3(3A'_{\mathrm{HF}} - A_{\mathrm{HF}})\right) \right]. \tag{5.5}$$

In general, using the selection rule $\Delta m_I = 0$ we can write the energy difference ΔE of an electronic transition as,

$$\Delta E = \mu_{\mathrm{B}} \frac{\alpha g_{J'} + \beta g_J}{2} B + \frac{m_I(\gamma A'_{\mathrm{HF}} + \epsilon A_{\mathrm{HF}})}{2} + \eta B'_{\mathrm{HF}}, \tag{5.6}$$

where the values of $\alpha, \beta, \gamma, \epsilon$ and η are determined by the choice of ground- and excited-state levels; the values of these coefficients for our case are shown in table 5.1. Here we note that the value of the magnetic field B is determined by both ground and excited state constants, where the latter are often not as well-reported as the former and represent sources of error in measurements such as those reported in [119, 144].

The idea of taking advantage of the different states involved in a transition to cancel out terms in the resulting energy shift can be expanded upon. Now, rather than using just one transition we consider pairs of transitions that, together, allow us to remove additional terms in equation 5.6. We want to focus specifically on removing all the terms that arise from the excited state constants (*i.e.* $g_{J'}, A'_{\mathrm{HF}}, B'_{\mathrm{HF}}$); to do this, ideally we want to consider pairs of transitions that have a common excited state level with the same values of m_J, m_I. However, we can begin by considering a pair of transitions of the same type, for instance, two σ^+ transitions. These two transitions will be chosen so that they begin at different energy levels in the ground state, which in turn means that they will not end in the same excited state energy level. Nevertheless, the two levels can be chosen so as to give a partial cancellation of the excited state terms.

As an example, we consider the energy shift for the transitions $|J = {}^1\!/_2 = m_J; I = {}^3\!/_2, m_I = {}^1\!/_2\rangle \rightarrow |J' = {}^3\!/_2 = m_{J'}; I = {}^3\!/_2, m_I = {}^1\!/_2\rangle$ and $|J = {}^1\!/_2, m_J = {}^-{}^1\!/_2; I = {}^3\!/_2 = m_I\rangle \rightarrow |J' = {}^3\!/_2, m_{J'} = {}^1\!/_2; I = {}^3\!/_2 = m_I\rangle$, as well as their difference (see figure 5.1):

$$\begin{aligned}
\Delta E_{\sigma_1^+} &= \tfrac{1}{4}\left(3A'_{\mathrm{HF}} - A_{\mathrm{HF}}\right) + \tfrac{1}{2}\mu_{\mathrm{B}}(3g_{J'} - g_J)B - \tfrac{5}{8}B'_{\mathrm{HF}} \\
\Delta E_{\sigma_2^+} &= \tfrac{3}{4}\left(A'_{\mathrm{HF}} + A_{\mathrm{HF}}\right) + \tfrac{1}{2}\mu_{\mathrm{B}}(g_{J'} + g_J)B - \tfrac{5}{8}B'_{\mathrm{HF}} \\
\therefore\ & (\Delta E_{\sigma_1^+} - \Delta E_{\sigma_2^+}) = -A_{\mathrm{HF}} + \mu_{\mathrm{B}}(g_{J'} - g_J)B. \qquad (5.7)
\end{aligned}$$

We can see in equation 5.7 that, compared to equation 5.4, there are fewer terms that contain excited state constants–here only the excited state g-factor is present. The result is that now we can determine the magnetic field strength by taking the laser frequency difference $\Delta\nu_{\sigma^+_{1\rightarrow 2}}$ equal to the energy difference

		Ground state	$m_J = 1/2$					$m_J = -1/2$				
			α	β	γ	ϵ	η	α	β	γ	ϵ	η
Excited state	$m_{J'} = 3/2$	$m_I = 3/2$	3	−1	3	−1	1/4					
		$m_I = 1/2$					−5/8					
		$m_I = -1/2$					−3/4					
		$m_I = -3/2$					−1/8					
	$m_{J'} = 1/2$	$m_I = 3/2$	1	−1	1	−1	−5/8	1	1	1	1	−5/8
		$m_I = 1/2$					−3/4					−3/4
		$m_I = -1/2$					−19/24					−19/24
		$m_I = -3/2$					−3/4					−3/4
	$m_{J'} = -1/2$	$m_I = 3/2$	−1	−1	−1	−1	−3/4	−1	−1	−1	−1	−3/4
		$m_I = 1/2$					−19/24					−19/24
		$m_I = -1/2$					−3/4					−3/4
		$m_I = -3/2$					−5/8					−5/8
	$m_{J'} = -3/2$	$m_I = 3/2$						−3	1	−3	1	−1/8
		$m_I = 1/2$										−3/4
		$m_I = -1/2$										−5/8
		$m_I = -3/2$										1/4

Table 5.1: Values of the coefficients for equation 5.6 corresponding to possible π, $\sigma^{\pm}$ ($\Delta m_J = 0, \pm 1$, respectively) transitions for ^{87}Rb in the hyperfine Paschen-Back regime. Gray spaces indicate transitions not allowed under the electric dipole selection rules stated in section 2.1.2.

to write

$$\begin{aligned} B &= \frac{1}{\mu_{\mathrm{B}}(g_{J'} - g_J)} \left((\Delta E_{\sigma_1^+} - \Delta E_{\sigma_2^+}) + A_{\mathrm{HF}} \right) \\ &= \frac{1}{\mu_{\mathrm{B}}(g_{J'} - g_J)} \left(\Delta E_{\sigma^+_{1\leftrightarrow 2}} + A_{\mathrm{HF}} \right). \end{aligned} \tag{5.8}$$

Here we can argue there is a potential increase in the precision of the measurement due to the presence of only the excited state $g_{J'}$ factor and the measurement of a frequency difference $\Delta E_{\sigma^+_{1\leftrightarrow 2}}$; the latter means no absolute frequency reference is necessary and systematic errors in the measurement of the frequencies can be reduced. Note that from table 5.1 we can determine other similar pairs of transitions that allow for the partial removal of the excited state constants in the expression for measuring the field strength. Some of these transitions can be found in table 5.2.

As previously stated, the aim of using such pairs of transitions is to attempt to remove all excited state constants. To do so, we want pairs of transitions with a common excited state level; following the selection rules for transitions in the hyperfine Paschen-Back regime this is only possible by taking pairs of transitions that start in different ground state levels but end in the same level of the excited state. To demonstrate this, we take the π ($\Delta m_J = 0$) transition and the σ^+ ($\Delta m_J = 1$) transition to the excited state $|m_{J'} = 1/2, m_I = 3/2\rangle$ energy level, as seen in figure 5.1. Using the adequate values from table 5.1 in equation 5.6, we can write the energy shift for each of the transitions and look at the difference,

$$\begin{aligned} \Delta E_{\pi} &= \tfrac{3}{4}\left(A'_{\mathrm{HF}} - A_{\mathrm{HF}}\right) + \tfrac{1}{2}\mu_{\mathrm{B}}(g_{J'} - g_J)B - \tfrac{5}{8}B'_{\mathrm{HF}} \\ \Delta E_{\sigma^+} &= \tfrac{3}{4}\left(A'_{\mathrm{HF}} + A_{\mathrm{HF}}\right) + \tfrac{1}{2}\mu_{\mathrm{B}}(g_{J'} + g_J)B - \tfrac{5}{8}B'_{\mathrm{HF}} \\ \therefore \quad & (\Delta E_{\sigma^+} - \Delta E_{\pi}) = \tfrac{3}{2}A_{\mathrm{HF}} + \mu_{\mathrm{B}} g_J B, \end{aligned} \tag{5.9}$$

where we see that there is still a linear dependence in the field strength B, but now there are no excited state constants in the expression. Equation 5.10 is expressed in a simple form and in terms of well-known experimental constants (A_{HF}, g_J), which could help further improve the precision in the measurement

of the field strength by using the expression,

$$\begin{aligned} B &= \frac{1}{\mu_{\mathrm{B}} g_J}\left((\Delta E_{\sigma^+} - \Delta E_{\pi}) - \frac{3}{2}A_{\mathrm{HF}}\right) \\ &= \frac{1}{\mu_{\mathrm{B}} g_J}\left(\Delta E_{\sigma^+ \leftrightarrow \pi} - \frac{3}{2}A_{\mathrm{HF}}\right), \end{aligned} \tag{5.10}$$

in a straightforward manner by means of a linear relation between field and frequency difference. Additional pairs of transitions that provide similar expressions to the one above can be found in table 5.3. The simplicity of the expression means that the few parameters must have precise values assigned; experimentally, this means that, in particular, the precise determination of the centres of the absorption features in a spectrum is fundamental. This, amongst other aspects, will be expanded upon in the next section of this chapter.

5.3 Experiment

5.3.1 Experimental setup

The experiments carried out for this chapter used the same experimental setup described in chapter 4. The main characteristics of the system will be summarised here; further details can be found in section 4.3.1. The magnetic field in the setup was once again provided by a cylindrical permanent magnet designed to have an axial field of 1.62 T, with this value rapidly falling off towards the ends of the magnet [165]; more details on the axial field profile are given in section 4.3.1. Inside the magnet's central bore of 22 mm we placed a custom-made PTFE and copper heater assembly, which houses the necessary optical components and a 1 mm cuboidal experiment vapour cell, for carrying out measurements in the Voigt geometry (see section 2.2.1). This heater assembly is passively temperature-stabilised by use of a resistive cartridge heater; the atomic vapour in the cell is heated to its operating temperature by thermal contact with the copper.

For probing the atomic system, a distributed feedback (DFB) laser with

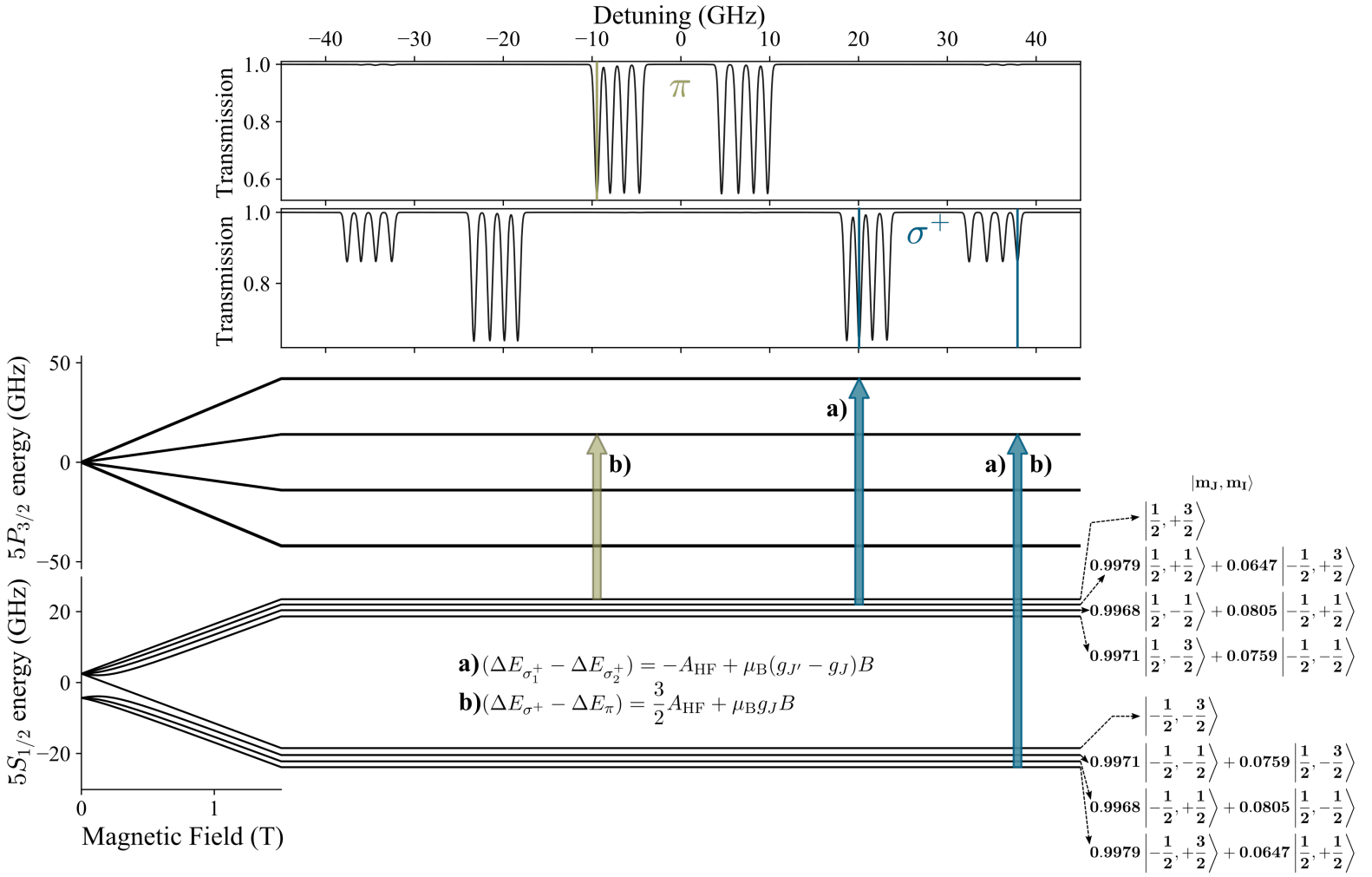

Figure 5.1: Diagram of the energy levels and pairs of transitions on the ^{87}Rb D2 line used to aid in cancelling out excited-state terms in the expression for the frequency difference. The top panels show the absorption spectra, decomposed into π (top) and $\sigma^{\pm}$ (bottom) transitions, calculated at $B = 1.5$ T. At the bottom of the figure, the evolution of the energy levels is plotted as a function of B, with the decomposition of states in the $|m_J, m_I\rangle$ basis. The coloured vertical lines and arrows corresponding to the pairs of transitions selected in the derivations for equations 5.7 and 5.10: **a)** pairs of σ^+ transitions; **b)** pair of π and σ^+ transitions. Also shown are the corresponding expressions for the theoretical frequency differences for each pair of transitions.

Type	Transition 1 $\lvert J, m_J; I, m_I\rangle \rightarrow \lvert J', m_{J'}; I, m_I\rangle$	Transition 2 $\lvert J, m_J; I, m_I\rangle \rightarrow \lvert J', m_{J'}; I, m_I\rangle$	Freq. difference $\Delta E_{1\leftrightarrow 2}$
π	$\lvert 1/2, 1/2; 3/2, 3/2\rangle \rightarrow \lvert 3/2, 1/2; 3/2, 3/2\rangle$	$\lvert 1/2, -1/2; 3/2, -3/2\rangle \rightarrow \lvert 3/2, -1/2; 3/2, -3/2\rangle$	$\mu_{\mathrm{B}}(g_{J'} - g_J)B$
	$\lvert 1/2, 1/2; 3/2, 1/2\rangle \rightarrow \lvert 3/2, 1/2; 3/2, 1/2\rangle$	$\lvert 1/2, -1/2; 3/2, -1/2\rangle \rightarrow \lvert 3/2, -1/2; 3/2, -1/2\rangle$	
	$\lvert 1/2, 1/2; 3/2, -1/2\rangle \rightarrow \lvert 3/2, 1/2; 3/2, -1/2\rangle$	$\lvert 1/2, -1/2; 3/2, 1/2\rangle \rightarrow \lvert 3/2, -1/2; 3/2, 1/2\rangle$	
	$\lvert 1/2, 1/2; 3/2, -3/2\rangle \rightarrow \lvert 3/2, 1/2; 3/2, -3/2\rangle$	$\lvert 1/2, -1/2; 3/2, 3/2\rangle \rightarrow \lvert 3/2, -1/2; 3/2, 3/2\rangle$	
σ^+	$\lvert 1/2, 1/2; 3/2, 1/2\rangle \rightarrow \lvert 3/2, 3/2; 3/2, 1/2\rangle$	$\lvert 1/2, -1/2; 3/2, 3/2\rangle \rightarrow \lvert 3/2, 1/2; 3/2, 3/2\rangle$	$\mu_{\mathrm{B}}(g_{J'} - g_J)B - A_{\mathrm{HF}}$
	$\lvert 1/2, 1/2; 3/2, -1/2\rangle \rightarrow \lvert 3/2, 3/2; 3/2, -1/2\rangle$	$\lvert 1/2, -1/2; 3/2, -3/2\rangle \rightarrow \lvert 3/2, 1/2; 3/2, -3/2\rangle$	$\mu_{\mathrm{B}}(g_{J'} - g_J)B + A_{\mathrm{HF}}$
σ^-	$\lvert 1/2, 1/2; 3/2, 3/2\rangle \rightarrow \lvert 3/2, -1/2; 3/2, 3/2\rangle$	$\lvert 1/2, -1/2; 3/2, 1/2\rangle \rightarrow \lvert 3/2, -3/2; 3/2, 1/2\rangle$	$\mu_{\mathrm{B}}(g_{J'} - g_J)B - A_{\mathrm{HF}}$
	$\lvert 1/2, 1/2; 3/2, -3/2\rangle \rightarrow \lvert 3/2, -1/2; 3/2, -3/2\rangle$	$\lvert 1/2, -1/2; 3/2, -1/2\rangle \rightarrow \lvert 3/2, -3/2; 3/2, -1/2\rangle$	$\mu_{\mathrm{B}}(g_{J'} - g_J)B + A_{\mathrm{HF}}$

Table 5.2: Expressions for the frequency difference of pairs of two π, $\sigma^{\pm}$ transitions in the hyperfine Paschen-Back regime for ^{87}Rb. The transitions shown were selected in order to reduce the number of terms containing excited state constants $(g_{J'}, A'_{\mathrm{HF}}, B'_{\mathrm{HF}})$, which can contribute to an increased uncertainty in measurements made.

Transition 1 $\lvert J, m_J; I, m_I\rangle \rightarrow \lvert J', m_{J'}; I, m_I\rangle$	**Transition 2** $\lvert J, m_J; I, m_I\rangle \rightarrow \lvert J', m_{J'}; I, m_I\rangle$	**Freq. difference** $\Delta E_{1\leftrightarrow 2}$
$\lvert 1/2, 1/2; 3/2, 3/2\rangle \rightarrow \lvert 3/2, 1/2; 3/2, 3/2\rangle$	$\lvert 1/2, -1/2; 3/2, 3/2\rangle \rightarrow \lvert 3/2, 1/2; 3/2, 3/2\rangle$	$\mu_B g_J B + m_I A_{HF}$
$\lvert 1/2, 1/2; 3/2, 1/2\rangle \rightarrow \lvert 3/2, 1/2; 3/2, 1/2\rangle$	$\lvert 1/2, -1/2; 3/2, 1/2\rangle \rightarrow \lvert 3/2, 1/2; 3/2, 1/2\rangle$	
$\lvert 1/2, 1/2; 3/2, -1/2\rangle \rightarrow \lvert 3/2, 1/2; 3/2, -1/2\rangle$	$\lvert 1/2, -1/2; 3/2, -1/2\rangle \rightarrow \lvert 3/2, 1/2; 3/2, -1/2\rangle$	
$\lvert 1/2, 1/2; 3/2, -3/2\rangle \rightarrow \lvert 3/2, 1/2; 3/2, -3/2\rangle$	$\lvert 1/2, -1/2; 3/2, -3/2\rangle \rightarrow \lvert 3/2, 1/2; 3/2, -3/2\rangle$	
$\lvert 1/2, 1/2; 3/2, 1/2\rangle \rightarrow \lvert 3/2, 1/2; 3/2, 1/2\rangle$	$\lvert 1/2, -1/2; 3/2, -3/2\rangle \rightarrow \lvert 3/2, 1/2; 3/2, -3/2\rangle$	$\mu_B g_J B - A_{HF}$
$\lvert 1/2, 1/2; 3/2, -3/2\rangle \rightarrow \lvert 3/2, 1/2; 3/2, -3/2\rangle$	$\lvert 1/2, -1/2; 3/2, 1/2\rangle \rightarrow \lvert 3/2, 1/2; 3/2, 1/2\rangle$	$\mu_B g_J B + A_{HF}$
$\lvert 1/2, -1/2; 3/2, 3/2\rangle \rightarrow \lvert 3/2, -1/2; 3/2, 3/2\rangle$	$\lvert 1/2, 1/2; 3/2, 3/2\rangle \rightarrow \lvert 3/2, -1/2; 3/2, 3/2\rangle$	$-(\mu_B g_J B + m_I A_{HF})$
$\lvert 1/2, -1/2; 3/2, 1/2\rangle \rightarrow \lvert 3/2, -1/2; 3/2, 1/2\rangle$	$\lvert 1/2, -1/2; 3/2, 1/2\rangle \rightarrow \lvert 3/2, -1/2; 3/2, 1/2\rangle$	
$\lvert 1/2 - 1/2; 3/2, -1/2\rangle \rightarrow \lvert 3/2 - 1/2; 3/2, -1/2\rangle$	$\lvert 1/2, -1/2; 3/2, -1/2\rangle \rightarrow \lvert 3/2, -1/2; 3/2, -1/2\rangle$	
$\lvert 1/2, -1/2; 3/2, -3/2\rangle \rightarrow \lvert 3/2 - 1/2; 3/2, -3/2\rangle$	$\lvert 1/2, -1/2; 3/2, -3/2\rangle \rightarrow \lvert 3/2, -1/2; 3/2, -3/2\rangle$	
$\lvert 1/2, -1/2; 3/2, -1/2\rangle \rightarrow \lvert 3/2, 1/2; 3/2, -1/2\rangle$	$\lvert 1/2, -1/2; 3/2, 3/2\rangle \rightarrow \lvert 3/2, 1/2; 3/2, 3/2\rangle$	$-(\mu_B g_J B + A_{HF})$
$\lvert 1/2, -1/2; 3/2, 3/2\rangle \rightarrow \lvert 3/2, 1/2; 3/2, 3/2\rangle$	$\lvert 1/2, -1/2; 3/2, -1/2\rangle \rightarrow \lvert 3/2, 1/2; 3/2, -1/2\rangle$	$-\mu_B g_J B + A_{HF}$

Table 5.3: Expressions for the frequency difference of pairs of one π and one $\sigma^{\pm}$ transition in the hyperfine Paschen-Back regime for ^{87}Rb. The transitions shown were selected in order to eliminate terms containing excited state constants ($g_{J'}, A'_{HF}, B'_{HF}$), which can contribute to an increased uncertainty in measurements made. The colour of each cell indicates the type of transition: green for π, blue for σ^+ and purple for σ^-.

$<$ 2 MHz linewidth was scanned over a mode-hop-free range of hundreds of GHz around the rubidium D2 line ($\sim$ 780 nm). This was the same laser used in the experiments carried out in chapter 4. In order to avoid optical pumping effects, a beam power of ~ 1 μW was used to remain in the weak-probe regime [51] while probing a volume of atoms that is roughly cylindrical, with a length of 1 mm and radius equal to the maximum beam waist ($1/e^2$) of 0.7 mm. Prior to entering the experiment vapour cell, the beam passes through a series of polarising elements that help control the beam power and polarisation purity used. For these experiments, linear polarisation at 45° from the horizontal (x-axis) was chosen in order to have access to both π and $\sigma^{\pm}$ transitions to use the scheme described in section 5.2. The total transmission of the beam (S_0; see section 2.1.4) through the atomic medium was measured using a single photodiode. However, it is worth noting that the absorption depth is not critical as all that is necessary is for the two selected features, corresponding to the transitions discussed in section 5.2, to be clearly resolved in order for their centre frequency to be determined. As such, the polarisation can be varied and is not a critical factor in this experiment.

5.3.2 Results

Optical magnetometry using a thermal vapour of ^{87}Rb atoms

As context for understanding the results obtained from our experiments, figure 5.2 shows the expected absorption spectrum as a function of linear detuning at a field strength of 1.5 T, along with the evolution of the atomic energy levels up to this value. These numerical results are obtained by using the theory presented in chapter 2 and sections 2.4 and 5.2. The atomic system used is a thermal atomic vapour, $T = 100$°C, of ^{87}Rb in the Voigt geometry. Coloured lines serve to highlight the position of the atomic transitions of interest for measuring the field strength. The corresponding coloured arrows in the bottom half of the figure indicate the initial and final states involved in the transitions.

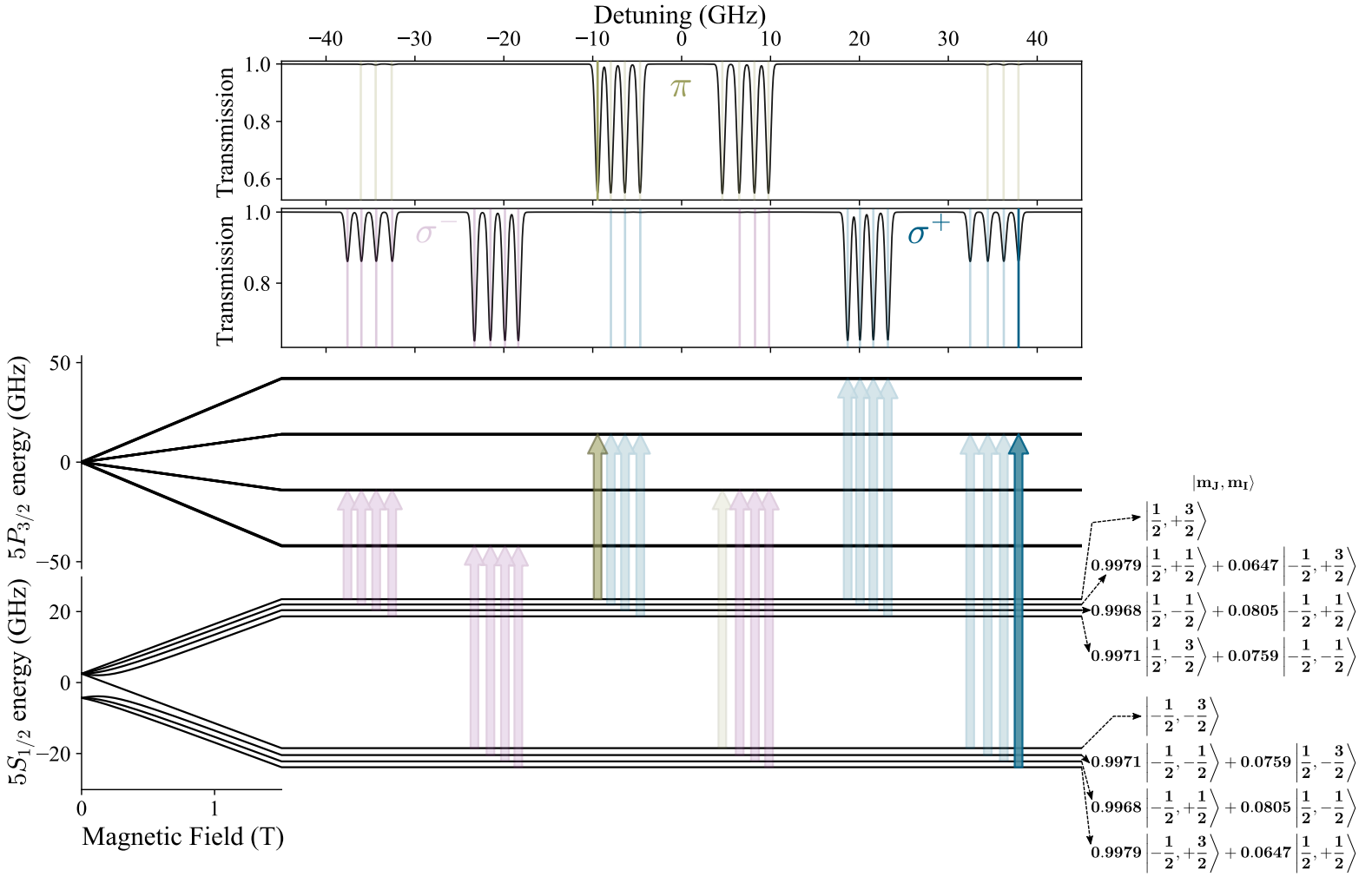

Figure 5.2: Diagram of the energy levels and selected transitions on the ^{87}Rb D2 line for measurement of the magnetic field strength B; the evolution of the energy levels, as well as the spectra in the top panels, have been calculated for demonstrative purposes at $B = 1.5$ T. The top panels show the absorption spectra for π (top) and $\sigma^{\pm}$ (bottom) transitions. Measuring the frequency difference between the two transitions allows for an expression that determines B without any excited state constants to be derived (see equation 5.10).

The transitions highlighted in figure 5.2 correspond to those used in writing equation 5.10. In the conditions used for calculating the spectra, the atomic system is operating in the hyperfine Paschen-Back regime; this allows for all of the absorption features to be clearly resolved despite the Doppler broadening ($\Gamma_{\text{Doppler}}/2\pi \approx 550$ MHz). As such, the scheme for measuring the magnetic field strength, using equation 5.10, experimentally becomes a question of determining the centre of the absorption features. For this we know that the expected lineshape is a Voigt profile (see section 2.1.3); we use the implementation of this function, as given by its relation to the Fadeeva function, in the `lmfit` Python package [149, 150] to fit the experimental data using tailor-made code for this scheme.

A sample of the experimental data acquired with our setup is shown in figure 5.3. The raw signals from the photodiode were processed in order to linearise the laser scan and calibrate the horizontal frequency axis as described in 3.3.2 and appendix B. The data shown (blue circles) have been fit using two approaches: the first consists of simultaneously fitting the chosen pair of transitions with a single expression (purple curve), while the second fits each of the transitions with an independent expression, albeit with the same lineshape widths, which are subsequently added together (red curve). Both of these approaches fit the transition of interest as well as adjacent transitions in the same multiplet in order to take into account possible effects due to the overlap of lineshapes. The residuals from both of these fits are shown in the bottom panel of figure 5.3. It is worth noting that the error bars in the experimental data are too small ($\sim 1 \times 10^{-3}$) to be seen in said figure.

From the fits shown in figure 5.3 we obtain two values for the magnetic field strength B. In both of these, there are only four free parameters for the absorption features of interest: the line centre x_c, Gaussian width Γ_{Gauss}, Lorentzian width Γ_{Lorentz} and amplitude A_0. For the remaining absorption features, both Gaussian and Lorentzian widths are maintained as a common parameter, leaving only the line centre and amplitude as free parameters. The first fit, indicated by the purple curve, returns a value of $B = (1.524 \pm 0.014)$ T. From the residuals we see that there is good agreement between the

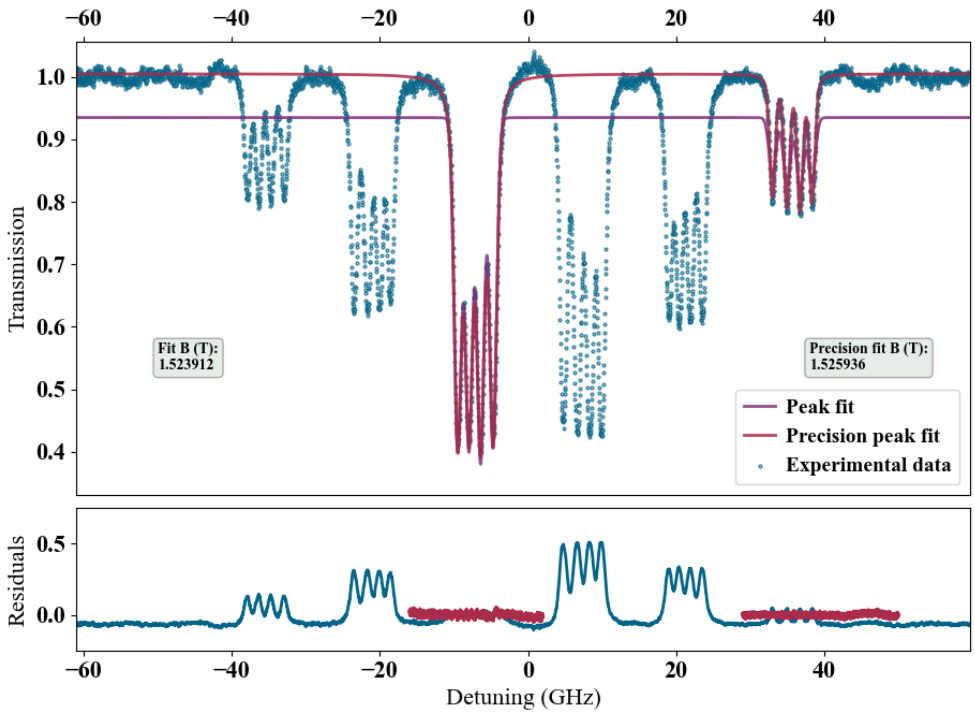

Figure 5.3: Experimental data (blue circles) used for determining the magnetic field strength with our optical magnetometry scheme (equation 5.10). The absorption (S_0) spectrum, taken as a function of linear detuning, is used to obtain the position of the transitions of interest (*i.e.* the π transition at ≈ -10 GHz and the σ^+ transition at ≈ 39 GHz) by fitting Voigt lineshapes; the line centre x_c, amplitude A_0, Gaussian Γ_{Gauss} and Lorentzian Γ_{Lorentz} widths are used as free parameters for the fit. Transitions in the same multiplet as that of the transition of interest are also fitted, using only the respective line centres and amplitudes as free parameters now, in order to take any effects of lineshape overlap in the multiplet into account. A fit using a common expression for *both* chosen transitions and their adjacent transitions (purple curve), as well as one using a separate expression for each multiplet and then adding both (red curve), are shown, together with their respective residuals in the bottom panel. From these fits we obtain values of $B = (1.5239 \pm 0.0142)$ and $B = (1.5259 \pm 0.0002)$ T, respectively. We note that the agreement between the data and the red curve is excellent [155], with an RMS error of $\sim 1\%$ in the regions of interest and no visible structure in the residuals.

experimental data and the fit of the lineshapes in the region of interest, yet there is little agreement in the surrounding regions. On the other hand, the second fit, indicated in the figure by the red curve, has much better agreement in the region of interest and in the immediate surroundings. We obtain a value of $B = (1.5259 \pm 0.0002)$ T from this fit which, together with the lack of any clear structure in the residuals, allows us to claim excellent agreement between the experiment and lineshape fit [155].

The precision in the measurement of B can be increased if we take advantage of the presence of all of the 'strong' $\pi, \sigma^{\pm}$ transitions to use the expressions in table 5.3. In practice, this means we have to determine the position of the absorption features for an additional 11 pairs of transitions: 4 for each m_I projection in each of the $m_J = \pm 1/2$ states, with the additional four corresponding to pairs that use different values of m_I for each transition in the pair to remove the dependency on this parameter (see table 5.3). This is readily done by virtue of the fits being carried out; a single fit allows for the necessary information of 6 pairs of transitions, coming from two distinct multiplets, to be used for calculating B. As such, only two fits of the experimental data need to be carried out for the full 12 pairs to be available. The results of this for a single experimental run, consisting of 70 spectra taken under similar conditions, is shown in figure 5.4.

The value of B obtained from each pair of transitions for each spectra in the run are indicated by the red crosses in figure 5.4; the average of the values corresponding to pairs of π, σ^+ transitions are indicated by blue circles, while those corresponding to π, σ^- pairs are indicated by the blue squares. Their respective averages are indicated by the dotted and broken purple lines. The average of *all* values is indicated by the black broken line. The coloured bands (purple for the averages of just $\pi, \sigma^+/\pi, \sigma^-$ pairs; blue for average of all values) represent one standard deviation of uncertainty from the average value. Also shown in the side panel are the histograms for the individual measurements of the field strength (red) and the average field strength value for each spectrum (blue). From this it can be clearly seen that the precision of our measurement increases, approximately by a factor of 2, by taking all

12 pairs of transitions into account.

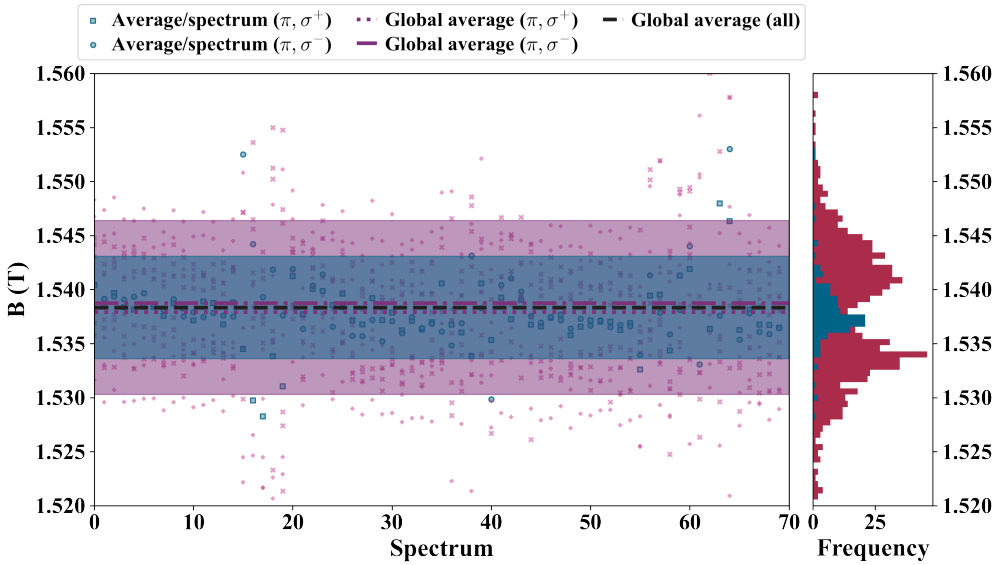

Figure 5.4: Values of the experimental field strength B obtained from the optical magnetometry scheme presented in section 5.2 and summarised in table 5.3. Spectra from a single experimental run were processed in order to obtain the position of the transitions in each pair necessary to determine the field strength (red crosses); for the 6 pairs of $\pi, \sigma^+(\pi, \sigma^-)$ transitions in each spectrum, the average value of B is taken and shown as a blue square (blue circle). On the right of the figure, histograms showing the previously mentioned values are constructed. The average value of all the π, σ^+ and π, σ^- transitions pairs, $B = (1.538 \pm 0.008)$ T and $B = (1.539 \pm 0.008)$ T, are shown by the purple broken and dotted lines, respectively. For these, one standard deviation of uncertainty is given, as shown by the purple coloured band. The average of *all* of the experimentally obtained values $B = (1.538 \pm 0.004)$ T is given by the black broken line, along with an uncertainty of one standard deviation represented by the blue coloured band.

Uncertainty budget for measurements of field strength using optical magnetometry scheme

In the results presented in figures 5.3 and 5.4 it is clear that the optical magnetometry scheme proposed allows for the magnetic field strength B to be determined with very good precision. Compared to the results obtained by fitting a spectrum with the theoretical model provided in *ElecSus* (see

section 4.3.2), the values obtained with our scheme (*e.g.* $B = (1.5239 \pm 0.0142), (1.5259 \pm 0.0002)$ T) are within the experimental error bars of those obtained with *ElecSus* ($B = (1.52 \pm 0.08)$ T; see figure 4.5). Furthermore, the values for B obtained from the magnetometry scheme have a smaller uncertainty than those determined by fitting the spectrum with *ElecSus*. This can be accounted for from the expressions used to determine B, given in table 5.3: as only ground state and fundamental constants are used (g_J, A_{HF} and μ_{B}, respectively), the precision of this scheme is limited by the precision in the determination of the frequency of each of the atomic transitions selected. In addition to this, the lack of need for an absolute frequency reference, as the quantity of interest is a frequency difference, also allows for a reduced impact from systematic effects on the uncertainty of our measurements.

Taking equation 5.10 as an example, we can see our uncertainty in the determination of B is given by five quantities. Of these, three quantities correspond to physical constants that are known to excellent precision (>100 p.p.b; 10^{-7} relative uncertainty): μ_{B} (30 p.p.b) [182, 183], g_J and A_{HF} (100 p.p.b & 1×10^{-5} p.p.b, respectively) [119, 141]. The remaining two quantities, ΔE_{π} and ΔE_{σ^+}, can be combined into a single parameter ($\Delta E_{\sigma^+ \leftrightarrow \pi} \equiv \Delta E_{\sigma^+} - \Delta E_{\pi}$) whose uncertainty only depends on the sum of the uncertainties of each quantity (obtained from fits to the experimental data as the standard error), omitting other systematic uncertainties (*e.g.* systematic errors in the frequency axis) by design [155]. This parameter is the only one experimentally determined and, as such, will contribute the greatest to the uncertainty in our measurement of B. The uncertainty budget obtained from this example of our scheme is presented in table 5.4. From this we find that with our current setup, the precision in our measurement of the field strength is limited to ~ 50 mT, corresponding to a relative uncertainty of $\approx 3.5 \times 10^{-2}$.

Bi-modal distribution of field strengths

We now proceed to further discussion of the results presented in figure 5.4, namely, the histograms for the distribution of values for B obtained using our

Quantity (units)	**Value**	**Uncertainty**	**Relative uncertainty**
Bohr magneton μ_{B} (Hz/T)	13,996,244,936.1	4.2	3×10^{-10}
^{87}Rb ground state g_J (a.u.)	2.00233113	2×10^{-7}	1×10^{-7}
^{87}Rb ground state hyperfine constant A_{HF} (Hz/2π)	3,417,341,305.452145	4.5×10^{-8}	1×10^{-14}
Frequency difference between transitions $\Delta E_{\sigma^+ \leftrightarrow \pi}$ (Hz)	$48,026 \times 10^6$	3.4×10^6	7.2×10^{-5}
Calibration error over frequency interval $\sigma_{\Delta E_{\sigma^+ \leftrightarrow \pi}}$ (Hz)	$1,681 \times 10^6$	1.2×10^5	3.5×10^{-2}
Magnetic field strength B (T)	1.531	5.4×10^{-2}	3.5×10^{-2}

Table 5.4: Uncertainty budget for the determination of the magnetic field strength using the optical magnetometry scheme (equation 5.10). The quantities involved in the calculation of the value for B, along with their values, uncertainties and relative uncertainties, are shown. At the bottom, the calculated value of B and its uncertainty is shown. Data for μ_{B}, g_J and A_{HF} are taken from [182, 183], [119] and [141], respectively. The value of $\Delta E_{\sigma^+ \leftrightarrow \pi}$ is taken from one of the spectra in the experimental run previously presented. We note that in this case, the precision in our measurement of B is limited by the calibration error associated with our determination of the frequency difference $\Delta E_{\sigma^+ \leftrightarrow \pi}$, which in this case is of the order of ~ 1.6 GHz ($\sim 3.5 \times 10^{-2}$ relative uncertainty).

optical magnetometry scheme. In particular, we highlight the presence of two modes in the distribution of the values obtained from our experimental data. These are located at approximately $B = (1.534 \pm 0.004)$ T and $B = (1.542 \pm 0.003)$ T. The difference between these two values corresponds to a frequency difference of (112 ± 70) MHz. The appearance of such a feature is not expected from the expressions given in table 5.3 and it is thus necessary to look in more detail at the nature of this bi-modal distribution.

Figures 5.5 and 5.6 show a breakdown of the histogram in terms of the values of B determined using π, σ^+ transitions and π, σ^- transitions, respectively. The top two panels of the figures once again present histograms of the values obtained yet now they are broken down by the m_I values used in each transition. The upper (lower) of these two panels in figure 5.5 (5.6) corresponds to the expressions from table 5.3 that use the pair of transitions with *different* m_I values, while the lower (upper) panel shows four histograms corresponding to the different m_I values used in the expression with m_I dependence from the same table. The bottom-most panel of both figures shows the relation between frequency difference of the transition pair and the magnetic field strength, with the experimental values plotted for reference.

Both figures clearly show that the bi-modal distribution can be broken down by considering $m_I = \pm 3/2$ and $m_I = \pm 1/2$ values. For the transition pairs that use different m_I values for each of the transitions, the histogram resulting from the values of B determined with these pairs once again show the presence of two distinct modes.

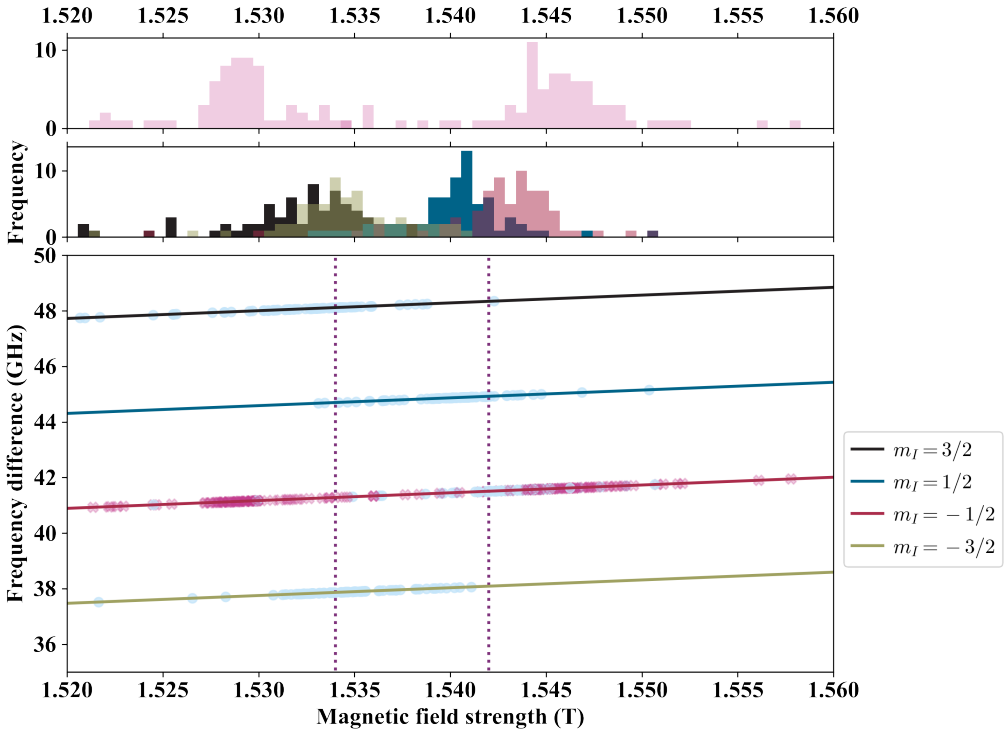

Figure 5.5: Breakdown of bi-modal histogram for the values of B determined using π, σ^+ transitions for the optical magnetometry scheme. The two upper panels show the breakdown of the histogram into two: the top panel corresponds to the m_I-indepedent expression in table 5.3 and the bottom panel corresponds to the first expression in table 5.3, coloured according to the m_I value used ($m_I = 3/2$ (black), $1/2$ (blue), $-1/2$ (red), $-3/2$ (green)). The bottom panel of the figure shows the relation between frequency difference and field strength, as given by the expressions in table 5.3, as a function of m_I value (light blue circles; red crosses correspond to pairs with different m_I values). It can be observed that the two modes in the distribution of values appear to correspond to those determined from $m_I = \pm 3/2$ and $m_I = \pm 1/2$ projections of the nuclear angular momentum.

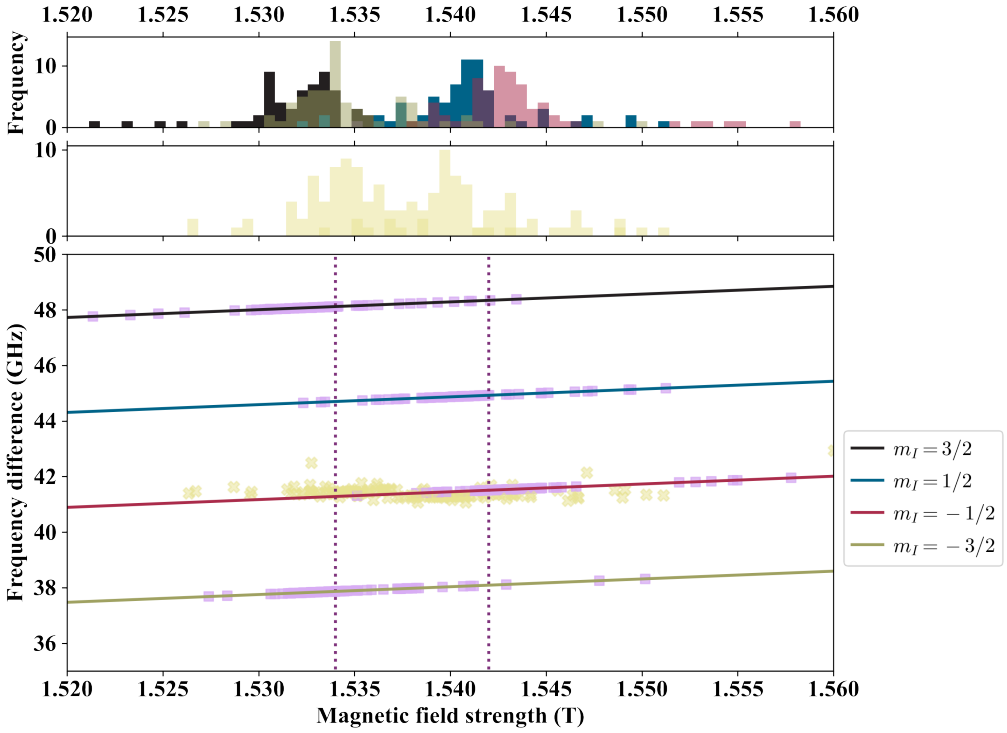

Figure 5.6: Breakdown of bi-modal histogram for the values of B determined using π, σ^- transitions for the optical magnetometry scheme. The two upper panels show the breakdown of the histogram into two: the top panel corresponds to the m_I-independent expression in table 5.3 and the bottom panel corresponds to the first expression in table 5.3, coloured according to the m_I value used ($m_I = 3/2$ (black), $1/2$ (blue), $-1/2$ (red), $-3/2$ (green)). The bottom panel of the figure shows the relation between frequency difference and field strength, as given by the expressions in table 5.3, as a function of m_I value (light purple squares; yellow crosses correspond to pairs with different m_I values). It can be observed that the two modes in the distribution of values appear to correspond to those determined from $m_I = \pm 3/2$ and $m_I = \pm 1/2$ projections of the nuclear angular momentum.

Origin of the bi-modal distribution of field strengths

We now proceed to discuss possible mechanisms that could give rise to the bi-modal distribution seen in figure 5.4.

1. Lineshape overlap The way in which the positions of the transitions are determined allows us to discard effects of lineshape overlap in the generation of the bi-modal distribution.

2. Diamagnetism & quadratic Zeeman shifts Similarly, we can rule out diamagnetic/second-order terms in the Zeeman effect as other work at higher fields (58 T) found no significant evidence of these effects [81]: as we are working at a field strength of ~ 1.5 T, the expected contribution of these effects is several orders of magnitude smaller (~ 0.39 MHz/T^2; 1.3 GHz at 58 T vs. ~ 880 kHz at 1.5 T).

3. Excited-state Landé factor Another possible origin for the two modes in the distribution of the determined values for B is the value used for the excited state $g_{J'}$ factor. In this work we use the value obtained from the Russel-Saunders coupling of the orbital and spin angular momenta [85, 117, 129] of $g_{J'} = 1.3341$. Recent work [81] has given a more precise experimental determination of this value, $g_{J'} = (1.33494 \pm 0.00015)$. The difference between these two values generates a shift of 17.63 MHz/T in the energies of the excited state, as given by equation 5.3; this shift is also translated to a shift in the position of the transitions by virtue of equation 5.6. However, as our proposed scheme does not rely directly on this factor (see equation 5.10), this can be discarded.

4. Frequency calibration and non-linearity The remaining possibility for generating the bi-modal distribution in figure 5.4 is the frequency calibration of our spectra, which is also the limiting factor in the precision of our measurements (see table 5.4). As discussed in section 3.3.2 and appendix B, the raw data is taken and processed in order to remove the non-linearity from our laser scan and calibrate the horizontal axis in terms of the frequency

of this scan. We would expect that this process would result in spectra where adjacent points on the frequency axis showed a linear relation between themselves, with the ideal being simply a constant difference between the two points. The results presented in chapter 4 show that this is for the most part true as we can obtain a very good agreement between our theoretical model and the experimental data. Nevertheless, we are aware that our experimental setup is prone to a large non-linearity in the scan of the laser, as well as errors in our calibration process (see figures 5.7 and 5.8), which is further evidenced in the context of the magnetometry scheme proposed.

Taking the spectrum shown in figure 5.3, we can evaluate the impact of the frequency calibration and linearisation on our optical magnetometry scheme. As a reference, figure 5.9 shows the experimental data plotted along with a theoretical spectrum generated with the model and values obtained in chapter 4. The difference between these two curves shown in the plot is consistent with a very good agreement with our model [155], yet one can also observe the presence of dispersion-like structures in the residuals in the areas close to resonance. These structures clearly indicate a shift along the frequency axis of the absorption features, with this being particularly evident towards the edges of the spectrum more so than near the centre. As mentioned above, we would expect for the separation along the frequency axis of adjacent points to be linear such that there is no particular region of the spectrum being shifted more than the other. We thus proceed with looking at the difference in frequency between adjacent points of our experimental data. The resulting plot is shown in figure 5.10.

Figure 5.10 clearly shows that there is a non-linearity in the intervals between adjacent points in our spectra as a result of our initial linearisation and calibration. We can see that this non-linearity is largest in the difference between adjacent points towards the edges of the spectrum and is approximately linear near the centre; we can possibly attribute this to a greater gradient (and value) of the deviation of original scan from a linear case (see figure 5.7), which in turn results in a lower sensitivity to the corrections applied. Together with the structures observed in the residuals of figure 5.9,

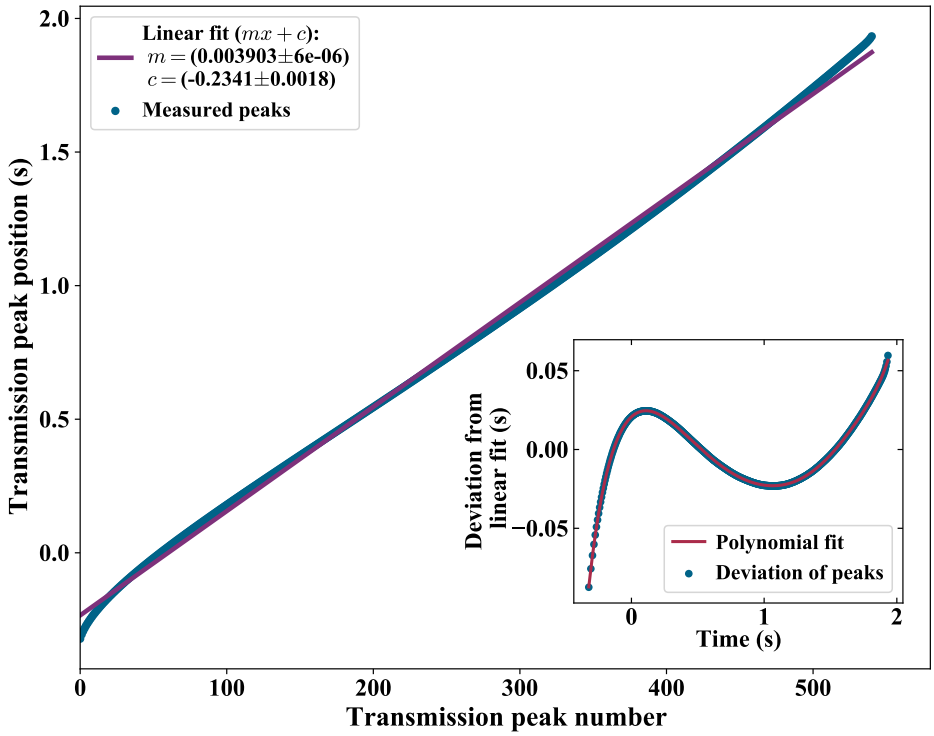

Figure 5.7: Deviation from linear fit of etalon peak positions as a function of peak number for the etalon used to calibrate the spectrum shown in figure 5.3. The calibration process has been discussed in detail previously in section 3.3.2. The etalon can be characterised by its free spectral range (FSR), which we assume to be constant over the range of the laser scan. As such, a linear relation (purple curve) can be calculated as a function of the number of peaks and their positions in time. By comparing the measured positions of these transmission peaks to their expected positions, given by the aforementioned linear relation, we obtain the deviation for each peak, as shown in the inset of the figure. These points are then fit using a high-order (≥ 10) polynomial (red curve) in order to obtain a correction factor to linearise the horizontal axis and later allow the conversion from time to frequency.

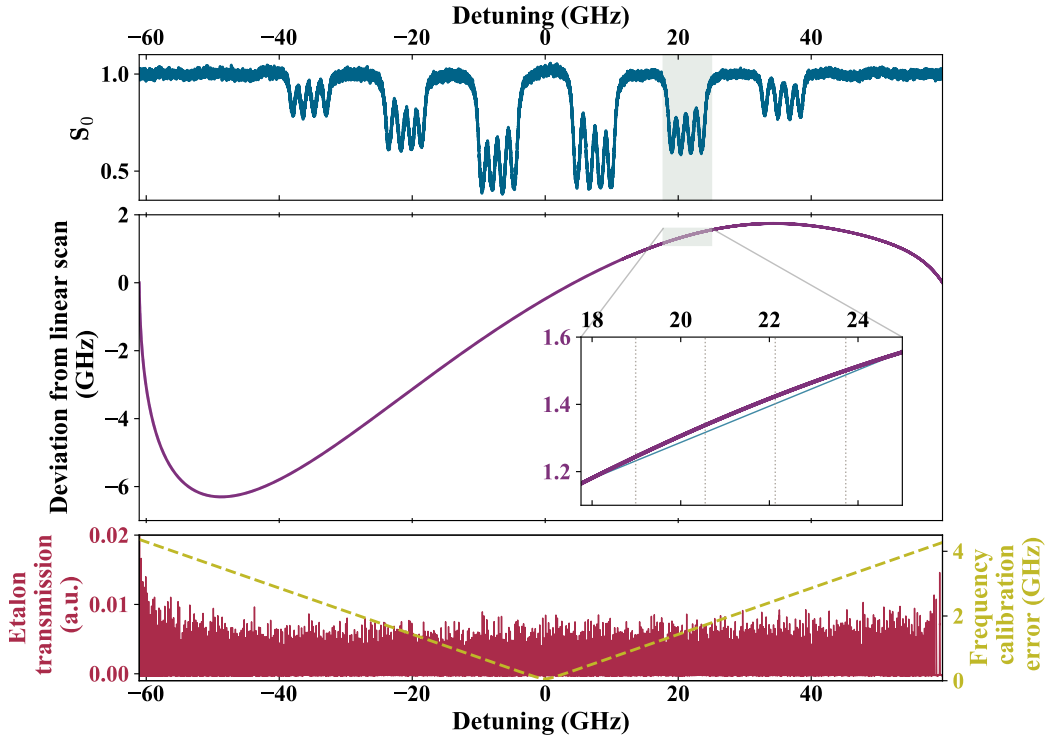

Figure 5.8: Deviation of experimental frequency scan from the ideal case with points on the frequency axis equally spaced, for the data shown in figure 5.3. As has been previously discussed (see section 3.3.2), the process of calibrating raw experimental signals involves the removal of background non-linearity using a high-order (≥ 10) polynomial, followed by a linear conversion of time to frequency with factors obtained from fitting the absorption in a natural abundance, room temperature Rb reference cell. The top panel shows the absorption (S_0) spectrum (blue curve) from our experimental cell, while the bottom panel shows the linearised and calibrated etalon transmission (red curve) acquired simultaneously. The bottom panel also shows the error in the calibration of the frequency axis (yellow broken curve) over the frequency scan. In the centre panel, the difference between the experimental frequency of the data points and that of an ideal frequency scan (purple curve), consisting of the same number of equally-spaced points along a scan with the experimental frequency end-points (*i.e.* the minimum and maximum detuning values), is shown. From these curves it is evident that the process of linearisation and calibration of the experimental signals causes the points on the frequency axis to be re-distributed in a non-linear manner. The inset in the centre panel shows how locally (in this case, in the detuning range corresponding to the absorption features highlighted in the top panel and whose theoretical positions are shown as broken vertical lines) this non-linearity can result in shifts of several MHz in the measured positions of local features, as well as a variation of this shift as a function of detuning.

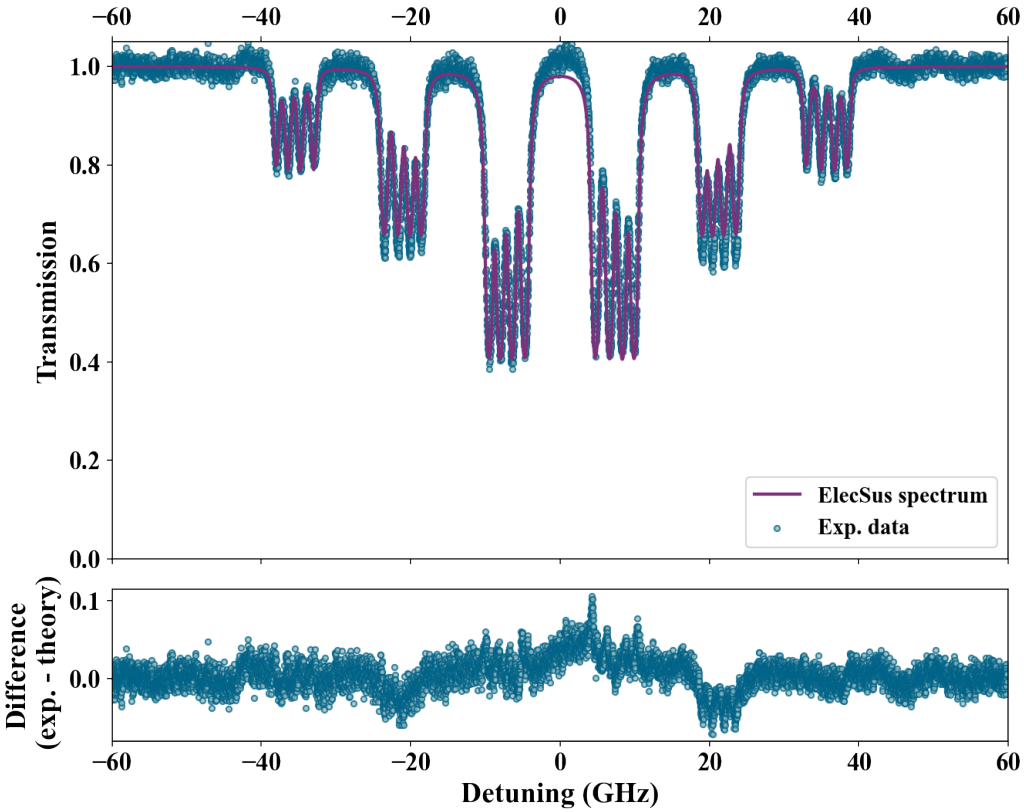

Figure 5.9: Experimental data (blue points) and theoretical spectrum (purple curve) generated for $B = (1.52 \pm 0.08)$ T. The model used for generating the theoretical spectrum, as well as the value for field strength, are those used in chapter 4. In the bottom panel, the difference between the experimental data and the model curve are shown. This is done in order to observe the presence of small dispersion-like features in the regions close to resonance. These are due to a small shift in the positions of the experimental absorption features in relation to their calculated positions. This shift could affect the precision of our magnetometry scheme by causing a change in the frequency differences measured.

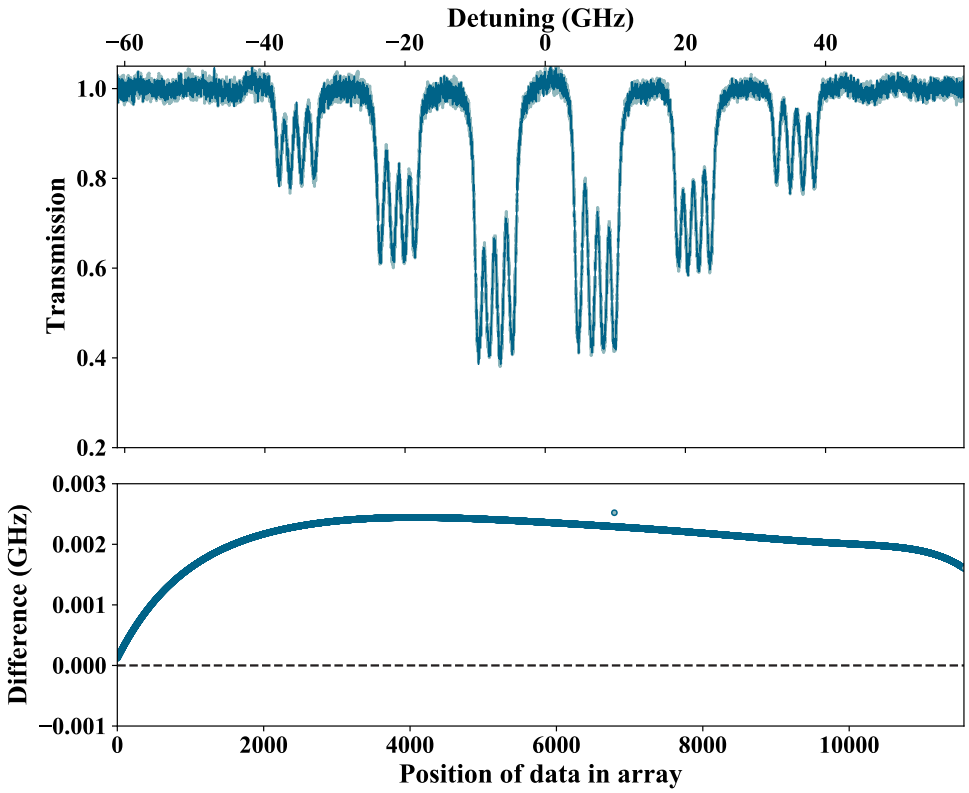

Figure 5.10: Effects of the scan non-linearity in the frequency difference between adjacent points of the experimental data used to test our optical magnetometry scheme. Raw data is processed according to the method described in section 3.3.2 and appendix B, which remove the majority of the non-linearity inherent in the laser scan used to obtain the spectrum shown; this would ideally result in a spectrum where the points on the frequency axis follow a linear relation that is at best a constant offset. However, looking at the difference in frequency between adjacent data points shows there is a non-linear variation in the interval between points across the spectrum. In particular we can observe how at the centre of the spectrum the variation is approximately linear, while towards the edges of the spectrum there is a clear curve describing the variation. Together with the shifts seen in the difference between our data and a theoretical model of the spectrum (figure 5.9), this non-linearity could be the underlying reason for the presence of two modes in the distribution of calculated values for B obtained with our optical magnetometry scheme (see figure 5.4).

this provides some initial support for the idea that it is this non-linearity that may be responsible for the bi-modal distribution seen in our results. At this point it is natural to try and quantify the effect this non-linearity could have on our measurements; our method to do so is to consider our experimental data in relation to a theoretical calculation using the global average value for B obtained with our scheme. This plot is shown in the upper panel of figure 5.11, with the corresponding difference between experiment and theory shown in the bottom panel. Once again, it can be clearly observed from the difference between experiment and theory that there are dispersion-like features which are greater in amplitude towards the ends of the spectrum. This can be taken as a result of a greater shift between the features due to the underlying non-linearity that remains in the scan.

From the previous discussion we have seen that the remaining non-linearity in our scan may be the possible cause for the bi-modal distribution in the histogram in figure 5.4. We continue to quantify this claim by carrying out a variation of our magnetometry scheme, namely that used in reference [81]; this modified scheme relies on the measurement of the position of a single σ^+ transition. This transition is chosen as it involves the stretched states in both the ground and excited states ($|m_J = 1/2, m_I = 3/2\rangle$ and $|m_{J'} = 3/2, m_{I'} = 3/2\rangle$, respectively), both of which have an energy shift with a linear dependence on the magnetic field strength B. This allows for analytic expressions for the Zeeman energy shift of these states (valid at any magnetic field [81]) to be used to determine the position of the absorption feature, which in turn is also linearly dependent on B. We proceed to fit Voigt lineshapes to the corresponding transition and its adjacent transitions in the multiplet in order to take into account any systematic effects from the overlap of lineshapes. From said fit we extract the centre of the lineshape for our chosen transition and proceed to calculate the field strength using equation 5.4. The resulting theoretical spectra will then serve as a reference, with the deviation of the experimental absorption features from their expected positions as an indicator of this remaining non-linearity and errors in our calibration procedure.

In this modified magnetometry scheme, we expect our precision to be limited

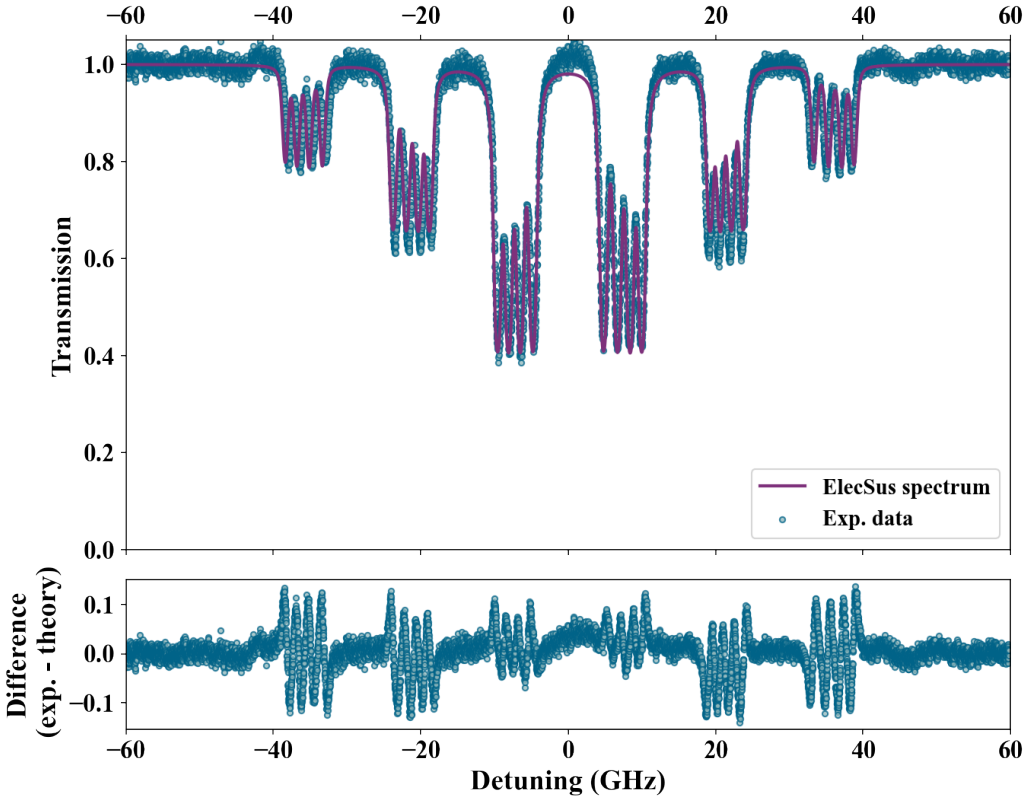

Figure 5.11: Experimental data (blue points) and theoretical spectrum (purple curve) generated at the value of B corresponding to the global mean shown in figure 5.4, $B = (1.538 \pm 0.004)$ T. The model used for generating the theoretical spectrum is that used in chapter 4. In the bottom panel, the difference between the experimental data and the model curve is shown. It can be clearly observed that in this difference there are dispersion-like features in the regions close to the position of the transitions. The origin of these structures is a shift in the positions of the experimental absorption features in relation to the calculated positions. We note that the amplitude of the features is larger towards the edges of the spectrum, in agreement with observations of a remnant non-linearity that is greater towards these areas of the spectrum than at the centre, as well as errors in our frequency calibration process.

by the excited state constants. Work in reference [81] provides a bound of 75 p.p.m. on the precision of B as a result of the uncertainty in the value of the excited state gyromagnetic ratio $g_{J'}$. From implementation of this modified magnetometry scheme we obtain a value of $B = (1.5256 \pm 0.0002)$ T. Taking the errors in our calibration into account, this returns a value of $B = (1.526 \pm 0.053)$ T. The uncertainty in this value is dominated by the precision of our frequency calibration and measurements and the uncertainty in the value of $g_{J'}$. It is worth noting that this value is within the values reported earlier in this section, as well as with the values presented in chapter 4. With this, we proceed to generate a theoretical spectrum in order to once again observe the difference between this and our experimental data. This comparison is shown in figure 5.12. As we have also seen in figure 5.11, the difference shows dispersion-like features that are greater in amplitude towards the ends of the spectrum, with a change in the sign of their slope at ≈ 10 GHz, and which are consistent with us considering the remnant non-linearity and calibration errors as a significant contribution to the distribution of the measurements of B using our scheme.

Using the value of B obtained from a single σ^+ transition we can follow the work presented in reference [81] and provide further support to the idea that the bi-modal distribution is due to a remnant non-linearity and calibration errors in our spectra. In particular, we use this value for the field strength to calculate the position of the adjacent lines to our selected transition in the multiplet. These values are shown in table 5.5, along with their corresponding experimental counterparts and the differences between the two.

From these values we can see that there is a significant shift in the positions of the transitions in the experiment. Furthermore, we can also see effects of the non-linearity in the separations between the transitions. Our calculated values for the positions of the transitions give a separation of ~ 1.58 GHz; these separations, in turn, vary by a constant amount equal to approximately 9 MHz. In contrast to this, our experimentally determined positions for the transitions are separated by a value of (1.5 ± 0.1) GHz. The separations also differ by approximately 100 MHz. Given the error in our calibration of

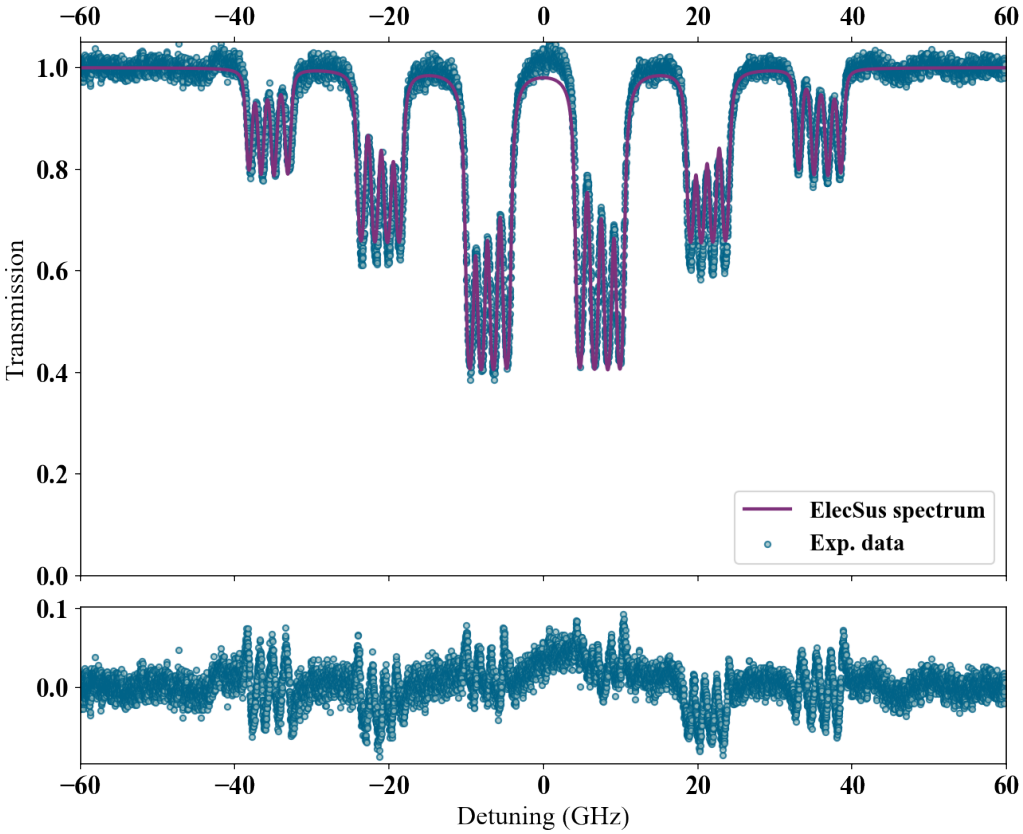

Figure 5.12: Experimental data (blue points) and theoretical spectrum (purple curve) generated at the value of B corresponding to the value determined using a single σ^+ transition, $B = (1.526 \pm 0.53)$ T. The model used for generating the theoretical spectrum is that used in chapter 4, while the value of B is determined using equation 5.4. In the bottom panel, the difference between the experimental data and the model is shown, with clearly visible dispersion-like features. The location of these features in regions close to resonance between the laser frequency and the transitions represents a shift in the position of the experimental absorption features relative to their theoretical positions. We note that the amplitude of the features is larger towards the edges of the spectrum, further supporting the notion that there is a non-linear effect, as well as errors in our calibration, that remains in our spectrum. This in turn could explain the appearance of two distinct modes in the histogram of values of B obtained with our magnetometry scheme (see figure 5.4).

Transition	Calculated position (MHz)	Separation from previous transition (MHz)	Measured position (MHz)	Separation from previous transition (MHz)	Difference between calculated and measured positions (MHz)
$\lvert m_J = {}^1\!/_2, m_I = {}^3\!/_2\rangle \rightarrow \lvert m_{J'} = {}^3\!/_2, m_{I'} = {}^3\!/_2\rangle$	(18983 ± 3)	–	(18983 ± 2)	–	(0 ± 4)
$\lvert m_J = {}^1\!/_2, m_I = {}^1\!/_2\rangle \rightarrow \lvert m_{J'} = {}^3\!/_2, m_{I'} = {}^1\!/_2\rangle$	(20553 ± 3)	(1571 ± 4)	(20397 ± 2)	(1414 ± 4)	(-156 ± 4)
$\lvert m_J = {}^1\!/_2, m_I = {}^{-1}\!/_2\rangle \rightarrow \lvert m_{J'} = {}^3\!/_2, m_{I'} = {}^{-1}\!/_2\rangle$	(22133 ± 3)	(1580 ± 4)	(21912 ± 2)	(1515 ± 4)	(-221 ± 4)
$\lvert m_J = {}^1\!/_2, m_I = {}^{-3}\!/_2\rangle \rightarrow \lvert m_{J'} = {}^3\!/_2, m_{I'} = {}^{-3}\!/_2\rangle$	(23723 ± 3)	(1589 ± 4)	(23546 ± 2)	(1634 ± 4)	(-177 ± 4)

Table 5.5: Values, in MHz, for the calculated and experimental positions for the σ^+ transitions coming from the $m_J = 1/2$ ground state energy levels. Also shown are the separations between the transitions, and the difference between the calculated and experimental positions. The value of B used for the calculations was obtained using equation 5.4 from the experimental position of the $\lvert m_J = {}^1\!/_2, m_I = {}^3\!/_2\rangle \rightarrow \lvert m_{J'} = {}^3\!/_2, m_{I'} = {}^3\!/_2\rangle$ transition in a sample spectrum (figure 5.3); this was then used in equation 5.3 to obtain the calculated positions for the remaining transitions. As such, the measured and calculated values for this particular transition coincide. We observe that the calculated separation between transitions is ~ 1580 MHz, with a variation of ~ 9 MHz between consecutive separations. In comparison, the experimental separation between the transitions varies from ~ 1410 to ~ 1630 MHz, with a larger variation of ~ 100 MHz between them. From this table it is clear that there is a significant discrepancy between the calculated and experimental positions of the transitions, as well as in their separation. Together with the results of previous analyses in this section, this further backs the idea that there is a remnant non-linearity in our spectra. In particular, the shift in the measured positions of the transitions in relation to their expected positions, along with the errors associated to our calibration process (~ 55 MHz), is of the same order of magnitude as the frequency difference between the two modes of the histogram shown in figure 5.4.

$\sim 3.5\%$ over 120 GHz (see bottom panel of figure 5.8), we see that over this frequency interval there is an associated uncertainty of ~ 55 MHz. A visual representation of this is shown in figure 5.13. Recalling the values of the two distinct modes in the histogram shown in figure 5.4 ($B = (1.534 \pm 0.008)$ T and $B = (1.542 \pm 0.007)$ T) we see that this difference in the position of the transitions and in their separations is consistent with the expected frequency difference of ~ 110 MHz. This allows us to be confident in stating that the bi-modal distribution in our histogram of values for B is a result of the combined effects of the non-linearity that remains in our spectra as well as the uncertainties associated to our calibration process.

Improving the precision of measurements made with the optical magnetometry scheme

As has been seen throughout section 5.3.2, the proposed optical magnetometry scheme is limited primarily by the precision in the frequency difference measured. For the results shown with our experimental setup, the precision available in the frequency measurements is a combination of the non-linearity of the laser scan and the frequency calibration, as described in appendix B, and the error in the determination of the line-centres when carrying out the fits. The effect of the latter is more easily reduced, as it involves increasing the resolution in the data acquisition process (*e.g.* increasing the resolution of the oscilloscope). However, there are also ways in which systematic errors coming from the laser scan and frequency calibration can be reduced.

One way of reducing the systematic errors due to the laser scan and frequency calibration could be by making use of commercial wavelength meter to carry out a direct frequency measurement. These are common pieces of equipment in most atomic physics laboratories, and state-of-the-art devices can achieve accurate measurements on the order of MHz [1]. These are often the cheapest option, and offer users a portable and compact solution at the expense of higher precision measurements. In the case of our scheme this however is not

[1] *e.g.* the HighFinesse WS8-2 Wavemeter can achieve 2 MHz accuracy & 200 kHz resolution; https://www.highfinesse.com/en/wavelengthmeter/wavelengthmeter-ws-8-2.html

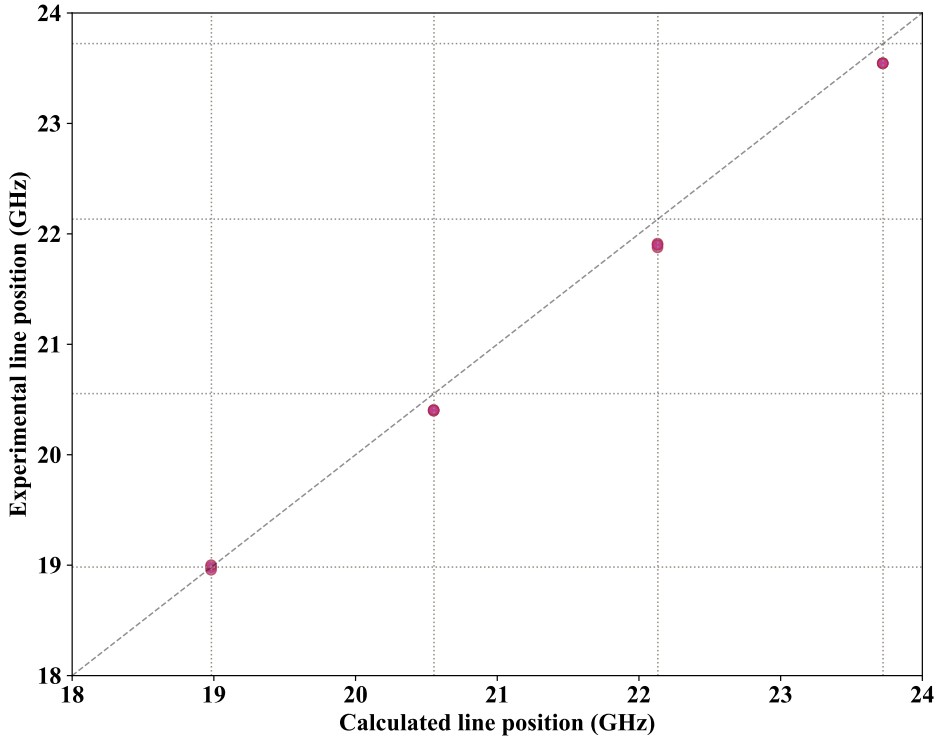

Figure 5.13: Comparison between the calculated and experimental positions for the σ^+ transitions with origin in the $m_J = 1/2$ ground state levels. The values for the calculated and experimental positions, given in table 5.5 for a sample spectrum, are used as the x and y coordinates, respectively, for each of the points shown. The broken diagonal represents the case where the calculated and experimental positions coincide. It can be observed that the first point, corresponding to the position of the σ^+ transition from the $|m_J = 1/2, m_I = 3/2\rangle$ ground-state energy level, falls on this line; this is due to the fact that this transition is used to determine a value for B (equation 5.4) which is then used in our calculation. The dotted lines along both axes correspond to the calculated positions and serve as a guide to the eye to highlight the shift in the experimentally determined position of the transitions. Furthermore, it can be seen that the deviation from the expected values is not constant, which can be attributed to the remnant non-linearity and calibration errors in our spectrum discussed previously.

desirable, as the relative uncertainty in our measurements is of a similar order of magnitude to those of these devices, as seen in table 5.4. Another possibility is the use of an optical frequency comb. This has been an increasingly common option for carrying out precision spectroscopy experiments [184, 185, 186, 187], as these optical frequency combs can provide a frequency reference with relative uncertainties of less than 10^{-11}. However, these systems typically require additional space and specific operating conditions, increasing the complexity of the experimental system; in addition to this, frequency combs are difficult to transport, making *in situ* measurements with this scheme unlikely. As such, alternative options such as the use of electro-optic frequency modulators (EOMs) have been explored, with promising applications to atomic spectroscopy [188, 189, 190, 191]. These devices have the advantage of a relatively small footprint in the experimental setup, as well as providing a means to precisely control the modulation via radio-frequency and microwave electronics.

For the scheme we have proposed, the use of an EOM is a simple and promising addition to the system that could allow greater precision. Following previously reported work with these devices [2, 189, 192], we consider the use of an EOM with a bandwidth of 20 GHz[2]. This would allow for the laser frequency to be kept at a fixed point, with modulation sidebands at ± 20 GHz generated to interrogate the transitions of interest; while not large enough for directly measuring the majority of the frequency differences in our scheme, this would allow effects from the laser scan and frequency calibration to be simultaneously removed. For the larger frequency differences, using the second harmonic of the EOM to allow for additional sidebands (*e.g.* at ± 40 GHz) would give the necessary light to interrogate all the transition pairs here proposed. Use of this system could allow for measurements of the required frequency differences to be made with relative uncertainties of $\sim 10^{-8}$, giving our proposed scheme a greater precision limited in said case by the precision of the ground-state gyromagnetic ratio g_J. More importantly, this method could also avoid the non-linearity inherent to the laser scan and provide a means to obtain more

[2]iXblue Photonics NIR-MPX800-LN-20 https://photonics.ixblue.com/store/lithium-niobate-electro-optic-modulator/phase-modulators

statistical weight for improving the precision our measurements. As the laser would no longer need to be scanned, more spectra could be acquired per second as the limit on the speed of data acquisition would be the bandwidth and response time of the electronics used. A simplified diagram of the experimental implementation of these proposed improvements is shown in figure 5.14.

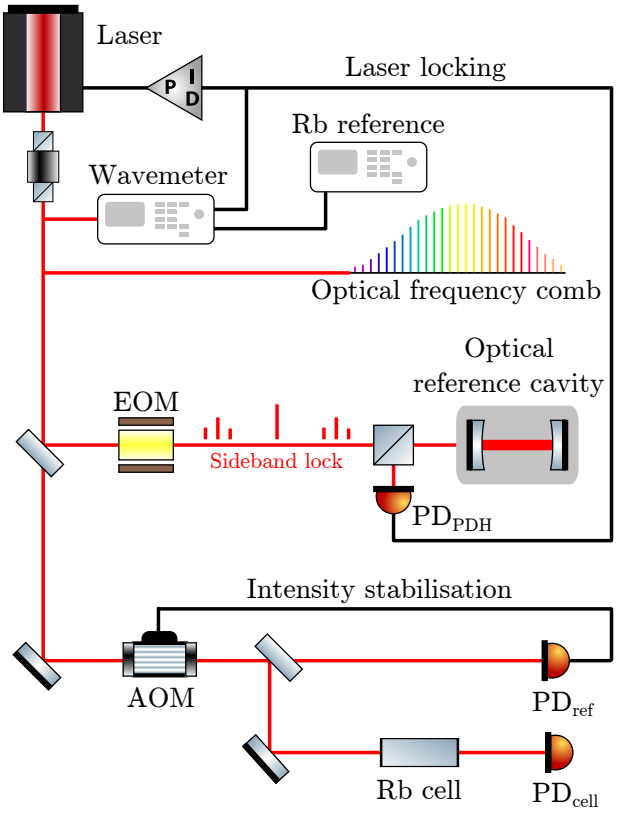

Figure 5.14: Simplified diagram of the optical layout necessary to implement the proposed methods for improving the precision of the frequency measurements in our experiment. In the case of using the commercial wavemeter, the measured wavelength would be processed electronically in order to generate an error signal which could then be fed to a PID circuit to control the emission frequency of the laser throughout the scan; we include here a Rb frequency reference, such as the one in reference [193], in order to improve the long-term accuracy and stability of the wavemeter. In the case of using the optical frequency comb, the laser emission frequency is compared directly to the comb as the former is scanned, allowing for an absolute frequency calibration, as well as an evaluation of the linearity of the frequency scan for later removal. In the case of using the EOM, the laser frequency is kept *fixed*, while the sidebands generated by the EOM are monitored via a Pound-Drever-Hall spectroscopy [194, 195, 196] (PD_{PDH}); the resulting signal would then be fed back to a PID circuit controlling the laser's frequency. In all cases, a small portion of the total output light of the laser is used for the equipment already mentioned while a similar amount is then used to obtain the absorption spectrum from a natural abundance, room temperature Rb reference cell. We include here an additional step to stabilise the power going into this reference cell using an AOM as described in reference [152].

5.4 Summary

This chapter has presented the theory and the experimental validation of an optical magnetometry scheme using a thermal vapour of ^{87}Rb. We have used the Voigt geometry, together with a field strength of ~ 1.5 T, to measure the frequency differences between pairs of transitions in order to increase the precision in the determination of the magnetic field strength. The large field strength, which allows for the atomic system to operate in the hyperfine Paschen-Back regime, along with adequate choice of transitions enables us to have a relative uncertainty of 3.5×10^{-2} in our measurement of B. We find that this uncertainty in our measurement of B is limited primarily by the accuracy and precision in the determination of the frequencies at which the transitions occur due to errors in our calibration: we can envision obtaining a much higher precision in these measurements by using state-of-the-art lasers and stabilisation techniques, or frequency sidebands generated using stable references and electronics, which have been shown to provide precision of over one part in 10^8. Application of this scheme in other alkali-metal atom vapours also allows for access to a wider range of field strengths, thus providing strong support for use of this scheme as an all-optical precision magnetometer for high fields. In the following chapter we will use the concepts treated thus far in this thesis to lay out a proposal for the use of thermal atomic vapours in precision thermometry for the definition of a secondary standard of fundamental constants.

Chapter 6

Towards precision thermometry with a Rb vapour –an all-optical secondary standard for the Boltzmann constant

6.1 Introduction

Throughout the years the need for measuring physical quantities precisely has become a fundamental part of everyday life. From time-keeping [5, 6, 7, 8] to measurements of distance [197] and mass [198, 199], the evolution of technologies and advances in research have allowed society to benefit from unprecedented levels of precision and accuracy. As such, the work of the international metrological community has expanded to include a wider range of areas of research. At the global scale this has lead to the 2019 redefinition of the SI of units by the BIPM [200, 201], which has now given a more precise definition based on constants to all but one of the fundamental quantities.

Under the 2019 redefinition of the SI units, the primary and secondary met-

rological standards used have seen significant changes. No longer are physical objects, such as platinum-iridium rods and weights [199, 202], required for the definition of fundamental units. In their place, fundamental constants –used and measured with extraordinary precision in our time– now serve as the starting point for the definition of units such as the metre, second and kilogram, amongst others [201]. While this allows for greater precision in the units used in common applications, an increasing need for a wider range of accessible and easily-reproducible measurement standards in order to accommodate these changes has become apparent. As the focus in now on maintaining, or in effect increasing, the precision of the measurement of the fundamental constants, the statistical importance of having different methods of measuring these constants ensures the associated units in the SI are kept precisely and accurately defined.

The redefinition of the SI unit of temperature, the Kelvin, in terms of a fundamental constant was a subtler change than that seen for other units [203, 204]. Regardless, this created a large interest in the standards that could now be used to precisely measure temperature and, as a consequence, the associated fundamental constant: Boltzmann's constant k_{B}. From this call for variety in the standards used, several approaches involving atom-based measurements were proposed. In particular, there were several proposals for the use of atomic/molecular spectroscopy [205, 206, 207, 208] to be considered. In these proposals of Doppler-broadened thermometry the spectral lineshape is carefully measured and, by using kinetic theory of gases to describe the velocity distribution of the atoms/molecules, a value for $k_{\mathrm{B}}T$ is extracted. The extensive experience and excellent precision in spectroscopic measurements makes these proposals of interest due to their relative ease of implementation.

The purpose of this chapter is to present work we have done to provide support for the idea of using atomic spectroscopy as a method for precision thermometry. We build upon other metrological applications of atom-based sensors to benefit from the high precision that can be obtained from spectral measurements. This allows us to conceive two variations of an optical ther-

mometry scheme, conceptually different to schemes for Doppler-broadened thermometry. In our first variation, a thermal vapour in the presence of a strong external magnetic field is probed with a resonant laser beam to generate a spectrum: the shifts in energy due to the Zeeman effect will have an effect on the ground-state level populations, which in turn will affect key spectroscopic properties, such as absorption depth, that can be measured with precision in the laboratory. With the other physically-relevant parameters fixed or measured to a high degree of precision, the values measured for the change in absorption and populations allow for the temperature of the vapour to be determined by a well-defined relation. Our second variation relies on observing the effects of a change in the population distribution via the optical rotation generated in the atomic vapour. In this case, the change in population is effectively converted into a shift in the position of a zero-crossing –visible only in the Voigt geometry–, which then allows for the temperature to be determined using precision frequency measurements. As such, our proposed technique for precision thermometry could additionally serve as a secondary standard for the fundamental SI unit of temperature, whereby the measurement of spectral properties or frequencies with readily available equipment allows a relation to be established between these properties and the factor $k_{\mathrm{B}}T$.

6.2 Theory

From the theory presented in chapter 2 we have identified several key physical parameters in the interaction of an atom with light and an external magnetic field. Once the geometry for the system has been fixed and a precise value for the magnetic field strength B has been obtained, the next parameter of significant physical importance is the temperature T of the atoms. At first glance, the importance of this parameter is clear: the temperature of the atoms is related to the mean kinetic energy in the system and consequently to a given velocity distribution which will determine the magnitude of the Doppler effect on the detuning of the light interacting with the atoms and on the broadening of lineshapes (see section 2.1.3). However, the dependence on

temperature of the interactions goes deeper and affects other aspects of the physical system.

We recall from section 2.1.2 that, experimentally, we observe the interaction of an atomic system with external electromagnetic fields via atomic spectroscopy. As such, the role of temperature T appears implicit in several aspects of the atomic spectra that will be studied. In the case of work carried out with a thermal vapour of atoms, T determines the vapour pressure in the vapour cell, in turn allowing greater absorption and signal-to-noise ratio (SNR) in the spectra. Upon closer inspection we can see that temperature, or thermal energy (as given by the factor $k_{\mathrm{B}}T$), is also present in quantities such as the strength of the transition and the atomic number density. For the former of these two quantities, the dependence on temperature is a consequence of another aspect of the atomic system: the statistical-mechanical population distribution of atoms in the ground state. We note that while this aspect is dependent on the thermal energy of the system, it differs from Doppler-broadened thermometry [205, 206] in that it looks at the distribution of *populations* rather than the associated velocity distribution at a given temperature.

Statistical mechanics tells us that for a set of particles with i discrete energy levels we can calculate the population of particles in each of these levels (p_i) by taking into account the average energy of the system. This will be determined by the temperature T of the atoms, and as such can be explicitly written as [209]

$$p_i = \frac{e^{-E_i/k_{\mathrm{B}}T}}{\sum_i e^{-E_i/k_{\mathrm{B}}T}}, \tag{6.1}$$

where E_i is the energy of the i-th discrete level and k_{B} is the Boltzmann constant. For the above expression to be valid we note that the system in question must have reached thermal equilibrium. It is also worth noting that since the dependence on the temperature is inversely proportional in the exponent, for a given fixed energy level E_i there will be less population as T increases; in the limit where $k_{\mathrm{B}}T \ll E_i$ (*i.e.* when the temperature of

the system is low or the energy of the level in question is very large), the population increases up to a maximum value of $p_i = 1$. Furthermore, as we are assuming that all of the atoms in the system are being considered we impose the condition that $\sum_i p_i = 1$, which is implict in equation 6.1 in the form of the normalisation factor in the denominator.

In practice we can easily take into account the populations in the ground-state energy levels of the atomic species being used. From equation 6.1, we see that we can write the energy of the ground state level with respect to the lowest energy of the atomic system. This will be given by solving the Hamiltonian of the system that considers the atom-light as well as the magnetic field interaction, as seen in chapter 2 and section 5.2. At this point, the calculated values of p_i for the $N = 2(2I + 1)$ ground-state levels can be incorporated into the calculations via an effective weight factor that modifies the strength of the transitions. The implementation of our theoretical model, *ElecSus* (see section 2.4), has taken this into account and been experimentally validated [134].

6.3 Simulations and experimental proposal

We begin by considering ^{87}Rb atoms in a thermal vapour at a given temperature T in the ground state. To this we add an external magnetic field B of high enough strength such that the atoms are now in the hyperfine Paschen-Back regime (see section 2.2.1). As we have seen in section 5.2, the presence of the magnetic field will generate a shift in the energies of the different levels of the atom due to the Zeeman effect that is proportional to B (see equations 5.1 and 5.2). This in turn will, according to equation 6.1, modify the populations in the ground-state energy levels. In the case here proposed, we known that there are 8 discrete ground-state energy levels for ^{87}Rb (regardless of the presence or strength of B) that must be populated, and we expect the majority of the atoms to be in these levels at the given temperature T as they are energetically lower than those in the first excited state. For other excited states the value of the exponent in equation 6.1

is even smaller as the energies of these states, with respect to the lowest ground-state energy, are significantly larger.

6.3.1 Absorption-based thermometry

For experimental purposes it is common to approximate the population in each of the ground-state levels to be equal, *i.e.* the total normalised population of atoms $N_{\text{atoms}} = 1$ is divided by the number N of levels available. In our system of ^{87}Rb atoms we know that $I = 3/2$, which gives $N = 2(2I + 1) = 8$ discrete energy levels in the ground state (see section 2.3.1). As such, the population of each level can be taken as $p_i = N_{\text{atoms}}/N = 1/8$. This typically provides a good enough approximation to the actual populations in each of the energy levels so that theoretical models can give reliable predictions of the experimentally observed behaviour. However, an alternate approach is to consider a thermal distribution of population in the ground-state energy levels given by equation 6.1. This change of distribution will generate small changes in the observed absorption of the medium, as shown in figure 6.1. We consider these as being the only energy levels populated due to the energy difference of the optical D-line transitions being on the order of 300 THz, which is equivalent to approximately 60 times the thermal energy at room temperature. The result of this is a factor of $e^{-60} \approx 10^{-28}$ attenuating the populations in the excited states, as calculated by equation 6.1.

The changes in the absorption spectra shown in figure 6.1 as a result of changing how the ground-state energy levels are populated can be interpreted as follows. As the population in the ground-state energy levels is redistributed, the number of atoms participating in each transition changes; the effective transition strength is thus increased or decreased, giving place to enhancement or reduction of the absorption of light by the atomic medium. The presence of an external magnetic field serves to further highlight this effect as the energy shifts generated by the Zeeman effect contribute to a larger overall shift of the discrete levels in the ground state. When compared to the thermal energy of the system ($k_{\text{B}}T \approx$ THz), these shifts are still orders of magnitude smaller; as a reference, in the case of ^{87}Rb in the hyperfine Paschen-Back

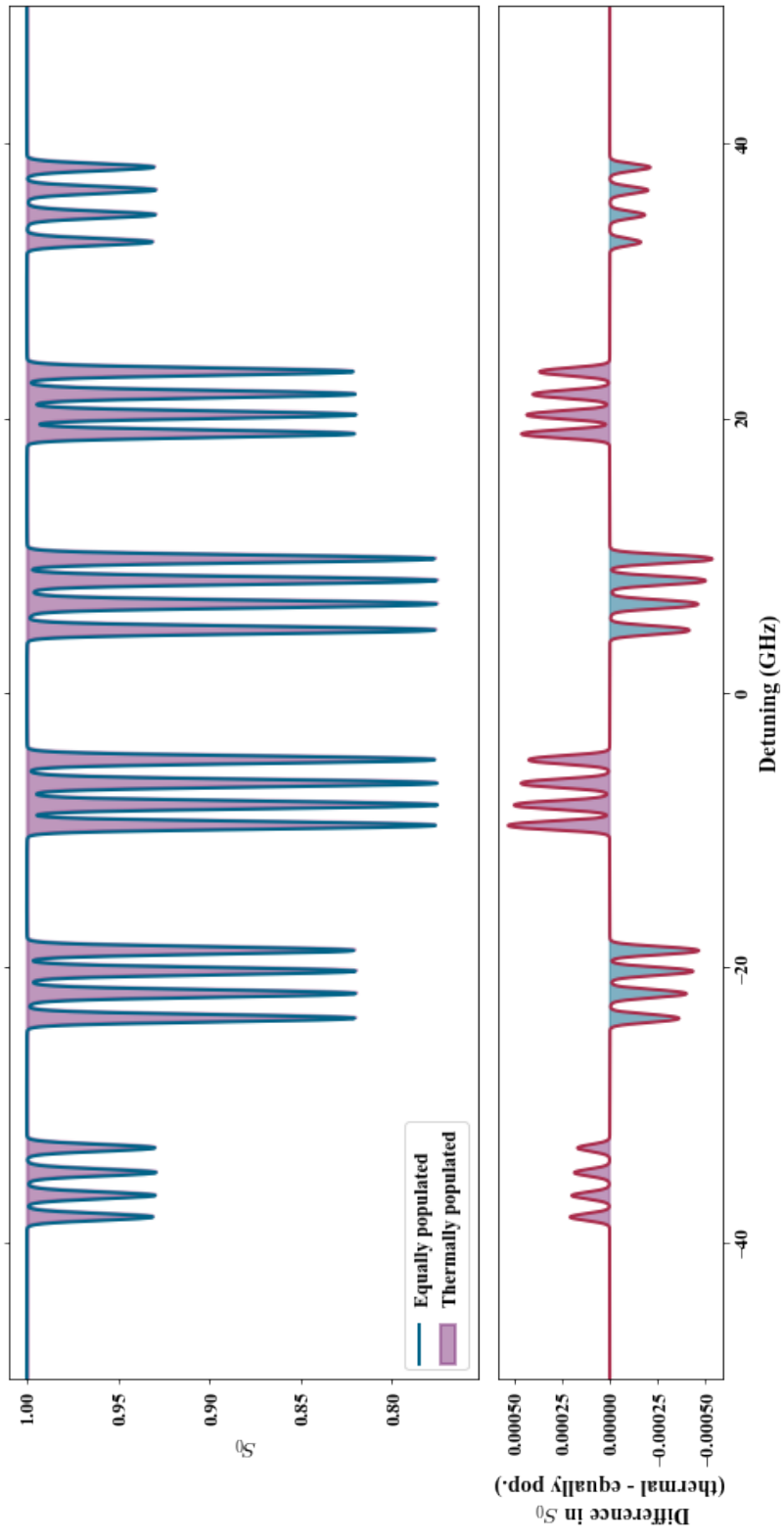

Figure 6.1: Calculated absorption (S_0) spectra for a sample of ^{87}Rb atoms at a fixed temperature ($T = 80°C$) in the hyperfine Paschen-Back regime ($B = 1.52$ T); shown in the upper panel are the spectra corresponding to the cases of equally populated ground state levels ($p_i = 1/8$; blue curve) and thermally populated ground state levels (see equation 6.1; shaded purple area). In the lower panel, the difference between the absorption in both cases is shown. The shaded red areas under the curve represent an increase in population of the associated ground-state energy levels when assuming a thermal distribution rather than an equal distribution; blue shaded areas represent a decrease in the population of the levels from the above assumption. These differences are small, less than 0.05%, and do not significantly alter the observed spectra. The small gradient seen in the difference in absorption for each of the multiplets is a result of the Zeeman shift in the energy levels (see equation 5.2).

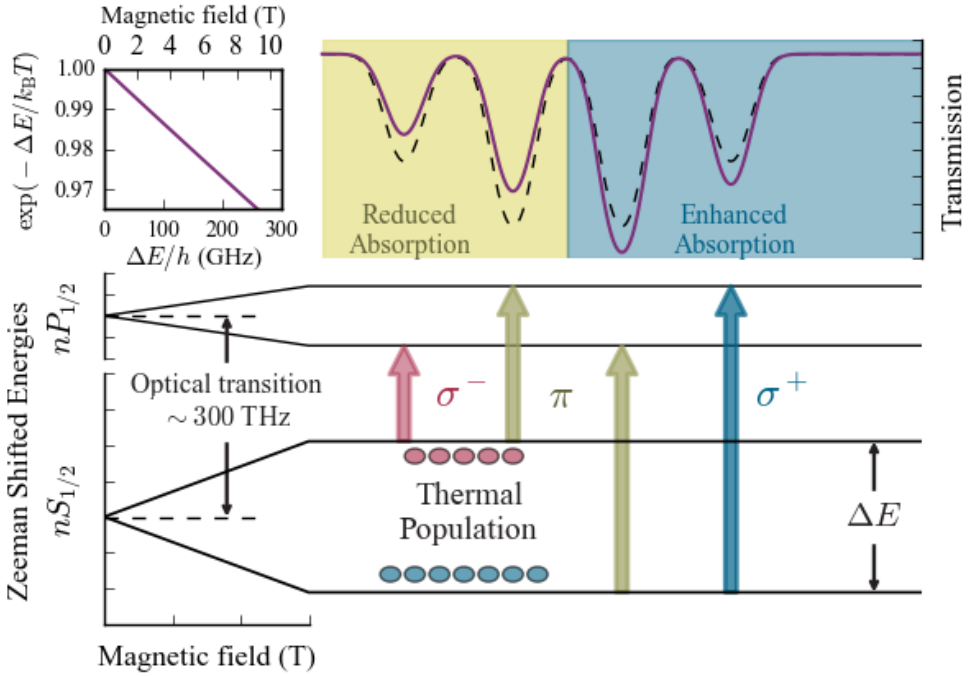

Figure 6.2: Simple diagram of the effects of a thermal population distribution on the absorption of light by an atomic medium. Shown at the bottom are the ground-state and excited-state Zeeman shifted energy levels for an alkali-metal atom optically excited on the $D1$ transition. The thermal distribution of population in the ground-state energy levels, taken as a function of the energy difference ΔE relative to the lowest level, gives rise to changes in the absorption of the light (top-right) used to excite the transition as the effective transition strength is changed. The change in population is given by the exponential term in equation 6.1, which is in turn a function of the strength of the magnetic field used; this is shown (top-left) for fields of up to 10 T, at which point the atom is well in the hyperfine Paschen-Back regime.

regime, the energy difference of the optical D-line transitions is on the order of 300 THz and the Zeeman energy shifts are on the order of tens of GHz. Despite this difference of several orders of magnitude, the contribution to the energy shifts from the Zeeman effect is still visible in the form of a gradient in the difference in absorption within each of the multiplets, as a result of the dependence on m_I in equation 5.2. A simplified diagram of the above interpretation can be seen in figure 6.2 for the simpler structure of the $D1$ line in an alkali-metal atom (see section 2.3 for details).

Using the concepts described above we can propose a scheme for precision

thermometry using atoms in an external magnetic field. The approximation of thermally-distributed populations leads to a natural method for this as a result of the exponent in equation 6.1, which relies both on the energy, in itself a function of the field strength B, of the ground-state levels ($E_i \equiv E_i(B)$), and temperature T of the atomic medium. To do this, we consider an atomic absorption spectrum where the total light transmitted for a given detuning, which will correspond to a transition between a particular ground-state and an excited-state energy level (*i.e.* an absorption feature), is carefully measured; the choice of the transition, or of pairs of transitions, allows for finding the greatest difference in the absorption relative to the case of an equal distribution of populations while simultaneously providing a way of measuring the field strength. Here we note that a precise measurement of the field strength B, using methods such as those proposed in chapter 5, in this scenario provides a means for the precise measurement of T as this allows for greater precision in the determination of the ground-state energies. Experimentally this scheme requires for spectra to be acquired with a very high signal-to-noise ratio (SNR) or to be acquired using a very strong (> 1 T) magnetic field in order to create greater contrast between the equally and thermally populated cases. Fulfilling one, or both, of these requirements then allows for the amount of light absorbed by the distribution of populations in the ground state to be precisely measured, even if the changes are small; the determination of T is then done by relating this change in absorption with the factor $E_i(B)/k_{\mathrm{B}}T$ seen in equation 6.1.

In figures 6.3 and 6.4 we can see the calculated changes to the absorption (S_0) spectra at field strengths of 0.4 T and 8 T, respectively. In both cases we have assumed there is no buffer gas content in the vapour cell that could lead to discrepancies in our calculations (see Appendix A for details). Under these conditions, the maximum energy shift due to the Zeeman effect (measured with respect to the lowest ground-state energy level) is on the order of ~ 15 GHz and ~ 250 GHz, respectively. When compared to the thermal energy of the system, $k_{\mathrm{B}}T \approx 4.9 \times 10^{-21}$ J (~ 7.4 THz), these shifts are at least one order of magnitude smaller. Despite this, the difference in population induced

in the ground state from equation 6.1 is within experimentally measurable limits, albeit with some challenges. For the spectrum at 0.4 T, the maximum absorption difference observed in the spectrum is $\sim 0.025\%$; at 8 T, this value is two orders of magnitude larger, $\sim 0.5\%$. These two values, in turn, correspond to a change in population of $\sim 0.2\%$ and $\sim 2.5\%$, respectively.

It must be noted at this point that the above proposal makes two important assumptions. First, we are assuming that the thermal population distribution is reached when the system is in thermal equilibrium. This is important in ensuring that we can define an average temperature for the atomic system with certainty, and to omit any effects on the distribution arising from the dynamics of the system [210]. In particular, we assume that the ground-state thermalisation is carried out by collisions between ^{87}Rb atoms and other atoms/molecules (^{87}Rb or buffer gas) in, as well as with the walls of, our experimental vapour cell on a timescale of $\sim$ 10 ms [55]. We note that additional non-thermal effects, such as optical and hyperfine pumping [211], can be largely avoided by working at low values of the saturation parameter of the system, although their effect can be taken into account when modelling the absorption in the atomic system [75].

The second assumption made is that the spin-states of the atomic vapour are also in equilibrium with the walls of the cell. Previous work in thermal vapours [52, 105, 212, 213, 214] has shown that collisions between the atoms and the container walls can lead to depolarisation of the system's spin state; the cross-section for these spin-exchange collisions are typically on the order of 10^{-14}cm^2 [55, 106]. This has lead to great interest in coatings for container walls that help reduce the depolarisation of the medium to levels where it does not significantly affect the measurements that depend on addressing specific spin states [53, 54, 215, 216, 217]. In this case, as we consider the system to be in thermal equilibrium, the collisions between the atoms and walls of our cell are assumed to lead to an equilibrium state for the overall spin state of the vapour.

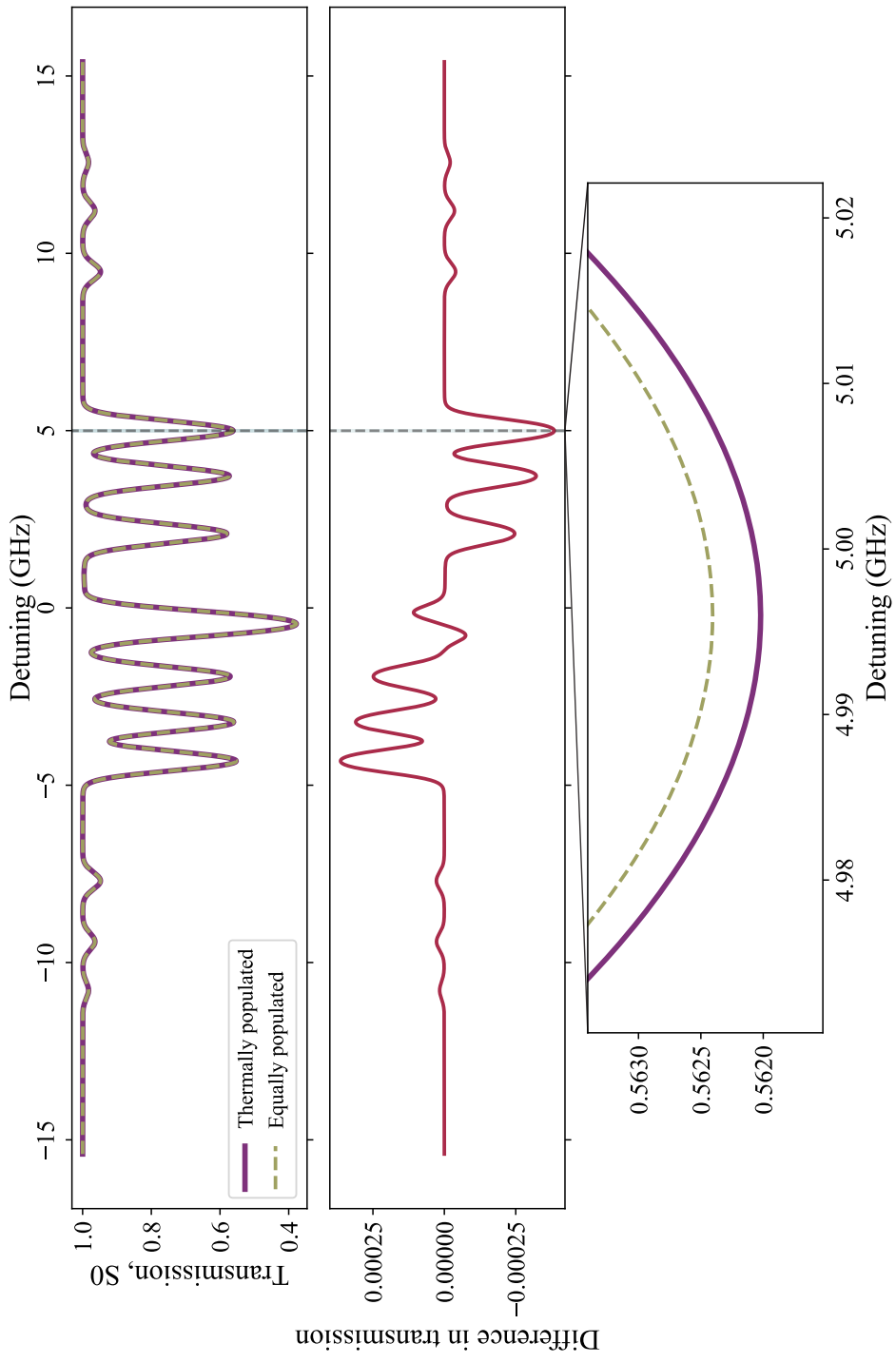

Figure 6.3: Calculated absorption (S_0) spectra for a ^{87}Rb vapour in the Voigt geometry, at $T = 80°$C and $B = 0.4$ T. The top panel shows the absorption spectra ,as a function of linear detuning, calculated for equally populated (*i.e.* $p_i = 1/N$, $N = 8$; green dashed line) and thermally populated ground state levels, as given by equation 6.1 (purple solid line). The panel directly underneath shows the difference in the absorption of these two cases; here the broken vertical line indicates the point in the spectra where the difference reaches an extremum value. At the bottom, a zoom of this point of the absorption spectra is shown to highlight the observable difference between the equally populated and thermally populated cases. For the conditions chosen here, the difference is $\sim 2.5 \times 10^{-4}$ (0.025%), requiring a large SNR in the spectrum for it to be experimentally observed.

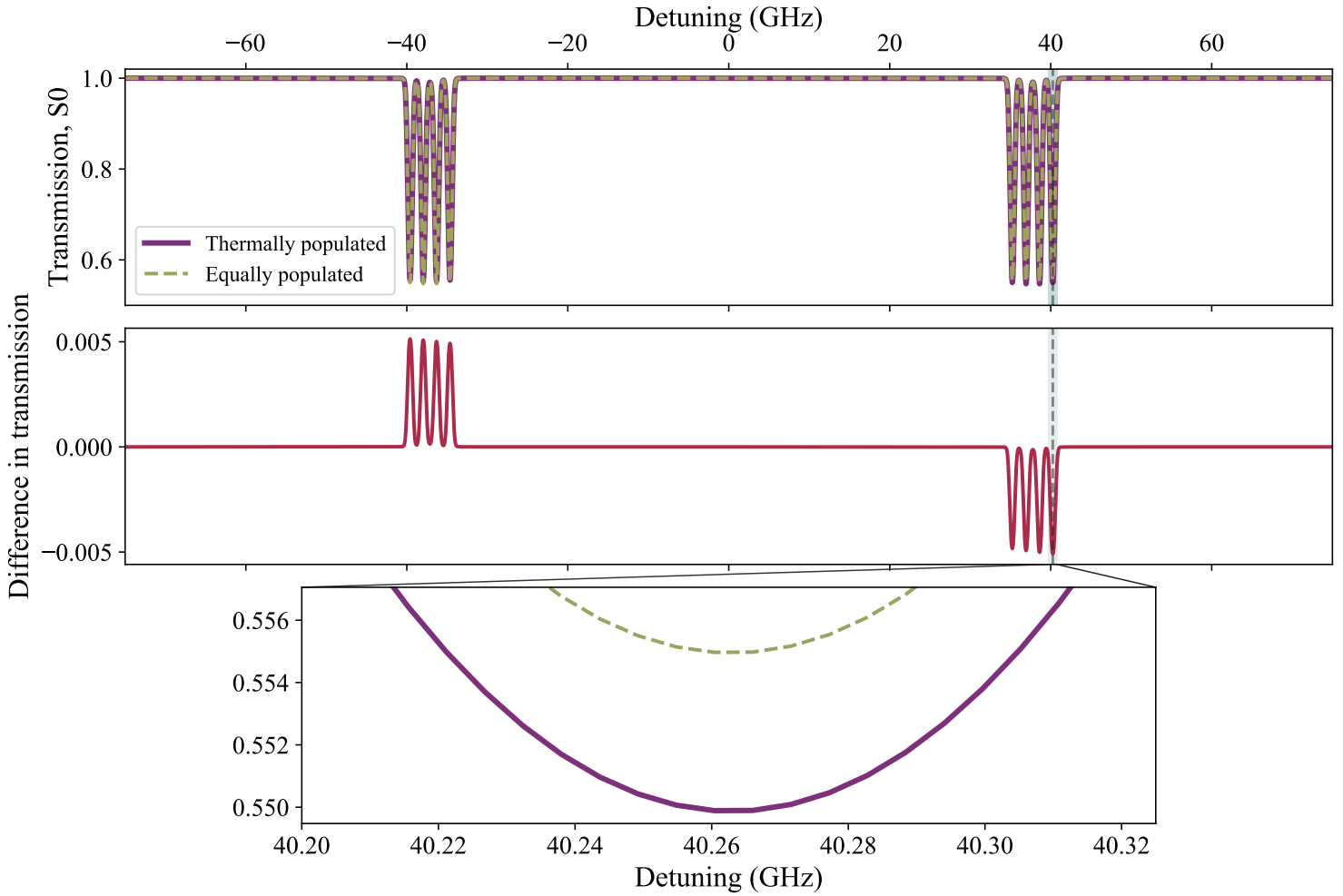

Figure 6.4: Calculated absorption (S_0) spectra for a ^{87}Rb vapour in the Voigt geometry, at $T = 80°$C and $B = 8$ T. The top panel shows the absorption spectra ,as a function of linear detuning, calculated for equally populated (*i.e.* $p_i = 1/N$, $N = 8$; green dashed line) and thermally populated ground state levels, as given by equation 6.1 (purple solid line). The panel directly underneath shows the difference in the absorption of these two cases; here the broken vertical line indicates the point in the spectra where the difference reaches an extremum value. At the bottom, a zoom of this point of the absorption spectra is shown to highlight the observable difference between the equally populated and thermally populated cases. For the conditions chosen here, the difference is $\sim 5 \times 10^{-3}$ (0.5%), requiring a lower SNR (compared to the case of $B = 0.4$ T) in the spectrum for it to be experimentally observed.

6.3.2 Optical-rotation-based thermometry

We can also consider a case where neither of the above mentioned requirements (*i.e.* a high SNR for the spectra or a very strong magnetic field) are available. To continue being able to make a precision measurement of the temperature T of the atomic vapour we must now consider the use of additional information, or of a different scheme, that does not rely on measuring small changes in the absorption. In particular, we will look at using the Voigt geometry to access the π transitions, allowing for additional features to appear in the optical measurements we make.

Whilst being amongst the easiest spectroscopic techniques to implement, absorption spectroscopy does not take advantage of *all* of the available information in the experimental system, some of which is more sensitive to small changes in the medium and can provide signals to measure said changes. An example of this is the loss of distinction of different polarisation components of the light used to excite the atoms, as the absorption can be described by the polarisation-basis-independent Stokes parameter S_0 (see section 2.1.4). In contrast, we know that polarisation sensitive detection techniques and the remaining Stokes parameters (see section 4.2 for their definitions) are sensitive to small changes such as the birefringence of the vapour cell windows, as shown in section 4.3.2, and optical rotation effects [52, 79, 95, 218]. Furthermore, there is a strong tradition in atomic physics of using optical rotation signals for the purpose of investigations into fundamental physics [3, 171, 219, 220, 221].

As before, we take the example of a thermal vapour of ^{87}Rb in an external magnetic field of strength large enough such that the atomic energy levels are in the hyperfine Paschen-Back regime. However, rather than measuring the change in populations in terms of a change in the absorption we now consider using another of the Stokes parameters in order to take advantage of additional information on the medium and increased sensitivity. While the effect of changing the ground state populations is small in a spectrum of S_0, the changes in population have a noticeable effect on a spectrum of S_3 (see

section 2.1.4); this effect will now be measured in terms of the differences in the atomic medium's response as given by the optical rotation due to birefringence, thus being more sensitive to small changes in the internal conditions of the medium, as seen in section 4.3.2, than the absorption. We can thus consider the use of the S_3 spectrum to determine the population difference in the ground state by looking at the zero crossings in the spectrum, particularly between groups of transitions, as seen in figure 6.5.

From figure 6.5 we see clearly the advantage of using the S_3 spectrum to measure ground state population differences for a ^{87}Rb vapour sample at $T = 100°$C and $B = 1.5$ T. Whereas in figures 6.3 and 6.4 the difference is in the depth of the absorption feature, in figure 6.5 the difference is now in the position of the zero-crossing highlighted in blue. It is important to note that the highlighted feature in the S_3 spectrum appears between the multiplets corresponding to π transitions; these are only observed when working in the Voigt geometry, as seen in chapters 4 and 5.

In this case, the maximum energy shift of the ground-state energy levels is of the order of ~ 50 GHz. While the corresponding difference in the absorption observed is $\sim 1\%$, the difference in the position of the zero-crossing, shown in the bottom panel of figure 6.5, is ~ 20 MHz. Current state-of-the-art frequency standards are commercially available that can easily measure values of this order of magnitude to a precision of $> 10^9$ [193]. Furthermore, by measuring a frequency shift (*i.e.* a difference in frequency relative to a reference point) systematic effects in the acquisition of the spectrum can be reduced and thus contribute to an increased precision in subsequent measurements [155].

As previously mentioned we will be working in the hyperfine Paschen-Back regime, and as such will require precise measurement of the field strength B. This can be accomplished using the magnetometry scheme described in chapter 5, which we have seen provides a relative uncertainty of $\sim 3.5 \times 10^{-2}$, limited by the precision to which the frequency difference between two transitions is measured; methods for improving this limit, such as the use of a frequency comb or an EOM, have been previously discussed in section 5.3.2. Assuming the errors in our frequency calibration ($\sim 3.5\%$) will be the primary

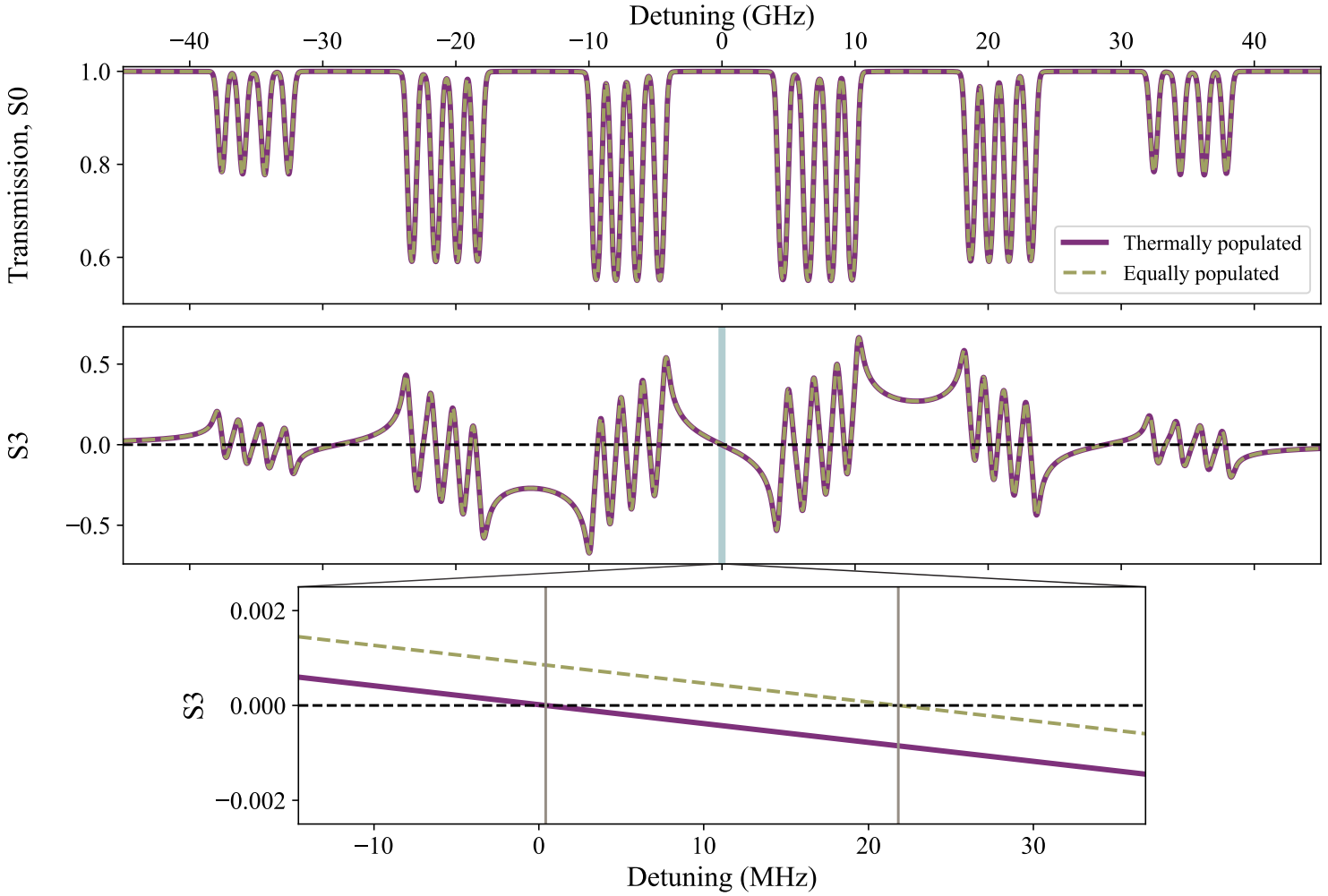

Figure 6.5: Calculated absorption and optical rotation (S_0, S_3) spectra for a ^{87}Rb vapour in the Voigt geometry, at $T = 100°$C and $B = 1.5$ T. The top panel shows the absorption spectra ,as a function of linear detuning, calculated for equally populated (*i.e.* $p_i = 1/N$, $N = 8$; green dashed line) and thermally populated ground state levels, as given by equation 6.1 (purple solid line). The panel directly underneath shows the spectrum for S_3 Stokes parameter for the two cases mentioned. At the bottom, a zoom of the zero-crossing around zero detuning in the S_3 spectrum is shown to highlight the observable difference between the equally populated and thermally populated cases; we note that here the difference in populations is translated to a shift in the position of the zero-crossing. For the conditions chosen here, the difference corresponds to ~ 20 MHz, which using standard RF equipment such as 10 MHz frequency references [193] is easily measured in the laboratory.

source of uncertainty in our measurement of the temperature T, we find that this is greater to the uncertainty of other proposed methods of atom-based thermometry [205]. As such, we can expect a relative uncertainty in the measurement of the temperature of the atomic system of $\approx 3.5 \times 10^{-2}$ with experimental conditions similar to those used in chapters 4 and 5; values for a rough uncertainty budget are shown in table 6.1.

It is worth noting here that, similar to other polarisation-sensitive spectroscopic schemes (*e.g.* polarisation spectroscopy or DAVLL), the polarisation purity and residual dichroism/birefringence of the optical system [222, 223, 224, 225, 226] play an important role in optimisation of the zero-crossing in the S_3 spectra. In addition to this, because the position of the zero-crossing is off-resonant by > 1 GHz to the atomic transitions (in this case, π transitions) it is reasonable to expect the scheme we propose in this section will be sensitive to the residual dichroism/birefringence. Under similar experimental conditions to those discussed in chapter 4, including an additional birefringence of 1 mrad (*e.g.* from cell windows) would generate a shift of ~ 35 MHz in the position of the zero-crossing and a change of $\sim 4 \times 10^{-8}$ in the slope of the S_3 signal. Effects of birefringence on the order of 10^{-8} rad have been experimentally measured using atomic spectroscopy in reference [168]; at this level, the effects on the position and slope of the zero-crossing are negligible. We will thus assume a high ($> 400 : 1$) polarisation purity in the system, together with stabilisation of the beam power via an AOM [152], to reduce the effect of polarisation fluctuations on the S_3 spectrum, as well as the ability to compensate the small birefringent effects of optics via optical elements or the addition of terms using the Jones matrix formalism into our theoretical model. A more detailed analysis of these effects is beyond the scope of this work, but would prove necessary for implementing the scheme we propose in a metrological context.

An additional advantage of using S_3 rather than S_0 spectra is the fact that the zero-crossing of the former provides additional sensitivity to small changes. This is due to the fact that in the Voigt geometry the separation between the π multiplets is smaller than that of the $\sigma^{\pm}$ multiplets, allowing for

Quantity (units)	**Value**	**Uncertainty**	**Relative uncertainty**
Bohr magneton μ_B (Hz/T)	13,996,244,936.1	4.2	3×10^{-10}
^{87}Rb ground state g_J (a.u.)	2.00233113	2×10^{-7}	1×10^{-7}
^{87}Rb ground state hyperfine constant A_{HF} (Hz/2π)	3,417,341,305.452145	4.5×10^{-8}	1×10^{-14}
Frequency difference between transitions $\Delta E_{\sigma^+ \leftrightarrow \pi}$ (Hz)	$48,026 \times 10^6$	3.4×10^6	7.2×10^{-5}
Calibration error in frequency interval $\sigma_{\Delta E_{\sigma^+ \leftrightarrow \pi}}$ (Hz)	$1,681 \times 10^6$	1.2×10^5	3.5×10^{-2}
Magnetic field strength B (T)	1.531	5.4×10^{-2}	3.5×10^{-2}
Boltzmann constant k_B (J/K)	1.380649×10^{-23}	(exact)	(exact)
Frequency shift of zero-crossing (Hz)	21,394,139	0.02	9.3×10^{-10}
Calibration error in position of zero-crossing (Hz)	748,795	7×10^{-4}	3.5×10^{-2}
Temperature T (K)	353.15	1.24×10^1	3.5×10^{-2}

Table 6.1: Uncertainty budget for the determination of temperature using the proposed thermometry scheme based on optical rotation. The quantities involved in the calculation of the value for T, along with their values, uncertainties and relative uncertainties, are shown. At the bottom, the calculated value of T and its uncertainty is shown. Data for μ_B, g_J, k_B and A_{HF} are taken from [182, 183], [119] and [141], respectively. The value of $\Delta E_{\sigma^+ \leftrightarrow \pi}$ is taken from an absorption spectra in order to determine the field strength as outlined in chapter 5. The precision in the measurement of B is limited by the precision available in the determination of the frequency difference $\Delta E_{\sigma^+ \leftrightarrow \pi}$, which in this case contributes a relative uncertainty of $\sim 3.5 \times 10^{-2}$ to our calculations. This is due to the associated error over this frequency interval due to errors in our calibration procedure. This is then the limiting factor in the precision to which we can obtain the temperature of the system, via the relation established in equation 6.1, under the assumption that the frequency shift of the zero-crossing is measured using a commercially available 10 MHz frequency reference and additional RF electronic components [193]. Methods to increase the precision in the measurement of B are discussed in detail in section 5.3.2.

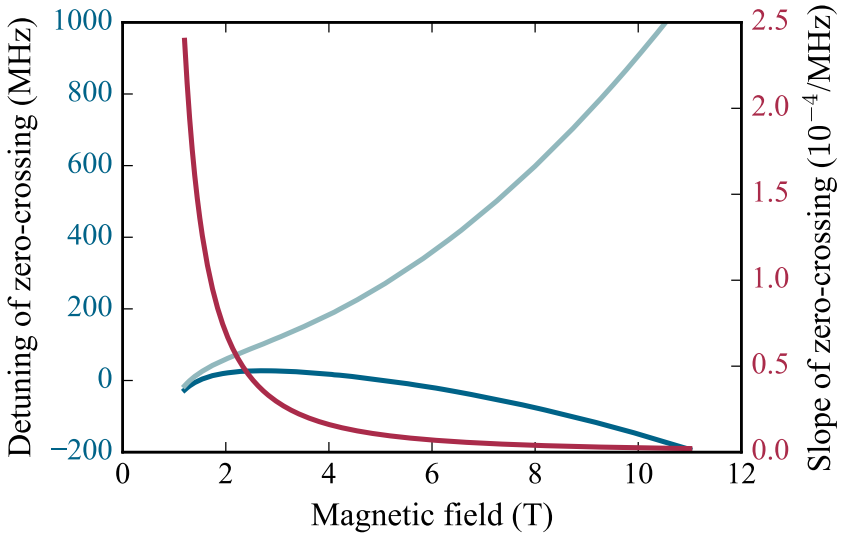

Figure 6.6: Numerical simulations of the position of the main zero-crossing in the S_3 spectrum of a thermal vapour of ^{87}Rb atoms at a fixed temperature of $T = 120°$C as a function of field strength B, from 1.2 T up to 10 T. This range of values was chosen as the zero-crossing is clearly visible and has no overlap with the atomic resonances. The position of the zero-crossing is calculated for the equally-populated case (light blue curve) and the thermally-populated case (blue curve). Also shown is the slope (red curve), calculated using a distance of ±200 MHz around the zero-crossing, as a function of B. We can see there is a clear difference in the behaviour of the position of the zero-crossing under the equally- and thermally-populated cases, with the former increasing as a function of B while the latter slowly increases before then decreasing as the value of B increases. Furthermore, we see how the slope of the zero-crossing, useful in precise determination of the position of this feature, decreases rapidly as a function of B.

the appearance of the well-defined zero-crossing in the S_3 spectra shown in figure 6.5. In particular, not only can we consider the position of the zero-crossing but we can also look at the slope of the signal around this point as an indicator of any changes in the ground state population distribution. We can calculate both of these measurable quantities as a function of field strength B and temperature T, as shown in figures 6.6 and 6.7, respectively, to see their dependence on these parameters. It is also convenient to calculate the quantities for the case of equally populated ground-state energy levels, so as to be able to have a reference and compare. This provides a method to discriminate the changes in population due to the assumption of a thermal distribution from other systematic effects in the system.

From figure 6.6 we can see that the detuning of the zero-crossing as a function of field strength B has a noticeably different behaviour when considering a equal (light blue curve) or a thermal (blue curve) distribution of the ground-state populations. We also see that the slope of the zero-crossing has a rapidly decreasing behaviour as B increases. As such, we see that the sensitivity in the measurement of the position of the zero-crossing can be optimised by choosing a value of B where the slope is greater and the difference in detuning between the two population distributions is greatest. In the calculations shown, this occurs at field strengths of ~ 2 T, suggesting that it is possible to carry out the thermometry scheme in fields readily available with permanent magnets.

In figure 6.7 we see the detuning of the zero-crossing as a function of temperature T, along with the slope of of the signal around the zero-crossing. The equally-populated ground-state energy levels give place to a zero-crossing whose position decreases as T increases; we know this is a result of the increase of optical depth of the atomic medium which also broadens the spectral features as a result of collisions. This increase in optical depth and broadening of the features is also present in the thermally-populated case, yet the position of the zero-crossing increases up to a critical temperature ($T \approx 160°$C) before decreasing. In addition to this, we see that the slope of the signal around the zero-crossing increases as a function of T. Together with the behaviour of the position of the zero-crossing, this allows us to determine an optimal value of T ($T \approx 100°$C) around which to operate our scheme with greater sensitivity to the changes in the ground-state population distribution.

From the above we can proceed to consider a set of optimised operating conditions for our thermometry scheme based on S_3 spectra. Ideally we want to work with an alkali-metal atom, as the vapour pressure at room temperature is sufficient to carry out spectroscopic measurements. In addition to this, the alkali metals with smaller values of nuclear angular momentum I may have the highest sensitivity as their structure in the hyperfine Paschen-Back regime could be better resolved; this singles out ^{23}Na or ^{87}Rb as the most convenient choices. Taking atoms of ^{87}Rb as our species of choice, we want to

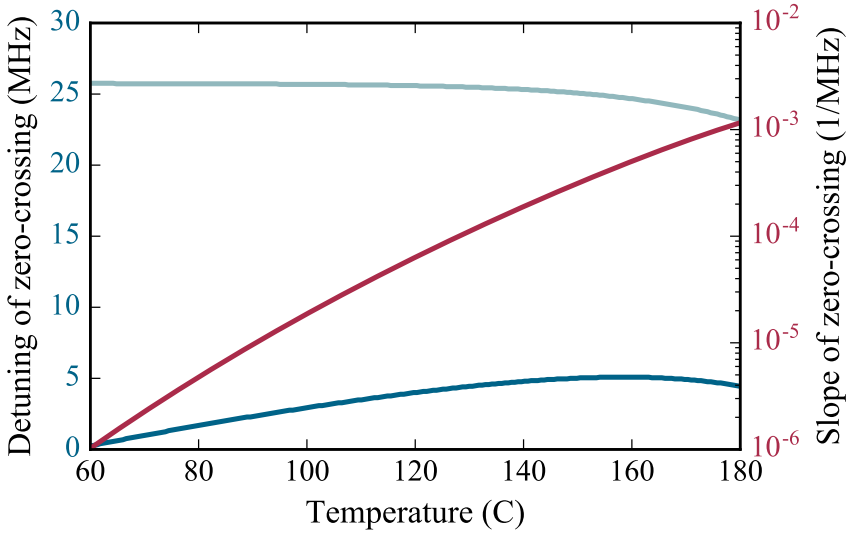

Figure 6.7: Numerical simulations of the position of the main zero-crossing in the S_3 spectrum of a thermal vapour of ^{87}Rb atoms at a fixed field strength of $B = 1.54$ T as a function of temperature T, from 60°C to 180°C. This range of values was chosen based on the typical operating temperatures for optically-bonded cells and on the optical depth of the atomic medium. The position of the zero-crossing is calculated for the equally-populated case (light blue curve) and the thermally-populated case (blue curve). Also shown is the slope (red curve), calculated using a distance of ±200 MHz around the zero-crossing, as a function of T. We see that while the position of the zero-crossing in the equally-populated case decreases as T increases, for the thermally-populated case the position of the zero-crossing increases as T increases until a critical temperature of $T \approx 160$°C, at which point it decreases. This is take to be the point at which the optical depth of the atomic medium and additional collisions that broaden the spectral features are dominant. We can also observe how the slope of the zero-crossing increases as a function of T, which allows us to determine an operating value of T at which we can obtain greater sensitivity and precision in our measurements.

be able to precisely measure the energy of the ground-state levels working at field strengths of ~ 2 T and temperatures close to 100°C. This will provide a large value for the slope, with which we can better resolve the position of the zero-crossing, as well as being more sensitive to fluctuations in temperature. Taking all of these factors into account, as well as increases in the precision of the frequency measurements taken, we can consider the precision in the temperature resulting from measurements in these conditions. A speculative uncertainty budget is shown in table 6.2 to provide a quantitative outlook of our optimised scheme.

Quantity (units)	**Value**	**Uncertainty**	**Relative uncertainty**
Bohr magneton μ_B (Hz/T)	13,996,244,936.1	4.2	3×10^{-10}
^{87}Rb ground state g_J (a.u.)	2.00233113	2×10^{-7}	1×10^{-7}
^{87}Rb ground state hyperfine constant A_{HF} (Hz/2π)	3,417,341,305.452145	4.5×10^{-8}	1×10^{-14}
Frequency difference between transitions $\Delta E_{\sigma^+ \leftrightarrow \pi}$ (Hz)	$61,321 \times 10^6$	1×10^5	1.6×10^{-6}
Calibration error in frequency interval $\sigma_{\Delta E_{\sigma^+ \leftrightarrow \pi}}$ (Hz)	920×10^6	1.5×10^3	1.5×10^{-2}
Magnetic field strength B (T)	2	3×10^{-2}	1.5×10^{-2}
Boltzmann constant k_B (J/K)	1.380649×10^{-23}	(exact)	(exact)
Frequency shift of zero-crossing (Hz)	40,948,094	0.02	4.8×10^{-10}
Calibration error in position of zero-crossing (Hz)	614,221	3×10^{-4}	1.5×10^{-2}
Temperature T (K)	373.15	5.6	1.5×10^{-2}

Table 6.2: Uncertainty budget for the determination of temperature using the proposed thermometry scheme, based on optical rotation, under optimised experimental conditions. The quantities involved in the calculation of the value for T, via equation 6.1, along with their values, uncertainties and relative uncertainties, are shown. At the bottom, the calculated value of T and its uncertainty is shown. Data for μ_B, g_J, k_B and A_{HF} are taken from [182, 183], [119] and [141], respectively. The precision in the measurement of B is limited by the precision available in the determination of the frequency difference $\Delta E_{\sigma^+ \leftrightarrow \pi}$, assumed here to be the calculated value between the pair of π, σ^+ transitions used in the scheme shown in chapter 5. This is due tothe associated error over this frequency interval due to errors in our calibration procedure, which we assume is optimised to an amount similar to that reported in chapter 3 of 1.5%. The frequency shift of the zero crossing is assumed to be acquired using a commercially-available 10 MHz frequency reference providing a measurement accuracy of 10^{-9} [193], and for the frequency difference $\Delta E_{\sigma^+ \leftrightarrow \pi}$ to be obtained using the optimised experimental setup described in section 5.3.2. Under these conditions, the limiting factor in the precision of our temperature remains the error in the calibration of our frequency axis, but with an increase in precision by an order of magnitude when compared to the unoptimised case.

6.3.3 Comparison of proposed thermometry schemes

The optical thermometry schemes presented in sections 6.3.1 and 6.3.2 each offer advantages over conventional thermometry schemes. However, between the two schemes there are also certain aspects that prove to be advantageous in the context of traditional precision measurement techniques in atomic physics. A brief summary of both schemes, together with the points in favour of or against them, will be given in this section.

The variant of the thermometry scheme presented in section 6.3.1 is based on being able to measure changes in populations from absorption (S_0) spectra. In this case, the change in the absorption depth is the indicative feature of the change in population. Experimental measurements of these depths can then be compared to those obtained using an equally-distributed population in order to obtain a value of T via the relation in equation 6.1. This requires very good signal-to-noise ratios in the spectra taken, as well as reducing systematics that could alter the depth or shape of the absorption features. Despite this, the change in populations is a function of the field strength B: a bigger field will generate a larger Zeeman shift in the ground state and, as a consequence, a more significant difference in the populations of the levels in this state. As such, the use of even larger magnets, including those at international facilities, for the experimental setup may be necessary.

On the other hand, the thermometry scheme presented in section 6.3.2 relies on close observation of a particular feature in optical rotation spectra, as given by the S_3 Stokes parameter. The feature, a zero-crossing between the two π transition multiplets, occurs due to the experiment happening in the Voigt geometry. Here, the change in population of ground-state energy levels causes a distinctive change in the position and slope of the zero-crossing to that caused by the assumption of equally-populated levels. We have shown that these changes can be more easily distinguished at conditions readily accessible in the laboratory; field strengths of $B \sim 2$ T can be obtained with permanent magnets and the shift, on the order of 20 MHz, can be measured precisely using commercially available RF electronic equipment. Both of these

points allow for the precision of the scheme to be easily improved, as discussed in the improvements to our magnetometry scheme in chapter 5, or by using higher precision frequency counters. All together, this optical-rotation-based thermometry scheme is more compatible with the state-of-the-art techniques used in precision metrology with atom-based systems.

6.4 Summary

We have presented a proposal to carry out precision thermometry using optical measurements with an atomic vapour. In particular, our thermometry scheme relies on the atomic vapour, in our case ^{87}Rb, being in the presence of a large magnetic field. This allows for the ground state populations to slightly change due to the Zeeman effect; these changes can then be measured from the atomic spectra as changes in absorption depth or shifts in the frequencies of features of interest on the spectra. The features used in the latter case are characteristic of spectra taken in the Voigt geometry, as they are present due to excitation of π transitions in the atoms. Our initial numerical calculations show that for readily obtainable experimental configurations our scheme could measure these changes at precisions of better than 10^{-2} (perspectives for achieving even higher precision are also briefly mentioned). As such, the precision offered by our scheme is on par with other state-of-the-art techniques. Building upon other work presented in this thesis, we propose that this scheme can potentially serve as an all-optical atomic standard for the Boltzmann constant, k_{B}, that is amenable to metrology and research labs worldwide.

Chapter 7

Conclusions and outlook

7.1 Summary

In this work we have looked at magneto-optical phenomena occurring in a ^{87}Rb thermal vapour in the Voigt geometry and at large magnetic fields. This particular geometric configuration allows us to take advantage of the decoupling of angular momenta in the atom to operate in the hyperfine Paschen-Back (HPB) regime, with the ability to address both π and $\sigma^{\pm}$ transitions. Under these conditions, spectroscopic studies, such as those using the full set of Stokes parameters, can be carried out without the thermal broadening, common in atomic vapour spectroscopy, being a concern. We have taken advantage of this to refine our understanding of atomic spectra in the HPB regime in the Voigt geometry and to propose applications of these atomic systems in areas such as large-field vector magnetometry and thermometry.

In chapter 3 we presented experiments realised with a thermal vapour of ^{87}Rb atoms at 0.4 T in the Voigt geometry. Although not fully in the HPB regime, as defined in section 2.3.1, the atomic vapour at this field strength presented features that were in excellent agreement with our theoretical model; we varied the field strength up to 0.4 T and the geometry of our system to further validate this model. This allowed a determination not only of the

field strength, with precision comparable to commercial systems, but also of the relative direction of the field with respect to the laser beam used to probe the atoms.

In chapter 4 we conducted spectroscopic studies of a vapour of ^{87}Rb atoms at 1.5 T in the Voigt geometry by measuring the complete set of Stokes parameters, defined in section 2.1.4. The larger value of field strength here allowed for individual features on the atomic spectra to be resolved, irrespective of the broadening in the lineshape due to the thermal nature of the vapour. Furthermore, use of the polarisation-basis dependent Stokes parameters (S_1, S_2 and S_3) allowed us to obtain additional information on the rotation of light through the atomic medium; we make additional use the S_3 spectrum to determine other systematic sources of birefringence, such as the vapour cell windows. We found very good agreement between our experiments and the theoretical model developed, further validating the use of atom-based large-field vector magnetometers.

In chapter 5 we expanded our study of thermal ^{87}Rb atoms by considering their use as a large-field optical magnetometer. In this case rather than using our theoretical model to fit the spectrum itself, we took advantage of the Zeeman induced energy shifts to create a measurement scheme that provides greater precision. We did this by measuring the relative frequency difference between two transitions, one π and one σ^+. We demonstrated that in our experimental conditions, we obtained a relative uncertainty of $\sim 3.5 \times 10^{-2}$ in the measurement of the field strength, limited primarily by the precision in our frequency measurements and our calibration error.

Finally, in chapter 6 we proposed the use of ^{87}Rb atoms in a thermal vapour for precision thermometry. We considered the case of using both absorption and optical rotation spectra, S_0 and S_3, respectively, to look at the change in populations in the ground-state energy levels. From numerical simulations we saw that S_0 spectra show these changes as reductions/enhancements of the absorption of light through the medium, while S_3 spectra showed them as shifts in the position of zero-crossings on the spectra. The zero-crossings of interest in the S_3 spectra come about as a result of the Voigt geometry,

which allows for π transitions to be excited in the atoms. This provides a way of clearly and precisely measuring the temperature of the vapour, limited once again by the precision in the measurement of frequencies.

In a time where increasing the precision of measurements has become necessary, and the associated experimental apparatus grows in complexity, atom-base sensors are an affordable, compact and accessible way to carry out measurements in a wide range of environments. With the results from the experimental investigations carried out we show that working with atomic vapours in the HPB regime *as well as* in the Voigt geometry provides a new set of tools that expands the understanding of atom-light interactions in an external magnetic field. The ability to address all of the dipole-allowed atomic transitions (*i.e.* π and $\sigma^{\pm}$) via selection of the polarisation of the probe beam provides a greater number of features that serve to enhance the statistical precision of a number of measurements. It also provides the means with which to observe a wider range of magneto-optical phenomena. Furthermore, the atomic system used can be quickly and accurately modelled due to the ability to select different types of transitions while in the HPB regime. This serves as a complement to previous work done in this regime [24, 59, 60, 89, 112, 227, 228, 229], where now the geometrical dependence of the system allows for new ways of observing magneto-optical phenomena and for innovative technological applications to be envisioned [230, 231]. In particular, the work presented here demonstrates the use of atom-based sensors for large magnetic fields with equipment that is easily accessible to both research and teaching laboratories.

7.2 Outlook

This thesis has presented work that covers a little studied combination of factors, and is thus by no means an exhaustive and definitive study of the interaction between atoms, light and external magnetic fields under the conditions here presented. As such, there still remains a range of possible lines of research both in fundamental and applied areas that take advantage

of atomic systems in the hyperfine Paschen-Back regime, configured in the Voigt geometry. In this section we will briefly mention some of the more immediate applications, and present some ideas that may help guide future work.

In our investigation of a ^{87}Rb thermal vapour at a field strength of 0.4 T we compared the results of our atom-based measurements to that of a commercial Hall probe sensor. From this comparison we found that our atomic system was able to provide equally-accurate and precise measurements of the magnetic field strength while also providing information regarding the relative orientation of the field with respect to the laser beam. As such, a natural area of application for these systems is atom-based vector magnetometry. The use of an atomic system would provide two dimensional resolution of the field geometry, as well as being able to operate over a much wider range of strengths than typical magnetometers: the model developed and tested in our work also provides a means to study field gradients [134]. Furthermore, use of atom-based sensors provides the possibility of real-time optical measurements of magnetic fields with a reduced equipment footprint.

At a higher field strength of 1.5 T we were able to further expand on the idea of using an atomic vapour as a precision magnetometer. This was done by showing the results of a polarimetric study of the light transmitted through the vapour, with the Stokes parameters as the measurement basis of choice, and by using the analytic expression for the energy shifts to find pairs of transitions that would enable high-precision readings of the field strength. Of particular interest is the ability of the optical rotation signals to provide a sensitive measurement of other experimental sources of birefringence, such as that of the vapour cell windows. A vapour of ^{87}Rb atoms like the one used in our investigation could have potential use in measuring the birefringence of other materials in the presence of large (> 1 T) magnetic fields, as well as being a viable system for operating in such environments under more restrictive geometrical considerations. This could provide a means for real-time monitoring and optimisation of large magnetic fields with optical feedback, which could potentially be automated for ease-of-use.

Another point of interest is the precision magnetometry: here we used the rubidium D2 line, but a similar experiment could well be carried out using the rubidium D1 line or on a transition to a second excited state, as seen in recent work [232]. In the case of using the D1 line the resulting spectra would have a simpler structure that could help to further increase the precision of the measurements. Use of a second excited state would not only allow for different sensitivities to the magnetic field to be accessed, but using the magnetometry scheme proposed in chapter 5 could also provide a way to better determine the gyromagnetic factors. The latter application is of special interest for precision spectroscopic measurements, such as those used in optical clock transitions or ion-based quantum logic systems [180, 181] as this could allow for more precise and reliable operation of state-of-the-art equipment. In addition to this, the limits of precision of our scheme – namely the precision of the frequency differences measured – can easily be overcome by use of a wavementer, an optical frequency comb or high-bandwidth electro-optic modulators (EOM). The use of commercially available modulators [1] together with a stable, low-noise laser and electronics for second-harmonic generation would be a relatively simple way of obtaining precisions of well over 1 p.p.m.

As discussed in chapter 6, another exciting and promising application of atomic vapours in large magnetic fields is the field of precision thermometry. Our work was partially limited by the availability of larger magnetic fields (> 1.5 T) with which to test the ideas proposed, but we are confident this line of work can be further developed in the near future. By taking advantage of the simplification of the theoretical model provided by working in the HPB regime, one can envision precision thermometry carried out in a "clean" two-level system. Doing this would allow for more sophisticated theoretical models that incorporate the quantum details of the system to be used, together with a reduced number of systematic errors that would be necessary to take into

[1] *e.g.* iXblue Photonics NIR-MPX800-LN-20 https://photonics.ixblue.com/store/lithium-niobate-electro-optic-modulator/phase-modulators or QUBIG PM11-NIR https://www.qubig.com/products/electro-optic-modulators-230/phase-modulators/pm11-nir.html

account.

This work has demonstrated some of the advantages of detailed spectroscopic studies of thermal atomic vapours. Our choice of operating in the Voigt geometry, in large field strengths and with a particular atomic species (^{87}Rb) is one of many possible systems for studying atom-light interactions in the presence of external fields. We hope that this rekindles the interest in carrying out "simple" spectroscopy experiments and for ongoing efforts in application of this knowledge to real-world problems. For the time being, world-domination by atoms, lasers and magnets has just begun, one sphere at a time.

Appendix A

Characterisation of MEMS vapour cells

For most of the applications of atomic vapours mentioned in previous chapters a fundamental component is the vapour cell in which the atoms are contained and the measurements are carried out. Over the past decades the development of techniques for the manufacture of these cells has greatly expanded. Current techniques allow for the manufacture of cells of varying sizes and geometries, with cavities smaller than centimetres possible [31, 169, 233, 234]. This, together with the development and availability of equipment for micro-manufacturing, has allowed for vapour cells to be incorporated into the catalogue of micro-electro-mechanical systems (MEMS) [91, 235, 236].

The work presented details the use of two MEMS ^{87}Rb vapour cells [1] in an absorption spectroscopy setup for exciting the D2 line in order to characterise their atomic/optical properties. In particular, spectroscopic measurements allow for a non-destructive characterisation of the cell contents to be made. This is possible due to the well-known effects of additional trapped gases in the cells [57, 237, 238], placed there deliberately or as a consequence of the manufacturing process, on the lineshapes of the atomic transitions; an overview of the most common such gases, and their effects, can be seen

[1] Fabricated by CSEM, http://csem.ch

Buffer gas	G_{Buf} **(MHz/torr)**	d_{Buf} **(MHz/torr)**
He	20.0	+0.37
Ne	9.47	-2.44
Ar	17.7	-5.76
Kr	17.2	-5.50
Xe	17.8	-6.19
N_2	18.3	-5.79

Table A.1: Coefficients for broadening (G_{Buf}) and shifts (d_{Buf}) due to common buffer gases in Rb vapour cells. The values presented here correspond to the Rb D2 line, but a similar table can be constructed with values corresponding to the D1 line [57].

in table A.1. Together with the ability to micro-fabricate cells, this has proven to be of interest in applications where control of atomic diffusion and collisions [239, 240, 241] is important, as well as in the development of miniature atomic clocks [29, 242].

Using a theoretical model to fit the spectra obtained allows these effects to be quantified, which in turn allows the contents of the cell to be determined in a relatively straight-forward manner. For this, we will use the open-source software *ElecSus* [134, 141], details of which were discussed in chapter 2. We note that *ElecSus* has not been previously used in atomic vapours where the broadening due to buffer gases is on the order of, or larger than, the Doppler width of the D-line transitions; the investigation presented serves as a validation of the model under these conditions and is of relevance to the results presented in chapters 3, 4 and 5.

Section A.1 will provide an overview of the experimental setup used in acquisition of the spectra. Samples of these results, as well as some discussions centred around them, are then provided in section A.2.

A.1 Experimental setup

The experimental setup used is shown in figure A.1. A distributed feedback (DFB) laser tuned to the Rb D2 line was used to excite the atoms in the MEMS cell. The laser frequency was scanned by slowly ($\sim$ 1 Hz) varying the diode temperature using a function generator to change the set point of a commercial temperature controller [2]. To protect the diode from stray retroreflected light an optical isolator (OI) was placed along the beam path. A portion of the light from the main beam was then taken using a half-wavelength retarder plate ($\lambda/2$) and polarising beam splitter (PBS) to be used in a reference 75 mm cell and an etalon (PD1 & PD2, respectively) to generate a frequency calibration for the spectra. The reference cell contained natural abundance Rb and was left at room temperature. All spectra were taken in the weak-probe regime [51, 72] to avoid distortions to the lineshape that could affect the frequency calibration or fit accuracy.

The remaining light from the main beam was then used in the characterisation of the MEMS cell by looking at the absorption of light by the atomic sample (PD3) and using our theory model, the publicly available software *ElecSus* [134, 141], to fit the resulting spectra. Data to characterise the MEMS cells was taken without an external magnetic field first and then placed in a magnetic field, generated by rare-earth permanent magnets, in the Faraday configuration ($\mathbf{k} \parallel \mathbf{B}$) with the intention of further testing the validity of *ElecSus* in a strongly pressure-broadened atomic vapour. The strength of the magnetic field was set by adjusting the separation between the magnets.

The MEMS cell was mounted in a custom-made copper block and PTFE enclosure that allows for temperature stability and optical access. Passive control of the temperature was achieved via a commercial heating element [3] and a thermistor to monitor the temperature changes. The laser beam was focused in order to pass through the available optical access in the design of the PTFE and copper block, as well as to avoid any clipping with the

[2] Thorlabs TED200C Temperature Controller
[3] Thorlabs HT15W Cartridge Heater

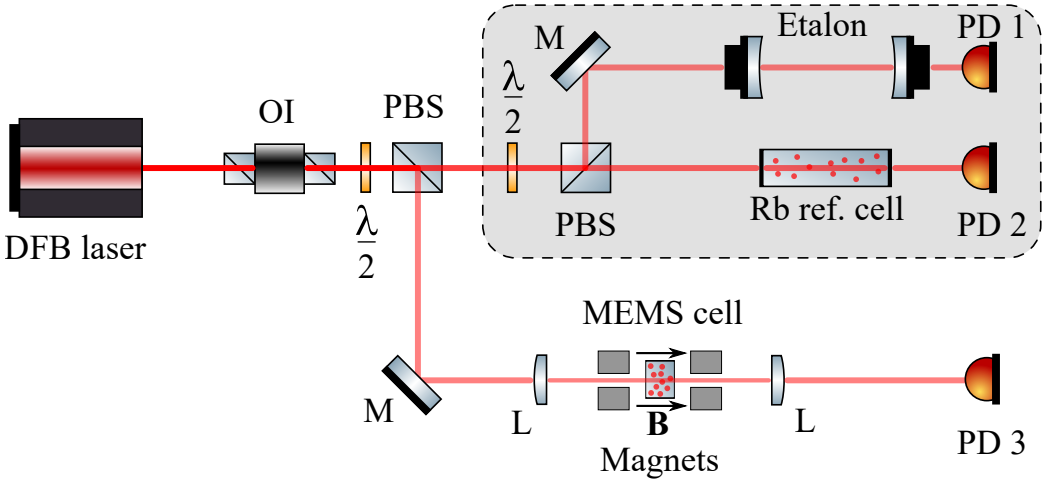

Figure A.1: A distributed feedback (DFB) laser was used to tune the Rb D2 transition in both the MEMS cell and a 75mm reference cell. Light transmitted through the MEMS cell was collected using a commercial photodiode. A secondary beam illuminating the reference cell was used, along with an etalon, to generate a frequency reference for the absorption spectra taken. OI: optical isolator, PBS: polarising beam splitter, M: mirror, L: lens, PD: photodiode.

walls of the cell cavity. Upon exiting the cell, the light was collimated onto a photodiode (PD3) and a signal was recorded as a function of the frequency scan of the laser.

A.2 Results and discussion

Typical spectra of the absorption signals obtained with the two MEMS cells provided, hereafter referred to by their manufacturer IDs, H12 and H20, are shown in figure A.2 and A.3 as functions of linear detuning, respectively, along with sample fits carried out using *ElecSus*. The fits were carried out leaving only three free parameters: the number density of Rb atoms (*i.e.* the temperature T of the gas), additional Lorentzian broadening Γ_{Buf} and line-centre shifts δ_{Buf} due to buffer gas in the cell. All other parameters remained constrained to the theoretical model used and to the experimental conditions. For the spectra shown in figure A.3 the fit gives $T = (62.89 \pm 0.03)°\text{C}$, $\Gamma_{\text{Buf}} = (2550 \pm 11)$ MHz and $\delta_{\text{Buf}} = (-642 \pm 4)$ MHz. For the spectra shown

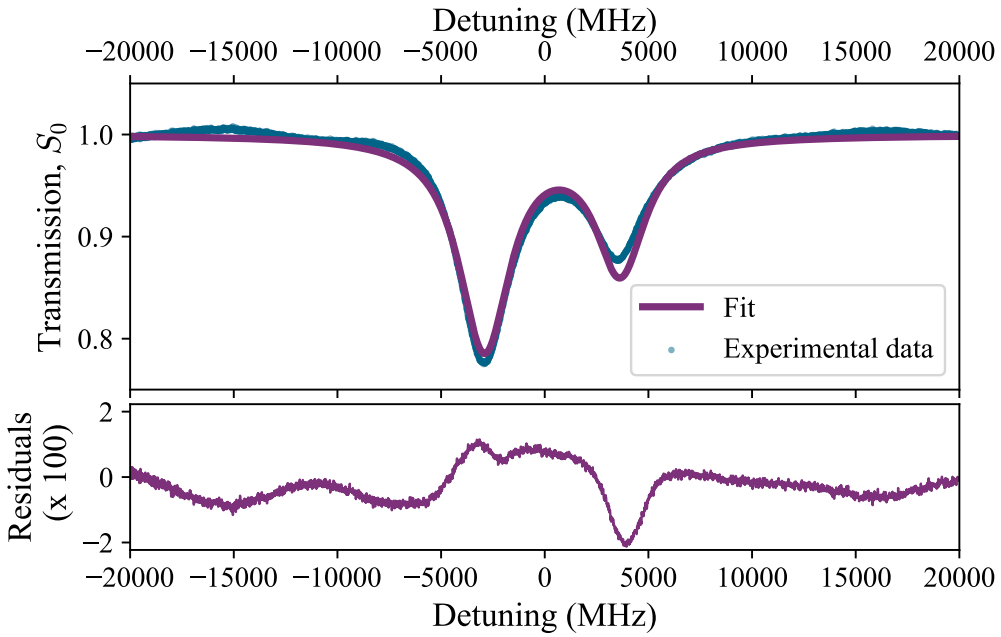

Figure A.2: Sample absorption spectrum using MEMS cell H12. In the top panel, experimental data and a fit from theory are shown while the fit residuals, multiplied by a factor of 100, are shown in the bottom panel. From the fit we obtain values of $T = (72.42 \pm 0.03)°\mathrm{C}$, $\Gamma_{\mathrm{Buf}} = (2632 \pm 11)$ MHz and $\delta_{\mathrm{Buf}} = (-515 \pm 5)$ MHz. The error in the fit is smaller than 1% RMS, which typically indicates very good agreement between theory and experimental data [155]. However, the visible presence of structure in the residuals around the regions corresponding to the peaks, as well as the mismatch between the data and fit in these regions, indicate there is a systematic variation not taken into account by our model.

in figure A.2 the fit gives $T = (72.42 \pm 0.03)°\mathrm{C}$, $\Gamma_{\mathrm{Buf}} = (2632 \pm 11)$ MHz and $\delta_{\mathrm{Buf}} = (-512 \pm 5)$ MHz. The uncertainties presented in the previous values correspond to the errors in the fit carried out for the spectra shown.

From the manufacturing specifications we can use the measured pressures of the buffer gasses in the cell to give an approximate value for the expected broadening and shift of the absorption features. Said values can be found in table A.2. Comparing these roughly-estimated values with the experimental results, given in table A.3, we see that there is little agreement between the values. The experimentally obtained additional broadening Γ_{Buf} is almost a factor of two greater than the value expected from the measured pressure. However, it is worth noting that the experimental values were obtained

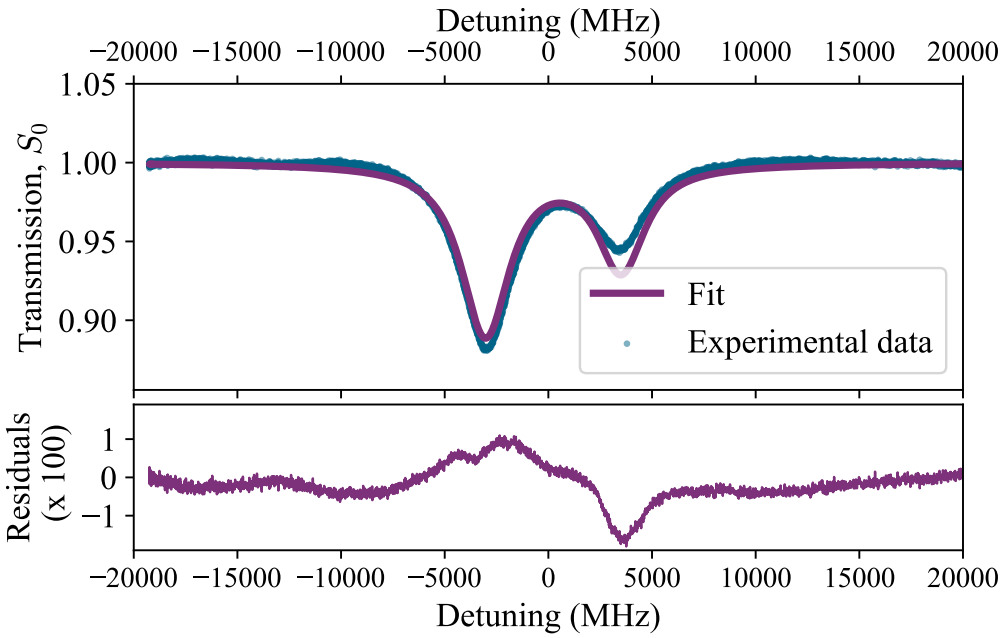

Figure A.3: Sample absorption spectrum using MEMS cell H20. In the top panel, experimental data and a fit from theory are shown while the fit residuals, multiplied by a factor of 100, are shown in the bottom panel. From the fit we obtain values of $T = (62.89 \pm 0.03)°\text{C}$, $\Gamma_{\text{Buf}} = (2550 \pm 11)$ MHz and $\delta_{\text{Buf}} = (-642 \pm 4)$ MHz. The error in the fit is smaller than 1% RMS, which typically indicates very good agreement between theory and experimental data [155]. However, the visible presence of structure in the residuals around the regions corresponding to the peaks, as well as the mismatch between the data and fit in these regions, indicate there is a systematic variation not taken into account by our model.

Cell	Measured Ar (mbar)	Measured N_2 (mbar)	Expected Γ_{Buf} (MHz)	Expected δ_{Buf} (MHz)
H12	57.4	61.1	1601	-513
H20	45.6	42.5	1189	-382

Table A.2: Measured pressure values of the different buffer gas components present in the MEMS cells, as measured by the manufacturer using the method in reference [243]. Measurements were carried out at room temperature (23° C). Using the coefficients in table A.1 we can give an approximation of the broadening and shift of the spectral features corresponding to the measured buffer gas pressures.

Cell	Temp. (°C)	Γ_{Buf} (MHz)	δ_{Buf} (MHz)
H12	62.89 ± 0.03	2632 ± 11	-515 ± 5
H20	72.42 ± 0.03	2550 ± 11	-642 ± 4

Table A.3: Experimental values for buffer gas effects (broadening and shift) in MEMS vapour cells obtained by fits using our theory model [134, 141]. These values correspond to the fit curves seen in figures A.3 and A.2.

with an atomic sample which was approximately three times hotter than the conditions used by the manufacturer for measurement of the buffer gas content. For the values of the frequency shift we can see that there is a slightly better agreement, with the experimental shift for cell H12 agreeing with the expected value while the value for cell H20 is a factor of two larger than the expected value.

Using the experimental values for the broadening of the absorption lineshape we can estimate the buffer gas content. To do this, we will use the values in table A.2 for the measured components of buffer gases in the cell in order to obtain the mole fraction of said components. We will be assuming that for the cell volume ($\sim 7\text{mm}^3$) we have a mixture of ideal gases and that the vapour pressure of Rb is much smaller than that of the buffer gases despite the cell being heated. With this in mind, we find that for cell H12 the ratio of the fraction of argon is $x_{Ar} \approx 48.4\%$ and that of N_2 is $x_{N_2} \approx 51.6\%$, while for cell H20 $x_{Ar} \approx 51.8\%$ and $x_{N_2} \approx 48.2\%$. Thus, taking the total additional broadening found from the fits, Γ_{Buf}, we can use a straightforward calculation between ratios to obtain the experimental values for the partial pressures of Ar and N_2, seen in table A.4.

Cell	**Ar fraction (%)**	**Exp. Ar pressure (torr)**	N_2 **fraction (%)**	**Exp.** N_2 **pressure (torr)**
H12	48.4	72 ± 11	51.6	74 ± 11
H20	51.8	75 ± 11	48.2	67 ± 11

Table A.4: Experimental values for the buffer gas pressures in the MEMS cells. The values were calculated by assuming no considerable pressure from the Rb in the cell and an ideal-gas mixture. The mole fraction for each of the gases, used to determine the fraction of Γ_{Buf} (see table A.3) due to each of the components, was obtained from the values in table A.2.

It can be clearly seen from figures A.2 and A.3 that while the overall fit is very good ($< 1\%$ RMS error) [155] there are areas of the spectra where the theory model does not coincide with the experimental data. In particular, the model does not reproduce the on-resonance absorption for both hyperfine transitions of the D2 line. This highlights the presence of a systematic effect not previously considered in the model due in particular to the large amount of buffer gas in the cell. As such, an independent fit using Voigt profiles with the necessary physical values for the width and centre parameters, but with freedom to adjust the individual values of amplitude for each of the profiles, was carried out. In this case, the only free parameters were Γ_{Buf} and δ_{Buf}; the temperature was taken directly from the thermistor in the cell mount and used to calculate the Gaussian component (Γ_{Dopp}) of the Voigt profile. The results of this fit can be seen in figures A.4 and A.5. With this simplified model, the fit gives $\Gamma_{\text{Buf}} = (1273 \pm 2)$ MHz and $\delta_{\text{Buf}} = (-446 \pm 4)$ MHz for cell H20; for cell H12, the fit values are $\Gamma_{\text{Buf}} = (1278 \pm 6)$ MHz and $\delta_{\text{Buf}} = (-380 \pm 10)$ MHz. When compared to figures A.2 and A.3 it can be clearly seen that this method of fitting spectra achieves even better agreement with the experimental data ($< 0.5\%$ RMS error) while also being closer to the expected values from table A.2.

Additional spectra were also taken by placing the cell in a magnetic field generated by two rare-earth magnets. Once again, a fit was carried out for the experimental data with T, Γ_{Buf}, δ_{Buf} as free parameters for the model, with the addition of the magnetic field intensity B as a parameter. The

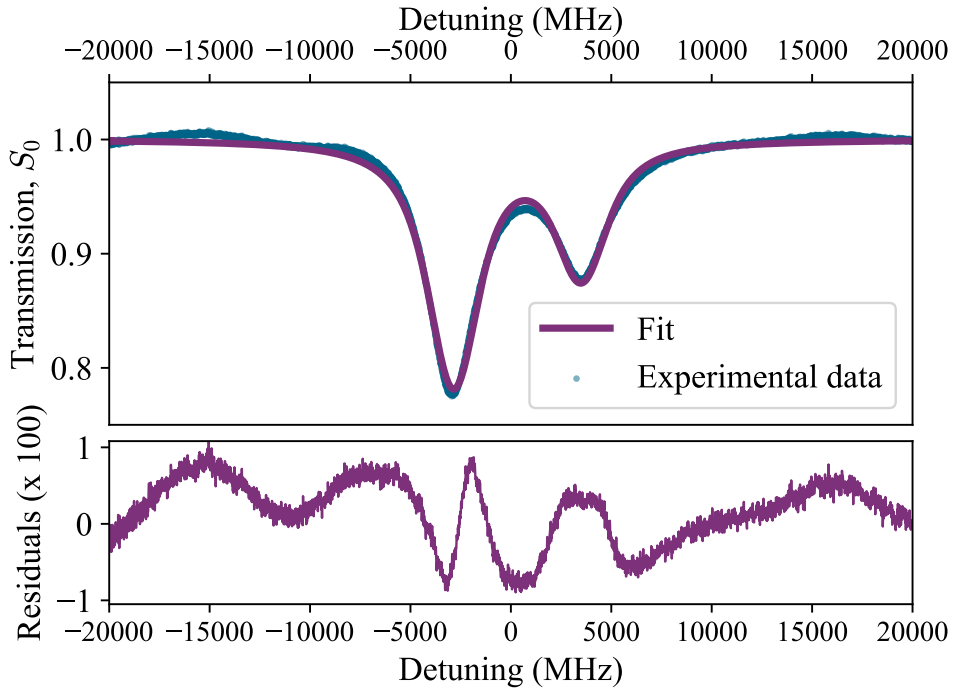

Figure A.4: Sample absorption spectrum using MEMS cell H12. In the top panel, experimental data and a fit from a simple model of two Voigt profiles are shown. Fit residuals, multiplied by a factor of 100, are shown in the bottom panel. From the fit we obtain values of $T = (82.23 \pm 0.05)°\mathrm{C}$, $\Gamma_{\mathrm{Buf}} = (1278 \pm 6)$ MHz and $\delta_{\mathrm{Buf}} = (-380 \pm 10)$ MHz. The error in the fit is smaller than 1% RMS, indicating better agreement between theory and experimental data [155] than that seen in figure A.2. In particular, the depth of the absorption features is correctly fit by using this simple model.

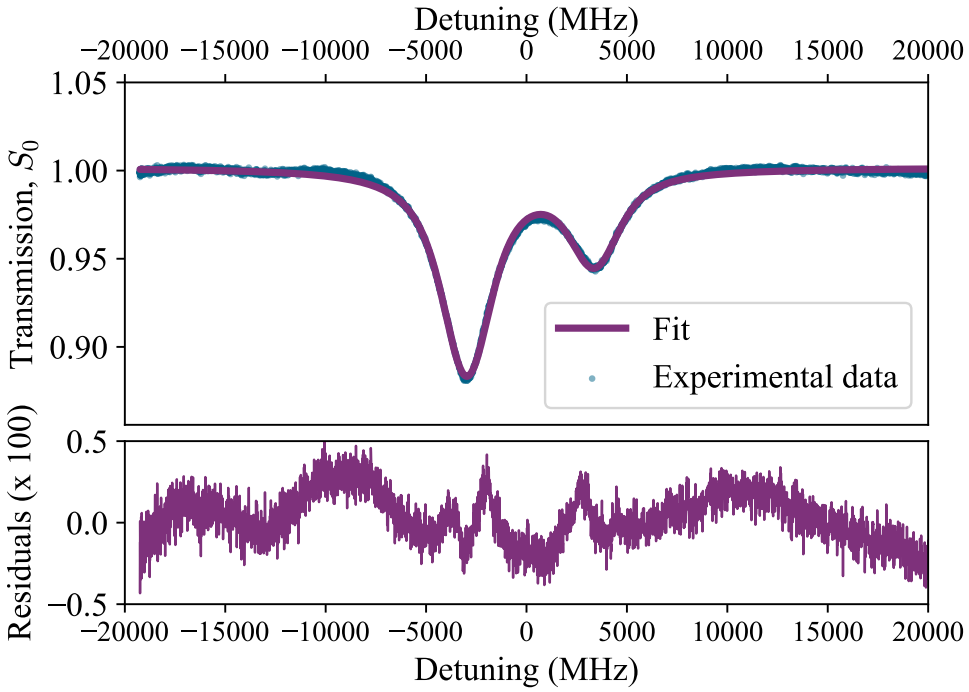

Figure A.5: Sample absorption spectrum using MEMS cell H20. In the top panel, experimental data and a fit from a simple model of two Voigt profiles are shown. Fit residuals, multiplied by a factor of 100, are shown in the bottom panel. From the fit we obtain values of $T = (72.17 \pm 0.05)°\mathrm{C}$, $\Gamma_{\mathrm{Buf}} = (1273 \pm 2)$ MHz and $\delta_{\mathrm{Buf}} = (-446 \pm 4)$ MHz. The error in the fit is smaller than 1% RMS, indicating better agreement between theory and experimental data [155] than that seen in figure A.3. In particular, the depth of the absorption features is correctly fit by using this simple model.

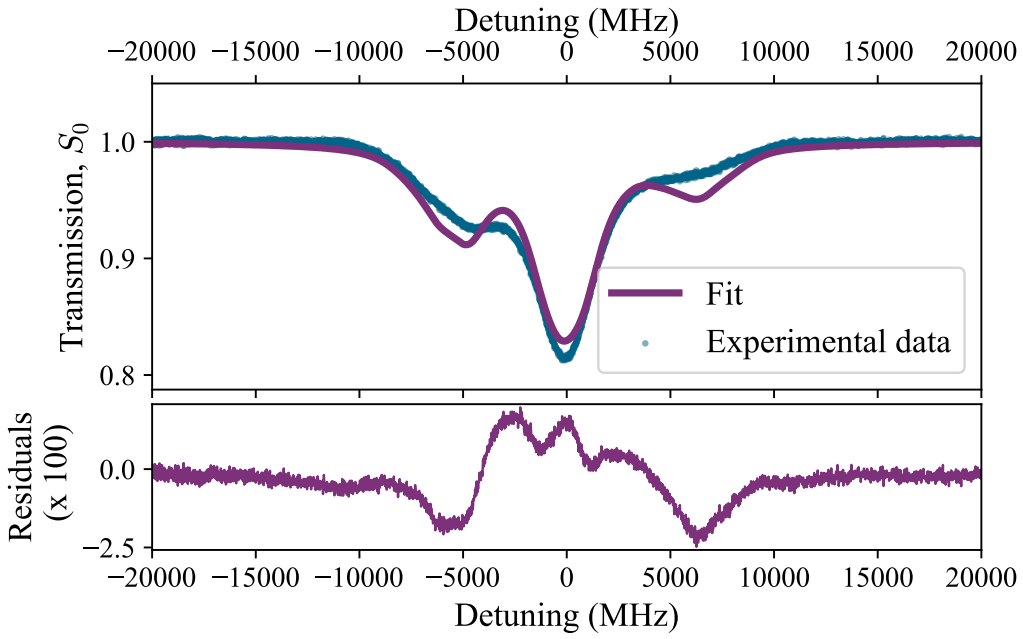

Figure A.6: Sample absorption spectrum using MEMS cell H12 in the presence of an external magnetic field. In the top panel, experimental data and a fit from theory are shown while the fit residuals, multiplied by a factor of 100, are shown in the bottom panel. From the fit we obtain values of $T = (70.95 \pm 0.03)°\text{C}$, $\Gamma_{\text{Buf}} = (1878 \pm 15)$ MHz and $\delta_{\text{Buf}} = (-636 \pm 6)$ MHz, with a magnetic field strength of $B = (127.5 \pm 2.4)$ mT. The error in the fit is smaller than 1% RMS, normally indicating very good agreement between theory and experimental data [155]. Nevertheless, there is a clear systematic variation in the depth of the calculated features as visible from the difference between data and fit and from the structure in the residuals.

results of this can be seen in figure A.6 and A.7. The values obtained for the spectrum shown are $T = (70.95 \pm 0.03)°\text{C}$, $\Gamma_{\text{Buf}} = (1878 \pm 15)$ MHz, $\delta_{\text{Buf}} = (-636 \pm 6)$ MHz and $B = (127.5 \pm 2.4)$ mT for cell H12 and $T = (78.94 \pm 0.04)°\text{C}$, $\Gamma_{\text{Buf}} = (2373 \pm 25)$ MHz, $\delta_{\text{Buf}} = (-642 \pm 11)$ MHz and $B = (199.9 \pm 0.1)$ mT for cell H20. Uncertainties are reported as the errors in the fit that was carried out for a single spectrum.

By using an external magnetic field in acquiring the spectra shown in figures A.6 and A.7 we were able to further support the idea of the presence of a systematic variation in the vapour cell that is unaccounted for in our model. It is evident once again that in these figures the quality of the fit

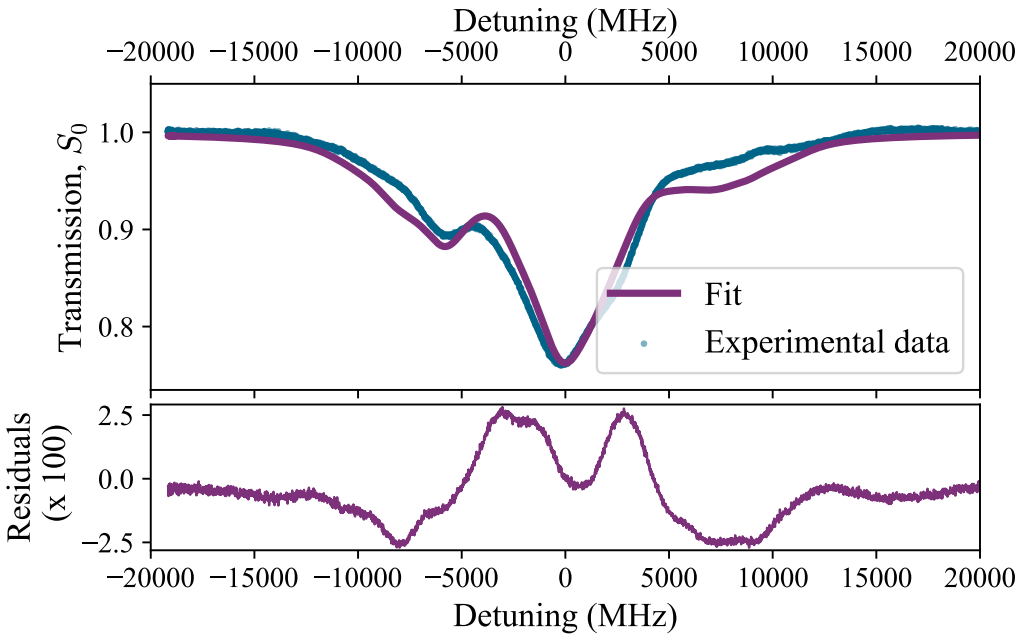

Figure A.7: Sample absorption spectrum using MEMS cell H20 in the presence of an external magnetic field. In the top panel, experimental data and a fit from theory are shown while the fit residuals, multiplied by a factor of 100, are shown in the bottom panel. From the fit we obtain values of $T = (78.94 \pm 0.04)°\mathrm{C}$, $\Gamma_{\mathrm{Buf}} = (2373 \pm 25)$ MHz and $\delta_{\mathrm{Buf}} = (-642 \pm 11)$ MHz, with a magnetic field strength of $B = (199.9 \pm 0.1)$ mT. The error in the fit is around 1% RMS, normally indicating good agreement between theory and experimental data [155]. Nevertheless, there is a clear systematic variation in the depth of the calculated features as visible from the difference between data and fit and from the structure in the residuals.

is good [155], with RMS errors of $\sim 1\%$, yet there are visible discrepancies between the experimental data and the fit. In particular we see that the depth of the absorption features in the experiment does not match that from our fit; in the presence of the magnetic field, we can observe that this systematic variation, seen in the zero-field case in the region of the main absorption peaks, is present at several other places in the spectra. This could indicate that the variation is due to a field-independent interaction, such as collisions between the buffer gas and rubidium atoms [56, 57] or due to changes in the populations in the atomic states [42, 55, 244].

A.3 Summary

From the absorption spectra obtained using the MEMS cells we get a value of $\Gamma_{\mathrm{Buf}} = (2632 \pm 11)$ MHz for cell H12 and $\Gamma_{\mathrm{Buf}} = (2550 \pm 11)$ MHz for cell H20 from fits carried out using our theoretical model *ElecSus*. Good agreement is found between experiment and theory, although the residuals present some remnant structure due to the fits not coinciding with the amplitude of the absorption features in the experimental data. Using a simple model, consisting of fitting Voigt profiles with a fixed Gaussian width of $\Gamma_{\mathrm{Dopp}} \approx 550$ MHz ($i.e$ $T \approx 80°\mathrm{C}$), but with independent amplitudes, different values for Γ_{Buf} were obtained, namely (1278 ± 6) MHz for cell H12 and (1273 ± 2) MHz for cell H20. Significantly better agreement is found between the model and experimental data in this case, indicating that our theoretical model does not completely reproduce the effects of large buffer gas pressures on the atomic system. This could indicate that there may be a change in the ground state populations due to the high buffer gas content in the cells.

Appendix B

Frequency calibration of spectra and removal of systematic errors in the background

B.1 Frequency calibration using a reference cell

The majority of the data presented in this work corresponds to atomic spectra, which are acquired as an electronic signal measured over the period of time the laser frequency is scanned. As such, the initial data is not directly useful when it is taken with equipment such as an oscilloscope or a data-acquisition (DAQ) module. In this case, the data is first processed to turn the electronic signal into a quantitative spectrum, where the time axis (x-axis) becomes a frequency axis based on a well-known reference and the vertical axis of the signal is transformed to represent the amount of light transmitted through the atomic vapour. A more detailed description of this process is given in section 3.3.2 with sample data from experiments in chapter 3. Here we present additional details to some of the aspects of the frequency calibration process.

In the context of the experiments performed, the frequency calibration of the horizontal axis is done by simultaneously recording the electronic signal from

two additional photodiodes, one monitoring the light transmitted through a 75 mm natural abundance Rb reference vapour cell at room temperature and the other monitoring the transmission of light through a Fabry-Pérot etalon. These two additional signals are then used to linearise and calibrate the horizontal axis of the electronic signal of interest so as to convert time units into frequency units: the signal from the Fabry-Pérot etalon, which has a well-known free-spectral range (FSR) (375 ± 1 MHz), allows us to extract the locations (in time) of the transmission peaks. The etalon in question is composed of two concave mirrors, with a 10 cm curvature radius[1], spaced approximately 30 cm apart.

For the frequency calibration in this work we have used custom code written in the Python programming language to analyse the spectra. Separate methods for the different aspects of the process discussed in section 3.3.2 are provided under a single class, allowing for ease of use. The positions in time of the etalon transmission peaks are obtained numerically by using custom Python code that uses the `numpy` package. This is done by looking for the maxima in the etalon transmission signal, taking into account a minimum height value and a minimum separation between peaks. Additional parameters allow for the detection of peaks to be tuned in order to identify a single position for each peak in the signal. This code, as well as its dependencies and a basic documentation, can be found in reference [245].

With the position of the peaks determined, a linear relation between peak positions and numbers (*i.e.* the order of appearance of the peaks) is determined via a least-squares fit using the `scipy.optimize` Python module. Uncertainties in these fit parameters are given as the standard error (1σ confidence interval). In order to take into account non-linear effects during the scan of the laser, the deviation of the peaks from their expected positions is calculate, as shown in figure 3.4. Using the `lmfit` package [149, 150], a high-order (≥ 5) polynomial is fit to these values using a differential evolution algorithm, followed by a least-squared minimisation in order to determine the uncertainties as mentioned above. The resulting polynomial is then used

[1] ThorLabs CM254P-050-E03

to convert the original time axis to a linearised time axis by generating a correction for each of the data points.

In order to fully calibrate the linearise time axis to absolute frequency reference values, the transmission spectrum from the natural abundance Rb reference cell is needed; using *ElecSus* (see section 2.4 for more details), the transmission signal is fitted and the hyperfine separations of the ground states (for both isotopes) are used to calibrate the frequency axis. This then allows for spectra with a well-defined frequency calibration, where the zero of the frequency axis corresponds to the centre of the ground state hyperfine manifold in the absence of external fields. Further details of this method can be found in references [72, 73, 154].

B.1.1 Calculation of the error in the frequency calibration

In order to calculate the error associated to the frequency calibration process, we proceed to carry out an analysis of the propagation of errors. Following the process described in section 3.3.2, we begin by writing an analytic expression for conversion of time to frequency. Given the raw time values for the experimental data, t_{raw}, we determine that the final frequency value ν along the horizontal axis is determined by the expression

$$\begin{aligned} \nu &= m_{t\to\nu} t_{\text{lin}} + c_{t\to\nu}, \\ &= m_{t\to\nu}(t_{\text{raw}} - t_{\text{corr}}) + c_{t\to\nu}, \end{aligned} \tag{B.1}$$

where t_{corr} is the non-linear correction applied in order to linearise the time axis, t_{lin} is the linearised time value, $(m_{t\to\nu} \pm \sigma_{m_{t\to\nu}})$ is the slope and $(c_{t\to\nu} \pm \sigma_{c_{t\to\nu}})$ is the y-axis intercept of the calibration obtained from fitting the reference absorption spectrum. We note that these last two parameters have an associated uncertainty, which we proceed to use in order to calculate the uncertainty σ_ν in the final frequency value. Taking the standard formulas for

the propagation of errors in reference [155], we arrive at the expression

$$\begin{aligned} \nu &= m_{t\to\nu} t_{\text{lin}} + c_{t\to\nu}, \\ \hookrightarrow \nu_{\text{lin}} = m_{t\to\nu} t_{\text{lin}} \ni \frac{\sigma_{\nu_{\text{lin}}}}{\nu_{\text{lin}}} &= \sqrt{\left(\frac{\sigma_{m_{t\to\nu}}}{m_{t\to\nu}}\right)^2 + \left(\frac{\sigma_{t_{\text{lin}}}}{t_{\text{lin}}}\right)^2}, \\ \therefore \sigma_\nu &= \sqrt{(\sigma_{\nu_{\text{lin}}})^2 + (\sigma_{c_{t\to\nu}})^2}. \end{aligned} \tag{B.2}$$

From this expression, we proceed to obtain a value of σ_ν for every point along the linearised time axis. The resulting curve can the be plotted, as shown in figure 3.6 (see section 3.3.2), and used to estimate the percentage error in the frequency calibration over the extent of the frequency scan.

B.2 Low-finesse etalons in the absorption background

In many cases processing the electronic signals into quantitative atomic spectra that can be analysed with the method described in B.1 allows for excellent agreement between the experimental data and the numerical model. However, in the cases where the laser frequency must be scanned over a range of tens or hundreds of GHz, systematic effects appear in the regions of the spectra that are far off-resonance. These effects appear in structured noise in the electronic signal background, and, in the case of optical systems with uncoated or misaligned surfaces, are due to the formation of low-finesse etalons in the optical setup [2, 205].

While usually not having a significant impact on the quality of the spectra, the presence of these low-finesse etalons can have an impact when carrying out measurements with high precision. For the experiments presented in this work these etalons can have an effect on the depth of the absorption features, which in turn affects the precision of the overall analysis performed.

In order to take into account the low-finesse etalons present in the signal background the model proposed in [2, 192, 205] is used. The model is based

on taking into account the transmission signal $\mathcal{T}$ of an etalon [132],

$$\mathcal{T} = \frac{\mathcal{T}_{\text{peak}}}{1 + (2\mathcal{F}/\pi)^2 \sin^2(\pi f / f_{\text{FSR}} + \phi)}, \tag{B.3}$$

where $\mathcal{F}$ is the finesse of the etalon, f_{FSR} is the free-spectral range (FSR), ϕ is the frequency offset of the etalon, f is the frequency of the light and $\mathcal{T}_{\text{peak}}$ is the peak transmission of the etalon signal. In the case where the finesse is low, $\mathcal{F} << 1$, we can modifiy equation B.3 by approximating the term $1/(1+x^2) \approx (1-x^2)$, thus giving an expression for the transmission in this regime of the form

$$\begin{aligned} \mathcal{T} &\approx \mathcal{T}_{\text{peak}}(1 - (2\mathcal{F}/\pi)^2 \sin^2(\pi f / f_{\text{FSR}} + \phi)), \\ &\approx \mathcal{T}_{\text{peak}}(1 - a \sin^2(\pi f / f_{\text{FSR}} + \phi)), \end{aligned} \tag{B.4}$$

where we have introduced the parameter $a = 4\mathcal{F}^2/\pi^2$ as the amplitude of the etalon.

From the expressions in equations B.3 and B.4 we can proceed to incorporate the effects of n distinct low-finesse etalons in the overall transmission by considering the measured transmitted light $\mathcal{T}_{\text{total}}$ as that due to the atomic absorption $\mathcal{T}_{\text{atom}}$ and the etalons $\mathcal{T}_{\text{etalon}}$,

$$\begin{aligned} \mathcal{T}_{\text{total}} &= \mathcal{T}_{\text{atom}} \times \mathcal{T}_{\text{etalon}}, \\ &= \mathcal{T}_{\text{atom}} \prod_{j=1}^{n} (1 - a_j \sin^2(\pi f / f_{j,\text{FSR}} + \phi_j)). \end{aligned} \tag{B.5}$$

We note that in equation B.5 we are considering that each of the n etalons has a unique finesse and free-spectral-range, as well as an offset, that characterises it.

Experimentally, we proceed to remove these etalons from the acquired optical signals in a straightforward manner. Once acquired, the spectrum of transmission $\mathcal{T}_{\text{total}}$ of light as a function of laser frequency through the atomic medium (S_0) is initially fit using *ElecSus*, as shown in figure B.1. This allows for the absorption due to the atoms, $\mathcal{T}_{\text{atoms}}$, to be determined; at this point we assume

there are no etalons in the signal and that, due to their low finesse, the characteristic absorption profiles of the atomic medium are not significantly altered. Using equation B.5 we can then obtain a signal for the etalon transmission by taking the quotient $\mathcal{T}_{\text{total}}/\mathcal{T}_{\text{atoms}}$. We fit this expression using a custom model built using the `lmfit` Python package [149, 150] using only three free parameters for each etalon: the etalon amplitude a, free-spectral-range (FSR) f_{FSR} and etalon offset ϕ. The number of etalons is increased iteratively from 1 to 6 until the residuals of the fit show no slowly-oscillating features and can be considered to be experimental noise; previous work using this method has found that this is typically achieved after introducing 3 etalons in the fit [2]. The results of carrying out this procedure are demonstrated in figure B.2

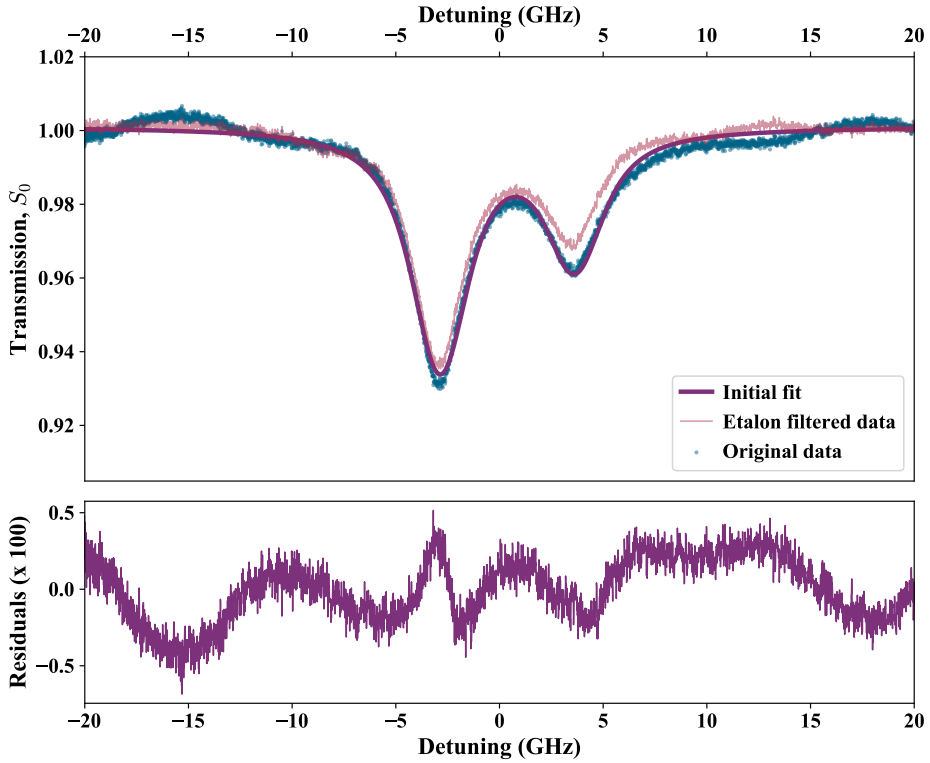

Figure B.1: Experimentally acquired absorption spectrum (S_0; blue dots) for a 1 mm ^{87}Rb vapour cell. An initial fit (purple curve) using *ElecSus* is carried out in order to obtain the transmission through the atomic medium $\mathcal{T}_{\text{atoms}}$ (see section 2.4); the residuals from this fit are shown, multiplied by a factor of 100 to better observe the presence of slowly-oscillating features. The fit RMS error here is 0.2%. The total transmission $\mathcal{T}_{\text{total}}$ is then divided by this fit (see equation B.5), leaving the transmission of a series of low-finesse etalons that correspond to the oscillating features in the residuals. These are fit, by iterating the number of etalons, using three free parameters: the etalon amplitude a, free-spectral-range (FSR) f_{FSR} and etalon offset ϕ. In this case, four etalons were included in the fit, resulting in a transmission signal with noticeably reduced background noise (red curve) which can subsequently be fit again for increased precision.

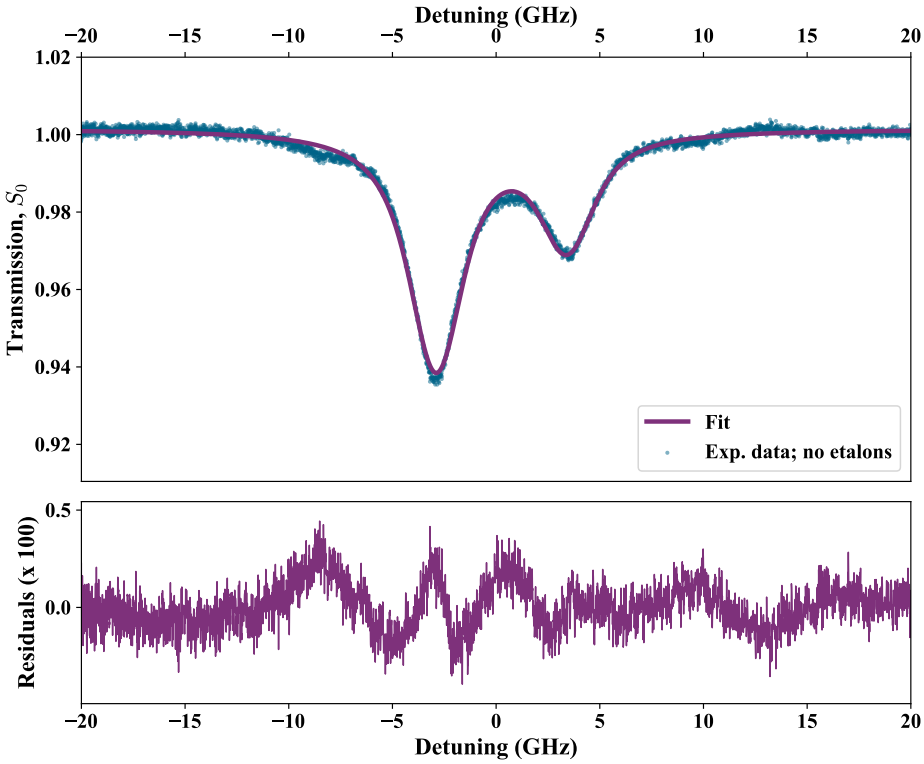

Figure B.2: Experimentally acquired absorption spectrum (S_0; blue dots) for a 1 mm ^{87}Rb vapour cell. A fit (purple curve) using *ElecSus* is carried out in order to obtain the transmission through the atomic medium $\mathcal{T}_{\text{atoms}}$ (as described in section 2.4); the residuals from this fit are shown, multiplied by a factor of 100 to better observe the removal of the slowly-oscillating features present in figure B.1. In this case, the RMS error of the fit is 0.1%, an improvement by a factor of two over the previous fit.

Bibliography

[1] T. H. Maiman. *Stimulated Optical Radiation in Ruby.* Nature **187**, 493 (1960).

[2] G.-W. Truong, J. D. Anstie, E. F. May, T. M. Stace, and A. N. Luiten. *Accurate lineshape spectroscopy and the Boltzmann constant.* Nat. Commun. **6**, 8345 (2015).

[3] M. S. Safronova, D. Budker, D. DeMille, D. F. J. Kimball, A. Derevianko, and C. W. Clark. *Search for New Physics with Atoms and Molecules.* Reviews of Modern Physics **90**, 025008 (2018). ArXiv: 1710.01833.

[4] R. Battesti, J. Beard, S. Böser, N. Bruyant, D. Budker, S. A. Crooker, E. J. Daw, V. V. Flambaum, T. Inada, I. G. Irastorza, F. Karbstein, D. L. Kim, M. G. Kozlov, Z. Melhem, A. Phipps, P. Pugnat, G. Rikken, C. Rizzo, M. Schott, Y. K. Semertzidis, H. H. J. ten Kate, and G. Zavattini. *High magnetic fields for fundamental physics.* Physics Reports (2018).

[5] J. Terrien. *News from the international bureau of weights and measures.* Metrologia **4**, 41 (1968).

[6] G. K. Campbell and W. D. Phillips. *Ultracold atoms and precise time standards.* Philos. Trans. R. Soc. A Math. Phys. Eng. Sci. **369**, 4078 (2011).

[7] A. D. Ludlow, M. M. Boyd, J. Ye, E. Peik, and P. O. Schmidt. *Optical atomic clocks.* Rev. Mod. Phys. **87**, 637 (2015).

[8] W. Loh, J. Stuart, D. Reens, C. D. Bruzewicz, D. Braje, J. Chiaverini, P. W. Juodawlkis, J. M. Sage, and R. McConnell. *Operation of an optical atomic clock with a Brillouin laser subsystem.* Nature **588**, 244 (2020). Number: 7837 Publisher: Nature Publishing Group.

[9] G. Bison, N. Castagna, A. Hofer, P. Knowles, J. L. Schenker, M. Kasprzak, H. Saudan, and A. Weis. *A room temperature 19-channel magnetic field mapping device for cardiac signals.* Appl. Phys. Lett. **95**, 173701 (2009).

[10] T. H. Sander, J. Preusser, R. Mhaskar, J. Kitching, L. Trahms, and S. Knappe. *Magnetoencephalography with a chip-scale atomic magnetometer.* Biomed. Opt. Express **3**, 981 (2012).

[11] O. Alem, T. H. Sander, R. Mhaskar, J. LeBlanc, H. Eswaran, U. Steinhoff, Y. Okada, J. Kitching, L. Trahms, and S. Knappe. *Fetal magnetocardiography measurements with an array of microfabricated optically pumped magnetometers.* Phys. Med. Biol. **60**, 4797 (2015).

[12] A. Osterwalder and F. Merkt. *Using high rydberg states as electric field sensors.* Phys. Rev. Lett. **82**, 1831 (1999).

[13] A. Horsley, G.-X. Du, and P. Treutlein. *Widefield microwave imaging in alkali vapor cells with sub-100 μ m resolution.* New J. Phys. **17**, 112002 (2015).

[14] C. G. Wade, N. Šibalić, N. R. de Melo, J. M. Kondo, C. S. Adams, and K. J. Weatherill. *Real-time near-field terahertz imaging with atomic optical fluorescence.* Nat. Photonics **11**, 40 (2016).

[15] C. G. Wade, M. Marcuzzi, E. Levi, J. M. Kondo, I. Lesanovsky, C. S. Adams, and K. J. Weatherill. *A terahertz-driven non-equilibrium phase transition in a room temperature atomic vapour.* Nature Communications **9**, 3567 (2018).

[16] M. H. Anderson, J. R. Ensher, M. R. Matthews, C. E. Wieman, and E. A. Cornell. *Observation of Bose-Einstein Condensation in a Dilute Atomic Vapor.* Science **269**, 198 (1995).

[17] C. C. Bradley, C. A. Sackett, J. J. Tollett, and R. G. Hulet. *Evidence of Bose-Einstein Condensation in an Atomic Gas with Attractive Interactions.* Phys. Rev. Lett. **75**, 1687 (1995).

[18] K. B. Davis, M. O. Mewes, M. R. Andrews, N. J. van Druten, D. S. Durfee, D. M. Kurn, and W. Ketterle. *Bose-Einstein Condensation in a Gas of Sodium Atoms.* Phys. Rev. Lett. **75**, 3969 (1995).

[19] G. C. Bjorklund. *Frequency-modulation spectroscopy: a new method for measuring weak absorptions and dispersions.* Opt. Lett. **5**, 15 (1980).

[20] S. Briaudeau, D. Bloch, and M. Ducloy. *Detection of slow atoms in laser spectroscopy of a thin vapor lm.* Eur. Lett. **35**, 337 (1996).

[21] I. Hamdi, P. Todorov, A. Yarovitski, G. Dutier, I. Maurin, S. Saltiel, Y. Li, and A. Lezama. *Laser Spectroscopy with Nanometric Gas Cells: Distance Dependence of Atom – Surface Interaction and Collisions under Confinement.* Laser Phys. **15**, 987 (2005).

[22] V. A. Sautenkov. *Line shapes of atomic transitions in excited dense gas.* Laser Phys. Lett. **8**, 771 (2011).

[23] J. Keaveney, A. Sargsyan, U. Krohn, I. G. Hughes, D. Sarkisyan, and C. S. Adams. *Cooperative Lamb Shift in an Atomic Vapor Layer of Nanometer Thickness.* Phys. Rev. Lett. **108**, 173601 (2012).

[24] D. J. Whiting, J. Keaveney, C. S. Adams, and I. G. Hughes. *Direct measurement of excited-state dipole matrix elements using electromagnetically induced transparency in the hyperfine Paschen-Back regime.* Phys. Rev. A **93**, 043854 (2016).

[25] L.-A. Liew, S. Knappe, J. Moreland, H. Robinson, L. Hollberg, and J. Kitching. *Microfabricated alkali atom vapor cells.* Appl. Phys. Lett. **84**, 2694 (2004).

[26] R. Straessle, M. Pellaton, C. Affolderbach, Y. Pétremand, D. Briand, G. Mileti, and N. F. de Rooij. *Microfabricated alkali vapor cell with anti-relaxation wall coating.* Appl. Phys. Lett. **105**, 043502 (2014).

[27] S. Knappe, V. Shah, P. D. D. Schwindt, L. Hollberg, J. Kitching, L.-A. Liew, and J. Moreland. *A microfabricated atomic clock.* Appl. Phys. Lett. **85**, 1460 (2004).

[28] M. Pellaton, C. Affolderbach, Y. Pétremand, N. de Rooij, and G. Mileti. *Study of laser-pumped double-resonance clock signals using a microfabricated cell.* Phys. Scr. **T149**, 014013 (2012).

[29] E. Kroemer, M. A. Hafiz, V. Maurice, B. Fouilland, C. Gorecki, and R. Boudot. *Cs vapor microcells with Ne-He buffer gas mixture for high operation-temperature miniature atomic clocks.* Optics Express **23**, 18373 (2015). Publisher: Optical Society of America.

[30] V. Shah, S. Knappe, P. D. D. Schwindt, and J. Kitching. *Subpicotesla atomic magnetometry with a microfabricated vapour cell.* Nat. Photon. **1**, 649 (2007).

[31] S. Woetzel, V. Schultze, R. Ijsselsteijn, T. Schulz, S. Anders, R. Stolz, and H. G. Meyer. *Microfabricated atomic vapor cell arrays for magnetic field measurements.* Rev. Sci. Instrum. **82**, 2 (2011).

[32] R. Mhaskar, S. Knappe, and J. Kitching. *A low-power, high-sensitivity micromachined optical magnetometer.* Appl. Phys. Lett. **101** (2012).

[33] S. Knappe, O. Alem, D. Sheng, and J. Kitching. *Microfabricated Optically-Pumped Magnetometers for Biomagnetic Applications.* J. Phys. Conf. Ser. **723**, 012055 (2016).

[34] C. L. Holloway, J. A. Gordon, S. Jefferts, A. Schwarzkopf, D. A. Anderson, S. A. Miller, N. Thaicharoen, and G. Raithel. *Broadband Rydberg atom-based electric-field probe for SI-traceable, self-calibrated measurements.* IEEE Trans. Antennas Propag. **62**, 6169 (2014).

[35] J. Kitching, E. A. Donley, S. Knappe, M. Hummon, A. T. Dellis, J. Sherman, K. Srinivasan, V. A. Aksyuk, Q. Li, D. Westly, B. Roxworthy, and A. Lal. *NIST on a Chip: Realizing SI units with microfabricated alkali vapour cells.* J. Phys. Conf. Ser. **723**, 012056 (2016).

[36] R. P. Abel, U. Krohn, P. Siddons, I. G. Hughes, and C. S. Adams. *Faraday dichroic beam splitter for Raman light using an isotopically pure alkali-metal-vapor cell.* Opt. Lett. **34**, 3071 (2009).

[37] Y. Wang, S. Zhang, D. Wang, Z. Tao, Y. Hong, and J. Chen. *Nonlinear optical filter with ultranarrow bandwidth approaching the natural linewidth.* Opt. Lett. **37**, 4059 (2012).

[38] M. A. Zentile, D. J. Whiting, J. Keaveney, C. S. Adams, and I. G. Hughes. *Atomic Faraday filter with equivalent noise bandwidth less than 1 GHz.* Opt. Lett. **40**, 2000 (2015).

[39] J. Keaveney, W. J. Hamlyn, C. S. Adams, and I. G. Hughes. *A single-mode external cavity diode laser using an intra-cavity atomic Faraday filter with short-term linewidth <400 kHz and long-term stability of <1 MHz.* Rev. Sci. Instrum. **87**, 095111 (2016).

[40] R. Dicke. *The Effect of Collisions upon the Doppler Width of Spectral Lines.* Phys. Rev. **89**, 472 (1953).

[41] N. Allard and J. Kielkopf. *The effect of neutral nonresonant collisions on atomic spectral lines.* Rev. Mod. Phys. **54**, 1103 (1982).

[42] B. A. Olsen, B. Patton, Y.-Y. Jau, and W. Happer. *Optical pumping and spectroscopy of Cs vapor at high magnetic field.* Phys. Rev. A **84**, 063410 (2011).

[43] M. Erhard, S. Nußmann, and H. Helm. *Power broadening and Doppler effects of coherent dark resonances in Rb.* Phys. Rev. A **62**, 061802(R) (2000).

[44] M. Erhard and H. Helm. *Buffer-gas effects on dark resonances: Theory and experiment.* Phys. Rev. A **63**, 043813 (2001).

[45] A. V. Taĭchenachev, V. I. Yudin, R. Wynands, M. Stähler, J. Kitching, and L. Hollberg. *Theory of dark resonances for alkali-metal vapors in a buffer-gas cell.* Physical Review A **67**, 033810 (2003).

[46] Z. D. Liu, D. Bloch, and M. Ducloy. *Absolute active frequency locking of a diode laser with optical feedback generated by Doppler-free collinear polarization spectroscopy.* Appl. Phys. Lett. **65**, 274 (1994).

[47] D. W. Preston. *Doppler-free saturated absorption: Laser spectroscopy.* Am. J. Phys. **64**, 1432 (1996).

[48] A. J. Olson, E. J. Carlson, and S. K. Mayer. *Two-photon spectroscopy of rubidium using a grating-feedback diode laser.* Am. J. Phys. **74**, 218 (2006).

[49] A. Cerè, V. Parigi, M. Abad, F. Wolfgramm, A. Predojević, and M. W. Mitchell. *Narrowband tunable filter based on velocity-selective optical pumping in an atomic vapor.* Opt. Lett. **34**, 1012 (2009).

[50] I. G. Hughes. *Velocity selection in a Doppler-broadened ensemble of atoms interacting with a monochromatic laser beam.* J. Mod. Opt. **0340**, 1 (2017).

[51] B. E. Sherlock and I. G. Hughes. *How weak is a weak probe in laser spectroscopy?* Am. J. Phys. **77**, 111 (2009).

[52] S. J. Seltzer and M. V. Romalis. *High-temperature alkali vapor cells with antirelaxation surface coatings.* J. Appl. Phys. **106**, 114905 (2009).

[53] S. J. Seltzer, D. J. Michalak, M. H. Donaldson, M. V. Balabas, S. K. Barber, S. L. Bernasek, M.-a. Bouchiat, A. Hexemer, a. M. Hibberd, D. F. J. Kimball, C. Jaye, T. Karaulanov, F. a. Narducci, S. a. Rangwala, H. G. Robinson, a. K. Shmakov, D. L. Voronov, V. V. Yashchuk, A. Pines, and D. Budker. *Investigation of antirelaxation coatings for*

alkali-metal vapor cells using surface science techniques. J. Chem. Phys. **133**, 144703 (2010).

[54] S. M. H. Khalkhali, M. Ranjbaran, D. Mofidi, S. M. Hamidi, and M. M. Tehranchi. *Improvement of the spin polarization lifetime in the 85Rb vapor cell by octadecyltrichlorosilane coating.* Chinese Journal of Physics **55**, 301 (2017).

[55] M. Arditi and T. R. Carver. *Hyperfine Relaxation of Optically Pumped* Rb^{87} *Atoms in Buffer Gases.* Physical Review **136**, A643 (1964).

[56] F. de Tomasi, M. Allegrini, E. Arimondo, G. S. Agarwal, and P. Ananthalakshmi. *Collision-enhanced resonance of laser-diode-excited Cs in a buffer gas.* Physical Review A **48**, 3820 (1993).

[57] M. D. Rotondaro and G. P. Perram. *Collisional broadening and shift of the rubidium D1 and D2 lines (52S12 → 52P12, 52P32) by rare gases, H2, D2, N2, CH4 and CF4.* Journal of Quantitative Spectroscopy and Radiative Transfer **57**, 497 (1997).

[58] L. Weller. *Absolute Absorption and Dispersion in a Thermal Rb Vapour at High Densities and High Magnetic Fields.* Phd thesis, Durham University (2013).

[59] M. A. Zentile. *Applications of the Faraday Effect in Hot Atomic Vapours Applications of the Faraday Effect in Hot Atomic Vapours.* Phd thesis, Durham University (2015).

[60] D. J. Whiting. *Nonlinear Optics in a Thermal Rb Vapour at High Magnetic Fields.* PhD Thesis, Durham University (2017).

[61] J. Maxwell. *The Scientific Letters and Papers of James Clerk Maxwell: Volume 2, 1862-1873.* Scientific Letters and Papers. Cambridge University Press (2009).

[62] D. P. Zeeman. *XXXIII. Doublets and triplets in the spectrum produced by external magnetic forces.—(II.).* The London, Edinburgh, and Dublin Philosophical Magazine and Journal of Science **44**, 255 (1897).

[63] D. P. Zeeman. *VII. Doublets and triplets in the spectrum produced by external magnetic forces.* The London, Edinburgh, and Dublin Philosophical Magazine and Journal of Science **44**, 55 (1897).

[64] D. P. Zeeman. *XXXII. On the influence of magnetism on the nature of the light emitted by a substance.* The London, Edinburgh, and Dublin Philosophical Magazine and Journal of Science **43**, 226 (1897).

[65] P. Zeeman. *The Effect of Magnetisation on the Nature of Light Emitted by a Substance.* Nature **55**, 347 (1897).

[66] F. v. Paschen and E. Back. *Normale und anomale Zeemaneffekte.* Annalen der Physik **344**, 897 (1912).

[67] F. Paschen and E. Back. *Liniengruppen magnetisch vervollständigt.* Physica **1**, 261 (1921).

[68] P. L. Kapitza, n. null, P. G. Strelkov, n. null, E. Laurman, and n. null. *The Zeeman and Paschen-Back effects in strong magnetic fields.* Proceedings of the Royal Society A: Mathematical, Physical and Engineering Sciences **167**, 1 (1938).

[69] W. D. Phillips and H. Metcalf. *Laser Deceleration of an Atomic Beam.* Phys. Rev. Lett. **48**, 596 (1982).

[70] J. Prodan, A. Migdall, W. D. Phillips, I. So, H. Metcalf, and J. Dalibard. *Stopping Atoms with Laser Light.* Phys. Rev. Lett. **54**, 992 (1985).

[71] J. Lawall, F. Bardou, B. Saubamea, K. Shimizu, M. Leduc, A. Aspect, and C. Cohen-Tannoudji. *Two-Dimensional Subrecoil Laser Cooling.* Phys. Rev. Lett. **73**, 1915 (1994).

[72] P. Siddons, C. S. Adams, C. Ge, and I. G. Hughes. *Absolute absorption on rubidium D lines: comparison between theory and experiment.* J. Phys. B **41**, 155004 (2008).

[73] L. Weller, R. J. Bettles, P. Siddons, C. S. Adams, and I. G. Hughes. *Absolute absorption on the rubidium D1 line including resonant dipole–dipole interactions.* J. Phys. B **44**, 195006 (2011).

[74] L. Weller. *Absolute Absorption and Dispersion in a Thermal Rb Vapour at High Densities and High Magnetic Fields.* Phd thesis, Durham University (2013).

[75] A. J. v. Lange, P. v. d. Straten, and D. v. Oosten. *Combined effect of non-linear optical and collisional processes on absorption saturation in a dense rubidium vapour.* Journal of Physics B: Atomic, Molecular and Optical Physics **53**, 125402 (2020). Publisher: IOP Publishing.

[76] D. Budker, W. Gawlik, D. F. Kimball, S. M. Rochester, V. V. Yashchuk, and A. Weis. *Resonant nonlinear magneto-optical effects in atoms.* Rev. Mod. Phys. **74**, 1153 (2002).

[77] P. Siddons, N. C. Bell, Y. Cai, C. S. Adams, and I. G. Hughes. *A gigahertz-bandwidth atomic probe based on the slow-light Faraday effect.* Nat. Photon. **3**, 225 (2009).

[78] P. Siddons, C. S. Adams, and I. G. Hughes. *Off-resonance absorption and dispersion in vapours of hot alkali-metal atoms.* J. Phys. B **42**, 175004 (2009).

[79] P. Siddons, C. S. Adams, and I. G. Hughes. *Optical control of Faraday rotation in hot Rb vapor.* Phys. Rev. A **81**, 043838 (2010).

[80] D. D. Budker and M. Romalis. *Optical magnetometry.* Nat. Phys. **3**, 227 (2007).

[81] D. Ciampini, R. Battesti, C. Rizzo, and E. Arimondo. *Optical spectroscopy of a microsized Rb vapour sample in magnetic fields up to 58 tesla.* Phys. Rev. A **96**, 052504 (2017).

[82] S. George, N. Bruyant, J. Béard, S. Scotto, E. Arimondo, R. Battesti, D. Ciampini, and C. Rizzo. *Pulsed high magnetic field measurement with a rubidium vapor sensor.* Rev. Sci. Instrum. **88**, 073102 (2017).

[83] M. R. Gomez, S. B. Hansen, K. J. Peterson, D. E. Bliss, A. L. Carlson, D. C. Lamppa, D. G. Schroen, and G. A. Rochau. *Magnetic field measurements via visible spectroscopy on the Z machine.* Rev. Sci. Instrum. **85**, 1 (2014).

[84] W. B. Garn, R. S. Caird, D. B. Thomson, and C. M. Fowler. *Technique for Measuring Megagauss Magnetic Fields Using Zeeman Effect.* Rev. Sci. Instrum. **37**, 762 (1966).

[85] I. Sobelman. *Atomic spectra and radiative transitions.* Springer Series on Atoms and Plasmas. Springer-Verlag, 2^{nd} edition (1992).

[86] C. Foot. *Atomic Physics.* Oxford Master Series in Physics. OUP Oxford (2004).

[87] L. Weller, K. S. Kleinbach, M. A. Zentile, S. Knappe, C. S. Adams, and I. G. Hughes. *Absolute absorption and dispersion of a rubidium vapour in the hyperfine Paschen–Back regime.* J. Phys. B **45**, 215005 (2012).

[88] A. Sargsyan, G. Hakhumyan, C. Leroy, Y. Pashayan-Leroy, A. Papoyan, D. Sarkisyan, and M. Auzinsh. *Hyperfine Paschen–Back regime in alkali metal atoms: consistency of two theoretical considerations and experiment.* J. Opt. Soc. Am. B **31**, 1046 (2014).

[89] L. Weller, T. Dalton, P. Siddons, C. S. Adams, and I. G. Hughes. *Measuring the Stokes parameters for light transmitted by a high-density rubidium vapour in large magnetic fields.* J. Phys. B **45**, 055001 (2012).

[90] E. Arimondo, D. Ciampini, and C. Rizzo. *Chapter One - Spectroscopy of Natural and Artificial Atoms in Magnetic Fields.* In E. Arimondo, C. C. Lin, and S. F. Yelin (editors), *Advances In Atomic, Molecular, and Optical Physics*, volume 65, pp. 1–66. Academic Press (2016).

[91] W. C. Griffith, S. Knappe, and J. Kitching. *Femtotesla atomic magnetometry in a microfabricated vapor cell.* Opt. Express **18**, 27167 (2010).

[92] J. Zhang, L. Xu, G. Bian, P. Fan, M. Li, W. Liu, and H. Yuan. *Diamond Nitrogen-Vacancy Center Magnetometry: Advances and Challenges.* arXiv:2010.10231 [physics, physics:quant-ph] (2020). ArXiv: 2010.10231.

[93] M. A. Zentile, R. Andrews, L. Weller, S. Knappe, C. S. Adams, and I. G. Hughes. *The hyperfine Paschen-Back Faraday effect.* arxiv.org p. 1401.1659 (2014).

[94] D. A. Smith and I. G. Hughes. *The role of hyperfine pumping in multilevel systems exhibiting saturated absorption.* Am. J. Phys. **72**, 631 (2004).

[95] S. L. Kemp, I. G. Hughes, and S. L. Cornish. *An analytical model of off-resonant Faraday rotation in hot alkali metal vapours.* J. Phys. B **44**, 235004 (2011).

[96] S. Xu, V. V. Yashchuk, M. H. Donaldson, S. M. Rochester, D. Budker, and A. Pines. *Magnetic resonance imaging with an optical atomic magnetometer.* Proceedings of the National Academy of Sciences **103**, 12668 (2006). Publisher: National Academy of Sciences.

[97] S. Xu, C. W. Crawford, S. Rochester, V. Yashchuk, D. Budker, and A. Pines. *Submillimeter-resolution magnetic resonance imaging at the Earth's magnetic field with an atomic magnetometer.* Phys. Rev. A **78**, 013404 (2008).

[98] E. Boto, S. S. Meyer, V. Shah, O. Alem, S. Knappe, P. Kruger, T. M. Fromhold, M. Lim, P. M. Glover, P. G. Morris, R. Bowtell, G. R. Barnes, and M. J. Brookes. *A new generation of magnetoencephalography: Room temperature measurements using optically-pumped magnetometers.* Neuroimage **149**, 404 (2017).

[99] L. Marmugi and F. Renzoni. *Optical Magnetic Induction Tomography of the Heart*. Sci. Rep. **6**, 23962 (2016).

[100] C. Deans, L. Marmugi, S. Hussain, and F. Renzoni. *Optical atomic magnetometry for magnetic induction tomography of the heart*. In *Proc. SPIE Photonic Europe, Quantum Optics*, volume 9900, p. 99000F. Belgium (2016). ISBN: 9781510601451_eprint: 1605.00839.

[101] Y. Hu, G. Z. Iwata, L. Bougas, J. W. Blanchard, A. Wickenbrock, G. Jakob, S. Schwarz, C. Schwarzinger, A. Jerschow, and D. Budker. *Rapid Online Solid-State Battery Diagnostics with Optically Pumped Magnetometers*. Applied Sciences **10** (2020).

[102] L. Marmugi, L. Gori, S. Hussain, C. Deans, and F. Renzoni. *Remote detection of rotating machinery with a portable atomic magnetometer* **56** (2017).

[103] L. Marmugi, C. Deans, and F. Renzoni. *Electromagnetic induction imaging with atomic magnetometers: Unlocking the low-conductivity regime*. Applied Physics Letters **115**, 083503 (2019).

[104] L. Q. Zhou, R. L. Patel, A. C. Frangeskou, A. Nikitin, B. L. Green, B. G. Breeze, S. Onoda, J. Isoya, and G. W. Morley. *Imaging damage in steel using a diamond magnetometer*. arXiv:2011.02459 [physics] (2020). ArXiv: 2011.02459.

[105] D. Budker, D. F. Kimball, S. M. Rochester, V. V. Yashchuk, and M. Zolotorev. *Sensitive magnetometry based on nonlinear magneto-optical rotation*. Physical Review A **62**, 043403 (2000).

[106] S. J. Seltzer. *Developments in Alkali-Metal Atomic Magnetometry*. PhD Thesis, Princeton University (2008).

[107] J. Kitching, S. Knappe, and E. a. Donley. *Atomic Sensors – A Review*. IEEE Sens. J. **11**, 1749 (2011).

[108] Y. Shapira, Y. Dallal, R. Ozeri, and A. Stern. *Measuring Magnetic Fields with Magnetic-Field-Insensitive Transitions*. Phys. Rev. Lett. **123**, 133204 (2019).

[109] C. Munuera-Javaloy, I. Arrazola, E. Solano, and J. Casanova. *Double quantum magnetometry at large static magnetic fields*. Physical Review B **101**, 104411 (2020). Publisher: American Physical Society.

[110] D. J. Whiting, R. S. Mathew, J. Keaveney, C. S. Adams, and I. G. Hughes. *Four-wave mixing in a non-degenerate four-level diamond*

configuration in the hyperfine Paschen–Back regime. J. Mod. Opt. **65**, 713 (2018).

[111] D. J. Whiting, E. Bimbard, J. Keaveney, M. A. Zentile, C. S. Adams, and I. G. Hughes. *Electromagnetically induced absorption in a nondegenerate three-level ladder system.* Opt. Lett. **40**, 4289 (2015).

[112] R. S. Mathew. *Single-Photon Generation via Four-Wave Mixing in a Thermal Rubidium Vapour at a High Magnetic Field.* PhD Thesis, Durham University (2021).

[113] J. Keaveney, F. S. Ponciano Ojeda, S. Rieche, M. J. Raine, D. P. Hampshire, and I. G. Hughes. *Quantitative optical spectroscopy of ^{87}Rb vapour in the Voigt geometry in DC magnetic fields up to 0.4 T.* Journal of Physics B: Atomic, Molecular and Optical Physics **52**, 055003 (2019).

[114] F. S. Ponciano-Ojeda, F. D. Logue, and I. G. Hughes. *Absorption spectroscopy and Stokes polarimetry in a ^{87}Rb vapour in the Voigt geometry with a 1.5 T external magnetic field.* Journal of Physics B: Atomic, Molecular and Optical Physics (2020).

[115] A. Messiah. *Quantum Mechanics.* Dover Publications (1999).

[116] M. Auzinsh, D. Budker, and S. M. Rochester. *Optically Polarized Atoms: Undestanding Light-Atom Interaction.* Oxford University Press, Oxford (2010).

[117] M. E. Rose. *Elementary Theory of Angular Momentum.* Dover Publications, Dover edition (1995).

[118] D. A. Steck. *Rubidium 85 D Line Data* (2009).

[119] D. A. Steck. *Rubidium 87 D Line Data* (2009).

[120] V. Gerginov, A. Derevianko, and C. E. Tanner. *Observation of the Nuclear Magnetic Octupole Moment of ^{133}Cs.* Physical Review Letters **91**, 072501 (2003). Publisher: American Physical Society.

[121] K. Beloy, A. Derevianko, V. A. Dzuba, G. T. Howell, B. B. Blinov, and E. N. Fortson. *Nuclear magnetic octupole moment and the hyperfine structure of the $5D_{3/2,5/2}$ states of the ${\text{Ba}}^{+}$ ion.* Physical Review A **77**, 052503 (2008). Publisher: American Physical Society.

[122] V. Gerginov, C. E. Tanner, and W. R. Johnson. *Observation of the nuclear magnetic octupole moment of 87Rb from spectroscopic meas-*

urements of hyperfine intervals. Canadian Journal of Physics (2011). Publisher: NRC Research Press Ottawa, Canada.

[123] N. C. Lewty, B. L. Chuah, R. Cazan, M. D. Barrett, and B. K. Sahoo. *Experimental determination of the nuclear magnetic octupole moment of ^{137}Ba^{+} ion*. Physical Review A **88**, 012518 (2013). Publisher: American Physical Society.

[124] A. K. Singh, D. Angom, and V. Natarajan. *Observation of the nuclear magnetic octupole moment of ^{173}Yb from precise measurements of the hyperfine structure in the ${{}^{3}P}_{2}$ state*. Physical Review A **87**, 012512 (2013). Publisher: American Physical Society.

[125] J. D. Jackson. *Classical Electrodynamics*. Wiley, 3rd edition (1999).

[126] M. O. Scully and M. S. Zubairy. *Quantum Optics*. Cambridge University Press (2001).

[127] H. J. Metcalf and P. van der Straten. *Laser Cooling and Trapping*. Springer (1999).

[128] M. Inguscio and L. Fallani. *Atomic Physics: Precise Measurements and Ultracold Matter*. OUP Oxford (2013).

[129] A. R. Edmonds. *Angular Momentum in Quantum Mechanics*. Princeton Landmarks in Mathematics and Physics. Princeton University Press, 4th edition (1996).

[130] E. Hecht. *Optics*. Pearson education. Addison-Wesley (2002).

[131] I. Kenyon and S. Kenyon. *The Light Fantastic: A Modern Introduction to Classical and Quantum Optics*. The Light Fantastic: A Modern Introduction to Classical and Quantum Optics. Oxford University Press (2008).

[132] C. S. Adams and I. G. Hughes. *Optics f2f - From Fourier to Fresnel*. Oxford University Press, Oxford, UK (2019).

[133] R. W. Boyd. *Nonlinear Optics*. Academic Press, USA, 3rd edition (2008).

[134] J. Keaveney, C. S. Adams, and I. G. Hughes. *ElecSus: Extension to arbitrary geometry magneto-optics*. Comput. Phys. Commun. **224**, 311 (2018).

[135] B. Schaefer, E. Collett, R. Smyth, D. Barrett, and B. Fraher. *Measuring the Stokes polarization parameters.* American Journal of Physics **75**, 163 (2007).

[136] W. H. McMaster. *Polarization and the Stokes Parameters.* American Journal of Physics **22**, 351 (1954). Publisher: American Association of Physics Teachers.

[137] B. Odom, D. Hanneke, B. D'Urso, and G. Gabrielse. *New Measurement of the Electron Magnetic Moment Using a One-Electron Quantum Cyclotron.* Phys. Rev. Lett. **97**, 030801 (2006).

[138] G. Gabrielse, D. Hanneke, T. Kinoshita, M. Nio, and B. Odom. *New Determination of the Fine Structure Constant from the Electron g Value and QED.* Phys. Rev. Lett. **97**, 030802 (2006).

[139] G. Woodgate. *Elementary Atomic Structure.* Oxford science publications. Clarendon Press (1980).

[140] M. Faraday. *On the magnetization of light and the illumination of magnetic lines of force.* Phil. Trans. R. Soc. Lond. **136**, 1 (1846).

[141] M. A. Zentile, J. Keaveney, L. Weller, D. J. Whiting, C. S. Adams, and I. G. Hughes. *ElecSus: A program to calculate the electric susceptibility of an atomic ensemble.* Comput. Phys. Commun. **189**, 162 (2015).

[142] I. Hirano. *Forward scattering magneto-optical spectra of the Cs ${\mathit{D}}_{2}$ line.* Physical Review A **50**, 4650 (1994).

[143] A. A. Fomin, M. Y. Petrov, G. G. Kozlov, M. M. Glazov, I. I. Ryzhov, M. V. Balabas, and V. S. Zapasskii. *Spin-alignment noise in atomic vapor.* Physical Review Research **2**, 012008 (2020). Publisher: American Physical Society.

[144] J. E. Sansonetti. *Wavelengths, transition probabilities, and energy levels for the spectra of rubidium (Rb i through Rb XXXVII).* J. Phys. Chem. Ref. Data **35**, 301 (2006).

[145] A. Kramida, Yu. Ralchenko, J. Reader, and and NIST ASD Team. NIST Atomic Spectra Database (ver. 5.8), [Online]. Available: `https://physics.nist.gov/asd` [2021, January 25]. National Institute of Standards and Technology, Gaithersburg, MD. (2020).

[146] J. Keaveney, I. G. Hughes, A. Sargsyan, D. Sarkisyan, and C. S. Adams. *Maximal Refraction and Superluminal Propagation in a Gaseous Nanolayer.* Phys. Rev. Lett. **109**, 233001 (2012).

[147] J. Keaveney, A. Sargsyan, D. Sarkisyan, A. Papoyan, and C. S. Adams. *Active narrowband filtering, line narrowing and gain using ladder electromagnetically induced transparency in an optically thick atomic vapour.* J. Phys. B **47**, 075002 (2014).

[148] A. Webber. *Optimization of Atomic Filters.* MPhys Report (unpublished), Durham University (2019).

[149] A. Newville, Matthew; Stensitzki, Till; Allen, Daniel B.; Ingargiola. *LMFIT: Non-Linear Least-Square Minimization and Curve-Fitting for Python* (2014).

[150] M. Newville, R. Otten, A. Nelson, A. Ingargiola, T. Stensitzki, D. Allan, A. Fox, F. Carter, Michał, D. Pustakhod, Y. Ram, Glenn, C. Deil, Stuermer, A. Beelen, O. Frost, N. Zobrist, Mark, G. Pasquevich, A. L. R. Hansen, T. Spillane, S. Caldwell, A. Polloreno, andrewhannum, J. Fraine, deep 42-thought, B. F. Maier, B. Gamari, A. Persaud, and A. Almarza. *LMFIT: Non-Linear Least-Square Minimization and Curve-Fitting for Python, v1.0.1* (2020).

[151] M. A. Zentile, R. Andrews, L. Weller, S. Knappe, C. S. Adams, and I. G. Hughes. *The hyperfine Paschen–Back Faraday effect.* J. Phys. B **47**, 075005 (2014).

[152] G.-W. Truong, J. D. Anstie, E. F. May, T. M. Stace, and A. N. Luiten. *Absolute absorption line-shape measurements at the shot-noise limit.* Phys. Rev. A **86**, 030501 (2012).

[153] B. L. Brandt, D. W. Liu, and L. G. Rubin. *Low temperature thermometry in high magnetic fields. VII. Cernox™ sensors to 32 T.* Rev. Sci. Instrum. **70**, 104 (1999).

[154] J. Keaveney. *Collective Atom–Light Interactions in Dense Atomic Vapours.* Springer Theses. Springer International Publishing, Cham (2014).

[155] I. G. Hughes and T. P. A. Hase. *Measurements and their Uncertainties: A Practical Guide to Modern Error Analysis.* OUP, Oxford (2010).

[156] N. W. Taylor and W. Rast. *The Diffusion of Helium and of Hydrogen Through Pyrex Chemically Resistant Glass.* The Journal of Chemical Physics **6**, 612 (1938).

[157] V. O. Altemose. *Helium Diffusion through Glass.* Journal of Applied Physics **32**, 1309 (1961).

[158] J. T. Banasek, J. T. Engelbrecht, S. A. Pikuz, T. A. Shelkovenko, and D. A. Hammer. *Measuring 10-20 T magnetic fields in single wire explosions using Zeeman splitting.* Rev. Sci. Instrum. **87**, 103506 (2016).

[159] L. Windholz. *Zeeman- and Paschen-Back-effect of the hyperfine structure of the sodiumD1-line.* Zeitschrift für Physik A Atoms and Nuclei **322**, 203 (1985).

[160] L. Windholz and M. Musso. *Zeeman- and Paschen-Back-effect of the hyperfine structure of the sodiumD2-line.* Zeitschrift für Physik D Atoms, Molecules and Clusters **8**, 239 (1988).

[161] C. Umfer, L. Windholz, and M. Musso. *Investigations of the sodium and lithium D-lines in strong magnetic fields.* Zeitschrift für Physik D Atoms, Molecules and Clusters **25**, 23 (1992).

[162] H. Hori, M. Miki, and M. Date. *Paschen-Back Effect of D-Lines in Sodium under a High Magnetic Field.* J. Phys. Soc. Japan **51**, 1566 (1982).

[163] A. Sargsyan, A. Tonoyan, G. Hakhumyan, A. Papoyan, E. Mariotti, and D. Sarkisyan. *Giant modification of atomic transition probabilities induced by a magnetic field: forbidden transitions become predominant.* Laser Physics Letters **11**, 055701 (2014).

[164] G. Hakhumyan, C. Leroy, R. Mirzoyan, Y. Pashayan-Leroy, and D. Sarkisyan. *Study of "forbidden" atomic transitions on D2 line using Rb nano-cell placed in external magnetic field.* The European Physical Journal D **66**, 119 (2012).

[165] G. Trénec, W. Volondat, O. Cugat, and J. Vigué. *Permanent magnets for Faraday rotators inspired by the design of the magic sphere.* Appl. Opt. **50**, 4788 (2011).

[166] E. Jahier, J. Guéna, P. Jacquier, M. Lintz, A. V. Papoyan, and M. A. Bouchiat. *Temperature-tunable sapphire windows for reflection loss-free operation of vapor cells.* Appl. Phys. B **71**, 561 (2000).

[167] A. Sargsyan, D. Sarkisyan, and A. Papoyan. *Dark-line atomic resonances in a submicron-thin Rb vapor layer.* Phys. Rev. A **73**, 1 (2006).

[168] A. Steffen, W. Alt, M. Genske, D. Meschede, C. Robens, and A. Alberti. *Note: In situ measurement of vacuum window birefringence by atomic spectroscopy.* Review of Scientific Instruments **84**, 126103 (2013).

[169] S. Knappe, V. Gerginov, P. D. D. Schwindt, V. Shah, H. G. Robinson, L. Hollberg, and J. Kitching. *Atomic vapor cells for chip-scale atomic clocks with improved long-term frequency stability.* Opt. Lett., OL **30**, 2351 (2005).

[170] H. Zijlstra. *Permanent magnet systems for NMR tomography.* Philips Journal of Research **40**, 259 (1985). Place: Netherlands.

[171] A. Ejlli, F. Della Valle, U. Gastaldi, G. Messineo, R. Pengo, G. Ruoso, and G. Zavattini. *The PVLAS experiment: a 25 year effort to measure vacuum magnetic birefringence.* arXiv:2005.12913 [hep-ex, physics:physics] (2020). ArXiv: 2005.12913.

[172] R. C. Jones. *A new calculus for the treatment of optical systems i. description and discussion of the calculus.* J. Opt. Soc. Am. **31**, 488 (1941).

[173] D. L. Carr, N. L. R. Spong, I. G. Hughes, and C. S. Adams. *Measuring the Faraday effect in olive oil using permanent magnets and Malus' law.* European Journal of Physics **41**, 025301 (2020).

[174] D. I. Hoult and R. E. Richards. *The signal-to-noise ratio of the nuclear magnetic resonance experiment.* Journal of Magnetic Resonance (1969) **24**, 71 (1976).

[175] P. Callaghan. *Principles of Nuclear Magnetic Resonance Microscopy.* Oxford science publications. Clarendon Press (1993).

[176] J. Wertz. *Electron Spin Resonance: Elementary Theory and Practical Applications.* Springer Netherlands (2012).

[177] R. Kleiner, D. Koelle, F. Ludwig, and J. Clarke. *Superconducting quantum interference devices: State of the art and applications.* Proceedings of the IEEE **92**, 1534 (2004). Conference Name: Proceedings of the IEEE.

[178] J. Clarke and A. I. Braginski. *The SQUID handbook*, volume 1. Wiley Online Library (2004).

[179] T. Rosenband, P. O. Schmidt, D. B. Hume, W. M. Itano, T. M. Fortier, J. E. Stalnaker, K. Kim, S. A. Diddams, J. C. J. Koelemeij, J. C. Bergquist, and D. J. Wineland. *Observation of the $^{1}S_{0}\ensuremath{\rightarrow}^{3}P_{0}$ Clock Transition in $^{27}\mathrm{Al}^{+}$.* Physical Review Letters **98**, 220801 (2007). Publisher: American Physical Society.

[180] S. M. Brewer, J.-S. Chen, K. Beloy, A. M. Hankin, E. R. Clements, C. W. Chou, W. F. McGrew, X. Zhang, R. J. Fasano, D. Nicolodi, H. Leopardi, T. M. Fortier, S. A. Diddams, A. D. Ludlow, D. J. Wineland, D. R. Leibrandt, and D. B. Hume. *Measurements of $^{27}\mathrm{Al}^{+}$ and $^{25}\mathrm{Mg}^{+}$ magnetic constants for improved ion-clock accuracy.* Physical Review A **100**, 013409 (2019). Publisher: American Physical Society.

[181] P. Micke, T. Leopold, S. A. King, E. Benkler, L. J. Spieß, L. Schmöger, M. Schwarz, J. R. Crespo López-Urrutia, and P. O. Schmidt. *Coherent laser spectroscopy of highly charged ions using quantum logic.* Nature **578**, 60 (2020). Number: 7793 Publisher: Nature Publishing Group.

[182] P. J. Mohr, D. B. Newell, B. N. Taylor, and E. Tiesinga. *Fundamental Physical Constants from NIST.*

[183] CODATA. *Fundamental Physical Constants* (2018).

[184] B. Sanguinetti, H. O. Majeed, M. L. Jones, and B. T. H. Varcoe. *Precision measurements of quantum defects in the n P 3/2 Rydberg states of 85 Rb.* J. Phys. B **42**, 165004 (2009).

[185] N. VVujičić, G. Kregar, T. Ban, D. Aumiler, and G. Pichler. *Frequency comb polarization spectroscopy of multilevel rubidium atoms.* The European Physical Journal D **68**, 9 (2014).

[186] D. A. Long, A. J. Fleisher, D. F. Plusquellic, and J. T. Hodges. *Multiplexed sub-Doppler spectroscopy with an optical frequency comb.* Physical Review A **94**, 061801 (2016).

[187] F. Zi, X. Wu, W. Zhong, R. H. Parker, C. Yu, S. Budker, X. Lu, and H. Müller. *Laser frequency stabilization by combining modulation transfer and frequency modulation spectroscopy.* Applied Optics **56**, 2649 (2017).

[188] N. B. Hébert, V. Michaud-Belleau, J. D. Anstie, J.-D. Deschênes, A. N. Luiten, and J. Genest. *Self-heterodyne interference spectroscopy using a comb generated by pseudo-random modulation.* Optics Express **23**, 27806 (2015).

[189] N. B. Hébert, V. Michaud-Belleau, C. Perrella, G.-W. Truong, J. D. Anstie, T. M. Stace, J. Genest, and A. N. Luiten. *Real-Time Dynamic Atomic Spectroscopy Using Electro-Optic Frequency Combs.* Physical Review Applied **6**, 044012 (2016).

[190] D. A. Long, A. J. Fleisher, D. F. Plusquellic, and J. T. Hodges. *Electromagnetically induced transparency in vacuum and buffer gas potassium cells probed via electro-optic frequency combs.* Optics Letters **42**, 4430 (2017).

[191] A. J. Metcalf, A. J. Metcalf, A. J. Metcalf, C. D. Fredrick, C. D. Fredrick, R. C. Terrien, R. C. Terrien, S. B. Papp, S. B. Papp, S. A. Diddams, S. A. Diddams, and S. A. Diddams. *30 GHz electro-optic frequency comb spanning 300 THz in the near infrared and visible.* Optics Letters **44**, 2673 (2019). Publisher: Optical Society of America.

[192] G.-W. Truong. *Quantitative atomic gas spectroscopy for the determination of the Boltzmann constant and primary thermometry.* PhD Thesis, University of Western Australia (2014).

[193] *Rubidium Frequency Standard - FS725.* Online.

[194] E. D. Black. *An introduction to Pound–Drever–Hall laser frequency stabilization.* American Journal of Physics **69**, 79 (2001). Publisher: American Association of Physics Teachers.

[195] R. V. Pound. *Electronic Frequency Stabilization of Microwave Oscillators.* Review of Scientific Instruments **17**, 490 (1946). Publisher: American Institute of Physics.

[196] R. W. P. Drever, J. L. Hall, F. V. Kowalski, J. Hough, G. M. Ford, A. J. Munley, and H. Ward. *Laser phase and frequency stabilization using an optical resonator.* Applied Physics B **31**, 97 (1983).

[197] BIPM. *Mise en pratique for the definition of the metre in the SI* (2019).

[198] H. Bettin and S. Schlamminger. *Realization, maintenance and dissemination of the kilogram in the revised SI.* Metrologia **53**, A1 (2016). Publisher: IOP Publishing.

[199] R. S. Davis, P. Barat, and M. Stock. *A brief history of the unit of mass: continuity of successive definitions of the kilogram.* Metrologia **53**, A12 (2016). Publisher: IOP Publishing.

[200] BIPM. *BIPM - SI Brochure.*

[201] M. Stock, R. Davis, E. d. Mirandés, and M. J. T. Milton. *The revision of the SI—the result of three decades of progress in metrology.* Metrologia **56**, 022001 (2019). Publisher: IOP Publishing.

[202] BIPM. *BIPM - Resolution of the 1st CGPM.*

[203] D. R. White and J. Fischer. *The Boltzmann constant and the new kelvin.* Metrologia **52**, S213 (2015).

[204] J. Fischer. *Progress towards a new definition of the kelvin.* Metrologia **52**, S364 (2015).

[205] G.-W. Truong, D. Stuart, J. D. Anstie, E. F. May, T. M. Stace, and A. N. Luiten. *Atomic spectroscopy for primary thermometry.* Metrologia **52**, S324 (2015).

[206] S. Mejri, P. L. T. Sow, O. Kozlova, C. Ayari, S. K. Tokunaga, C. Chardonnet, S. Briaudeau, B. Darquié, F. Rohart, and C. Daussy. *Measuring the Boltzmann constant by mid-infrared laser spectroscopy of ammonia.* Metrologia **52**, S314 (2015). Publisher: IOP Publishing.

[207] C.-F. Cheng, J. Wang, Y. R. Sun, Y. Tan, P. Kang, and S.-M. Hu. *Doppler broadening thermometry based on cavity ring-down spectroscopy.* Metrologia **52**, S385 (2015). Publisher: IOP Publishing.

[208] E. Fasci, M. D. D. Vizia, A. Merlone, L. Moretti, A. Castrillo, and L. Gianfrani. *The Boltzmann constant from the H2\hspace0.167em18O vibration–rotation spectrum: complementary tests and revised uncertainty budget.* Metrologia **52**, S233 (2015). Publisher: IOP Publishing.

[209] L. Landau and E. Lifshitz. *Statistical Physics*, volume 5 of *Course of Theoretical Physics.* Elsevier Science, 3rd edition (2013).

[210] P. Todorov, J. C. d. A. Carvalho, A. Laliotis, and D. Bloch. *Search for deviations from the ideal Maxwell-Boltzmann distribution for a gas at an interface.* arXiv:1810.04876 [physics] (2018). ArXiv: 1810.04876.

[211] W. Happer. *Optical Pumping.* Rev. Mod. Phys. **44**, 169 (1972).

[212] M. V. Balabas, T. Karaulanov, M. P. Ledbetter, and D. Budker. *Polarized Alkali-Metal Vapor with Minute-Long Transverse Spin-Relaxation Time.* Phys. Rev. Lett. **105**, 070801 (2010).

[213] M. V. Balabas. *Dependence of the longitudinal relaxation time of the polarization of cesium atoms in the ground state on the temperature of an antirelaxation coating.* Technical Physics **55**, 1324 (2010).

[214] S. J. Seltzer, M.-A. Bouchiat, and M. V. Balabas. *Surface coatings for atomic magnetometry*, p. 205–224. Cambridge University Press (2013).

[215] Y. W. Yi, H. G. Robinson, S. Knappe, J. E. Maclennan, C. D. Jones, C. Zhu, N. a. Clark, and J. Kitching. *Method for characterizing self-*

assembled monolayers as antirelaxation wall coatings for alkali vapor cells. J. Appl. Phys. **104**, 023534 (2008).

[216] S. J. Seltzer and M. V. Romalis. *High-temperature alkali vapor cells with antirelaxation surface coatings.* J. Appl. Phys. **106**, 114905 (2009).

[217] M. V. Balabas and O. Y. Tretiak. *Comparative study of alkali-vapour cells with alkane-, alkeneand 1-nonadecylbenzene-based antirelaxation wall coatings.* Quantum Electronics **43**, 1175 (2013).

[218] S. Li, P. Vachaspati, D. Sheng, N. Dural, and M. V. Romalis. *Optical rotation in excess of 100 rad generated by Rb vapor in a multipass cell.* Phys. Rev. A **84**, 061403 (2011).

[219] R. A. Hegstrom, J. P. Chamberlain, K. Seto, and R. G. Watson. *Mapping the weak chirality of atoms.* American Journal of Physics **56**, 1086 (1988). Publisher: American Association of Physics Teachers.

[220] D. N. Stacey. *Experiments on the Electro-Weak Interaction in Atoms.* Physica Scripta **T40**, 15 (1992). Publisher: IOP Publishing.

[221] F. D. Valle, U. Gastaldi, G. Messineo, E. Milotti, R. Pengo, L. Piemontese, G. Ruoso, and G. Zavattini. *Measurements of vacuum magnetic birefringence using permanent dipole magnets: the PVLAS experiment.* New Journal of Physics **15**, 053026 (2013). Publisher: IOP Publishing.

[222] K. L. Corwin, Z. T. Lu, C. F. Hand, R. J. Epstein, and C. E. Wieman. *Frequency-stabilized diode laser with the Zeeman shift in an atomic vapor.* Appl. Opt. **37**, 3295 (1998).

[223] G. Wasik, W. Gawlik, J. Zachorowski, and W. Zawadzki. *Laser frequency stabilization by Doppler-free magnetic dichroism.* Appl. Phys. B Lasers Opt. **75**, 613 (2002).

[224] T. Petelski, M. Fattori, G. Lamporesi, J. Stuhler, and G. Tino. *Doppler-free spectroscopy using magnetically induced dichroism of atomic vapor: a new scheme for laser frequency locking.* The European Physical Journal D - Atomic, Molecular, Optical and Plasma Physics **22**, 279 (2003).

[225] A. Millett-Sikking, I. G. Hughes, P. Tierney, and S. L. Cornish. *DAVLL lineshapes in atomic rubidium.* Journal of Physics B: Atomic, Molecular and Optical Physics **40**, 187 (2006).

[226] M. L. Harris, S. L. Cornish, A. Tripathi, and I. G. Hughes. *Optimization of sub-Doppler DAVLL on the rubidium D2 line.* Journal of Physics B: Atomic, Molecular and Optical Physics **41**, 085401 (2008).

[227] L. Weller, K. S. Kleinbach, M. A. Zentile, S. Knappe, I. G. Hughes, and C. S. Adams. *Optical isolator using an atomic vapor in the hyperfine Paschen-Back regime.* Opt. Lett. **37**, 3405 (2012).

[228] M. A. Zentile, D. J. Whiting, J. Keaveney, C. S. Adams, and I. G. Hughes. *Atomic Faraday filter with equivalent noise bandwidth less than 1 GHz.* Opt. Lett. **40**, 2000 (2015).

[229] J. Keaveney, W. J. Hamlyn, C. S. Adams, and I. G. Hughes. *A single-mode external cavity diode laser using an intra-cavity atomic Faraday filter with short-term linewidth <400 kHz and long-term stability of <1 MHz.* Rev. Sci. Instrum. **87**, 095111 (2016).

[230] J. Keaveney, S. A. Wrathmall, C. S. Adams, and I. G. Hughes. *Optimized ultra-narrow atomic bandpass filters via magneto-optic rotation in an unconstrained geometry.* Optics Letters **43**, 4272 (2018). ArXiv: 1806.08705.

[231] J. Keaveney, D. A. Rimmer, and I. G. Hughes. *Self-similarity of optical rotation trajectories around the Poincare sphere with application to an ultra-narrow atomic bandpass filter.* arXiv:1807.04652 [physics] (2018). ArXiv: 1807.04652.

[232] M. Abe, R. Itoyama, Y. Komiyama, T. Ito, T. Mashimo, and S. Tojo. *Quantitative investigation of the Zeeman and Paschen-Back effects of the hyperfine structure during the rubidium $5{\phantom{\rule{0.16em}{0ex}}}^{2}{S}_{1/2}\ensuremath{\rightarrow}5{\phantom{\rule{0.16em}{0ex}}}^{2}{D}_{5/2}$ two-photon transition.* Physical Review A **99**, 053420 (2019).

[233] L. Nieradko. *New approach of fabrication and dispensing of micromachined cesium vapor cell.* J. Micro/Nanolithography, MEMS, MOEMS **7**, 033013 (2008).

[234] E. Eklund, A. Shkel, S. Knappe, E. Donley, and J. Kitching. *Glass-blown spherical microcells for chip-scale atomic devices.* Sensors Actuators A Phys. **143**, 175 (2008).

[235] M. Hasegawa, R. Chutani, C. Gorecki, R. Boudot, P. Dziuban, V. Giordano, S. Clatot, and L. Mauri. *Microfabrication of cesium vapor cells*

with buffer gas for MEMS atomic clocks. Sensors Actuators A Phys. **167**, 594 (2011).

[236] G. Hakhumyan, A. Sargsyan, C. Leroy, Y. Pashayan-Leroy, A. Papoyan, and D. Sarkisyan. *Essential features of optical processes in neon-buffered submicron-thin Rb vapor cell.* Opt. Express **18**, 14577 (2010).

[237] B. L. Bean and R. H. Lambert. *Temperature dependence of hyperfine density shifts. IV. $^{23}\mathrm{Na}$, $^{39}\mathrm{K}$, and $^{85}\mathrm{Rb}$ in He, Ne, Ar, and ${\mathrm{N}}_{2}$ at low temperatures.* Physical Review A **13**, 492 (1976).

[238] J. Vanier, R. Kunski, N. Cyr, J. Y. Savard, and M. Têtu. *On hyperfine frequency shifts caused by buffer gases: Application to the optically pumped passive rubidium frequency standard.* Journal of Applied Physics **53**, 5387 (1982). Publisher: American Institute of Physics.

[239] J. F. Sell, M. A. Gearba, B. M. Patterson, D. Byrne, G. Jemo, T. C. Lilly, R. Meeter, and R. J. Knize. *Collisional excitation transfer between Rb(5P) states in 50-3000 Torr of 4He.* J. Phys. B At. Mol. Opt. Phys. **45** (2012).

[240] M. Parniak and W. Wasilewski. *Direct observation of atomic diffusion in warm rubidium ensembles.* Applied Physics B **116**, 415 (2014).

[241] S. Christopoulos, P. Moroshkin, L. Weller, B. Gerwers, R. Forge, T. Ockenfels, F. Vewinger, and M. Weitz. *Rubidium spectroscopy at high-pressure buffer gas conditions: detailed balance in the optical interaction of an absorber coupled to a reservoir.* Physica Scripta **93**, 124006 (2018). ArXiv: 1911.12586.

[242] M. Merimaa, T. Lindvall, I. Tittonen, and E. Ikonen. *All-optical atomic clock based on coherent population trapping in ^{85}Rb.* JOSA B **20**, 273 (2003).

[243] S. Karlen. *Fabrication and characterization of MEMS alkali vapor cells used in chip-scale atomic clocks and other atomic devices.* PhD Thesis, Universite de Nuechatel (2017).

[244] M. I. Fedorov, S. V. Ermak, M. V. Petrenko, E. N. Pyatyshev, and V. V. Semenov. *Investigation of coherent population trapping signals in 87Rb cells with buffer gas.* Journal of Physics: Conference Series **769**, 012046 (2016).

[245] F. S. Ponciano-Ojeda. *Francisco S. Ponciano - GitHub repository* (2021).